

Mechanical Regulation of Apoptosis and Calcification within Valvular Interstitial Cells

A Dissertation Submitted to the Faculty of the
WORCESTER POLYTECHNIC INSTITUTE

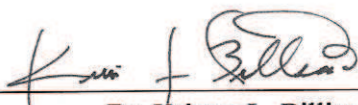
In partial fulfillment of the requirements for the Degree of Doctorate of Philosophy in Biomedical Engineering

March 9th, 2016

By



Heather A. Cirka



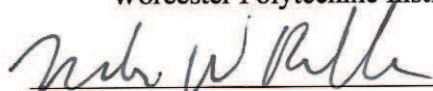
Dr. Kristen L. Billiar
Dissertation Advisor

Professor and Department Head
Department of Biomedical Engineering
Worcester Polytechnic Institute



Dr. Diane Hoffman-Kim
Associate Professor

Department of Molecular Pharmacology,
Physiology, and Biotechnology
Brown University



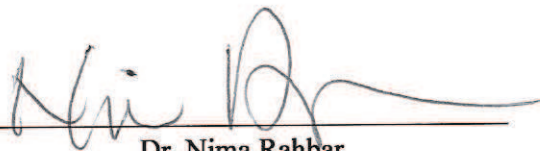
Dr. Marsha Rolle

Associate Professor, Head of Committee
Department of Biomedical Engineering
Worcester Polytechnic Institute



Dr. Qi Wen

Assistant Professor
Department of Physics
Worcester Polytechnic Institute



Dr. Nima Rahbar
Assistant Professor

Department of Civil and Environmental Engineering
Worcester Polytechnic Institute

Dedication

I would like to dedicate this work to my grandmother, "Babci", Barbara B. Cirka.

Acknowledgements

There are a number of people I would like to thank and acknowledge for all their assistance in different aspects of this project. First and foremost, I would like to thank my advisor, Dr. Kristen Billiar, for all the education, guidance, and opportunities. Thank you for challenging me to work hard as well as giving me the chance to become involved in all aspects of the lab, from grant writing and reviewing manuscripts, to lab management, student mentoring, as well as encouraging me to present my research in so many different places. Thank you for your enthusiasm for my project and supporting additional analysis techniques to better define my system. I certainly have become a better researcher, writer, speaker, and leader because of it all.

I would also like to thank my committee members: Dr. Marsha Rolle, Dr. Qi Wen, Dr. Nima Rahbar, and Dr. Diane Hoffman-Kim for their advising, guidance, training, mentorship, and the invaluable experience they have provided to me during the course of my graduate studies.

I would like to acknowledge the following WPI graduate students past and present who have helped me with experiments, data analysis, and scientific advising: Dr. Angela Throm-Quinlan, Dr. Jenna Balestrini, Dr. John Favreau, John Burford, Katrina Hansen, Dr. Amanda Clement, Dr. John Grasman, Dr. Mehmet Kural, Jason Forte, Dr. Benny Yin, Dina Rassias, David Dolivo, Dr. Sarah Hernandez, Gawain Thomas, Mina Shojaei, Ross Lagoy, Laura Aurilio, Sina Askarinejad, Mathilda Lutynski, Will Linthicum, and Siamak Faal. Thank you for the advice, comradery and memories. Many thanks to Ngozi Eze, PhD, Megan O'Brien, and Zach Goldblatt for their proof-reading and editing insights for this document. I would also like to thank the Gateway community as a whole for the open, friendly lab environment which has enabled interesting scientific discussions that has helped me with many different aspects of my project.

For all their assistance in the lab and contributions towards this and other projects, I would like to thank the following WPI undergraduate students, REU students, and exchange students: Vivian Liang, Johana Uribe, Nicole Diamadates, Melissa Monterosso, Tom Jones, Xuyu Qian, Jennifer Mann, Jeffrey Kelley, Jeffrey Pruden, Daniella Garcia, Brent Duoba, Joseph Lombardo, Kyaw Thu Minn, and Juan Rodriguez and Emma Marinescu.

I would like to thank Vicki Huntress for the countless hours of guidance during my imaging and confocal work as well as Hans Synder for assistance with histological stain preparation and sample tissue section preparation.

For guidance on various projects I worked on at WPI, I would like to thank the following faculty: Nancy Burnham, PhD, William Farr, PhD, and Domhull Granquest-Frasher, PhD. I would also like to specially thank Dean Terri Comesano, PhD, Glenn Gaudette, PhD, and Frank Hoy, PhD for the IGERT fellowship and translational research opportunities and education.

WPI personnel for administrative assistance and lab support: Elizabeth Stephien, Lynda Hammett, Tina Stratis, and Nancy Gaudette.

Thank you to the Sue Wheeler of the Animal Department at University of Massachusetts Medical School as well as the Blood Family and Blood Farm for assistance in obtaining tissue specimens. Thank you to Dr. Greg Hendricks of the University of Massachusetts Medical School Electron Microscopy Core for assistance with and teaching me the fundamentals of scanning electron microscopy and X-ray diffraction analysis.

Last, but certainly not least, I would like to thank my family and friends for supporting me through this journey. Most especially, I am grateful to my parents, David and Eileen, my sisters, Hillary and Haley, and my fiancé, John for all their love and support. I could not have done this without you.

Table of Contents

Dedication	i
Acknowledgements.....	ii
Table of contents	iv
Table of figures	x
Table of tables.....	xii
List of abbreviations and symbols	xiii
Glossary of terms	xv
Abstract.....	1
1 Introduction	3
2 Background	9
2.1 Calcific aortic valve disease overview.....	10
2.1.1 Risk of aortic stenosis	10
2.1.2 Progression of disease	11
2.1.3 Location of calcification on valve leaflets	14
2.1.4 Valve replacement	15
2.1.5 Calcification of Bioprosthetic Replacement Valves	17
2.2 Normal aortic valve physiology and function	18
2.2.1 Calculation of aortic valve area	18
2.2.2 Anatomy.....	20
2.3 Valvular interstitial cell mechanobiology	21
2.3.1 Cell-ECM and cell-cell connections	23
2.3.2 Mechanical characterization of VIC phenotype.....	24
2.3.3 Effect of substrate modulus on VIC phenotype.....	25
2.3.4 Cyclic stretch regulation of VIC phenotype apoptosis.....	27
2.3.5 Integration of multiple mechanical cues	29
2.3.6 Interactions between mechanical and soluble stimuli	30
2.4 <i>In Vitro</i> models of calcific aortic valvular disease	32
2.4.1 Mechanoregulation of calcification	33
2.4.2 Mechanoregulation of apoptosis.....	34
2.4.3 The apoptotic pathway and methods for quantifying apoptosis	35
2.5 Traction Force	37
2.5.1 Traction force trends	38
2.5.1.1 Measures of cell shape	40

2.6 Simultaneous measurement of stretch and traction force	40
2.7 Other measures of cell tension state.....	42
2.8 Geometric control of cell behavior	43
2.9 Rationale for quantitative methods.....	45
2.10 Summary	46
3 Role of Cell prestress on active traction force response	47
3.0 Abstract.....	48
3.1 Introduction	47
3.2 Methods.....	52
3.2.1 Cell culture	52
3.2.2 Stretch system and culture well development.....	52
3.2.3 Tunable-Stiffness Traction Force Substrate Preparation.....	55
3.2.4 Traction force measurements.....	56
3.2.5 Orientation and area measurements	59
3.2.6 Statistics	59
3.3 Results.....	60
3.4 Discussion.....	68
3.4.1 Effects of stretch on cytoskeletal structure and mechanics.....	69
3.4.2 Effect of long- and short-term stretch on cell traction force	70
3.4.3 Change in traction force with stretch	72
3.4.4 Reorientation of initially spread cells and effect of prestress.....	73
3.4.5 Reorientation and spreading of initially rounded cells with stretch	75
3.4.6 Limitations and future studies	76
3.5 Conclusions	77
3.6 Acknowledgements.....	77
4 Micro-contact printing for control of valvular interstitial aggregate formation as a novel <i>in vitro</i> model system for calcific aortic valvular disease	79
4.0 Abstract.....	80
4.1 Introduction	80
4.2 Methods.....	84
4.2.1 Micro-contact printing stamp design	84
4.2.2 Tunable gel substrate preparation	85
4.2.3 Micro-contact printing.....	85
4.2.4 Cell culture	87
4.2.5 Caspase activity.....	88

4.2.6 Immunohistochemistry.....	89
4.2.7 Calculation of average cell area.....	89
4.2.8 Calcium staining.....	89
4.2.9 Traction force microscopy.....	90
4.2.10 Image analysis.....	91
4.11 Scanning Electron Microscopy and X-ray Micro-Analysis.....	91
4.2.12 Statistics.....	91
4.3 Results.....	92
4.4 Discussion.....	107
4.4.1 Rapid Calcification Formation In Vitro.....	108
4.4.2 Calcifying Apoptotic Cells and Mineralized Particles.....	109
4.4.3 Geometric Control of Cell Behavior.....	111
4.4.4 Substrate Modulus and Calcification.....	111
4.4.5 Mechanical Characterization of VIC Aggregates.....	112
4.4.6 TGF- β 1 and the <i>In Vitro</i> Model of CAVD.....	113
4.4.7 Statins for preventing CAVD.....	114
4.5 Conclusions.....	115
4.6 Acknowledgements.....	115
5 Differential tension states within valvular interstitial cell aggregates contribute to pathological apoptosis: Implications for calcific aortic valvular disease.....	117
5.0 Abstract.....	118
5.1 Introduction.....	118
5.2 Methods.....	121
5.2.1 Micro-contact printing stamp design.....	121
5.2.2 Tunable gel substrate preparation.....	121
5.2.3 Micro-contact printing.....	121
5.2.4 Finite Element Modeling.....	122
5.2.5 Cell culture.....	123
5.2.6 Ligand coating magnetic beads.....	123
5.2.7 Applying ligand coated magnetic beads to aggregates.....	124
5.2.8 Magnetic pull.....	124
5.2.9 Caspase.....	125
5.2.10 Immunohistochemistry.....	126
5.2.11 Regional cell spread area analysis.....	126
5.2.11 Stress fiber analysis.....	126

5.3 Results	127
5.4 Discussion.....	143
5.4.1 Distribution of tension	144
5.4.2 YAP in myofibroblastic differentiation.....	149
5.4.3 Altering myofibroblast behavior with mechanical force	150
5.4.4 Comparison of computational model and experimental data	151
6 Thesis Discussion, Limitations, and Future Work	155
6.1.1 Study objectives Aim 1.....	155
6.1.2 Study objectives Aim 2.....	158
6.2.1 Study limitations and future work: Aim 1.....	163
6.2.2 Study limitations and future work: Aim 2.....	165
6.2.3 Clinical Significance	178
7 Thesis Conclusions	166
8 References.....	184
9 Appendix	198
Appendix A: Protocols.....	198
A.1 Valvular Interstitial Isolation	198
A.2 PDMS well mold design	199
A.3 Creation of PDMS wells, releasing wells from mold, and cleaning mold...	199
A.4 Attachment of polyacrylamide gels onto the PDMS wells.....	201
A.5 Activation of glass coverslips.....	207
A.6 Creating PDMS stamps	208
A.7 Preparing bead glass.....	208
A.8 Preparing petri dishes for traction force measurement	209
A.9 Micro-contact printing protocol	209
A.10 Gluing coverslips to petri dishes for TFM.....	211
A.11 Antibiotic solution for gel sterilization	211
A.12 Image Acquisition for Traction force	212
A.13 Collagen attachment to PDMS and polyacrylamide gels	213
A.14 Cell culture media.....	213
A.15 Traction force calculation and codes.....	214
A.16 Caspase live cell detection reagent	220
A.17 Fixing Cells	220
A.18 Staining for α -SMA, phalloidin, and Hoesct with cover slipping details ..	221

A.19 Staining for Alkaline Phosphatase, phalloidin and Hoescht	223
A.20 Staining for vinculin, Phalloidin and Hoescht	224
A.21 Staining for YAP, Phalloidin and Hoescht	225
A.22 Ligand Coating Magnetic Beads.....	226
A.23 Adding Magnetic Beads to Aggregates.....	227
Appendix B: Supporting Information	229
B.1 Chapter 3 Supporting Information	229
B.2 Chapter 4 Supporting Information	240
B.3 Chapter 5 Supporting Information	241
Appendix C: Reprint Permissions	242
C.1 Chapter 2 Reprint Permissions	242

Table of Figures

Figure 2.1: Representative images of a healthy valve and a calcified valve	11
Figure 2.2: The whole heart is affected by aortic valve calcification	13
Figure 2.3: VIC aggregates <i>in vivo</i>	15
Figure 2.4: Schematic of tri-laminar structure of aortic valve leaflet.	21
Figure 2.5: VICs are exposed to myriad mechanical forces in a dynamic environment <i>in vivo</i>	23
Figure 2.6: Valvular interstitial cells (VICs) are mechanosensitive.....	26
Figure 2.7: VICs are capable of integrating multiple mechanical cues.....	29
Figure 2.8: Effect of substrate stiffness and tension on release of latent TGF- β	32
Figure 2.9: <i>In vitro</i> model of calcific aortic valvular disease.....	33
Figure 2.10: Schematic of the apoptotic pathway	36
Figure 2.11: Illustration of cell traction force generation against a substrate.....	38
Figure 2.12: Myofibroblasts generate increased traction force.....	39
Figure 2.13: Combining micro-contact printing with micro-posts	39
Figure 2.14: Relationship between cell tension and cell stiffness	43
Figure 2.15: Mechanical stresses predict cellular behaviors.....	45
Figure 3.1: Overview of traction force with stretch method	54
Figure 3.2: Overview of traction force measurements	58
Figure 3.3: Overview of experiments	61
Figure 3.4: Cell traction force and area change with long-term cyclic stretch	62
Figure 3.5: Cell shape and elongation changes with long-term cyclic stretch	63
Figure 3.6: Cells reorient with 24 hour stretch regardless of substrate stiffness	64
Figure 4.1: Overview of micro-contact printing on tunable modulus substrate.....	87
Figure 4.2: α -SMA incorporation into stress fibers is present in valvular interstitial cell aggregates	93
Figure 4.3: Micro-contact printing model of CAVD results in calcification with high fidelity	94
Figure 4.4: Rounded cells in center of aggregate contain mineralization with calcium	96
Figure 4.5: Rounded cell with internal accumulation of mineralized nanoparticles.....	97
Figure 4.6: Cell originating mineralized nanoparticles may be involved in CAVD <i>in vivo</i>	98
Figure 4.7: Calcification occurs in all aggregates, regardless of size.....	99
Figure 4.8: Aggregate overall traction force increases with aggregate size.....	101
Figure 4.9: Aggregate overall traction force increases with substrate stiffness	102

Figure 4.10: Calcification occurs in 200 μm diameter aggregates on all moduli of PA gels tested	104
Figure 4.11: TGF- β 1 increased mineralization activity, but did not increase caspase 3/7 activity	106
Figure 4.12: Pravastatin did not reduce apoptotic or calcification	107
Figure 5.1: Schematic of finite element model	123
Figure 5.2: Schematic of magnetic bead experiment.....	125
Figure 5.3: Preliminary support for hypothesis.....	129
Figure 5.4: Regional cell spread area analysis	130
Figure 5.5: Stress fiber analysis	132
Figure 5.6: Sub-image FFT analysis for stress fiber alignment	133
Figure 5.7: YAP undergoes nuclear translocation for cells on the aggregate periphery.....	134
Figure 5.8: Constitutively active YAP interferes with mechanosensing	135
Figure 5.9: Constitutively active YAP results in micro-contact printed patterns	136
Figure 5.10: α -SMA intensity and Max Principal Stress predicted by pre-strain model.	137
Figure 5.11: Caspase activity occurs most frequently in areas of low cell tension	139
Figure 5.12: Presence of magnetic microbeads affects α -SMA incorporation into stress fibers.....	142
Figure 5.13: Presence of magnetic microbeads reduces caspase activity	143
Figure 6.1: Human dermal on polyacrylamide	176
Figure 6.2: 24 time course shows migration and proliferation within aggregates.	177

Table of Tables

Table 2.1: CAVD stage classification, management, and patient outcomes.....	12
Table 2.2: Review of studies examining the mechanobiology of valvular interstitial cells.....	27
Table 2.3: Summary of studies combining traction force with stretch.....	42
Table 3.1 Cell traction force with stretch results	66
Table 4.1 Mini review of the <i>in vitro</i> model for CAVD	84

List of Abbreviations and symbols

μm	Micro-meter
μN	Micro-newton
$\mu\text{-print}$	Micro-contact printing
$^{\circ}$	Degrees
2D	Two dimensional
3D	Three dimensional
AFM	Atomic force microscopy
ANOVA	Analysis of variance
CAVD	Calcific aortic valvular disease
CCD	Charge coupled device
CTF	Cell traction force
DMEM	Dulbecco's modified eagle's medium
E	Young's modulus
ECM	Extracellular matrix
FBS	Fetal bovine serum
HDM	High density mapping
kPa	KiloPascal
M	meter
M	Molar
mm	millimeter
N	Newton
nN	Nano-newtwon

Pa	Pascal
PA	Polyacrylamide
PDMS	Polydimethyl siloxane
ROI	Region of interest
TCPS	Tissue culture polystyrene
TEHV	Tissue engineered heart valves
TGF- β 1	Transforming growth factor-beta one
VIC(s)	Valvular interstitial cell(s)
α -SMA	Alpha smooth muscle actin
θ	Angle
mRNA	Messenger ribonucleic acid
SEM	Scanning electron microscopy
ng	Nano-gram
K	Kelvin
C	Celsius
siRNA	Silencing RNA

Glossary of Terms

Activation	<p>Term used in the literature referring to the differentiation of fibroblasts to the myofibroblastic phenotype</p> <p>Additionally, used in this dissertation to describe treatment of polyacrylamide gels in hydrazine hydrate</p>
Aggregates	<p>A group/cluster of cells. Within Valvular interstitial cell aggregates pathology initiates from currently unknown mechanisms</p>
Aortic valve	<p>Tricuspid valve located between the left ventricle and the aorta</p>
Apatite	<p>Highly organized structure of calcium phosphate similar in structure to that of bone</p>
Apoptosis	<p>Programmed cell death which follows a specific, known pathway</p>
Atomic force microscopy	<p>Essentially a micro-indentation technique where a cantilever makes contact with the surface. The Young's modulus of the sample is calculated knowing the cantilever stiffness, tip geometry, and cantilever deflection.</p>
Cadherin	<p>One of the types of cell-to-cell linkages</p>
Caspase 3/7	<p>Known as the "effector" caspases. Part of the apoptotic signaling cascade</p>
Cell Stress	<p>A measure of cell tension normalized to the size of the cell. Low cell stress does not necessarily indicate low cell tension as it is divided by the area of a cell. A cell could be large and have great contractile ability but a low cell</p>

stress. For this reason, cell tension was the preferred term used throughout the dissertation and the variable evaluate experimentally.

Cell tension	The amount of tension within the network of cytoskeletal filaments. In this dissertation, it was evaluated by traction force microscopy in the case of single cell experiments.
Coadaptation	Term which refers to the leaflet overlay or “tight seal” , preventing the back flow of blood from the aorta to the ventricle
Contractile moment	the combination of the traction forces in the x- and y direction weighted by their respective coordinates
Dystrophic	Associated with cell death
<i>Ex vivo</i>	Biologic tissue or organ normally found inside the body or within an organism but is being studied outside of the body or organism
Extracellular matrix	Protein network found outside of the cell within which cells normally reside in the body
Form factor	A ratio of the cell spread area and cell perimeter. It is used as a measure of the number of cytoskeletal extensions
Fourier transform infrared spectroscopy	a technique which is used to obtain an infrared spectrum of absorption or emission of a solid, liquid or gas

Hoechst	A nuclear stain
<i>In vitro</i>	Within a petri dish
<i>In vivo</i>	Within the body
Integrin	Proteins which group together forming focal adhesions allowing cells to bind to the extracellular matrix
Media	Nutrient solution which is feed to cells to keep them alive
Micro-contact printing	A technique, similar to stamping with ink, where protein is deposited in specific patterns upon a substrate. Cells are restricted to growth within the protein islands
Nodule	Usually refers to a calcific nodule, a large calcified region which forms in the center of valvular interstitial cell aggregates
Osteogenic	Relating to mechanisms involved with bone formation
Phalloidin	Stains filamentous actin of the cytoskeleton
Regurgitation	The backflow of blood from the aorta to the left ventricle due to poor coadaptation of thickened valve leaflets
Scanning electron microscopy	A type of electron microscope that produces images of a sample by scanning it with a focused beam of electrons. The electrons interact with atoms in the sample, producing various signals that can be detected and that contain

	information about the sample's surface topography and composition
Stenosis	The process of valve leaflet thickening. As leaflets become thicker, they can no longer nicely co-adapt, reducing heart pumping efficiency
Substrate	Term in two-dimensional cell culture which refers to the surface of material cells are cultured on.
Traction force microscopy	Experimental method for determining the tractions on the surface of a biological cell by obtaining measurements of the surrounding displacement field within an <i>in vitro</i> extracellular matrix. In this dissertation, traction force microscopy was used to determine tension state of a cell.
Transforming growth factor- β	A cytokine that encourages differentiation to the myofibroblastic phenotype
Valvular interstitial cell	Main cell type in the heart valve
Yes associated protein-1 (YAP-1)	A nuclear transcription factor which locates to the nucleus when the cell is under high tension. It remains sequestered in cell cytosol when cell is in a low tension environment.
Young's modulus	A material property, often referred to in mechano-biology literature as "stiffness", though this is not entirely accurate
α -smooth muscle actin	Protein which becomes incorporated into stress fibers when cytoskeleton is under high tension. Considered the premier marker of activated valvular interstitial cells

Abstract

Calcific aortic valvular disease (CAVD) is the most common valvular pathology in the developed world. CAVD results in calcifications forming on the aortic valve leaflets, inhibiting proper closure and causing complications of stenosis and regurgitation. Although, the mechanisms behind the disease initiation are unknown, it is believed to be a cell-mediated phenomenon, and not the result of passive degradation of the valve as once believed due to the increased prevalence with age. Currently, there are no pharmaceutical options for the prevention or reversal of calcifications, the only treatment option is complete valve replacement, an imperfect solution. Hindering the development of potential therapeutics is that currently there are no adequate animal models which replicate the calcification and cell death seen in disease explanted valves.

An *in vitro* model has been developed where valvular interstitial cells (VICs), the main cell type of the valve, are seeded at high density into tissue culture polystyrene dishes and cultured with TGF- β 1. This results in VICs activating to the myofibroblast phenotype and forming cell aggregates. Due to currently unknown mechanisms, apoptosis occurs within the center of the aggregates and calcification ensues. Although simplistic, this model has been used to show that rate and frequency of aggregation is affected by cellular tension; conditions of high tension increase aggregation response, while conditions of low tension prevent aggregation and calcification from occurring. It is important to note; however, that despite its wide usage, the current model is limited as the aggregation and subsequent calcification are random occurrences and are not consistent across literature where same conditions for control samples are used.

The motivation of the presented work is two-fold. First, high intracellular tension has been suggested as one of the mechanisms leading to disease in the valve. Despite the clear and important

role of cell tension, VIC tension has never before been measured in a dynamic environment. The ways in which dynamic stimulation affects individual VIC tension is not known. In aim one, a method is developed to allow for long-term cyclic stretch of VICs with measurement of cell traction force. It was found that cyclic stretch decreased cell tension in cells with high prestress and increased cell tension for conditions of low prestress. Combined, these findings indicate a homeostatic cellular tension which is dependent upon the mechanical environment.

In the second aim, a novel method for creating VIC aggregates is validated. Micro-contact printing, essentially “stamping” of a protein in a defined pattern, is used to create circular aggregates on polyacrylamide gels. This method allows for the separation of the aggregation from the subsequent calcification, an improvement over the current *in vitro* model. The method is then used to explore the role of the distribution of tension in the initiation of disease

Chapter 1: Introduction

Calcific aortic valve disease (CAVD) is the most prevalent valvular disorder in the United States [1]. Currently, 2.8% of the population over 65 is believed to be affected by the disease [2]; the prevalence increases to 9.8% in octogenarians [3]. There are no medicinal or pharmaceutical interventions which can be prescribed to slow, halt, or reverse the progression of disease. The only remedy is a complete valve replacement surgery [4]. Due to the high risk and associated complications, valve replacement surgery is usually reserved for patients with late-stages of disease (see section 2.1.1 for details) [3]. Patients experience decreased quality of life until the disease progresses to the point that they are symptomatic and eligible for valve replacement [3]. The medical cost associated with such surgeries is a huge economic burden, estimated in the billions [5], and is expected to increase as the population ages.

CAVD results in calcific lesions forming on the valve leaflets. These calcifications inhibit normal function of the valve, resulting in stenosis and regurgitation [6]. There are two types of calcification that have been identified in explanted valves: dystrophic and osteogenic, present in 82% and 13% of diseased valves, respectively [7]. As defined, dystrophic calcification is calcification that occurs along with cell death [8], while osteogenic calcification is defined as calcifications created by bone-forming cells (osteoblasts) and is structurally similar to hydroxyapatite [9]. CAVD typically affects older patients, and for many years it was believed to be the result of degenerating valve cusp matrix. However, in recent decades, the study of valvular cells *in vitro* has given rise to the hypothesis that calcification may be cell-mediated, giving hope that future development of medicinal treatments is achievable [4].

CAVD is challenging to study as currently there are no acceptable animal models [10]. Additionally, examination of calcified pathological valves only reveals one time-point of the disease [7, 11] making it impossible to study the initiating factors and disorder progression. An *in vitro* model has been developed which replicates the dystrophic calcification seen *in vivo* [12]. The *in vitro* model of CAVD is created by seeding valvular interstitial cells (VICs), which are the main cell type in the aortic valve [13], onto tissue culture treated polystyrene dishes at high density in the presence of TGF- β 1 [12, 14]. The VICs “activate” from a fibroblast-like phenotype found in a healthy valve to myofibroblasts [13], which are a highly contractile and synthetic cell type characterized by the presence of alpha-smooth muscle actin (α -SMA) [15]. After approximately one week in culture, VICs aggregate together. VICs within the center of the aggregate undergo apoptosis, and calcification ensues. Although two-dimensional and relatively simplistic, this model has revealed a number of important factors which affect rates of VIC aggregate formation and subsequent calcification including the following: type of ligand coating [9], substrate stiffness [16], presence of stretch [17], Rho-pathway activity [18] as well as *in vitro* assessment of the efficacy of statins [19, 20] - a potential medicinal treatment for CAVD. However, the mechanisms behind the cell death within the center of the aggregate remains incompletely understood.

Despite the wide usage of the *in vitro* model to study CAVD, it does have certain limitations. It requires the aggregation to occur in order to initiate apoptosis and calcification. However, this approach is inefficient since the aggregation process is random, resulting in unpredictable aggregate formation. Aggregates for controls *in vitro* (on TCPS) have been reported by the same author in different manuscripts to range from 9-90 aggregates per sample [9, 18]. Further, aggregate size is not controlled; a range of sizes has been reported in the literature [9, 18]. Additionally, TCPS (E = 1 GPa) is not representative of the stiffness of the native heart valve, which has been reported as 4-20

kPa [21, 22], depending upon method of mechanical testing. Finally, calcifications take approximately one week or longer to form, making the *in vitro* studies slow and laborious.

High intracellular tension has been suggested as one of the mechanisms leading to disease in the valve. However, VIC tension has never before been measured in a dynamic environment. The ways in which dynamic stimulation affects individual VIC tension is not known. Although studies with VICs suggest that stretch regulates α -SMA expression [23] and collagen production [24], two measures of myofibroblast activity, these studies were done on VICs in high-density culture. Expression of α -SMA has previously been shown to be dependent upon cell density [25]; additionally, cyclic stretch on other types of fibroblasts has shown to prevent activation of the contractile myofibroblast phenotype [26]. More research is needed to determine how individual VIC tension is affected by cyclic stretch.

The motivation for this project is two-fold and arises from the need to study the following aspects of VIC behavior: 1) VIC traction force of cells undergoing dynamic stimulation, and 2) understanding of the differential behavior of VICs within the central aggregate region in contrast to that of cells along the aggregate periphery. Two aims have been established to explore these research areas. In the first aim, a method for measuring the cell traction force of isolated VICs undergoing 24-hour cyclic stretch at physiologically relevant strain magnitudes was developed and validated. In the second aim, a high-content *in vitro* model for calcific aortic valve disease is validated. This novel *in vitro* system can be employed to study apoptosis and calcification within the center of the VIC aggregates and potentially be used to test effectiveness of promising pharmaceuticals that could be used to treat CAVD.

The first aim, as detailed in Chapter 3, a method is developed for applying physiologically relevant cyclic stretch to VICs cultured on tunable modulus substrates which enables cell traction force

measurements. We then compare VIC traction force with stretch to control, statically cultured cells. By varying the pre-stress conditions, defined in the literature as the initial tension state of the cell, we can understand how the traction force response with stretch depends upon the initial cell tension state. This is important as stiffness and stretch have been shown to regulate many aspects of cell behavior including migration [27], spreading [28, 29], reorientation [30], proliferation [31], differentiation [32], and apoptosis [33, 34].

Chapter 4 addresses the need for a more repeatable and reliable method for studying cell apoptosis within VIC aggregates. By using micro-contact printing of bovine type-I collagen on polyacrylamide gels in defined shapes, we can remove the aggregation step of the *in vitro* model and focus solely on the apoptosis and subsequent calcification. Currently, the *in vitro* model relies on aggregate formation to study the subsequent apoptosis and calcification, a random process that does not have a repeatable time-course. In order to effectively investigate mechanisms of cell death, a more repeatable and concise method for aggregate generation is needed. Micro-contact printing enables investigation of factors affecting apoptosis and calcification, such as TGF- β 1, which is required in most *in vitro* cultures to induce VIC aggregation. The utility of this method is demonstrated with studies that vary both the stiffness of hydrogels and the size of aggregates, as well as with and without TGF- β 1.

Chapter 5 investigates the mechanisms behind apoptosis and calcification within the central portion of the aggregate. We hypothesize that the cells in the center of the aggregate undergo apoptosis due to a decrease in cell tension. Previously, tension distribution levels have been correlated with proliferation in micro-contact printed endothelial cells. However, it is currently unknown how apoptotic behavior is regulated on the macroscale with geometric control of aggregate shape.

Chapter 6 discusses study limitations, future directions and clinical significance of the work presented herein. Knowledge of cellular mechanisms initiating apoptosis and calcification within the central portion of the aggregate is essential for the development of pharmaceutical treatments that would allow patients to avoid risky valve replacement surgery and would reduce the economic burden of the disease. Chapter 7 summarizes thesis conclusions.

Chapter 2: Background

Calcific aortic valvular disease (CAVD) is the third most prevalent cardiac disease in the United States. It affects 2.8% of the population over the age of 65 [2], or about 81 million Americans; The prevalence of CAVD increases to 9.8% in octogenarians [3]. Although mortality does not increase when aortic stenosis is asymptomatic, the risk of death is more than 50% at two years for patients with symptomatic diseases unless aortic-valve replacement is preformed promptly. A total of 65,000 aortic-valve replacements were performed in the United States in 2010, the majority of which were necessitated by aortic stenosis; 70% of these procedures were done in patients greater than 65 years of age, which contributes to the high cost of health care.

CAVD results in sclerosis and calcification of the valve tissue, which inhibit normal function, causing complications such as valve stenosis (improper valve opening) and regurgitation (retrograde blood flow from the aorta to the left ventricle) [6]. In patients with CAVD, risk of another cardiovascular complication increases by 50%. Importantly, patients with CAVD are at risk of left ventricular hypertrophy and heart failure. In patients that present with symptomatic CAVD, death can occur within two years if medical intervention is not taken. Although previously thought to be a degenerative condition, studies with valvular interstitial cells have shown that they are capable of creating calcifications *in vitro*, suggesting that CAVD might be a cell-mediated disease. This finding gives hope that pharmaceutical interventions could be developed to halt, slow, or reverse the progression of CAVD.

Examination of explanted calcified valves shows multiple mechanisms of cell mediated calcification. Currently, there appears to be two types of cell-mediated calcification: dystrophic (83% of explanted valves) and ossific (13% of explanted valves) [7]. Dystrophic calcification is identified by

myofibroblast cell aggregates with an apoptotic core that is co-localized with calcifications with poor crystalline structure [8]. On the contrary, ossific calcifications are highly structured analogous to hydroxyapatite found in bone.

In this background chapter, normal heart valve function and biology will be discussed, as well as the medical management of CAVD. Theories of pathophysiology of CAVD will be introduced and *in vitro* models of CAVD highlighted. Culture factors which increase aggregation *in vitro* will be noted, as well as the mechanoregulation of apoptosis and its relevance to *in vitro* models of CAVD. As dystrophic calcification is believed to be caused by the cellular activation to a highly contractile myofibroblastic state, methods of measuring cellular tension and stiffness will be discussed. Since the valve is a dynamic environment, studies that combine measurement of cell tension and stretch will be recounted. Finally, I will review measurement metrics used

2.1 Calcific Aortic Valve Disease Overview

2.1.1 Risk of Aortic Stenosis

Anatomical, genetic, and clinical factors all contribute to the pathogenesis of aortic stenosis. Although aortic stenosis occurs in many patients with a normal tricuspid valve, 60% of patients presenting aortic stenosis have a bicuspid valve. Rheumatic heart disease can also cause aortic stenosis in association with mitral-valve disease. However, rheumatic fever is rare in the United States and conditions of rheumatic heart disease are mostly located in developing nations, where improvements in streptococcal throat infection treatments are needed [1].

Several genetic mutations appear to be associated with CAVD. These include abnormalities in the NOTCH1 protein [35] (a transmembrane receptor associated with many signaling pathways) and a specific lipoprotein(a) polymorphism, which has been shown to be associated with elevated serum

levels of lipoprotein(a) and aortic valve calcification [36]. Risk of aortic stenosis increases in populations that are older, male sex, have elevated serum levels of low-density lipoprotein cholesterol and lipoprotein(a), hypertension, smoking, diabetes, and metabolic syndrome [37].

2.1.2 Progression of Disease

CAVD is a spectrum disorder. The disease starts initially with leaflet changes, which progresses from early calcification lesions to valve obstruction, and then eventually becomes severe with or without clinical symptoms. Figure 2.1a shows a representative image of a healthy aortic valve. Figure 2.2b shows a calcified valve undergoing replacement; notice the calcified nodules which inhibit normal valve function as well as the thickened leaflets. The severity of aortic stenosis is grouped into 7 stages (A, B, C1, C2, D1, D2, and D3) which are distinguished between one another by hemodynamics, symptoms, and left ventricular response to pressure overload [3]. A summary of the different stages of disease, outcome, and disease management are shown in table 2.1.

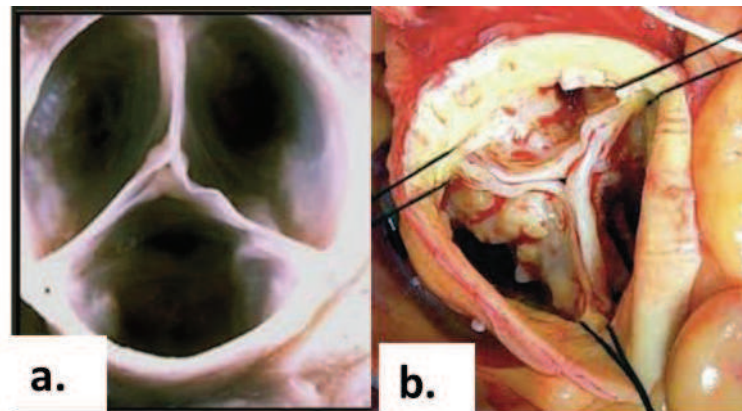


Figure 2.1: Representative images of a healthy valve (a) and a calcified valve undergoing replacement (b). Notice how the healthy valve is very thin and the three leaflets nicely cohere enabling the efficient pumping capacity of the heart. When diseased, valve leaflets are thickened (termed sclerosis) and do not nicely cohere, resulting in regurgitation and decreased cardiac output adapted from <https://science.nichd.nih.gov/confluence/display/~michael.hoaglin/Aortic+Valve> and www.usccardiology.org respectively.

Table 2.1 Classification of CAVD based upon blood ejection velocity, patient outcomes and disease management. Adapted from [3].

Stage	Description	Definition	Outcome	Management
A	At risk	Aortic valve sclerosis; V_{\max} of <2 m/sec	50% increase in risk of myocardial infarction and cardiovascular death over 5 years	Assessment of cardiovascular risk factors and primary prevention
B	Progressive	Mild to moderate calcification; V_{\max} of 2 to 3.9 m/sec	Hemodynamic progression in most patients	Monitoring every 6 months to track disease progression
C	Asymptomatic, severe aortic stenosis	Reduced leaflet motion, V_{\max} of >4 m/sec, Severe calcification or rheumatic changes	Symptom onset in 50% to 80% of patients within three years	AVR is recommend if ventricular function is compromised
D	Symptomatic, severe aortic stenosis	Sever calcification, aortic valve area less than 1 cm^2	Mortality at 2 years is about 80% with medical therapy, compared to 40% with AVR	Prompt AVR is necessary

The factors which are responsible for CAVD onset may not be the same factors responsible for its progression. One such example is elevated lipid levels, which are associated with aortic valve sclerosis. Currently, there is no convincing evidence that links high serum levels to CAVD progression [38]. Therefore; the relevance of many animal models currently being used to study calcific aortic disease is questionable. This includes the murine model, which requires high cholestermia to induce aortic valve calcification [10], however, elevated lipid levels in humans does not predict CAVD onset or progression. Additionally, systemic markers of inflammation are not associated with progression of aortic-valve disease. Once aortic sclerosis is present, aortic obstruction occurs in 15% of patients over a period of two to five years [3]. On average, the maximum transvalvular velocity increases 0.1 to 0.3 m/s per year, with the mean gradient increasing by 3-10 mmHg per year, and the valve area decreasing by 0.1 cm^2 [3, 39].

Anatomical changes caused by the onset of CAVD and aortic sclerosis affect the whole heart and are not isolated to the aortic valve alone. Aortic sclerosis and valve thickening affect the upstream left ventricle, left atrium, and often the ascending aorta. Left atrial enlargement is common with aortic stenosis due to the elevated left ventricular filling pressures [3]. The wall of the left ventricle often undergoes hypertrophy as more force is needed to push the blood through a narrow aorta. In many patients, there is also altered coronary blood flow. For a schematic of the aforementioned changes, please see figure 2.2.

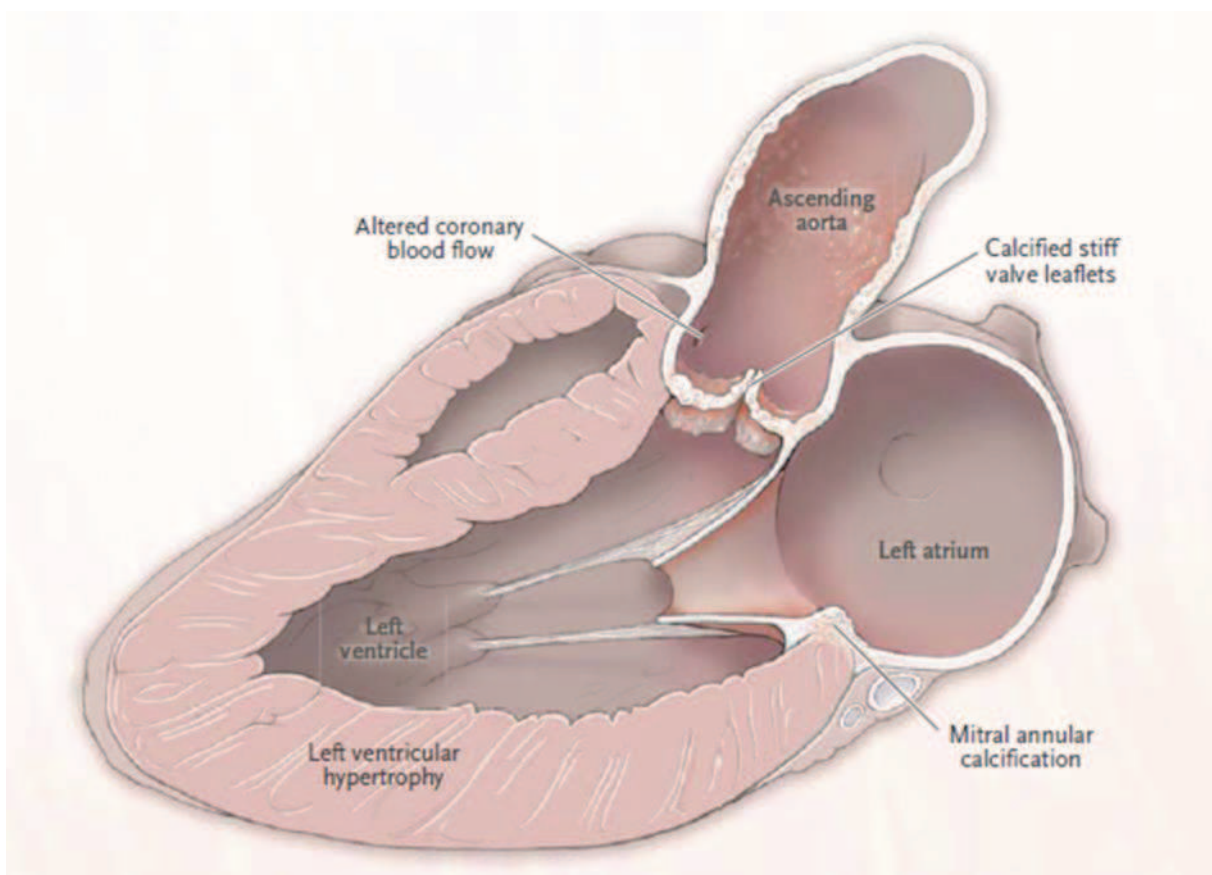


Figure 2.2. The whole heart is affected by aortic valve calcification. Left atrium often enlarges to account for increased left ventricular filling pressures. Although ejection fraction is often normal, left ventricular hypertrophy (muscle thickening) is common to allow the blood to be pushed through the aorta. Many patients also experience altered coronary blood flow. Reproduced with permission from Otto, C. M., & Prendergast, B. (2014) reproduced with permission, Copyright Massachusetts

Medical Society.

2.1.3 Location of Calcification on Valve Leaflets

The heart valve consists of a tri-laminar structure: the ventricularis, spongiosa, and fibrosa. Each leaflet stratum has a distinct protein composition for the unique mechanical loading conditions experienced by each respective layer. The ventricularis side of the valve faces the left ventricle and is exposed to shear flow when the valve opens during systole. Rapid closure of the valve during diastole results in blood flowing in a “swirl”-like motion over the fibrosa. Examination of explanted disease valves exhibiting early calcific lesions show that the fibrosa is the predominant site of calcification [40]. Early lesions show sub endothelial thickening between the basement membrane and the elastic lamina, extracellular and intracellular lipids, mineralization, and disruption of the basement membrane over the lesion [41]. Regions of the fibrosa adjacent to these lesions showed disruption in extracellular matrix proteins and accumulation of lipids and calcification. Sites of increased mechanical stress are more likely to experience calcification [42, 43]. Figure 2.3 shows an immunohistological section of a disease valve. Notice the increased cell density compared to healthy native valves.

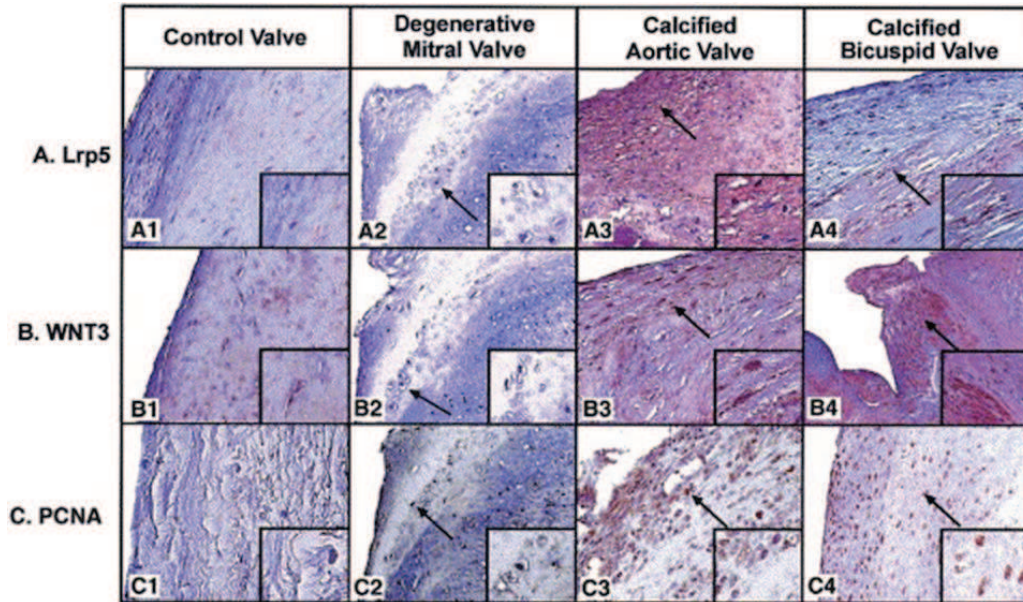


Figure 2.3 Cell aggregates within disease valve leaflet. The first column shows a healthy native valve. Cell density increases within the calcified aortic valve suggesting that CAVD is the result of an active tissue response to some stimulus. Image from [44], reproduced with permission.

2.1.4 Valve Replacement

Several types of valve replacements exist for patients, which include mechanical valves and bio-prosthetic (tissue) valves. Tissue valves are created from bovine or porcine tissue. Valves made from bovine tissue are made from the bovine pericardium. Unlike the aortic valve whose structure is highly anisotropic due to different fiber alignment in the radial and circumferential directions, bovine pericardium is an isotropic material [45]. Porcine valves are taken from pig aortic valves. In addition, allografts from cadavers and autografts (pulmonary valve replaced to the aortic root) are also potential options [45]. All tissue valves require glutaraldehyde fixation to render the valves non-immunogenic via collagen crosslinking which serves to stabilize the collagen fibers and reduce immunogenicity. Currently, no non-treated valves have achieved successful implantation [42]. However, glutaraldehyde fixation appears to make the valve susceptible to calcification as bio-prosthetic valve calcification increases with severity with increasing fixative concentration [46]. The mechanisms of calcification of glutaraldehyde treated valves are likely different than those of CAVD.

The initial mechanical valve was the Starr-Edwards ball and cage prosthesis which was first used successfully in 1961 [47]. Several patients who had the original prosthesis design implanted are still alive today, and the ball and cage prosthesis is still available commercially in a slightly modified form. Other popular mechanical valve designs include the disc valve and the bileaflet valve. The first disc valve was created by Bjork-Shiley [47]. This prosthesis is comprised of a single disc coated in pyrolite carbon which tilts between two struts of the housing, typically made of stainless steel or titanium. Unfortunately, due to the combination of a slight design modification and change in manufacturing process, some generations of the Bjork-Shiley valve were prone to rupture, allowing the disc to escape, resulting in several hundred fatalities [47]. The Bjork-Shiley valve is no longer manufactured, but single disc valves continued to be available commercially through Medtronic and others. The third mechanical valve prosthesis design is the bileaflet valve. The first bileaflet valve was developed by St. Jude Medical in 1977 [47]. It has two semicircular leaflets which open and close creating one central and two peripheral orifices. Over 600,000 bileaflet valves have been implanted to date and is currently the most commonly implanted type of mechanical prosthesis in the world [47].

The disadvantage to a mechanical valve is that all designs alter the hemodynamic flow sufficiently to increase the risk of thrombotic complications. This increased risk necessitates patients to take warfarin or another antithrombotic agent to reduce thromboembolic complications such as stroke, pulmonary embolism, or heart attack [45]. As such, mechanical valves are not recommended for women of child-bearing age as currently there are no medical guidelines for correctly prescribing warfarin or other anticoagulation medication as all have negative consequences for fetal development [48, 49].

Despite the increased quality of life, improved ability to complete activities of daily living, and prolonged lifespan for many patients, valve replacement has yet to become optimal and is associated with significant complications postoperative. Within 10 years, greater than 50% of patients experience complications with replacement valves [50]. Almost always, the complication requires urgent surgical intervention. The most common medical problems associated with aortic valve replacement include thromboembolic problems, infective endocarditis, paravalvular leak, intrinsic degradative dysfunction, and tissue overgrowth [51].

2.1.5 Calcification of Bioprosthetic Replacement Valves

Calcification is the most common type of failure of bioprosthetic heart valves. Calcific deposits result in decreased motion of the valves, causing tearing, resulting in regurgitation and the need for a second replacement valve [52]. For calcification to initially deposit onto the bioprosthetic valve leaflet from the blood stream, energy is required to achieve the phase transformation [53]. The presence of collagen fibrils, implant surface defects, and cell residues within the bioprosthetic valve all reduce the amount of energy needed for this phase transformation [54]. Additionally, the glutaraldehyde fixative used to reduce immunogenicity of the bioprosthetic valve is toxic; it has been demonstrated that the chemical persists for many months, causing death of host fibrocytes and macrophages it comes in to contact with [52]. This too, increases the number of sites the calcium can nucleate.

It is difficult to say whether mechanistically, the calcification pathways between natural valves and bioprosthetic valves are similar, as much remains unknown about both types of calcification [53]. Examination of the calcium deposits on valve leaflets of both natural heart valves and bioprosthetic valves by scanning electron microscopy shows similarly shaped calcification deposits. Elemental analysis of calcified areas by energy dispersive x-ray spectroscopy (EDS) shows approximately

equivalent calcium to phosphorous (Ca/P) ratios for both calcified natural heart valves and calcified bioprosthetic valves (1.79 for native heart valves and 1.72 for bovine pericardium). These ratios of Ca/P are approximately what is expected for hydroxyapatite (HAP) found in bone. Stevens and colleagues analyzed mineralized nano-particles found on the surface of disease cardiovascular tissue with selected-area electron diffraction and showed that the crystallinity was higher than anything found within the body, including bone, suggesting different mineralization mechanisms in calcified valvular and vascular tissue, than osteogenesis [55] (to be discussed in more detail in chapter 4).

2.2 Normal Aortic Valve Physiology and Function

The aortic valve is one of four valves within the heart. As the heart is essentially a pump, the valves help prevent retrograde blood flow, as well as ensure pumping efficiency. The aortic valve is located between the left ventricle and the aorta. During systole, or heart contraction, the pressure inside the left ventricle exceeds that of the aorta, and the aortic valve opens. During diastole, the heart relaxes from its contracted state to allow for the filling of the left ventricle. When this happens, the pressure in the left ventricle is lower than that of the aorta, and the aortic valve closes to prevent retrograde blood flow.

2.2.1 Calculation of Aortic Valve Area

Clinically, there are several metrics to evaluate efficiency of heart pumping and health of the valve. These include cardiac output, systolic ejection period, mean valvular pressure gradient, and heart rate. These metrics can be used to assess and estimate valve area and determine the degree of aortic stenosis. Determination of when and if a patient should get an aortic valve replacement is mostly decided by the calculated aortic valve area.

There are three equations (which have different assumptions) and are used to calculate valve area from the aforementioned parameters. These include: the continuity equation, the Gorlin equation, and the Hakki equation.

The continuity equation states that the flow in one area must equal the flow in a second area if there are no shunts between the two areas. The flow from the left ventricular outflow tract (LVOT) is compared to the flow at the level of the aortic valve. In echocardiography, the aortic valve area is calculated using the velocity time integral (VTI). The LVOT and LVOT VTI can be measured using pulse-wave Doppler, and the aortic VTI can be measured using continuous-wave Doppler. Once the values are obtained by the sonographer, equation 2.1 is used to calculate the valve area.

$$AV \text{ Area (cm)}^2 = \frac{LVOT \text{ diameter} * 0.78540 * LVOT \text{ VTI}}{Aortic \text{ Valve VTI}} \quad \text{Equation 2.1}$$

The Gorlin equation states that the aortic valve area is equal to the flow through the aortic valve during ventricular systole divided by the systolic pressure gradient across the valve multiplied by a constant. The flow across the aortic valve is computed by dividing the cardiac output (milliliters/minute) by both the heart rate (to give output per cardiac cycle) and the systolic ejection period (seconds per beat), to give flow per ventricular contraction.

$$AV \text{ Area (cm)}^2 = \frac{CO \frac{ml}{min}}{HR \frac{beats}{min} * systolic \text{ ejection fraction (s)} * 44.3 * \sqrt{Pressure \text{ gradient (mmHg)}}} \quad \text{Equation 2.2}$$

Where AV is the aortic valve, CO is cardiac output and HR is heart rate.

The Hakki equation shown in equation 2.3 is a simplified version of the Gorlin equation as in most patients the heart rate times the systolic ejection fraction *44.3 is approximately equal.

$$AV \text{ Area (cm)}^2 = \frac{CO \frac{ml}{min}}{\sqrt{\text{Pressure gradient (mmHg)}}} \quad \text{Equation 2.3}$$

2.2.2 Anatomy

The normal aortic valve is comprised of three leaflets which co-adapt to form a barrier against retrograde blood flow. Although, three leaflets are considered normal for aortic valve anatomy, congenital conditions do exist where the aortic valve consists of two (bicuspid aortic valve) or even one leaflet. Patients with bicuspid aortic valves account for 50% of valve replacements for CAVD; this highlights the importance of mechanical factors and altered blood flow contributions of the disease.

The valve leaflet is composed of three distinct layers: fibrosa, spongiosa, and ventricularis, and each layer has a different protein composition, which allows for its different mechanical properties. In a normal valve, the three layers remain stratified with valvular interstitial cells (VICs) being found uniformly throughout the valve; Figure 2.4 shows the different layers of the valve. In patients with CAVD, the stratified organization of the valve is completely disintegrated, with all extracellular matrix (ECM) proteins being found throughout the valve.

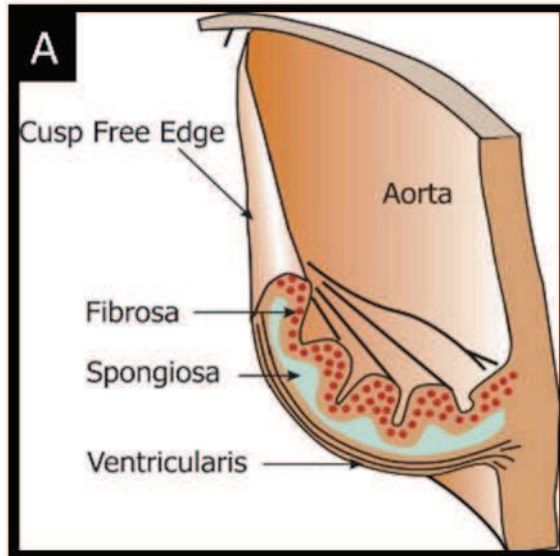


Figure 2.4. Schematic of tri-laminar structure of aortic valve leaflet. The ventricularis is mainly exposed to shear flow as the blood exits from the ventricle to the aorta. The ventricularis is composed mainly of a network of collagen and elastin fibers. The spongiosa or middle layer is believed to function as a lubricating layer and is composed of glycosaminoglycans. The fibrosa faces the aorta and is composed of type I and type III collagen fibers. Figure adapted from M.S. Sacks and A.P. Yoganathan (2007) with permission.

2.3 Valvular Interstitial Cell Mechanobiology

The following subsections appeared originally Cirka et al. "*Mechanoregulation of Aortic Valvular Interstitial Cell Life and Death.*" Journal of long-term effects of medical implants 25.1-2 (2015). and are reproduced here with permission.

There are two cell types in the valve: valvular endothelial cells (VECs) and valvular interstitial cells (VICs). Both VECs and VICs appear to be sensitive to mechanical signals, as well as hemodynamic flow. A single layer of VECs line the surfaces of the aortic valve. VECs are distinct from endothelial cells populating the aorta. Additionally, VECs' gene expression profiles differ with respect to which side of the aortic leaflet they are covering. VECs covering the fibrosa have upregulated proteins that are believed to promote calcification, while VECs lining the ventricularis side, which experience oscillating blood flow, have increased expression of Kruppel-like factor2 (KLF2), an "atheroprotective" transcription factor considered to downregulate calcification [56]. Additionally, it is believed that valvular endothelial cells can regulate valvular interstitial cell activation to the myofibroblast phenotype. VICs cultured *in vitro* often have high percentages of myofibroblast

activation (>99%); however, when cultured in the presence of VECs, the number of myofibroblasts decreases [57]. How this *in vitro* finding translates *in vivo* is still relatively unexplored.

Valvular interstitial cells are a fibroblast-like cell that normally exists in the valve in its quiescent state [13]. When the valve is damaged, activation to the myofibroblast phenotype allows the cells to secrete matrix proteins, cytokines, and increase their cellular tension, analogous to a wound healing environment. Expression of alpha smooth muscle actin protein (α SMA) is an indicator of myofibroblast activation [15] and is often examined in studies assessing the VIC response to extracellular matrix composition and the mechanical cues of stiffness and stretch. In a healthy valve, approximately one percent of the cell population expresses α SMA. In a diseased valve, this number increases dramatically to 60% of the cell population. Myofibroblast persistence is believed to be a predominating factor in CAVD. Upon repair, the VICs deactivate and undergo numerous cellular processes including senescence and apoptosis, although the exact pathways remain unclear. The protein composition and cellular density of the valve changes over time. The cellular density of an adult is approximately 10% of what it is compared to fetal valves [58]. Clearly signals regulating valvular interstitial cell fate are not only important for understanding pathology, but also normal tissue histomorphogenesis.

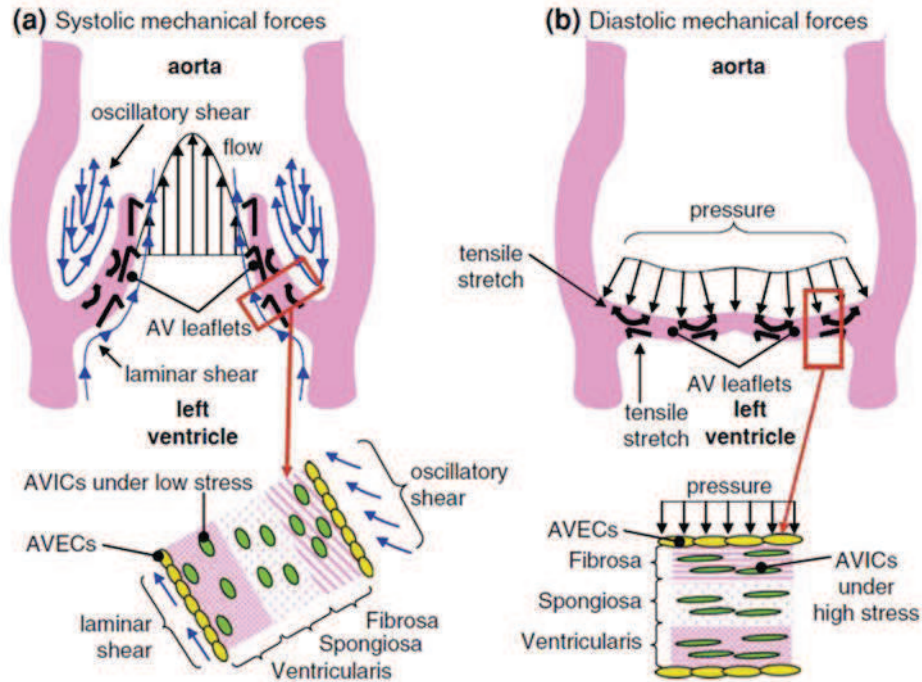


Figure 2.5. VICs are exposed to myriad mechanical forces in a dynamic environment *in vivo*. These forces include shear stress from the passing of blood through the valve, buckling stresses from when the valve opens and closes, and planar stress from when the valve is closed. Figure from [59] reproduced with permission.

2.3.1 Cell-ECM and cell-cell connections

Under normal physiological conditions, VICs do not usually come into contact with one another as they are embedded in large amounts of extracellular matrix. Focal adhesions on the cell serve as attachment points to ECM proteins. Focal adhesions grow larger when loaded, e.g. by pulling with microbeads [60, 61] or stretching the substrate [62]. With increasing tension, fibroblasts transition to proto-myofibroblasts; this phenotype expresses α SMA-negative stress fibers [63]. The myofibroblast phenotype is characterized by *de novo* expression of α SMA [64, 65]. Although shown in a different cell type than VICs, the tension generation capacity of myofibroblasts is much greater than that of fibroblasts due to α SMA actin incorporation into stress fibers [66]. It remains an open

research question if the integrins expressed by myofibroblasts differ from those expressed by fibroblasts, as transforming growth factor- beta (TGF- β), a potent myofibroblast activator, up-regulates the expression of many integrins [67].

While a comprehensive comparative study of cell-cell junctions in fibroblasts and myofibroblasts has not been completed, cadherin expression likely differs between these phenotypes [63]. N-cadherin was the first cadherin to be identified in fibroblasts [68, 69]. Additional cadherins such as P-cadherin [70, 71], R-cadherin [72], VE-cadherin [72, 73] and OB-cadherin (cadherin-11) [72, 74] are expressed in fibroblasts. N-cadherin, cadherin-11, plaque proteins: α -and β -catenin, plakoglobin, and p120, together with minor amounts of protein p0071 are expressed by VICs. Cadherins likely play a role in valve diseases, as they are necessary for the aggregation of VICs as discussed in the 'Mechanoregulation of Calcification' sub-section.

2.3.2 Mechanical characterization of VIC phenotype

As the cell cytoskeleton (CSK) is integral in mechanotransduction, characterization of VIC mechanical properties may provide insight into cellular mechanoregulation. The cell Young's modulus can be measured by micropipette aspiration (MA), atomic force microscopy (AFM) indentation, and magnetic bead twisting rheometry (MBR). Using atomic force mapping, VIC modulus has been shown to increase with culture on substrates of increasing modulus [75]. VIC modulus also increases during myofibroblast differentiation as shown by studies using micropipette aspiration [76]. This increase in modulus was not fully explained by substrate stiffness and appears to be the result of α SMA incorporation into the cytoskeleton. Due to the viscoelastic nature of the biopolymer network of the CSK, the modulus is also dependent upon the loading rate of the pipette/probe during the measurement. However, negligible effects of viscoelasticity on VIC micropipette

deformation are reported over physiological timescales (0.05 s to 0.5 s), suggesting that the VIC cytoskeletal response is purely elastic in the physiological range [77].

The response of a cell to mechanical probing and thus the calculated modulus, is a complex function of both the intrinsic stiffness of the cytoskeletal elements, as well as the active tension in the cytoskeleton. Work by Stamenović and colleagues suggests that there is a positive correlation between cell modulus and cell prestress (i.e., cytoskeletal tension, as measured by traction force microscopy) [78, 79], but whether this correlation holds true for VICs and activated myofibroblasts remains to be resolved.

2.3.3 Effect of substrate modulus on VIC phenotype and apoptosis

Extensive experimental evidence suggests that VIC phenotype is sensitive to the elastic modulus of the substrate on which the cells are cultured [80, 81]. The substrate modulus is known to regulate the amount of tension a cell can generate [82]. When VICs are cultured on compliant substrates (less than 3 kPa), they have a rounded morphology with little α SMA incorporated into the cytoskeleton [81]. Spread area, which is correlated with cell generated tension in other cell types [82], [82][70] is also smaller for VICs on more compliant substrates. However, on high modulus substrates (greater than 10 kPa), VICs are elongated and spindle shaped with α SMA incorporated into the stress fibers [81].

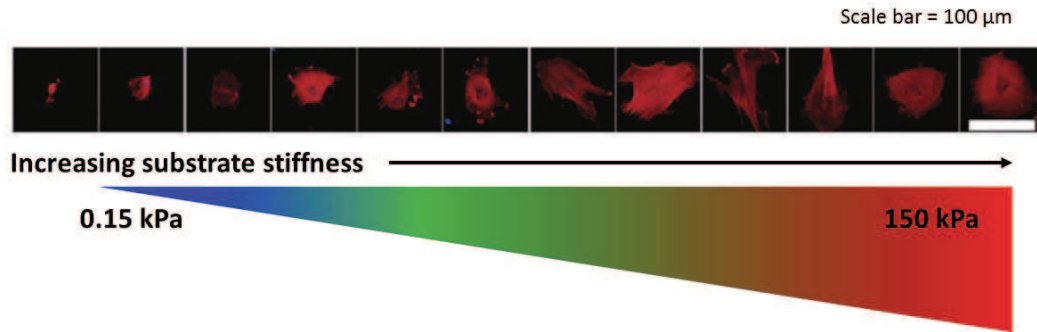


Figure 2.6. Valvular interstitial cells (VICs) are mechanosensitive. VICs expressed differential amounts of α SMA incorporation into stress fibers, an indication of the contractile myofibroblastic phenotype, when cultured on substrates of increasing modulus. Cell area is also correlated to substrate stiffness. Figure adapted from [81] with permission.

Several research groups have attempted to identify a “transitional” stiffness, where VICs differentiate from quiescent fibroblast-like cells to highly contractile myofibroblasts [80, 81, 83]. Quinlan et al. activated VICs to the myofibroblast phenotype by culturing them for two days on stiff tissue culture plates before transferring them to collagen-coated polyacrylamide hydrogels. Identification of transitional stiffness was accomplished by using eleven different substrates with moduli that ranged from 0.15 kPa-150 kPa [81]. The transitional modulus was found to be 2.5 kPa-7kPa [80, 81]. Anseth and colleagues also demonstrated that the activated VIC phenotype is reversible [80, 84]. Specifically, myofibroblasts were cultured for three days on photodegradable hydrogels and then irradiated to reduce the modulus from 32 kPa to 7 kPa. Within two days after modulus reduction, myofibroblasts reverted to quiescent VICs without significant changes in cell viability [80, 84]. These data indicate that myofibroblasts can be dedifferentiated without inducing apoptosis, which has implications for the development of treatments of CAVD and fibrotic diseases as apoptosis has been identified in calcified diseased valves [11]. A better understanding of the

precise magnitude of stiffness and cell tension reduction required for phenotypic regulation is needed. For a brief review of studies examining the mechanobiology of VICs, please see table 2.2.

Table 2.2- Review of studies examining the mechanobiology of valvular interstitial cells

Authors	Mechanical/Biological Environmental Cue	Valvular Interstitial Cell Response
Quinlan et al. (2012) Kloxin et al. (2010)	Culture on high modulus substrates (> 32 kPa)	Expression of α SMA contractile protein within stress fibers
Quinlan et al. (2012) Kloxin et al. (2010)	Culture on low modulus substrates (< 7 kPa)	No α SMA positive stress fibers, some α SMA present in cytosol
Walker et al. (2004)	Culture in presence of TGF β on high modulus substrates	Expression of α SMA contractile protein within stress fibers
Kloxin et al. (2010) Wang et al. (2012)	Dynamically changing substrate modulus from rigid to compliant	Decreased expression of α SMA positive stress fibers
Kural and Billiar (2013)	Culture with stiff boundary conditions (1 nN/nm) in three dimensional culture	No α SMA positive stress fibers, but
Kural and Billiar (2013)	Culture with soft boundary conditions (0.15 nN/nm)	No α SMA muscle positive stress fibers
Kural and Billiar (2013)	Culture with stiff boundary conditions (1 nN/nm) in three dimensional culture TGF β	Expression of α SMA contractile protein within stress fibers, but α SMA appears in small 'rod' shape in cytosol
Kural and Billiar (2013)	Culture with soft boundary conditions (0.15 nN/nm) with TGF β	No α SMA positive stress fibers
Ku et al. (2006)	Culture in the presence of dynamic stretch	α SMA incorporation into stress fibers and collagen production are increased with magnitude of stretch
Quinlan et al. (2011)	Culture on soft (0.6 kPa) and stiff (50 kPa) substrates in the presence of 10% equibiaxial stretch for 6 hours	VICs are initially rounded on soft substrates, increase spread area with stretch. VICs initially on stiff substrates decrease spread area with stretch.

2.3.4 Cyclic stretch regulation of VIC phenotype and apoptosis

As VICs are exposed to a highly dynamic environment *in vivo*, the effects of stretch and fiber anisotropy on VIC mechanoregulation are important to understand.

Several bioreactors have been developed by different research groups which can replicate the strains and strain rates experienced *in vivo* for *ex vivo* whole-leaflet and whole-valve studies.

Balachandran et al. have demonstrated in whole valve cusps that cyclic stretch upregulates collagen production by VICs [85]. Studies with whole valves reveal a side-specific activation of VICs, with most α SMA expression being localized to the ventricularis [85]. VICs also appear to respond to local tissue stiffening by changing collagen biosynthesis [24]. VIC apoptosis has been shown to increase with cyclic stretch in a magnitude-dependent manner in *ex vivo* organ culture studies; however, physiological levels of stretch (10% and 15%) were shown to be preventative against apoptosis when compared to static controls. These studies suggest that the magnitude of cyclic stretch is an important regulator of both VIC phenotype and fate [86].

Anisotropy present within the valve layers may also regulate VIC function. Using a novel bioreactor design, Butcher and colleagues [87][75][77] investigated the effect of biaxial strain anisotropy on cell function in 3D collagen hydrogels. They found that increasing the anisotropy of the biaxial strain increases cellular realignment towards the direction of maximum principal strain, and that cell realignment precedes fiber reorganization [87]. The presence of cyclic strain decreases the expression of vimentin and α SMA as compared to unstretched controls, yet there were higher levels of apoptotic and proliferative markers in stretched samples compared to controls [87].

Cyclic stretch has been shown in 2D experiments to regulate aspects of VIC phenotype including cytoskeletal rearrangement and gene and protein expression. In particular, α SMA incorporation into stress fibers and collagen production, both hallmarks of the myofibroblast phenotype, are increased with the magnitude of stretch [24]. It has been shown in cardiac fibroblasts that stretch by ligand-coated ferromagnetic beads allows for α SMA incorporation into stress fibers [88].

Additionally, stretch magnitude has been shown to regulate genetic profiles. For example the lowest expression of inflammatory genes has been shown to be expressed with 15% equibiaxial stretch [89] [89][77][79]. Cyclic stretch has also been shown to induce VIC production of spheroid microparticles;

this production was cytoskeletal tension dependent and was abolished when RhoA/Rock was inhibited [90].

2.3.5 Integration of multiple mechanical signals

Although the number of studies investigating the response of cells to matrix stiffness and stretch has increased rapidly over the past few years, very little is known about the relative importance of these mechanical signals or their interactions. Visual observations indicate that VICs on compliant substrates, which generally have a rounded morphology and small spread area when in isolation, are able to “generate tension against each other” and increase their spread area when in contact with other cells [81]. This observation highlights the importance of cell-cell contacts (cadherins) in the mechanoregulation process.

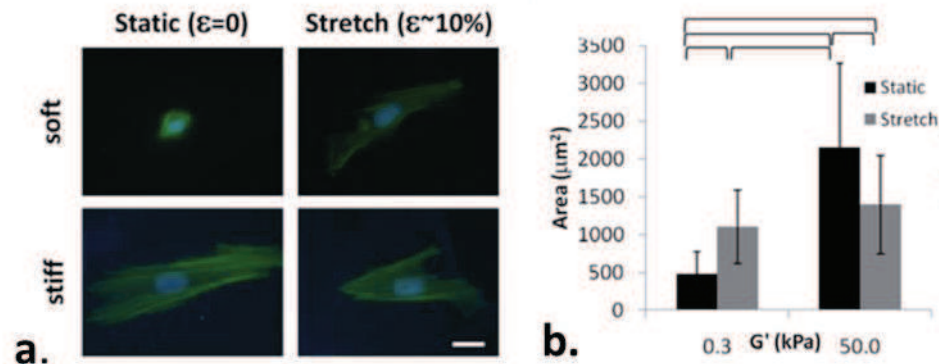


Figure 2.7. VICs are capable of integrating multiple mechanical cues. (a) VICs cultured on soft (0.3 kPa) and stiff (50 kPa) PA gels cultured with and without cyclic stretch. (b) Effect of static and stretch culture on cell area for two substrate stiffness levels of culture. Figure adapted from [28], copyright Throm Quinlan.

Findings from recent studies, which incorporate a compliant PA gel on a flexible silicone culture substrate, indicate that VICs are able to integrate multiple mechanical signals from the substrate, including the local modulus and dynamic stretch, see Figure 2.7. Using this method, we have demonstrated that VICs on stiff substrates decrease spread area slightly when subjected to cyclic equibiaxial stretch, possibly to maintain certain levels of homeostatic tension [28]. In contrast, VICs cultured on soft substrates increase in spread area when subjected to the same stretch stimulus. It remains to be determined if similar mechanosensory mechanisms are utilized by the cells for static inside-out sensing (of substrate modulus) and cyclic outside-in sensing (of stretch). Although cell area has been shown to be an adequate proxy for cell tension for some cell types [82], the relationship between fibroblast cell area and cell tension appears complex, with a possible dependency on TGF- β 1 [91]. A shortcoming of cell area measurements is that if the cell generated traction-cell area relationship is not known, interpretation of mechanobiological data becomes imprecise. Future studies should include more robust measurements of cell tension, such as by traction force microscopy, rather than relying on cell area measurements alone. To date, little is known about cell tension changes in the presence of long-term cyclic stretch.

2.3.6 Interactions between mechanical and soluble stimuli

Substrate stiffness and stretch modulate the sensitivity of cells to soluble factors such as TGF- β 1; therefore, mechanical and chemical stimuli must be studied simultaneously to determine potential synergistic interactions. For example, TGF- β 1 and boundary stiffness act in concert to induce the myofibroblast phenotype in static 3D culture systems. With very compliant beams, TGF- β 1 supplementation (up to 5 ng/mL) does not change VIC-generated forces [92]. However, increasing boundary stiffness and TGF- β 1 concentration together increase force-per-cell levels synergistically [92]. Similar interactions have been reported in 2D systems. The traction force generated by lung fibroblasts cultured on polyacrylamide gels reaches a plateau of 13 kPa without TGF- β 1, yet

continues to increase for cells cultured in the presence of TGF- β 1 [91]. These studies provide evidence for a cooperative mechanism between substrate and boundary stiffness and TGF- β .

Studies employing cyclic stretch of porcine aortic valve leaflet tissue strips also indicate that stretch and TGF- β 1 act in a cooperative manner to activate VICs. Merryman et al. [23] cultured strips cut from heart valves for 7 or 14 days in the presence of 15% equibiaxial stretch and 0.05 ng/mL TGF- β 1 or neither chemical nor mechanical stimuli. The greatest number of myofibroblasts, as characterized by α SMA expression, were found in the group cultured simultaneously in the presence of stretch and TGF- β .

When secreted by cells, TGF- β binds to the matrix in a latent form preventing its interaction with transmembrane receptors on the surface of the cells. Recent evidence suggests that integrins may play a critical role in the process of releasing the active TGF- β from the latent complex. This is accomplished by using a physical force to modify the protein configuration, allowing for releases of the molecule [93], shown schematically in Figure 2.8. Additional mechanisms of latent TGF- β activation that have been identified include heat, pH, and reactive oxygen species [94]. The physical or chemical mechanisms which activate latent TGF- β have not been explored for VICs specifically, and further study may prove valuable for tissue engineering purposes as TGF- β is a key phenotypic regulator of this cell type.

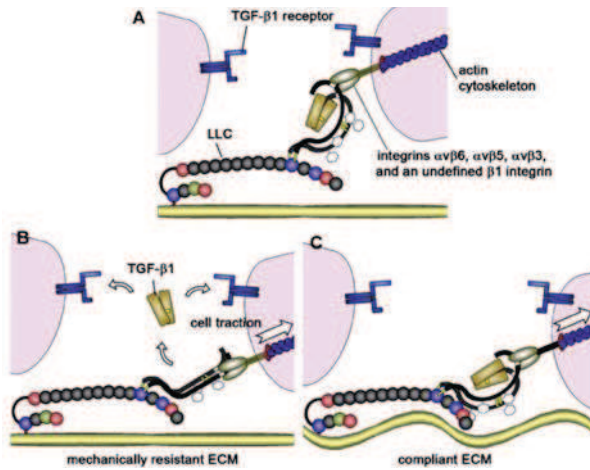


Figure 2.8: Effect of substrate stiffness and tension on release of latent TGF-β. Stiff substrates aid in release of latent TGF-β. As a cell pulls on the extracellular matrix, a conformational change is induced, releasing TGF-β molecules. Compliant substrates do not allow for this conformational change.

2.4 In Vitro Models of Calcific Aortic Valve Disease

There are two believed mechanisms behind calcification seen in heart valves. These include ossific calcification (present in 13% of explanted valves) and dystrophic calcification (present in 83% of valves) [7]. *In vitro* models have been developed in order to replicate calcification that is observed *in vivo* [12]. However, no model currently simultaneously replicates ossific and dystrophic nodules as seen in some diseased heart valves. Ossific nodules have been created on both thick collagen gel substrates [16] and on 24 kPa polyacrylamide gels [95]. Dystrophic nodules are created by culturing VICs at high density in the presence of TGF-β1 on stiff substrates for a period of 5-7 days. Although both ossific and dystrophic nodules will stain positive for calcium, there are distinct phenotypic differences between the cells which comprise each nodule [10]. Dystrophic nodules have apoptosis co-localized with calcification in the center of the aggregate, while ossific nodules are living and will exclude propidium iodine. This is verified with mechanical characterization by atomic force microscopy; dystrophic nodules will have heterogeneous modulus throughout the aggregate, while ossific nodules have the modulus similar to that of a single VIC and no noticeable differences between the central and peripheral cells [95]. As dystrophic calcification is more prevalent, the

remainder of the discussion will focus on the mechanoregulation of dystrophic calcification.

Representative images for the dystrophic model of calcification are shown in Figure 2.9.

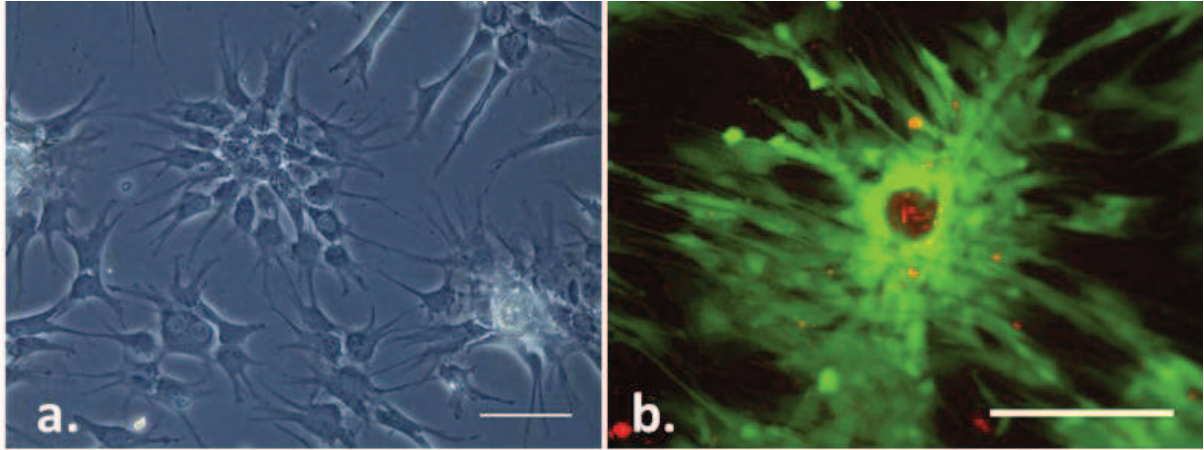


Figure 2.9. *In vitro* model of calcific aortic valvular disease. a.) Representative image of aggregates on day 7. Note that some aggregates are undergoing calcification within the central region as evidence by the white nodule. Other aggregates have yet to develop a nodule. These differences in time course make determining mechanisms behind calcification difficult. *Scale bar = 100 μ m.* b.) Live/dead assay of aggregate. Cells within the central region of the aggregate undergo apoptosis and will then uptake ethidium homodimer-1 (red). Live cells exclude the dye and are stained with calcein (green). *Scale bar = 100 μ m.*

2.4.1 Mechanoregulation of calcification

Cell tension has a clear connection to the rate and frequency of aggregation. Current culture methods require a high number of cells, the presence of TGF- β , and take on the order of a week to form aggregates; cyclic strain has been used in conjunction with TGF- β to accelerate the aggregation process. Merryman and colleagues cyclically stretched VIC monolayers for 24 hours [17] and found that cells cultured in the presence of TGF- β before or during stretch (but not after) were activated to the myofibroblastic phenotype. Although cyclic stretch alone did not activate VICs, the two stimuli together accelerated aggregation appreciably observed at 24 hrs compared to 1 week for static culture). Apoptosis and calcification have also been shown to increase in a stretch-dependent manner; 15% strain results in a 100-fold change over samples strained at 10% or static controls [90].

Other methods of increasing cell tension include increasing expression of key cytoskeletal signaling proteins, such as RhoA and the ROCK pathway [96]. When RhoA/ROCK are upregulated, the rate of aggregation and number of aggregates observed increases [18]. On the contrary, when VICs were treated with ROCK inhibitors (H1152), there was reduced myofibroblast nodule formation as shown by a decrease in nodule number and area, reduced number of α SMA stress fibers, and an absence of apoptosis [18].

In addition to high cell tension, high cell-cell forces appear to be necessary for aggregate formation. Results from a recent study indicate that blocking cadherin-11 reduces intracellular tension in VIC monolayers and inhibits aggregation [97]. When cadherin-11 was inhibited using siRNA, VIC aggregation was also blocked. Although these findings support the importance of high cell forces in aggregation, no direct cell-cell tension measurements have been made.

2.4.2 Mechanoregulation of apoptosis

Apoptosis, or programmed cell death, is associated with calcific deposits in CAVD, and is also known to be regulated by physical cues. Apoptosis is a powerful mechanism for removal of excess cells following wound healing and during morphogenesis. Dysregulation of apoptosis can lead to fibrosis and cancer [98], but little is known how it may contribute to CAVD. Decreases in CSK tension initiate apoptosis in fibroblastic cells. Such conditions include 1) release of contractile cell-populated collagen gels from rigid anchors [99], 2) inhibiting adhesion to the ECM proteins [100], 3) low substrate modulus [33, 101, 102], and 4) restricted cell spread area [103] [104]. Although cytoskeletal tension is not generally measured with apoptosis, separate studies demonstrate 1) cells in free-floating gels generate minimal tension [105], 2) blocking integrin-ECM binding leads to a decrease in traction force [106], 3) cells with smaller spread area generate weaker traction forces [82, 107-109], and 4) cells cultured on soft substrates generate lower traction force compared with

those cultured on stiffer substrates with identical ECM coating [33, 110]. Very little is known in particular about the sensitivity of VICs to these stimuli, and whether a stimulus that changes cytoskeletal tension will trigger a reversal of myofibroblastic phenotype to quiescent VICs or initiate apoptosis. More studies that take a quantitative approach to assess VIC tension are needed to determine the answer to this important question.

2.4.3 The Apoptotic Pathway and Methods for Apoptosis Detection

Apoptosis is a well-studied cell phenomenon that consists of a specific sequential series of events. A cell death event can be “triggered” by either external or internal signals. External cues, such as binding to lethal ligands, initiate the extrinsic pathway of apoptosis, and internal signals of cell stress initiate the internal pathway. Although the initial steps of these pathways are different, they converge with a caspase cascade, as seen in Figure 2.10.

A dying cell exhibits several “hallmark” features, including initial cytoplasmic condensation, blebbing of the plasma membrane, and finally release of apoptotic bodies.

Several methods of apoptotic detection exist and are typically grouped into early and late of apoptosis. Early detection methods use Annexin V, which binds to the biomarker protein phosphatidylserine (PS). Phosphatidylserine appears in the plasma membrane of apoptotic cells and is used as a signal for T-cells, signaling phagocytosis. This method can be used *in vivo* and is often used to assay the death of cancer cells and response to treatment. Late detection methods include TUNEL and caspase detection. TUNEL assays for DNA degradation by binding to DNA that has been nicked by the cellular enzyme terminal deoxynucleotidyl transferase. TUNEL inserts dUTPs, which can be detected a priori by antibody staining. Caspase detection methods exist for both initiator caspase (caspase 8/9) and effector caspase (3/7).

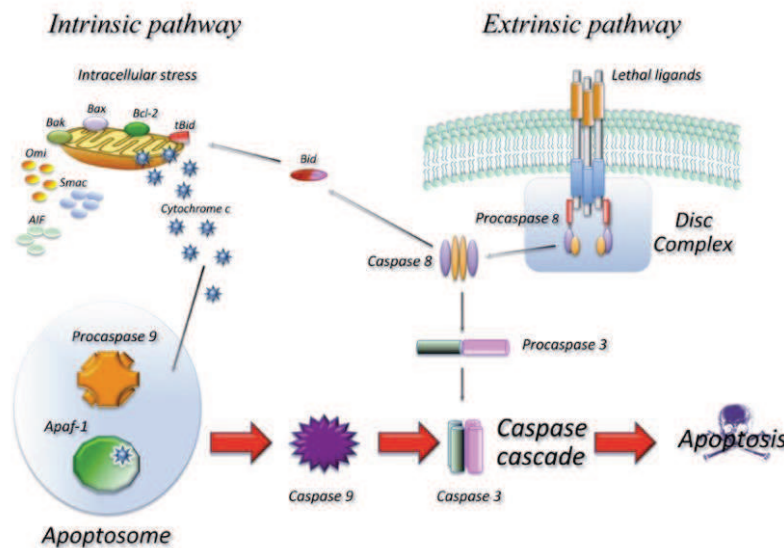


Figure 2.10. Apoptotic pathway is a well defined signaling cascade which can be initiated by either extrinsic or intrinsic signals. Caspase 3/7 are cleaved at the final stage of apoptosis. [111], Reproduced with permission

2.5 Traction Force

Traction forces are created by the acto-myosin machinery of the cell. These contractile forces are transferred to the extracellular matrix at discrete points called focal adhesions. For an illustration of traction force generation, please see Figure 2.10. These forces create a stress and strain field in the surrounding extracellular matrix. The external stress and strain in the ECM in return modulate cellular functions such as extracellular matrix protein secretion and differentiation. Many disease states such as cancer, fibrosis, and hyper-tension all have traction force dysregulation. Traction forces are essential for all cellular processes which require adhesion to the extracellular matrix and tension within the cytoskeleton. This includes cell migration [112], cell differentiation, extracellular matrix assembly [113, 114], and cell proliferation.

These forces were first described by Harris et al. [114] as wrinkles on a flexible silicone substrate. Dembo and Wang [115] later created a more accurate technique, which uses micro-fluorescent beads embedded in a flexible substrate with a known modulus (or “stiffness”). Polyacrylamide gels are the most frequently used material in the literature, but in theory, a hydrogel would be adequate. The traction force is calculated using a combination of image analysis and finite element method calculations. For each cell, three images are captured. A phase image, showing the cell boundary, a fluorescent image of the microbeads below the cell, and a fluorescent image of the relaxed substrate after the cell has been trypsinized. Using the bead images, a displacement field is determined. Knowing the substrate modulus, the substrate stress can be calculated. From the phase image, cell boundaries and cell area can be determined. The substrate stress is then multiplied by the cell area and the cell traction force is determined.

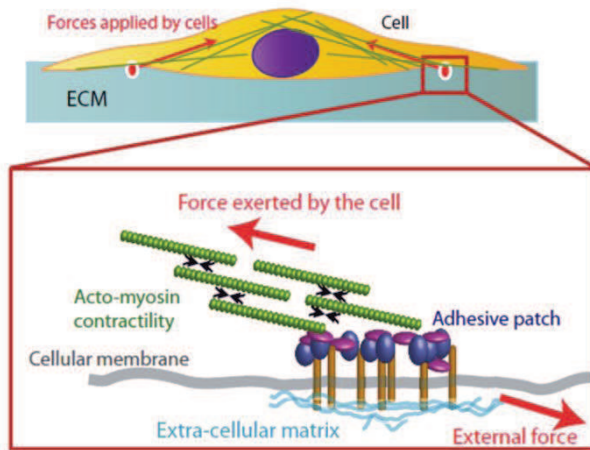


Figure 2.11. Illustration of cell traction force generation against a substrate. The cell actin-myosin machinery connects to the extracellular matrix at discrete points known as focal adhesions. The focal adhesions comprise several types of proteins, such as integrins, which assemble together to form the focal-adhesion complex. Schematic originally appear in [116] and is reproduced here with permission.

2.5.1 Traction Force Trends

Traction force has been shown to correlate with cell spread area. As cells increase in size, cells are able to generate increased amounts of traction force [82]. Cell spread area, as well as the amount of traction force a cell is able to generate, increases as substrate stiffness increases [82].

Additionally, cell shape affects the amount of tension a cell is able to generate. With cell area held constant, the greater the cell elongates, the more traction force the cell is able to generate [107].

For example, for a rectangular cell and square cell of the same area, the rectangular cell will generate larger traction forces than the square cell. Fibroblastic cell types have increased traction force when cultured in the presence of growth factor TGF- β 1. This effect was stronger as the substrate stiffness increased [91]. As stated previously, fibroblastic cells can differentiate into myofibroblastic cells in the presence of TGF- β 1 by incorporation of the α SMA protein into the f-actin stress fibers [64]. A study by Chen et al. showed that traction forces are predictive of cell phenotype, which can be seen with myofibroblastic cells staining α SMA positive and generating increased levels of traction force, as seen in Figure 2.12 [66].

An elegant study by Han et al. used micro-contact printing on micro-posts to decouple the effects of

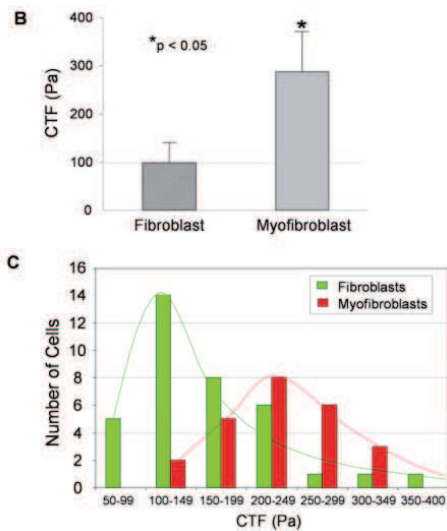


Figure 2.12. Myofibroblasts generate increased traction force. α SMA positive cells, indicating myofibroblastic phenotype, are capable of generating increased traction forces. Cell traction force is increasingly being recognized as a measure of cell phenotype. Figure adapted from [66] and reprinted with permission.

cell area and focal adhesions [117]. As cells increase in size, they also increase in the number of focal adhesions. As traction forces are created at focal adhesions, it was unknown prior to this study if cell size or the number of focal adhesions was the primary contributor to traction force. As cellular focal adhesions can only form on a micro-post, the number of focal adhesions can be controlled by the number of micro-posts on which the cell is able to bind. By controlling the density of micro-posts, they were able to create two cell areas with the same number of micro-posts, as seen in Figure 2.13. Interestingly, despite the difference in size, cells generated identical levels of traction force, indicating that the number of focal adhesions determines the amount of traction force a cell is able to generate, and not the cell size.

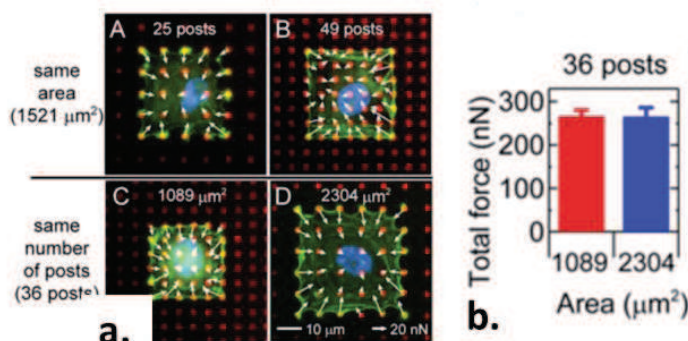


Figure 2.13. Combining micro-contact printing with micro-posts allows for examination of the relationship between cell spread area and number of focal adhesions. Cells that had the same number of micro-posts generate identical levels of traction force. Figure modified from [117] with permission.

2.5.1.1 Measures of Cell Shape:

Cell shape is an important regulator of cellular processes, such as traction force. Two measures of cell shape will be referenced in this thesis. These include form factor and elongation. Shape factor was first used by Chen et al. and is a measure of the number of cellular extensions. Form factor is calculated using the following formula:

$$\text{Form factor} = \frac{4\pi * \text{area}}{\text{perimeter}^2}$$

Form factor values range from 0 to 1. Cells with many filipodia and high elongation will have a shape factor closer zero. Cells that are perfectly circular will have a shape factor of 1. Shape factor gives some indication of the mechanical environment of the cell; cells that are cultured on soft substrates are often highly circular with low spread area, while cells on stiffer substrates will be more spread and have a lower shape factor.

Elongation ratio is an indication of how elongated a cell is. It is determined by fitting an ellipse to the cell and taking a ratio of the major and minor axis of the ellipse using the following formula:

$$\text{Elongation ratio} = \frac{(A_{\text{maj}} - A_{\text{min}})}{(A_{\text{maj}} + A_{\text{min}})}$$

where A_{maj} is the major axis of the ellipse and A_{min} is the minor axis of the ellipse

2.6 Simultaneous Measurements of Cell Traction with Stretch

As studies that combine traction force with stretch have increased complexity and are technically very challenging, all the studies to date are of short duration (< 4 hours). While these studies have been short in duration, they have revealed that cell traction force changes rapidly with stretch, and the response depends upon a variety of factors, including the magnitude, type, duration, and direction of stretch with respect to cell orientation. On polyacrylamide gels, Fredberg and colleagues

observed that the traction force response to a single stretch depends upon the strain field. Under a homogenous strain field, cells decrease their traction force immediately, with a recovery over about 15 minutes. On the contrary, when exposed to a non-uniform strain field, the traction force a cell is able to generate actually increases [118]. Sub-cellular measurements of traction force microscopy using micro-posts show that the area of the cell generating the traction force are not uniform, and occur primarily along the cell periphery.

The duration of stretch also affects the traction force response; Fu and colleagues observed that cell-generated traction forces increase initially in response to a rapid step stretch of cells cultured on micropillar arrays, and then return to or fall below initial baseline values over the next 60 minutes as the stretch is held [119]. More recently, the same research group utilized micro-contact printed areas of various geometries and demonstrated that cell shape and orientation control the cell's traction response to stretch [120]; notably, elongated cells oriented perpendicular to stretch exhibited little response to stretch, whereas those aligned with stretch exhibited large changes in traction force. Mertz and colleagues stretched cells onto soft micro-pillars for four hours. Stretch waveforms were varied to determine if it is the stretch in general, the holding of the stretch, or the release of the stretch that cues a cell to elongate. Cells were initially rounded and then increased in size, area, proliferation, and traction force with time [29]. A complete summary of studies combining traction force is summarized in Table 2.3.

Table 2.3- summary of studies combining traction force with stretch

Author	Type of stretch	Magnitude	Duration	Main Finding
Krishnan et al. (2009)	Homogenous isotropic, homogenous anisotropic, non-homogenous	10%	Instantaneous stretch and release over 4s; one subset experiment had repeated stretching every 100s	Cell contractile moment immediately decreases following instantaneous stretch in a homogenous strain field. Non-homogenous stretch resulted in increased contractile moment. Repeated homogenous stretching resulted in decreased contractile moment that did not recover to initial levels. Repeated Non-homogenous stretch resulted in increased traction force following each subsequent stretch which eventually reached a maximum value.
Chen et al. (2010)	Homogenous bi-axial	10%	Instantaneous stretch and release over 4 s	Cell contractile moment immediately decreases following instantaneous stretch. Contractile moment recovered after 300s.
Nagayama et al. (2011)	uniaxial	6%	Two cycles of stain over 10 minutes	Traction force varies with location within the cell during stretch. Greatest forces occur at cell periphery. Temporal changes in cell traction force correlate with strain-waveform
Mann et al. (2012)	Uniaxial	6%, 15%	Stretch and hold for 60 minutes	Cell traction force increases initial following step stretch. Cell traction force returns to initial baseline values within 30 minutes
Shao et al. (2014)	Uniaxial	20%	Stretch and hold for 60 seconds	Micro-posts were micro-patterend with different shapes. Cell traction force response to stretch was related to global architecture of the cytoskeleton
Cui et al. (2014)	Uniaxial	5%	4 hours	Cells initial rounded on soft micro-pillars increased in spreading and proliferation with stretch. Traction force increased as cells spread.

2.7 Other measures of cell tension state

Atomic force microscopy, magnetic bead twisting rheometry, and micropipette aspiration have all been used to assess cytoskeletal tension. Although not a direct measure of cell tension, these methods have been correlated with the amount of traction force a cell is able to generate. Using variations in cell stiffness to indicate changes in cell tension was first proposed by Wang and colleagues in 1996 [121]. In 2002, Stamenovic and colleagues showed linear correlation between cell tension, as measured by contractile moment, and stiffness measured by magnetic bead twisting rheometry, as seen in figure 2.14.

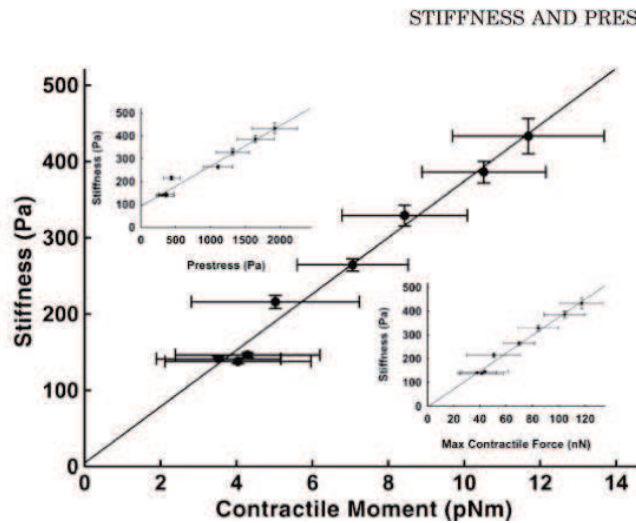


Figure 2.14. Relationship between cell tension and cell stiffness. Cell stiffness is positively correlated with contractile moment, a measure of cell contractility, indicating that stiffness measurements may be used to determine tension state of the cell. Adapted from [78] with permission.

2.8 Geometric Control of Cell Behavior

Micro-contact printing involves “stamping” proteins in defined geometric shapes. Analogous to stamping with ink on the macro-scale, the stamps create protein islands of the desired geometry.

Initial studies were done on glass coverslips, but it has since been combined with polyacrylamide gels and micro-posts as described above for concomitant studies of cell shape and traction force.

Micro-contact printing has been used with both single cells and groups of cells. With single cells, the effect of cell shape and size on cell behavior has been investigated. Micro-contact printing of cell aggregates reveals differential behaviors with geometric location (i.e. periphery or center), which may give insight into spatial cues required in tissue morphogenesis.

Studies in single cells have determined that there is a geometric component in apoptosis induction.

Cells that had been restricted to 20 μm diameter circles underwent higher rates of apoptosis than cells on 50 μm diameter circles [103]. Cell shape also impacts lineage commitment of mesenchymal stem cells. By controlling cell geometry, differentiation of stem cells into a specific lineage commitment could be directed [122]; shapes that allowed for local areas of high cell tension (i.e.

pointed features between concave surfaces) promoted increased myosin activity that was associated with pathways of osteogenesis. Ablating the tension with various agents such as blebbistatin and cytochalasin-D pushed cells towards adipocyte lineage commitment.

Studies with aggregates of cells on micro-contact printed geometries have shown the proliferation rates vary with location within the aggregate. Chen and colleagues modeled micro-contact printed monolayers using a bi-layer model with a passive and contractile layer. Thermal strain was used to model contractility [123]. This model predicted areas with highest stresses to occur along the periphery of the geometry. Although simplistic, this model predicted proliferation behavior of bovine pulmonary endothelial cells on micro-patterned substrates as measured by BrdU incorporation. Piccolo and colleagues examined YAP nuclear localization with multicellular aggregates and found that areas of high stress, such as along the micro-pattern perimeter, promoted YAP translocation to the nucleus [124]. Vunjak-Novakovic and colleagues examined MSC differentiation on large (1000 μm) rings (200 μm inner diameter) and found osteoblastic lineage commitment varied with location within the ring. This differentiation was primarily localized to regions where cell area was small yet cells still remained elongated (such as the inner edge of a ring and the regions next to the short edges of rectangles) [125]. The differentiation and proliferation activity observed was abolished with the use of cytoskeletal inhibitors, such as blebbistatin and Y-27632. Combining these studies show the power of mechanical stresses in regulating multi-cellular behavior, and that cellular behavior within aggregates can vary due to the differences in mechanical stresses throughout the geometry.

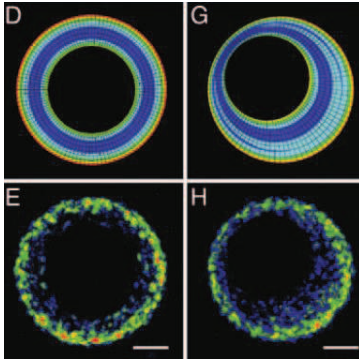


Figure 2.15. Mechanical stresses predict cellular behaviors.

Thermal cooling model of an annulus shows regions of high stresses localized primarily along the geometry periphery (D, G). Heat map of BrdU incorporation, a measure of proliferation, varies within geometry in agreement with predicted substrate mechanical stress. Cell proliferation varies with mechanical tension state highlighting the importance of multicellular mechanics in regulating individual cell behaviors. Figure adapted from [123], copyright PNAS.

2.9 Rationale for quantitative methods

Traction force was used as an overall metric to determine the contractile ability of a cell, or in the case of multicellular use, an aggregate. Traction force is most commonly used in the literature to measure cell tension, while other techniques such as atomic force microscopy measure “stiffness” which is an indirect measure of cell tension. Determining tension of a single cell within an aggregate is challenging, and in certain experiments stiffness was used as a proxy measurement for this reason. Maximum substrate stress was used as a measure of peak stress applied to the substrate. Location of peak stress with respect to cell geometry was noted. For multicellular aggregates, location of peak stress with respect to position in the aggregate, was of interest. As cell shape and area can be indicative of phenotypic state, cell area was reported in Chapter 3. Shape factor and elongation was used to give an indication as to how many cellular filopodia (extensions) were present and the degree of polarization, respectively. Since cells can reorient with stretch and the rate of reorientation is cell type specific [126], the angle of orientation was also quantified. Alazarin Red S intensity was used as an indicator of calcium mineralization (reviewed by Merryman [10]). Caspase 3/7 activity was used to determine the presence of apoptosis within valvular interstitial cell aggregates. As a terminal measurement of cell death, calcein AM and ethidium homodimer-1 were used. The α SMA incorporation into stress fibers, YAP translocation to the nucleus [124, 127], and

vinculin size [128] were used as semi-quantitative immunohistochemistry markers of high cell tension states.

2.10 Summary

The valvular interstitial cell is a mechanosensitive cell type which expresses a range of phenotypic states from quiescent fibroblasts to highly contractile myofibroblasts. This range in phenotypes is affected by substrate stiffness and the presence of soluble factors. The amount of cell tension is influenced by the phenotypic state. Stretch, indirectly measured by cell area, has also been shown to affect cell tension. As the valve is a highly dynamic environment, understanding the traction force response to long-term cyclic stretch is of critical importance for understanding valvular interstitial cell tension and phenotypic regulation in physiologically relevant mechanical environments. The ability of these cells to undergo aggregation *in vitro* appears to be influenced by many things, such as cell tension, aggregation frequency increases in the presence of TGF- β 1, increased Rho-pathway activity, being cultured on stiff culture surfaces, and cyclic stretch when cultured with TGF- β 1. However, to date, no study has examined the distribution of tension within the aggregate, and induction of apoptosis and calcification. This is partly due to the random nature of the aggregation process. In order to facilitate investigation of the underlying disease mechanisms where valvular interstitial cells undergo apoptosis and calcification after aggregation, more reliable, repeatable, and controllable methods of aggregation must be established.

Chapter 3: Active traction force response to long-term cyclic stretch is dependent upon cell prestress

Heather Cirka¹, Melissa Monterosso², Nicole Diamantides³, John Favreau¹, Qi Wen⁴ and Kristen Billiar¹

1. Department of Biomedical Engineering, Worcester Polytechnic Institute, Worcester, MA
2. Engineering Science, Sweet Briar College, Sweet Briar, VA
3. Department of Biomedical Engineering, Bucknell University, Lewisburg, PA,
4. Department of Physics, Worcester Polytechnic Institute, Worcester, MA

The following chapter was submitted to the Biophysical Journal and has been accepted for publication as of February 15th, 2016.

3.0 Abstract

Mechanical stimulation is recognized as a potent modulator of cellular behaviors such as proliferation, differentiation, and extracellular matrix assembly. However, the study of how cell-generated traction force changes in response to stretch is generally limited to short-term stimulation. The goal of this work is to determine how cells actively alter their traction force in response to long-term physiological cyclic stretch as a function of cell prestress. We developed a novel method to assess traction force following long-term (24 h) uniaxial or biaxial cyclic stretch under conditions of high cell prestress with culture on stiff (7.5 kPa) polyacrylamide gels (with or without TGF- β 1) and low prestress by treating with Blebbistatin or culture on soft gels (0.6 kPa). In response to equibiaxial stretch, valvular interstitial cells (VICs) on stiff substrates decreased their traction force (300 nN to 100 nN) and spread area (3000 to 2100 μm^2). With uniaxial stretch, the cells had similar decreases in traction force and area and reoriented perpendicular to stretch. TGF- β 1 treated VICs had higher prestress (1100 nN) and exhibited a larger drop in traction force with uniaxial stretch, but the percentage changes in force and area with stretch were similar to the non-TGF- β 1 treated group. Cells with inhibited myosin II motors increased traction force (41 nN to 63 nN) and slightly reoriented towards stretch direction. In contrast, cells cultured on soft gels increased their traction force significantly from 15 nN to 45 nN, doubled their spread area, elongated from an initially rounded morphology, and reoriented perpendicular to uniaxial stretch. Contractile moment measurements provided results consistent with total traction force measurements. Combined, the results indicate that the change in traction force in response to external cyclic stretch is dependent upon the initial cell prestress. This finding is consistent with depolymerization of initially high-tension actin stress fibers, and reinforcement of an initially low-tension actin cytoskeleton.

3.1 Introduction

Cell traction forces are essential to numerous cell processes such as migration [112, 129], adhesion [115], and extracellular matrix (ECM) assembly [113]. Cells generate traction forces through the actin-myosin machinery of the cytoskeleton which are transmitted to the surrounding extracellular matrix (ECM) via integrins. Cell traction forces produce stress and strain in the surrounding matrix, and the external stress and strain in the ECM modulate cellular functions such as ECM protein secretion [130] and differentiation [114]. Many disease states such as hypertension, fibrosis, and cancer result in the dysregulation of a cell's ability to generate traction forces [131-133]; as such, traction force is an important functional readout of cell phenotype [134].

Traction force is also a useful measure of a cell's integrated response to physical and biochemical cues. Cell traction forces have been shown to be influenced by substrate stiffness [82, 91], restriction of both cell shape [107] and spreading [82, 117], ECM composition [135], and the presence of soluble factors [91]. Recently, rapid increases and decreases in traction force in response to stretch have been documented [118, 119]; however, the ways in which the traction forces are altered upon remodeling of the cytoskeleton in response to long-term external stretch remains largely unknown. Understanding the ways in which cell-generated forces change with long-term cyclic stretch would provide insight into the regulation (or dysregulation) of cell tension during cell differentiation, proliferation, and apoptosis – biological events that occur over time-scales not currently investigated in combination stretch/traction force studies.

Collectively, observations from a variety of studies indicate that many concomitant factors affect the ability of a cell to generate traction force in static culture. As substrate stiffness increases, the ability of cells to generate traction force increases [82, 91]. On stiffer substrates, spread area [117], cell

form factor (a function of cell area and perimeter) [107], and elongation [117] may also increase. These morphometric parameters affect the traction force that a cell is able to generate; it has been demonstrated that cells with larger spread area [117] and greater elongation [136] generate higher magnitudes of traction force compared to their respective controls. Stiffness, area, and cell shape relationships become even more complicated with the addition of dynamic stimulation. We have previously demonstrated that, with cyclic equibiaxial stretch for six hours, cells that are small and rounded in static culture on soft (0.6 kPa) substrates increase in area and elongation at levels similar to cells cultured statically on stiff substrates [137]. Additionally, increases in traction force and cell proliferation have been reported with short-term stretch on soft micropillar substrates [29].

The cell's ability to generate traction force changes rapidly with stretch and depends on the magnitude, direction, type, and duration of stretch, as well as the cell's orientation with respect to the stretch direction. On polyacrylamide gels, Fredberg and colleagues observed that cell traction, as represented by the contractile moment, decreases precipitously in cells subjected to a rapid step and release of stretch [118, 138]. The recovery following the immediate loss of traction depends upon the uniformity of stretch. With a homogeneous strain field, the traction recovers to baseline over approximately 10 minutes, whereas with a non-homogeneous strain field, cells increase their contractile moment [138]. With multiple cycles of repetitive homogeneous stretch and release, the cells were not able to recover their baseline contractile moment within the 10-minute dwell time. Subcellular measurements of traction force utilizing stretch of micropillar arrays indicate that the cell traction response can vary with location within the cell, with the largest changes in traction force occurring along the periphery [139]. The duration of stretch also affects the traction force response; Fu and colleagues observed that cell-generated traction forces increase initially in response to a rapid step stretch of cells cultured on micropillar arrays, then return to or fall below initial baseline values over the next 60 minutes as the stretch is held [119]. More recently, the same

research group utilized micro-contact printed areas of various geometries and demonstrated that cell shape and orientation control the cell's traction response to stretch [120]; notably, elongated cells oriented perpendicular to stretch exhibited little response to stretch, whereas those aligned with stretch exhibited large changes in traction force. These pioneering studies indicate that the traction force changes rapidly with short-term stretch (<1 hr); however, extrapolating the cytoskeletal response observed in each of these studies to how the traction force will change with long-term cyclic stretch is not possible due to active adaptations of the cytoskeleton to stretch, such as alpha-smooth muscle actin incorporation into stress fibers and reorientation of the cell "away" from stretch.

The goal of this work is to determine how cells alter their traction force in response to long-term physiological cyclic stretch. We hypothesize that changes in traction force with stretch are dependent upon the cell prestress. As defined in prior reports [140], cell prestress is the overall level of cytoskeletal tension under static conditions (prior to stretch). Cell prestress can be quantified by total traction force as we do herein, or by total contractile moment applied to the substrate, although it is understood that neither of these metrics have units of engineering stress. In the present studies, cell prestress was modulated by culturing valvular interstitial cells (VICs) and U2OS cells on tunable-modulus polyacrylamide hydrogels (7.5 kPa and 0.6 kPa) and treatment with TGF- β 1 or Blebbistatin. The hydrogels were attached to custom-designed PDMS wells and 10% biaxial or uniaxial stretch was applied with micro-controlled motors. After 24 hours of stretch, wells were removed from the stretch device and imaged for traction force measurements and analysis of cell morphology.

3.2 Methods

3.2.1 Cell Culture

Valvular interstitial cells (VICs) were chosen as a fibroblastic cell which is capable of alternating its prestress level with TGF- β 1 supplementation [14]. VICs were isolated from porcine heart valve leaflets obtained from a local abattoir (Blood Farm, Groton, MA) within three hours of tissue harvest per published protocols [137]. Cells from passages 3-4 were used for all experiments. U2OS (human osteosarcoma) cells, generously donated by Dr. Roland Kaunas (Texas A&M University), were used as comparison cells to determine if there is a cell-type specific traction force response with stretch.

For all experiments, cells were seeded at a density of 2,500 cells/cm² and cultured for 24 hours at 37° C, 10% CO₂, in standard media (1X DMEM, 10% FBS, and 1% antibiotic-antimycotic). To pre-differentiate the VICs to the myofibroblast phenotype and thus increase the cell prestress, a subset of VICs were pre-treated with 5 ng/mL TGF- β 1 (AcroBiosystems, Newark, DE) for five days prior to cell seeding. To inhibit myosin-II activity and reduce the cell prestress, a separate subset of cells were treated with 10 μ m Blebbistatin (Sigma-Aldrich, St. Louis, MO) prepared according to manufacturer's directions for one hour before stretching. Following addition to the wells, Blebbistatin remained in the media for the duration of the experiment.

3.2.2 Stretch System and Culture Well Development

A custom stretch system and compliant culture well system was developed with maximum optical clarity and uniformity in the strain field to apply long-term cyclic stretch to the cells (please see Supplementary Information for details). The stretch device consists of four micro-controlled stepper motors on a low-profile aluminum base that can be mounted on an inverted microscope or placed in a standard temperature and CO₂-controlled incubator. The system is controlled by an open-source

Multi-Platform Integrated Development Environment (MPIDE) program which allows for stretch patterns, such as pure uniaxial stretch and uniaxial stretch of alternating direction each cycle, not available on commercial cell stretching systems (e.g., Strex,).

Custom compliant culture wells were designed to circumvent limitations of commercially available systems for stretching cells which make traction force measurements challenging, namely: thick membranes and non-uniform strain fields in Flexcell© and Strex wells. The inverse molds for the custom wells were created with a thin metal spacer to form the bottom membrane. This allowed for the wells to be created in one casting of material, enabling the bottom to be formed without prestretch (for more information on the design of the well, please see Supplementary Information). The molds for the wells were drawn in Solidworks (Dassault Systems, Waltham, MA) (Figure 3.1a) and machined out of polycarbonate sheets (Tap Plastics, Stockton, CA) using a CNC machine. The wells were optimized for uniformity of strain field using finite element analysis (ANSYS, Canonsburg, PA). Wells were cast with 16:1 base to cross-linker ratio of polydimethylsiloxane (PDMS, Sylgard 184 Silicone Elastomer Kit, Dow Corning, Midland, MI) and strain patterns under various stretch regimens were validated using high-density displacement mapping software (courtesy of Dr. Glenn Gaudette, Worcester Polytechnic Institute) (Figure 3.1c). The custom well has an integrated bottom membrane which is sufficiently thin (<150 μm) to allow for quality images to be obtained even with attachment of a 70 μm thick polyacrylamide gel (details in the next sub-section).

For all experiments, wells were stretched 10% (equibiaxial or uniaxial) at 1 Hz with a saw-tooth waveform for 24 hours in a temperature and CO_2 -controlled incubator. The well was then transferred to a microscope for traction force measurements in the zero-strain configuration. Measurements were completed approximately 15 minutes following cessation of stretch to allow for equilibration of cell-generated traction forces in the undeformed configuration. Static control

cells, cultured in identical wells that were not mounted on the stretch device, were analyzed in the same manner to serve as controls.

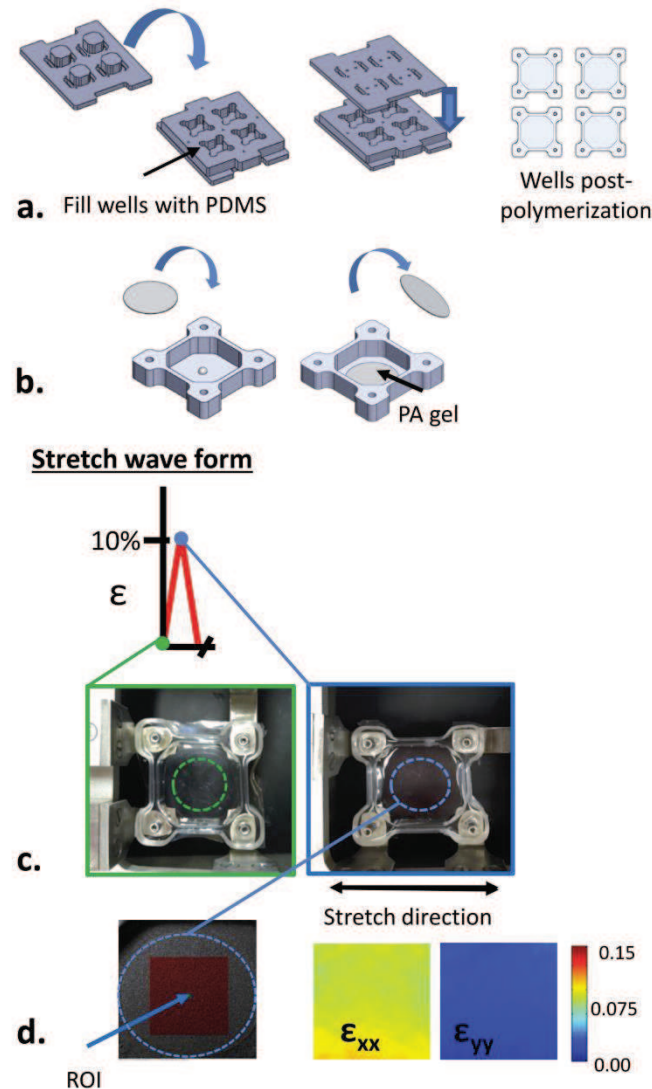


Figure 3.1- Overview of method. (a.) Wells were created in a custom polycarbonate mold out of 16:1 PDMS. (b) Polyacrylamide gels were attached to PDMS wells using previously published protocol. After chemical treatment which activates silicone substrate, an unpolymerized droplet of polyacrylamide was placed onto well. A 22mm coverslip was placed onto droplet (1b, left) and a uniform gel thickness was acquired by capillary action. (1b, right) post-polymerization coverslip was removed. (c) Stretch wave form of strain field analysis. Color dots indicate where representative images of wells were taken, and are outlined for clarity. (d) Analysis region of uniaxial stretched gel for strain field analysis indicated with transparent red square. Longitudinal (ϵ_{xx}) and lateral (ϵ_{yy}) strain fields shown.

3.2.3 Tunable-Stiffness Traction Force Substrate Preparation

For traction force measurements, polyacrylamide (PA) hydrogels were chosen as the compliant substrate as they are optically clear, have well-defined mechanical properties, and have an easily tunable modulus. To attach 70 μm thick PA to the PDMS wells, our previously published method was utilized with minor modifications [137]. Briefly, the PDMS surface was plasma treated then activated with a series organic solvents to facilitate PA bonding to the PDMS membrane, then 50 μl of PA solution was pipetted on the surface and cover slipped under continuous nitrogen flow. Even with these aggressive treatments, often when removing coverslips following polymerization, the low modulus gels (<1 kPa) stick to the glass coverslip and pull off the PDMS membranes. To facilitate more robust attachment, a thin (50 μm) PA gel with modulus of 7.5 kPa was attached to the gel first, and then 50 μl the low modulus (0.6 kPa) solution was pipetted onto the high modulus gel. Attachment was validated using different color fluorescent beads within the gels for verification of each layer.

Next, to allow for traction force measurements, 0.2 μm fluorescent beads were embedded into the top surface of the gel. This was accomplished by evaporating 35 μL of a 0.5% solution of 0.2 μm fluorescent beads (Life Technologies, Grand Island, NY) in 100% ethanol (Sigma-Aldrich, St. Louis, MO) onto 22 mm circular glass coverslips (VWR, Randor, PA). The beaded coverslip was placed on top of the unpolymerized top gel. The gels were allowed to sit undisturbed for 1 hour before the coverslips were removed.

To facilitate cell attachment, PA gels were coated with 0.5 mg/ml solution of sulpho-SANPAH (Thermo-Fischer, Waltham, MA) and reacted under ultraviolet light as per [137]. A monomeric pepsin-extracted collagen solution (PurCol, Fremont, CA) of 3 mg/ml was diluted to 200 $\mu\text{g}/\text{ml}$ in 1 mL of 0.02 N acetic acid and was placed on the gels. The collagen solution remained on the gels

overnight at 4°C. As the process is not sterile, to avoid contamination, gels were treated with an antibiotic solution and rinsed with PBS prior to cell seeding.

The modulus of polyacrylamide gels was measured by atomic force microscopy indentation at 1 $\mu\text{m/s}$ (Asylum AFM, 0.06 N/m cantilever, conical tip). Ten measurements were made over the gel, and two gels per stiffness were analyzed. A custom MATLAB (Mathworks, Natick, MA) script was then used to extract the Young's modulus from each curve by fitting the first 200 nm of indentation data to the Hertz model for a conical indenter. The extracted values were averaged to determine the mean modulus for each gel.

3.2.4 Traction Force Measurements

Images were captured using a Zeiss inverted microscope and CCD camera (Thornwood, NY). Using a motorized stage and Zeiss Axiovision software (v. 4.8.2 SP1), three images were acquired for each cell: a phase contrast image of cell, fluorescent image of beads within substrate beneath the cell, and a fluorescent image of beads in relaxed substrate when cell was removed via 0.25% trypsin with EDTA (Gibco, Grand Island, NY), see figure 3.2c. 6-20 cells per treatment/stretch condition were imaged in each the static control and stretched groups. Please see table 3.1 for exact number. Cell traction force present in table 3.1 is a population average and standard deviation, not a reflection of individual cells before and after stretch. Due to the flexible nature of the PDMS membrane, the weight of the liquid media and trypsin caused slight image distortion. A custom well holder was created with a No. 1 25 mm square coverslip (VWR, Logan, UT) to support the thin membrane during imaging (Figure 3.2b).

A custom MATLAB program (Mathworks, Natick, MA) was created for image processing. Drift from the stage was removed by averaging the displacement of beads within small selected areas of the image corners. The images were then cropped around the cell of interest and cell boundaries were

manually selected. Bead displacements were calculated using mass particle image velocimetry (code available from MATLAB Central). Substrate material properties, substrate dimensions, bead displacements, and the cell boundary were imported into ANSYS 14.0 (Ansys, Canonsburg, PA). Using FEA, stresses at the nodes under the cell were calculated. A custom MATLAB program was used to calculate total cell traction force magnitude, F , from the surface shear stresses, S , in the substrate and unit mesh area, da , using the following equations:

$$S_i = \sqrt{S_{i_{xz}}^2 + S_{i_{yz}}^2} \quad (\text{Equation 3.1})$$

$$F_{total} = \sum_{i=1}^n (S_i \times da) \quad (\text{Equation 3.2})$$

Only stresses from nodes which lie within the cell boundary were integrated for the traction force calculation in (2).

As a second measure of overall cell contractility, contractile moment was computed as described previously in [141].

$$\mu = M_{xx} + M_{yy} \quad (\text{Equation 3.3})$$

Where M_{xx} is the combination of the traction forces in the x-direction weighted by their coordinates in the x-direction and M_{yy} is the combination of the traction forces in the y-direction weighted by their coordinates in the y-direction. As defined, the net contractile moment is negative for a cell that is pulling inward and positive for a cell that is pushing outward. The angle of principle stress was also computed as described in [141].

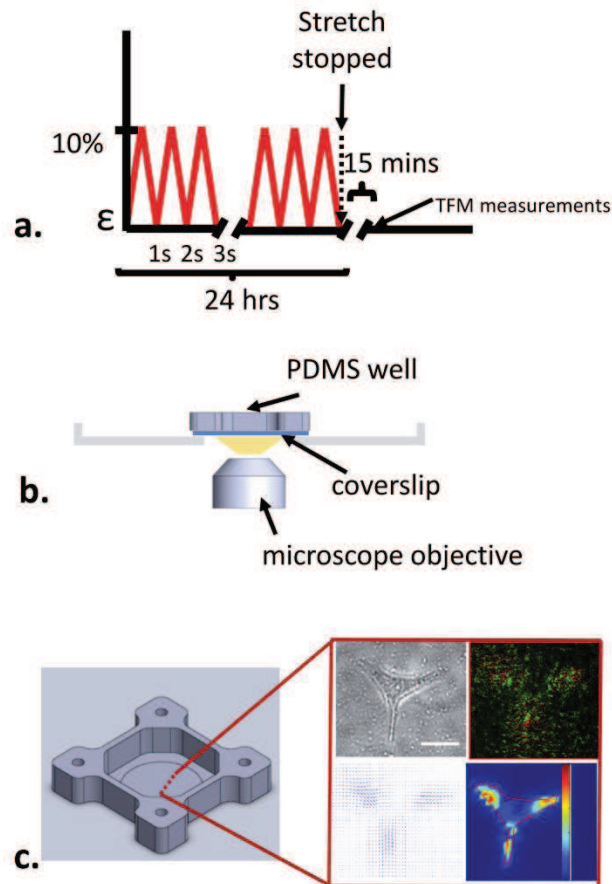


Figure 3.2. Overview of traction force measurements. (a) Time course schematic of experiment. All stretch experiments were at 10% magnitude (either uniaxial or biaxial stretch). At 24 hours, stretch was stopped and the well was removed from the stretch device and placed in microscope viewing dish for image acquisition. Wells were in original conformation during the image acquisition process. (b) Image acquisition set up, side view. (c) Representative images of traction force calculation. Phase image of cell were acquired as well as a fluorescent image of beads embedded within the polyacrylamide gel. Green and red colorizations show the stressed and relaxed (cells trypsinized) substrate, respectively. Using a particle tracking algorithm, bead displacements were calculated. Finally, knowing the modulus of the substrate and the bead displacements, a stress map of the substrate was created.

3.2.5 Orientation and Area Measurements

Phase images were acquired at 24 hours, and cell morphological measurements were made using ImageJ [142]. To determine alignment angle relative to the stretch axis, a line was fit through the long axis of the cell nucleus. For angles over 90 degrees, the supplementary angle is reported due to symmetry. A minimum of 90 cells from each group were measured. Cell area, perimeter, and major and minor axis dimensions were measured, and form factor [137, 143], an indication of the number of cellular extensions, and elongation [144] were calculated using the following formulas:

$$\text{form factor} = \frac{4\pi \cdot \text{area}}{\text{perimeter}^2} \quad (\text{Equation 3.4})$$

$$\text{elongation} = \frac{(A_{\text{maj}} - A_{\text{min}})}{(A_{\text{maj}} + A_{\text{min}})} \quad (\text{Equation 3.5})$$

where A_{maj} and A_{min} are the major and minor axes of a fitted ellipse, respectively.

3.2.6 Statistics

All values reported are mean \pm standard deviation. Differences in metrics between static and stretch were compared for each treatment using two-tailed student t-tests assuming equal variance. Due to dissimilarity in the baseline levels between treatment groups (e.g., TGF- β 1, Blebbistatin, soft, stiff), these treatment groups were not compared statistically. A p-value less than 0.05 is considered to be statistically significant. Each stretched group was compared to its respective control with a student t-test using Sigma-Plot v. 11.0 (Systat Software, Inc., San Jose, California). Angle was measured with respect to stretch direction, stretch direction was defined as 0 - 180 $^{\circ}$.

3.3 Results

To assess the effect of long-term stretch on traction force, we first cyclically stretched the cells equibiaxially on stiff substrates to reduce effects of stretch avoidance by cell reorientation. The maximum substrate stress decreased significantly with stretch, as did the overall cell traction force and contractile moment ($p < 0.05$). As our current experimental set up does not allow for tracking individual cells over time, traction force measurements reported herein are population averages of stretched cells compared to a separate, paired control group of statically cultured cells.

Representative stress plots for cells from each culture condition are shown in Figure 3.3. Figure 3.4 shows the relative (%) changes in cell traction force, cell area, and contractile moment for each experimental group as compared to their respective controls. Figure 3.5 shows cell elongation and average form factor changes with long-term cyclic stretch and Table 3.1 lists the population averages as numerical values for all the aforementioned variables. Following cyclic equibiaxial stretch, cells appeared to have less cellular extensions than respective controls and average cell area was smaller (n.s.). The average form factor was significantly larger in stretched cells indicating that cyclic equibiaxial stretch induced cells to adopt a more rounded phenotype (Figure 3.5). As expected, there was no preferential angle of orientation for VICs under cyclic equibiaxial stretch; both static culture and stretch cells exhibited a random orientation (Figure 3.6).

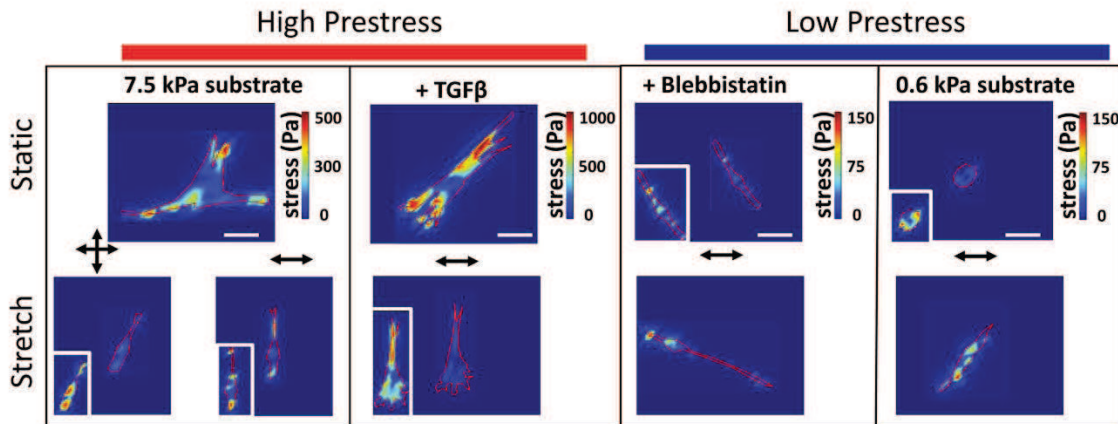


Figure 3.3. Overview of experiments. VICs were cultured on 7.5 kPa substrates unless otherwise indicated. Pre-treatments are indicated on the representative static stress map. Type of stretch indicates whether uniaxial or biaxial stretch was used for a given experiment. For cells cultured under high prestress conditions, mean traction force, mean contractile moment, mean cell area and mean maximum substrate stress all decreased with stretch. Mean form factor increased for both equibiaxially stretched cells and TGF- β 1 pre-treated cells when uniaxially stretched indicating a decrease in extent of cell extensions. The opposite was true for cells under low prestress conditions: mean traction force, mean maximum substrate stress and mean cell area all increased when cells were stretched compared to static control cells. Scale bar = 50 μ m.

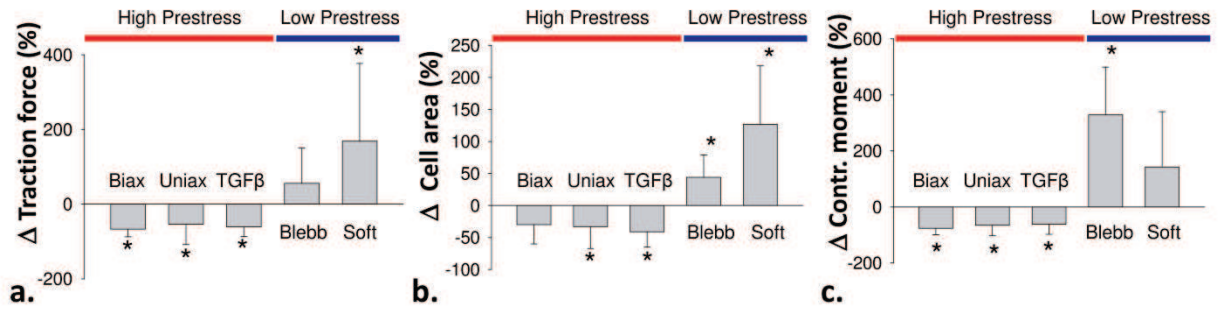


Figure 3.4. Cell traction force and area change with long-term cyclic stretch. (a) % change in cell traction force was normalized to respective controls for each treatment group. Error bars reflect raw stretch traction force values divide by the mean of the controls then multiplied by 100%. Cell traction force decreases with biaxial stretch, uniaxial stretch, and uniaxial stretch with TGF- β 1 pre-treatment (TGF β) on a 7.5 kPa substrate. Cell traction force increases with stretch slightly when cells were pre-treated with 10 μ M Blebbistatin (Bleb) prior to stretch and with cells that were stretched on a soft substrate. (b) % change in cell area was normalized to respective controls for each treatment group. Error bars reflect raw stretch cell area values divide by the mean of the controls. Cell area decreases with biaxial stretch, uniaxial stretch, and uniaxial stretch with TGF- β 1 pre-treatment on a 7.5 kPa substrate. Cell area with stretch when cells were pre-treated with 10 μ M Blebbistatin prior to stretch and with cells that were stretched on a soft substrate. (c) % contractile moment followed same trends as traction force, the average contractile moment decreasing significantly for cells under high prestress. For cells under low prestress, there was an increase in average contractile moment with stretch. * indicates significance when compared via student t-test to respective static controls (p<0.05).

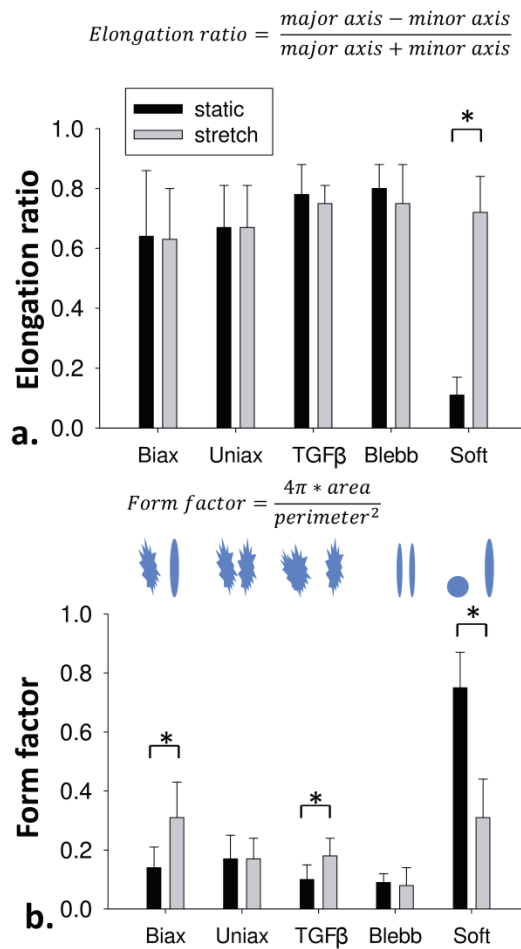


Figure 3.5. Cell shape and elongation changes with long-term cyclic stretch. (a) elongation ratio was unaffected by stretch with most treatment conditions, except with culture on a soft (0.6 kPa) gel (b) Form factor increased with biaxial stretch and uniaxial stretch with TGF-β1 (TGF β) as cell perimeter decreased with depolymerization of many cellular extensions in the direction for stretch. Form factor decreased with stretch on a soft substrate as cells elongated from a circular morphology. * indicates p<0.05

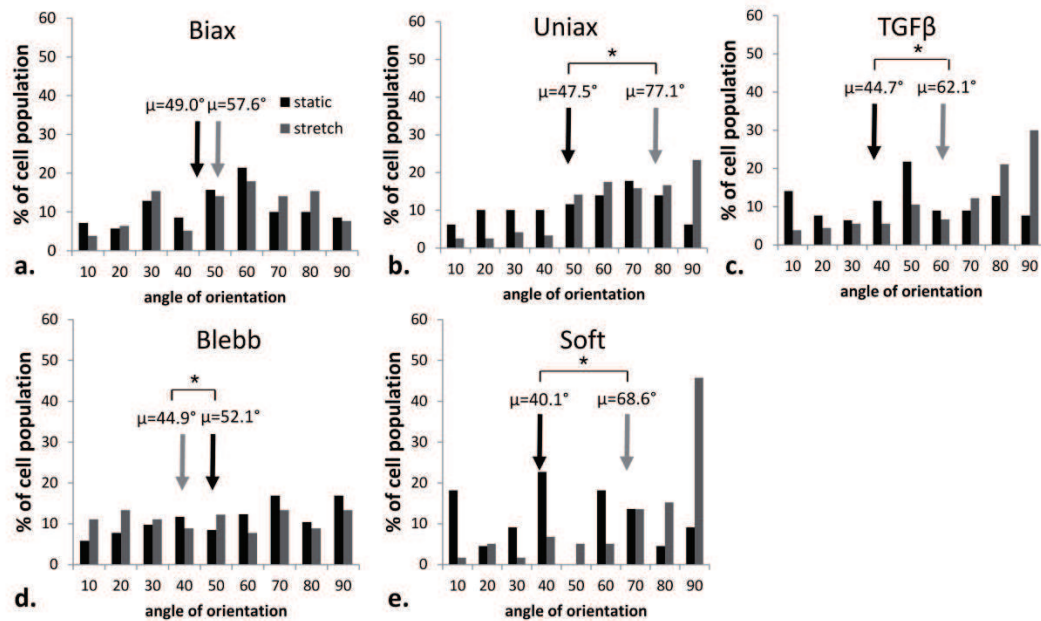


Figure 3.6. Cells reorient with 24 hour stretch regardless of substrate stiffness. Angle of orientation for static and stretched cells represented as 0-90° histograms. Angle of orientation was measured with respect to the stretch direction (0°-180°). Cells that oriented perpendicular to stretch had an angle of orientation of 90°.

We then investigated if VICs would maintain their level of traction force when allowed to reorient away from the direction of stretch (the membrane is essentially static perpendicular to the stretch direction). Despite orientation to the direction of zero stretch, cyclic uniaxial stretch caused a significant decrease in maximum substrate stress and traction force. The decrease in traction relative to matched static controls for uniaxial stretch was somewhat lower than for equibiaxial stretch (43% and 67% decrease, respectively). The average contractile moment also decreased significantly with stretch, though it was slightly less than for equibiaxially stretch (65% and 76%, respectively). The average cell area decreased significantly with stretch, but no significant changes in average elongation ratio or form factor changes were measured.

In the presence of TGF- β 1, VICs cultured on stiff substrates differentiate into myofibroblasts with α -SMA positive actin stress fibers [14] which can withstand high forces; thus, a 5-day pre-treatment

with TGF- β 1 was used to increase the cell prestress. VICs cultured under static conditions with TGF- β 1 pre-treatment generated two and a half times the maximum substrate stress and traction force as the untreated static controls (see Table 3.1 for numerical values) and appendix B for the distributions). These cells also had a greater average cell area and appeared to have more cell extensions under static conditions when compared to untreated VICs under static conditions. Despite the ability of the actin cytoskeleton to withstand tension with TGF- β 1 treatment, these cells exhibited a significant decrease in the cell traction force after 24 hours of uniaxial stretch similar to the untreated cells (Figure 3.4). Areas of locally high stress that concentrated under the cellular extensions in statically cultured cells were not apparent with stretched cells, and there was a decrease in maximum substrate stress following stretch (n.s.). Average contractile moment decreased significantly with stretch. Average cell area decreased significantly with stretch, likely due to the decreased number of cellular extensions as indicated by the significant increase in form factor (Figure 3.5). The average elongation ratio of the cells was not significantly altered by stretch. Like non-treated VICs, TGF- β 1 pre-treated cells were oriented perpendicular to stretch direction, and there was no statistical difference in orientation between untreated VICs and VICs pre-treated with TGF- β 1 after 24 hours of cyclic uniaxial stretch.

Table 3.1- the mean average stress for a group can be approximated within a few % error by dividing the mean traction force by the mean cell area.

Cell type	Stretch type	Modulus (kPa)-treatment	# of cells	Cell area (μm^2)	Traction force (nN)	Contractile moment (pNm)	Angle of principal stress ($^\circ$)	Max stress (Pa)	Shape factor	Elongation ratio	Angle of orientation ($^\circ$)
VICs	static	7.5	6	3007 \pm 1180	304 \pm 152	-14.1 \pm 8.3	66.8 \pm 72.1	311 \pm 171	0.14 \pm 0.07	0.64 \pm 0.22	49.0 \pm 23.6
	10% equi-biaxial		17	2080 \pm 907	99 \pm 64*	-3.32 \pm 3.26*	49.4 \pm 60.0	141 \pm 69*	0.31 \pm 0.12*	0.63 \pm 0.17	57.6 \pm 21.7
VICs	static	7.5	20	2525 \pm 1002	519 \pm 386	-15.4 \pm 15.7	88.5 \pm 49.6	203 \pm 142	0.17 \pm 0.08	0.67 \pm 0.14	47.5 \pm 24.1
	10% uniaxial		19	1680 \pm 877 *	239 \pm 292*	-5.3 \pm 5.8*	80.0 \pm 35.3	129 \pm 93*	0.17 \pm 0.07	0.71 \pm 0.13	77.1 \pm 12.06*
VICs	static	7.5-5 ng/ml TGF β	6	3898 \pm 1007	1130 \pm 1182	-57.0 \pm 52.0	99.9 \pm 55.2	844 \pm 643	0.10 \pm 0.05	0.78 \pm 0.10	44.7 \pm 25.3
	10% uniaxial		14	2411 \pm 984*	510 \pm 340*	-21 \pm 20*	98.4 \pm 39.2	591 \pm 353	0.18 \pm 0.06*	0.75 \pm 0.06	62.1 \pm 24.7 *
VICs	static	7.5-10 μM Bleb	21	1625 \pm 744	41 \pm 37	-1.16 \pm 3.7	111 \pm 51.7	79 \pm 68	0.09 \pm 0.03	0.80 \pm 0.08	52.1 \pm 25.2
	10% uniaxial		10	2341 \pm 641*	63 \pm 41	2.66 \pm 1.97*	102 \pm 46.6	98 \pm 49	0.08 \pm 0.06	0.75 \pm 0.13	44.9 \pm 26.4 *
VICs	static	0.6	11	533 \pm 271	14 \pm 10	-0.10 \pm 0.14	94.9 \pm 54.8	92 \pm 65	0.75 \pm 0.12	0.11 \pm 0.06	40.1 \pm 26.1
	10% uniaxial		9	1214 \pm 489*	43 \pm 37*	0.03 \pm 0.17*	72.7 \pm 56.5	127 \pm 88	0.31 \pm 0.13*	0.72 \pm 0.12*	68.6 \pm 23.1*
U2OS	static	7.5	9	1847 \pm 647	108 \pm 63	-2.45 \pm 1.88	97.0 \pm 49.2	63 \pm 80	0.10 \pm 0.03	0.73 \pm 0.55	50.1 \pm 22.0
	10% uniaxial		10	1685 \pm 272*	26.7 \pm 18.7*	-0.51 \pm 0.61*	56.3 \pm 30.6*	37.1 \pm 22.2*	0.13 \pm 0.04	0.55 \pm 0.24	81.7 \pm 7.6*

Table 3.1. Summary of experimental results. Experimental details given in columns, including number of cells analyzed in each group, as well as measured values for cell area, traction force, contractile moment, maximum substrate stress, form factor, elongation ratio and average angle of orientation. Data presented as mean \pm standard deviation and represent a population average and not a calculation from individual tracked cells. * indicates significance compared to static control, student t-test ($p < 0.05$)

Following the observation that the cells reduced their traction in response to long-term stretch, we sought to determine if stretch could increase cytoskeletal tension for cells below their optimal cytoskeletal tension level. Cell prestress was decreased in two ways. First, Blebbistatin, a myosin II inhibitor, was used as a chemical means of decreasing the cytoskeletal tension prior to stretch. VICs

treated with Blebbistatin generated about ~25% of the traction force of static, untreated VICs. Although not significant, maximum substrate stress and cell traction force increased with cyclic uniaxial stretch. The average contractile moment increased its magnitude significantly with stretch (Figure 3.4). Additionally, the contractile moment for some control Blebbistatin treated VICs and all stretched Blebbistatin treated VICs was positive. The Blebbistatin treated VICs had outward displacement vectors near the cell periphery. This non-intuitive finding may possibly indicate outward forces due to polymerization of actin stress fibers and/or non-recoverable stretch in the stress fibers which push outward upon cessation of cyclic stretch. In these cells, the myosin II motors were inhibited and unable to provide necessary inward contractile force (see representative images in Appendix B, supporting information). VICs treated with Blebbistatin had a smaller spread area, though they remained elongated, exhibiting a very thin, spindle shape. Average cell area increased significantly with stretch (Figure 3.4), while average form factor and average elongation ratio (Figure 3.5) were not statistically different for static and stretched Blebbistatin-treated VICs. Blebbistatin-treated cells had a slight, yet significant, orientation parallel to the stretch direction.

Second, as a mechanical means of reducing prestress, VICs were cultured on low modulus (0.6 kPa) polyacrylamide gels (termed “soft” herein in accordance with mechanobiology literature). Cells statically cultured on these soft substrates had a circular morphology with low traction force and low maximum stress values (Figure 3.3). With uniaxial stretch, the traction force and cell area increased significantly (Figure 3.4) and the maximum stress increased slightly (n.s.). The mean contractile moment was positive for cells cultured on soft substrates with stretch compared to static controls which had a negative contractile moment (Figure 3.4). The positive contractile moment for the stretched cells on soft may indicate that the cells are spreading outward, as evidenced by the increase in mean cell area, due to dynamic stimulation. VICs became elongated with a significant increase in the average elongation ratio. The average form factor significantly decreased, and

average elongation significantly increased (Figure 3.5), indicating a transition to a more polarized cell phenotype. Similar to VICs cultured on stiff substrates, VICs on soft substrates had a statistically significant orientation away from the direction of stretch ($p < 0.05$). There was a uniform distribution of angles for static cells, whereas the average angle for stretched cells was 70 degrees relative to the axis of stretch (Figure 3.6). As orientation away from stretch on a soft substrate contradicted previous findings by Kaunas and colleagues with U2OS cells (human, osteosarcoma) cultured on soft collagen substrates [30], an additional study with U2OS cells on soft substrates was done to compare orientation responses on soft (0.6 kPa) and very stiff (1 MPa) substrates. Similar to VICs, U2OS cells reoriented away from stretch when cultured on both the soft and stiff substrate (appendix B, supporting information). After cyclic uniaxial stretch, U2OS cells on soft substrates were equivalent in size to stretched U2OS cells on 1 MPa substrates. An additional experiment was conducted on U2OS cells to ascertain how cells integrate stretch signals over time in the PDMS culture wells. U2OS cells were subjected to three patterns of stretch: 10% uniaxial stretch, 10% equibiaxial stretch, or alternating uniaxial stretch (10% uniaxial x-direction stretch, followed by 10% uniaxial y-direction of stretch). The cytoskeleton of alternatingly uniaxial stretched groups appeared diamond in shape with peaks at approximately 45 degrees from the directions of stretch; see appendix B, supporting information.

3.4 Discussion

In this study, we tested the hypothesis that changes in cell-generated traction forces in response to long-term cyclic stretch are dependent upon the prestress in the cell. We developed and implemented a system capable of measuring traction force generated by cells cultured on substrates with tunable elastic modulus. Following cyclic stretch for 24 hours, decreases in traction

force in cells with high prestress (for the particular cell phenotype) and increases in traction force for cells with low prestress were observed. This behavior, along with reorienting away from uniaxial stretch, is consistent with maintaining homeostatic cytoskeletal tension during dynamic stretch, i.e., if the cytoskeletal tension is at a maximal level in static culture, it is reduced to accommodate dynamic stretch by retraction of cellular extensions and/or reorientation, whereas if it is below the maximal level (e.g., on a soft substrate), the cytoskeletal tension is increased toward its optimal level. The method and data presented herein can be used to validate future mathematical and phenomenological models of cell reorientation and cell shape changes with stretch based upon cytoskeletal tension.

3.4.1 Effects of stretch on cytoskeletal structure and mechanics

Rapid cytoskeletal remodeling with stretch has been observed with metrics other than traction force including immunofluorescence, storage modulus, and cell spread area. Early work by Pender and McCulloch showed rapid changes in the cytoskeleton with stretch using immunofluorescence; F-actin in gingival fibroblasts is reduced by 50% at 10 s after stretch, but increases more than 100% at 50 s after stretch [145]. Further, Costa et al. observe that release of stretch causes human aortic endothelial cells cultured on pre-stretched silicone membrane to depolymerize stress fibers in the direction of stretch release when release rates were greater than 5% stretch per second, and rapid remodeling was observed within 60 s of release of stretch [146]. In response to transient stretch-unstretch, human bladder smooth muscle cells rapidly disassemble F-actin [118]. In parallel to changes in the actin cytoskeleton, cell mechanical properties also change with stretch. Fredberg and colleagues demonstrated that human airway smooth muscle cells abruptly soften (as measured by G' decrease) with transient equibiaxial stretch with cell stiffness recovery over ~10 minutes [138]. This behavior was interpreted as “fluidization” and “resolidification” of the cytoskeleton [147]. Thom et al. demonstrated cytoskeletal remodeling (via an increase in cell spread area) of VICs when

they were cultured on 0.6 kPa substrates and stretched equibiaxially at 1 Hz for 6 hours [137].

Although traction force was not measured in these studies, these works support rapid cytoskeletal remodeling with stretch which would likely lead to changes in cellular forces.

3.4.2 Effects of long- and short-term stretch on cell traction force

Prior to this study, changes in cell traction force have been measured with stretch on short timescales (less than one hour) using stretch and release as well as stretch and hold experimental designs. Navajas and colleagues [148] rapidly stretched epithelial cells cultured on collagen gels. They observed an initial passive increase in traction force with stretch (with 5.5% and 11% stretch); with release of stretch, there was a significant decrease in traction with recovery over 10 minutes. Fredberg and colleagues applied a transient homogeneous strain field and, in contrast to Gavara, found that the contractile moment decreased rapidly following stretch and recovered over a period of approximately 10 minutes [138]. Fu and colleagues applied an instantaneous step-stretch (without release) to smooth muscle cells cultured on a micropillar device and observed the cell-generated forces for one hour [119]. Cells increased their traction force within the first half hour of observation and decreased to below baseline after 60 minutes. Although the time-course of these studies is not long enough to observe cytoskeletal adaptation to stretch involving protein incorporation (such as α SMA which has been reported to take 72 hours [64]), these studies shed light on the passive transfer of load within the cytoskeleton and the ways in which the rapid reorganization of the existing cytoskeletal proteins translates into the evolution of localized active cell-generated traction.

Several theories have been developed which predict that cell tension is either maintained or increased with stretch [149]; however, no combination studies of simultaneous traction force and stretch have reached long enough time scales to allow for changes in protein expression and

differentiation which many groups report with stretch [26]. Many studies have observed reorientation with stretch; however, substrates outside of the physiologically relevant range of stiffness are generally utilized [150-152]. To date, the only study of simultaneous cell reorientation and traction force has been done with very slow tidal stretches [141]. Human embryonic vascular endothelial cells were subjected to a trapezoidal waveform (~1 s loading, 3 s hold, ~ 1 s unloading) every 49 seconds for two hours. There was an initial drop in cell tension at approximately 50 minutes into the experiment. Once cells reoriented perpendicular to stretch, they report that cells recover their full contractile moment in contrast to the depressed traction exerted by the cells on our stiff substrates following 24 hours of stretch at 1 Hz. The difference in frequency or length of culture may be responsible for the differences: repeated rapid stretching for an extended duration may change protein levels so that VICs become less contractile, which has been shown with pulmonary fibroblasts [26] as well as vascular smooth muscle cells (Marsha Rolle, Worcester Polytechnic Institute, personnel communication).

Changes in traction force with stretch are heterogeneous within and between cells. Fu and colleagues observed the largest changes in force along the cell periphery [119, 139]. We also found that the stresses under cellular extensions at the periphery of the cells cultured on stiff substrates had the most markedly decreased following stretch. In contrast, on very soft substrates, cells were rounded in static culture and elongated and created areas of high substrate stress under the cellular extensions. The ways in which the peripheral tension fluctuations due to external loading are translated into a global cell response, such as cell reorientation and cell shape are still unknown. In terms of cell-to-cell difference in the response to stretch, Gavara et al. reported highly variable changes in traction between cells upon release of equibiaxial stretch [148]. The authors attributed these differences to biological variations in the initial traction force (i.e., prestress). Epithelial cells with low initial traction force had greater recovery of traction force and recovered to baseline levels,

but cells with high initial traction force did not recover their ability to generate traction on the collagen substrate over the 10-minute timespan measured. Matsumoto and colleagues found biological variability in how smooth muscle cells respond to two cycles of slow stretch [139]. Cells either increased their traction force following the first cycle of stretch (termed an active myogenic response) or decreased their traction force following the first cycle of stretch (a passive response). The baseline traction force (i.e., prestress) was similar between groups, and the authors did not discuss a mechanism that would account for the differences. We also saw variability in traction force with stretch, with the greatest differences on the soft (0.6 kPa) substrates. Although the average traction force was greater for the stretched cells, several of the stretched cells on soft substrates had lower traction forces than did the average for static control cells. These cells were as elongated as those that generated higher tractions.

3.4.3 Changes in traction force and spreading with stretch depend upon initial prestress

Combined, our results indicate that the traction force response to long-term cyclic stretch is dependent upon the cell prestress level. In the presence of TGF- β 1, the cell incorporates α SMA into the actin stress fibers and increases contractile activity. The cell is thus able to generate more tension (>1000 nN); however, when cyclically stretched beyond homeostatic tension level for long duration, the cytoskeleton is remodeled by retraction of cellular extensions and/or reorientation away from stretch, resulting in a decrease in traction force. The actin cytoskeleton of U2OS cells appears to have a lower homeostatic tension level compared to VIC cells cultured upon the same substrate stiffness (7.5 kPa), (Figure 3.3). However, U2OS cells reorient similar to the VICs and decrease traction force indicating that stretch increased homeostatic tension despite starting at a relatively low prestress (~100 nN) when compared to VICs (~500nN). Our results indicate that initial prestress is dependent upon cell type. In contrast to cells on stiff substrates, VICs cultured on soft substrates and those with inhibited myosin-II motor activity generate submaximal cytoskeletal

tension when cultured statically. The traction force increased in these cells with long-term cyclic stretch, yet not to the level of cells culture on stiff substrates (either static or stretched). Sheetz and colleagues observed similar spreading of fibroblasts cultured on soft micropillars that were cyclically stretched equibiaxially [29].

In contrast, Krishnan et al. found that changes in cell traction in response to homogeneous stretch are not dependent upon substrate modulus (and thus initial cell prestress level) [138]. Their reported results indicate that in response to a transient equibiaxial stretch, the contractile moment is decreased to 20% of its initial value then recovers to initial levels within three minutes regardless of the modulus of the substrate (1, 4, or 6.2 kPa). The soft substrate utilized in our experiments has a somewhat lower modulus (0.6 kPa) resulting in a rounded cell morphology; this distinct morphological change was not reported by Krishnan et al.

3.4.4 Reorientation of initially spread cells and the effect of prestress

Both VICs (Figure 3.6) and U2OS cells (see Supplemental Figure 3.5) cultured on stiff substrates orientated away from the direction of uniaxial stretch in agreement with the literature for a variety of cell types [126, 153-156]. With equibiaxial stretch, the decrease in spread area was significant for both VICs and U2OS cells and, as expected, neither cell type reoriented. Alternating uniaxial stretch resulted in diamond-shaped cells with stress fibers at approximately $\pm 45^\circ$ from the alternating directions of stretch. These data provide additional support for the theory that stress fibers exposed to high magnitude stretch depolymerize and that those with low tension are reinforced with stretch (appendix B, supporting information). To our knowledge, this is the first time that an alternating uniaxial stretch regimen has been utilized.

It is possible that the rate of reorientation with cyclic stretch is related to the amount of cell prestress. Specifically, lower cell traction force and associated weaker substrate adhesion, we

predicted that cells would reorient more readily, and with higher traction forces to a lesser extent. Differences in reorientation was found between the two cell types we tested. U2OS cells, which on average generate less than a third of the overall traction force of VICs (Table 3.1) , were shown to reorient to a greater degree than VICs over 24 hours of uniaxial stretch (Figure 3.6 and appendix B, supporting information). Like VICs, U2OS cells had statistically lower traction force and statistically smaller area with stretch (Table 3.1). Differences in reorientation rate have been reported between cell types in the literature, but the relationship with traction force has not been measured simultaneously [126]. It was surprising that TGF- β 1 treated VICs (myofibroblasts), which generate more than double the traction force of non-treated VICs and have mature focal complexes [157], reoriented to a similar extent as the untreated VICs and had an equivalent relative decrease in cell area with cyclic stretch. Thus, it appears that degree of reorientation is more strongly associated with cell type than prestress . One possible explanation as to why TGF- β 1 pre-treated VICs were still able to reorient is that stretch may also act to modulate phenotype in mechanosensitive cells reverting them to less contractile phenotype [26] and allowing them to reorient, although more experimentation needs to be done to test this hypothesis.

Culture in the presence of Blebbistatin, a myosin-II motor inhibitor, resulted in cells with lower prestress. VICs that had been treated with Blebbistatin reoriented parallel to stretch. This observation is in agreement with comparable studies of Blebbistatin and stretch on PDMS substrates in the literature [144]. It has been proposed that myosin-II cross-bridge cycling helps maintain stress fiber tension, and stress fibers depolymerize when they are not at their homeostatic level of tension [158]. However, with myosin-II inhibited, the stress fibers are below their ideal tension level. With uniaxial stretch, stretch fiber tension is passively increased by the dynamic stimulus in the direction of stretch. Active tension generation by the cell is decreased with myosin-II inhibited, but stress fibers are able to form likely by using the passive tension generation of the

stretch. This would explain why the Blebbistatin treated cells orient parallel to stretch and not perpendicular. As Blebbistatin can affect some myosin-II independent processes [159], future work to determine myosin's contribution to stress fiber tension and cell reorientation should also include myosin light chain inhibitors ML-7 and ML-9. Interestingly, approximately half of the Blebbistatin-treated control cells and all of the Blebbistatin-treated stretched cells had a positive contractile moment, indicating outward (away from the cell body) forces. Outward pushing forces have been reported by Sheetz and colleagues for cells that had been stretched when the membrane returned to its original conformation [29]. To our knowledge, this is the first reported finding of outward pushing forces in Blebbistatin treated cells and in any non-stretched cells. A possible explanation for the outward displacements by these cells is the outward polymerization of actin stress fibers while the myosin motors are inhibited and unable to provide an inward (contractile) force. These contractile moment values are above the level of noise in the measurement, and U2OS cells had similar measured cell traction force magnitudes but negative contractile moments (indicating inward, towards the cell body displacements).

3.4.5 Reorientation and spreading of initially rounded cells with long-term stretch

Both VICs and U2OS cells reoriented away from the direction of stretch when cultured on soft substrates. Results of similar experiments reported by Kaunas and colleagues showed that cells reorient parallel to the direction of stretch when cultured on soft collagen gels (10% uniaxial at 1 Hz for 3 hours) [30]. This finding raises questions about the time-course of cell spreading and reorientation on soft substrates, whether the cells first spread out and then reorient, and what mechanism is allowing cells to maintain their area on soft substrates once they have reoriented (as in theory, the angle of zero strain should have no mechanical stimulation). An additional study of cell reorientation on soft substrates showed no reorientation with 16 hours of stretch; however, this

study was done at mHz frequencies and low strain amplitude (3%). Cell reorientation has been shown to be dependent on frequency [30, 160].

Many models have been developed to examine the mechanisms of cell reorientation and stress fiber dynamics with cyclic stretch [160-162]. Few models can predict the reorientation behavior of cells cultured on the soft (0.6 kPa) substrates. The Wei model [162], a polymerization based model, predict cell reorientation if the cell is not elongated (as is the case with the soft substrate) but does not include a term for matrix stiffness and is not predictive of an already elongated cell (as is the case for cells cultured on the 7.5 kPa gel). Stamenovic et al. developed a model incorporating the phenomena of cytoskeletal fluidization and resolidification in response to cyclic stretching [149]. This model accurately predicts the increase in cell traction force and cell lengthening we observed with stretch on soft 0.6 kPa substrates. To our knowledge, there is no model that can simultaneously predict the prestress dependent behaviors of traction force and elongation with reorientation in the cells cultured on soft and stiff substrates.

3.4.6 Limitations and future studies

As traction force, reorientation, and cell morphology were only assessed after 24 hours of stretch, we cannot comment on the time-course of changes in these metrics during stretch or following cessation of stretch. In the future, tracking the same cells over time on both the soft and stiff substrates presented here would be ideal. This will help to better address how traction force changes as a measure of prestress, cell orientation with respect to stretch direction, and total strain. Additionally, it will allow the study of cell elongation and reorientation on the very soft substrates. We also did not measure changes in protein expression (e.g., α SMA) which may explain changes in traction force with long-term stretch. Although not studied in VICs, reversal of the myofibroblastic phenotype in the presence of stretch was shown with lung myofibroblasts [90]. We believe that

traction force can be used as a powerful functional indicator of cell phenotype than can add to biochemical metrics (protein synthesis, gene expression).

3.5 Conclusions

Here, we report the first traction force measurements after 24 hour cyclic stretch. We observed that the traction force response to stretch is dependent upon initial cell prestress. The cell traction force decreased with long term cyclic stretch when the cell prestress levels were high, while traction force increased when cell prestress levels were low. The decrease in traction force with stretch was larger in the case of equibiaxial stretch than uniaxial stretch, as cells were unable to undergo reorientation. Cell prestress levels were further increased with culture in TGF- β 1. However, TGF- β 1 treated cells still decrease traction force following long-term stretch. From these observations, we conclude that although TGF- β 1 increases cell prestress, 10% stretch exceeded the maximal cytoskeletal tension, initiating the process of cytoskeletal reorganization. Decreasing prestress levels either chemically with blebbistatin or by culture on soft substrates resulted in increasing traction force with stretch. We conclude that when cell prestress is low, mechanical stimulation may serve as means to increase cytoskeletal tension. The methods and data from this study will enable the development and validation of models of cell reorientation and cell spreading with stretch which take into account cell prestress. To our knowledge, this study is the first study to measure cell reorientation and traction force with stretch at frequencies and stiffness levels relevant to the cardiovascular system.

3.6 Acknowledgements

We would like to thank Dr. Domhnull Granquist-Fraser, Jennifer Mann, Jeffrey Kelley, Jeffrey Pruden, Brent Duoba, Joseph Lombardo, Kyaw Thu Minn, and Juan Rodriguez for development of stretch device and design and analysis of the initial compliant wells. We would also thank Gawain Thomas

for guidance on polyacrylamide hydrogel modulus characterization, Mina Shojaei for assistance with Matlab and ANSYS, Matt Dipento for help with mold manufacturing, Dr. Mehmet Kural with assistance isolating valvular interstitial cells, and Dr. Glenn Gaudette and John Favreau for equipment used for strain field characterization and strain field characterization analysis. We thank Dr. Roland Kaunas for donation of the U2OS cells and for formative discussions of this work and comments regarding preparation of the manuscript as well as Dr. Ngozi A. Eze for editorial insights. This work was funded in part by an American Heart Association Pre-doctoral Fellowship to HC (14PRE18310016), the NSF (IGERT DGE-1144804) and the NIH (2R15HL087257-02).

Chapter 4: A Controlled *In Vitro* Model of Calcific Aortic Valvular Disease

Heather A. Cirka¹, Johana Uribe², Vivian Liang¹, and Kristen L. Billiar¹

1. Department of Biomedical Engineering, Worcester Polytechnic Institute, Worcester, MA, 01609
2. Department of Bioengineering, University of Massachusetts at Dartmouth, Dartmouth, MA

4.0 Abstract

Calcific aortic valvular disease (CAVD) is the most prevalent valvular pathology in the United States, necessitating nearly all aortic valve replacements in the industrialized world. Despite the high incidence of CAVD, much remains elusive about the mechanisms initiating the disease. Hindering development of preventative treatments is the lack of adequate animal models for CAVD, as well as limited insights of factors initiating disease onset provided by the examination of explanted calcified valves. Although an *in vitro* model exists, its utility is limited as calcifications form randomly and are of variable sizes without a consistent time-course. In this chapter, we introduce and validate a high-content method for studying CAVD *in vitro*. By utilizing micro-contact printing, we are able to recreate dystrophic calcification seen *in vivo* characterized by valvular interstitial cell aggregates with myofibroblastic activity, calcium-positive mineralization, and cell death. This method was highly repeatable with consistent apoptotic activity and calcification seen throughout multiple trials of one-week time-courses. X-ray micro-analysis revealed details behind calcification within the micro-contact printed aggregates. Further, micro-contact printing enables the study of the effect of cytokines, substrate stiffness, and pharmacologics on calcification which is not possible using the current *in vitro* model as high cell tension is needed to initiate the aggregation and subsequent calcification. Finally, micro-contact printing enables biophysical characterization of valvular interstitial cell aggregates via traction force microscopy which was previously impossible.

4.1 Introduction

Calcific aortic valvular disease (CAVD) is the most prevalent valvular disorder in the United States, affecting 81 million Americans [2]. The prevalence rises to 9.8% in octogenarians [3]. The increase in incidence of CAVD with age leads many people to believe that it was the result of the passive degeneration of the valve, but recently it has been shown to be a cell-mediated phenomenon. CAVD

results when calcifications form on the aortic heart valve leaflets, inhibiting normal function, leading to stenosis and regurgitation. The number of patients with CAVD is expected to increase exponentially in the coming decade as the population ages. Valve replacement surgeries have been increasing in the United States over the last several decades; a total of 95,000 aortic-valve replacements were performed in the United States in 2010, the majority of which were necessitated by CAVD [1, 163]. To date, there are no pharmaceutical interventions to halt, slow, or reverse the progression of CAVD.

Several hypotheses exist as to the mechanisms behind calcification. These include passive calcification of the collagen fibers, calcification via active cellular mineralization via differentiation to osteoblastic phenotype, calcification associated with cell death, as well as aggregation on calcium micro-particles into hydroxyapatite structures. Examination of explanted valves reveals two mechanisms of calcification: osteogenic calcification, observed in 13% of diseased valves, and dystrophic calcification which is more common and present in 83% of explanted valves [7]. By definition, osteogenic mechanisms are “active” cellular processes in which osteoblastic cells lay down hydroxyapatite, which has highly organized molecular structure [9]. Dystrophic calcification involves cell death. Unlike osteogenic calcification, dystrophic calcification is not organized [8]. The mechanisms by which cells initiate death within dystrophic calcification are currently unknown.

Currently, CAVD remains challenging to study as there are no adequate animal models which can replicate the calcification seen within human valves [10]. Study of diseased explanted human valve cusps only reveals end-stages of disease and does not indicate disease progression. From these studies it is difficult to identify pharmacological targets for early treatment and intervention. A two-dimensional *in vitro* model for dystrophic calcification has been developed to replicate the cell death and calcification seen clinically. This model involves seeding valvular interstitial cells (VICs) at high

density (60,000-100,000 cells/cm²), often in the presence of TGF- β 1. VICs then undergo aggregation. Following aggregation, cells within the center of the aggregate apoptose and calcification ensues [12].

The current 2-D *in vitro* model, although simplistic, has revealed a significant amount of information about the extracellular, chemokine, and mechanical signals which affect aggregation. Notably, factors which appear to increase intracellular tension also increase rates of aggregation. Increased aggregation rates are observed with culture in the presence of TGF- β 1 [12], on stiff surfaces [16], on fibrin-coated surfaces [9], and in conditions that combines TGF- β 1 and cyclic mechanical strain [17]. However, how the aggregation of VICs progresses into calcification remains incompletely understood as currently there is no method for separating the aggregation process from the calcification process.

A major challenge in understanding how cell death initiates within VIC aggregates is the large variability seen within rates of VIC aggregation. Table 1 shows the reported values found in literature for aggregate size. *In vitro*, aggregates take a week or more to form, form randomly and variably, and have a distribution of sizes which makes examining the mechanisms of pathology difficult. Different time-courses for aggregation and subsequent calcification have been reported for controls in papers which use the same methodology for aggregate development [9, 18]. In addition, a range of sizes have been reported in the literature [9, 18] for control aggregates formed under the same conditions. Furthermore, all *in vitro* models to date rely on the aggregate formation to study apoptosis and calcification. In order to better study the mechanisms of pathology, a method must be developed to separate the two phenomena.

The goal of this study is to validate a novel method for creating the *in vitro* model of calcific aortic valve disease, allowing for the regulation of parameters such as aggregate size, substrate stiffness,

and cytokines for high-content analysis of effects on apoptosis initiation and dystrophic calcification within valvular interstitial cell aggregates. Our approach is to use micro-contact printing on polyacrylamide gels to control aggregate formation to a defined size. Not only will this method enable studies into the factors contributing to apoptosis and dystrophic calcification in VIC aggregates *in vitro*, this method also offers the potential to be used as a high-content mechanism for screening promising therapeutics. Aggregate size can be varied, allowing for study of aggregate cell number and the effect on apoptosis. As aggregate size increases, so too does number of cells within the aggregate as well as the number of cell-cell contacts. Cadherin-11 has been shown to be essential for aggregate formation [97], as well as having been found in disease valves [97]. In addition, modulus of the polyacrylamide gels can be varied allowing for the study of how substrate stiffness affects apoptosis and calcification, as currently it is believed that dystrophic calcification initiates only on stiff substrates [16]. Finally, micro-contact printing enables the study of cytokines and their effect on cell apoptosis and calcification as TGF- β 1 is not required to induce aggregation. Although TGF- β 1 is found in diseased explanted valves, it is uncertain if high TGF- β 1 levels initiate and perpetuate the disease or if high levels of TGF- β 1 are a result of calcific aortic valvular disease [12].

Table 4.1 Mini-review of literature for studies employing *in vitro* model. Notice micro-contact printing method allow to control size of aggregates, as well as increases number of aggregates by an order of magnitude

Author	TGF- β 1 (Y/N)	Seeding density per cm ²	Media	Substrate material	Time in culture	Aggregate size(mm ²)	# of aggregates per cm ²	Effective diameter (μ m)
Monzack et al. (2009)	5 ng/mL for 5 days	50,000 cells	Low Serum (1%) or Low Serum with TGF- β 1	TCPS, Laminin & Fibrin TCPS	7-10 days	0.02-0.03	15 per well [§]	159-195
Rodriguez et al. (2009)	No	50,000 cells	Low Serum (1%)	TCPS, collagen, fibronectin, fibrin	5 days	0.02-0.1	7 per well [§]	159-356
Gu et al. (2011)	No	50,000 cells	Low Serum (1%)	TCPS, collagen, fibronectin, fibrin	5 days	0.01-0.035	40	112-211
Yip et al. (2009)	5 ng/mL for 6 days	Not reported	DMEM or Calcifying media (with TGF- β 1)	Collagen gels and TCPS	6 days	0.05*	50 per well [§]	252
Cloyd et al. (2012)	10 ng/mL for 21 days	Not reported	Control media supplemented with TGF- β 1 and osteogenic media	TCPS	21 Days	0.001-0.03**	Not reported	35 -195
Fisher et al. (2012)	1 ng/mL for 2 days	50,000 cells	10% Serum w/ or w/o 1 ng/mL TGF- β 1	Flexcell plate	2 days	> 0.008***	0-5 with increasing strain	32
This study	No	12,500 cells	10% Serum in DMEM	Collagen coated PA gels	7 days	0.001, 0.03, 0.07, 0.12	4900, 900, 400, 200	50, 200, 300, 400

4.2 Materials and Methods

4.2.1 Micro-Contact Printing Stamp Design

A 2-D computer-aided design (CAD) software, DraftSight (Dassault Systems), was used to create a stamp master design. The stamp master design consisted of twelve stamp templates, each with circles of a specific diameter that correspond to sizes of aggregates reported in literature[9, 17, 18, 164]. The CAD drawing was sent to CAD/ART services for the formation of a high resolution (20,000 dots per inch) photomask, which was then used to create a master stamp silicon wafer utilizing

standard photo-lithography methods with assistance from Dr. Dirk Albrecht (WPI). Subsequently, PDMS stamps were synthesized by placing the silicon wafer in a 100 mm petri dish and pouring 100 g of 10:1 polydimethylsiloxane (Dow Corning) over the wafer. The petri dish was then placed under house vacuum for one hour, until all bubbles had been removed from the PDMS solution. Afterwards, the solution was allowed to polymerize for three hours in *an* oven at 65^o C. Stamps were removed from the wafer once the PDMS had cooled to room temperature.

4.2.2 Tunable-Stiffness Substrate Preparation

Polyacrylamide (PA) gels were chosen as the substrate for the model, as they are optically clear, have a tunable modulus over several orders of magnitude, and have been used successfully for micro-contact printing in the literature [107, 165, 166]. 22 mm glass cover slips (Ted Pella) were activated for polyacrylamide attachment by soaking in a 1.5% (aminopropyl)trimethoxysilane solution (Sigma-Aldrich) for 30 minutes, rinsing with diH₂O, and incubating in 0.5% glutaraldehyde solution (Sigma-Aldrich) for three hours at 4°C. The activated coverslips were then dried using vacuum aspiration. Four different stiffness values of PA gels (9.6, 19.2, 38.4, and 76.8 kPa) were formed by varying the concentration of acrylamide and bis-acrylamide (BioRad) as described by Quinlan, et al. [81]. Once the un-polymerized gel solution was made, 50 μ L were pipetted onto each glutaraldehyde-treated coverslip. The droplet was then sandwiched with an untreated coverslip to allow for uniform gel distribution by capillary action. After gel polymerization, the two coverslips were separated using a standard razor blade, with the polyacrylamide gel remaining affixed to the glutaraldehyde-treated glass slide.

4.2.3 Micro-Contact Printing

Polyacrylamide gels were functionalized prior to protein micro-contact printing by submersion in a solution of 55% hydrazine hydrate (stock solution purchased from: Sigma-Aldrich, St. Louis, MO) for

two hours. As hydrazine hydrate is reactive with most plastics and metals, a ceramic rack from Thomas Scientific was used to arrange the coverslips. After soaking in hydrazine hydrate, the ceramic rack was transferred to a solution of 5% glacial acetic acid (Sigma-Aldrich) for one hour to neutralize the PA gels, and finally submerged in diH₂O for an additional hour.

An overview of the sample preparation is shown in Figure 1. Collagen protein solution was prepared by conjugating 1 ml of collagen at concentration of 100 μ g/ml (Advanced Biomatrix) with Alexa Fluor-488 succinimidyl ester (Thermo-Fischer) in 9 mL of 50 mM sodium acetate buffer, and 3.6 mg of sodium periodate crystals. Once complete protein transfer was observed, the fluorescent collagen labeling step was omitted.

Prior to protein incubation, PDMS stamps were thoroughly rinsed with diH₂O, 100% ethanol, and diH₂O. The stamps were incubated with protein solution for 45 minutes, while the functionalized PA gels were dried completely in a desiccator under vacuum. Excess protein on the PDMS stamps was removed using a nitrogen gun. Each stamp was then placed gently on top of a polyacrylamide gel and left to sit for two minutes within a 60° C oven, which we found were the best conditions for complete protein transfer.

As sample preparation is not sterile, following micro-contact printing gels were treated with an antibiotic/antifungal cocktail in 1X PBS overnight containing 100 μ g/mL penicillin–streptomycin (MediaTech), 2.5 μ g/mL amphotericin B (Corning), 10 μ g/mL ciprofloxacin (Alfa Aesar), and 100 μ g/mL gentamycin (Alfa Aesar) described by Clement et al. [167] Aggregates formed by this method were highly repeatable < 4% variability in area (see supplemental information).

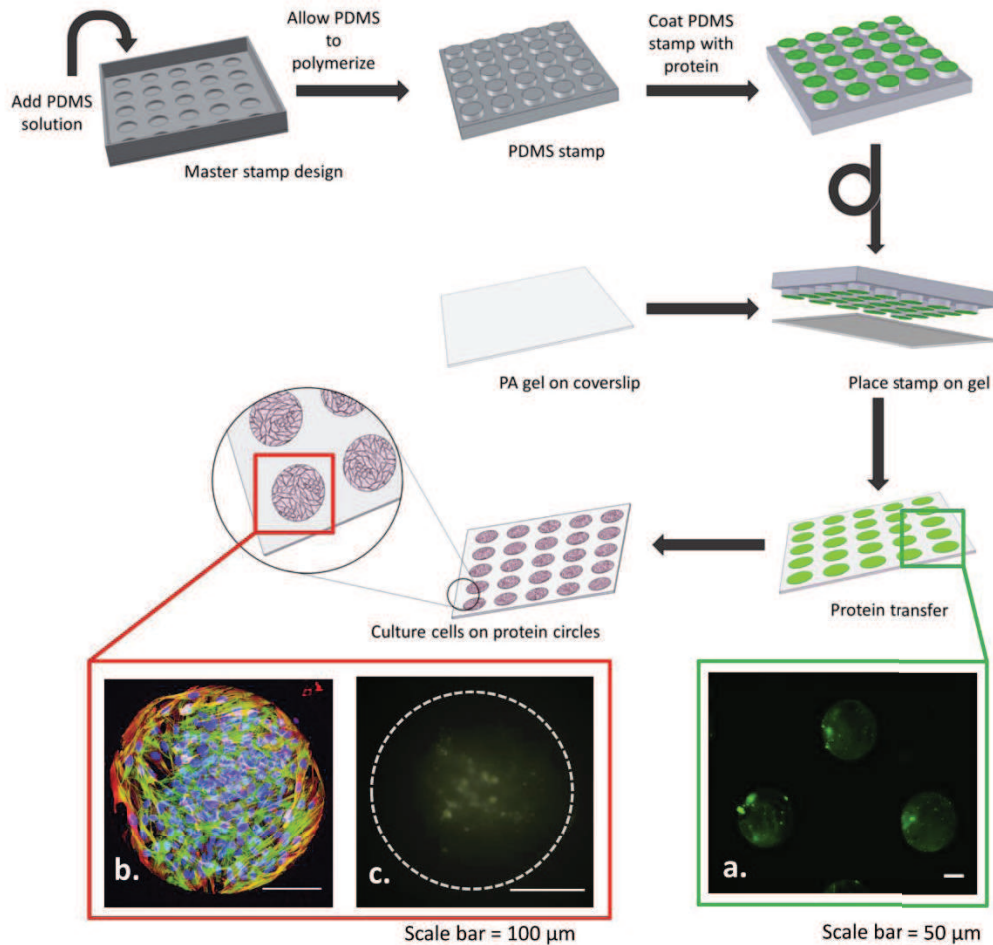


Figure 4.1: Overview of micro-contact printing on tunable modulus substrate. Master of inverse stamp design is created using standard photolithography methods. 10:1 PDMS is poured over stamp and allowed to polymerize. Stamps are coated with collagen (shown in fluorescent green). PA gel is treated with series of hydrazine hydrate, acetic acid, and diH₂O to allow protein to bind. Stamp is inverted onto PA gels. Protein is transferred to substrate. VICs are cultured on these circles forming the engineered aggregates. Inset a) Micro-contact printed collagen circles fluorescently labeled on a 38 kPa polyacrylamide gel. b) Micro-contact printed aggregate stained for α SMA (red), f-actin (green), and nuclei (blue). α SMA incorporates into stress fibers indicative of myofibroblastic phenotype present in dystrophic calcification. c) Caspase 3/7 activity present within central region of aggregates indicating cell death via apoptotic pathways.

4.2.4 Cell Culture

Valvular interstitial cells (VICs) were isolated from porcine heart valve leaflets obtained from a local abattoir (Blood Farm, Groton, MA) within three hours of tissue harvest per published protocols [168]. Cells from passages 3-7 were used for all experiments. Cells were seeded at densities

consistent with literature to encourage monolayer formation and complete cell coverage of the micro-contact printed area (12,500 cells/cm²). Media was changed every 4 days.

Transforming growth factor-beta 1 (TGF- β 1, Sigma-Aldrich) was used as a pre-treatment for some experiments to encourage differentiation to a highly contractile myofibroblastic phenotype [12]. In this scenario, 5 ng/ml of TGF- β 1 was added to the media for five days prior to seeding cells onto micro-contact printed hydrogels.

Pravastatin (Sigma) was used in a subset of cells to demonstrate potential to be used to as a pharmaceutical screen. Cells were treated with 100 μ M Pravastatin for five days. Cells were seeded onto samples as described above. Pravastatin treatment continued for three days.

To inhibit apoptosis in a subset of samples, VICs were pretreated with 20 μ M ZVAD-FMK (ApexBio) for five days prior to seeding. ZVAD-FMK treatment continued for three days for VICs in culture.

4.2.5 Caspase Activity

Caspase 3/7 activity was used as a measure of apoptosis detection. CellEvent[®] Caspase 3/7 Green ReadyProbes[®] Reagent (Thomas-Scientific) was used according to the manufacturer's guidelines. As a positive control, cells were treated with 1 μ M staurosporine (Apex Bio), a broad spectrum protein kinase inhibitor, for 48 hours. Caspase 3/7 activity was quantified using a custom MATLAB (MathWorks, Natick MA) program. The perimeter of the aggregate of interest was outlined manually in a phase image. The marked phase image and corresponding fluorescent image were then used as inputs in the MATLAB program. The program then subtracted the background pixel intensity of the fluorescent image from the area of interest and converted the pixels within the aggregate to either Caspase 3/7 positive (white pixel) or negative (black pixel). The threshold of pixel intensity can be adjusted by the user to accurately dictate Caspase 3/7 positive or negative pixels. The total number of Caspase 3/7 positive pixels are then computed, and the program outputs the total number of

positive pixels as well as the aggregate area for further analysis. For an example of caspase analysis, please see supplemental data.

4.2.6 Immunohistochemistry

Cells were fixed with 4% Paraformaldehyde (USB Products) for fifteen minutes and permeabilized with 0.25% Triton-X (Calbiochem). Cells were blocked with 1.5% goat serum (Invitrogen) and stained for alpha smooth muscle actin (Sigma). Cells were counter stained with Alexa-fluor 488 phalloidin (Thermo-Scientific) and Hoechst (Thermo-Scientific). Antibodies used: anti- α SMA (Sigma, A2547).

To allow for imaging, coverslips were affixed to glass slides using SHUR/Mount™ Toluene-Based Liquid Mounting Medium (Ted Pella). Prolong-gold (Life Technologies, Grand Island, NY) was then added to the polyacrylamide gel.

Images for time-course imaging of caspase activity were acquired using a using a Zeiss inverted microscope and CCD camera. Z-stacks of micro-contact printed aggregates were also acquired at 63x magnification with a confocal microscope (Leica Microsystems).

4.2.7 Calculation of Average Cell Area

Average cellular area was determined on day seven by staining for nuclei with Hoechst and f-actin with phalloidin (see above methods). Aggregate area was determined using image J. Number of nuclei were counted. Average cell area was calculated by dividing the aggregate area by number of cells within the aggregate.

4.2.8 Calcium Staining

Calcium nodules were assayed by using Alazarin Red S dye (Fischer Scientific). Samples were fixed as described above, and 20 μ L of dye was placed on the sample for two minutes. Samples were then

rinsed with copious amounts of diH₂O to remove excess stain. Positively stained nodules were confirmed by visible red-orange color [169].

4.2.9 Traction Force Microscopy

Polyacrylamide gels for traction force measurements were fabricated as described above with the following exception: prior to gel polymerization, a glass coverslip (Ted Pella, Redding, CA) was prepared imbedded with fluorescent microbeads. This coverslip was used instead of the plain glass coverslip mentioned above and allowed for deposition of fluorescent microbeads within the top surface of the gel. To create these bead glass coverslips, 0.5% fluorescent bead solution (Invitrogen) was prepared in 100% ethanol. Coverslips were cleaned and treated with nitrogen plasma (SPI) for 30 seconds to ensure a hydrophilic surface. 35 μ L of bead solution was then pipetted onto the glass coverslips and evaporated at 150°C in a vacuum oven under house vacuum for 30 seconds.

To ensure optimal image quality, the amount of material from sample surface to the microscope objectives was reduced by removing a 20 mm diameter hole from 60 mm petri dishes using a metal tissue biopsy heated with a Bunsen burner.

The coverslip sample was then glued into the petri dish using Norland Optical Glue 68 (Norland Adhesives). As sample preparation was not sterile, gels were treated with antibiotics as described above.

Images and aggregate traction force calculation were acquired using methods previously described in Chapter 3.

4.2.10 Image Analysis

Time course heat maps of caspase activity were created using a custom MATLAB program (Mathworks, Natick, MA). Phase images and fluorescent images of the caspase signal were taken at

40x using a Zeiss inverted microscope and CCD camera (Thornwood, NY). The program allowed users to identify the aggregate center from the phase contrast image. The caspase image was translated so that all the aggregate centers were in the identical pixel location. Peak caspase signals were then averaged over 40 aggregates for each time-point measured.

4.2.11 Scanning Electron Microscopy and X-ray Micro-Analysis

For SEM-EDS analysis, micro-contact printed samples were fixed in 2.5% gluteraldehyde in 0.1M sodium cacodylate buffer solution for 1 h at room temperature and 24 h at 4°C. Samples were subsequently washed three times with sodium cacodylate buffer. Samples were then dehydrated by a series of ethanol washes (30%, 50%, 70%, and 95% ethanol) for 15 min each. Dehydration was completed with two 15 min washes with 100% ethanol. Samples underwent critical point drying in liquid CO₂. The polyacrylamide gels on cover slips were then mounted to aluminum stubs with silver conductive paste and coated with carbon to electrically ground the hydrogel matrix. The specimens were examined using an FEI Quanta 200 field emission scanning electron microscope (SEM) equipped with an Oxford-Link X-ray analyzer for X-ray microanalysis. All scans were done at 10 KV, images were taken at various magnifications for viewing apoptotic cells, calcifications, as well as intra-cellular and extra-cellular vesicles.

4.2.12 Statistics

Data presented are the mean and standard deviation, unless otherwise indicated. Statistical significance was determined between treatments with appropriate test using Sigma-Plot v. 11.0 software (Systat Software, Inc., San Jose, California). A p-value of less than 0.05 was considered statistically significant.

4.3 Results

4.3.1 Dystrophic Calcification is Present in Micro-Contact Printing Aggregates

Dystrophic calcification is currently believed to be mediated by highly contractile myofibroblastic cell aggregates which undergo apoptosis and calcify. This apoptosis and calcification initiates in the central region of the aggregate and spreads radially outward over time. The myofibroblastic phenotype is characterized by α -SMA-positive stress fibers. Our α -SMA staining confirmed that the myofibroblastic phenotype is present within our micro-contact printed aggregates (See Figure 4.2). Caspase 3/7 detection reagent indicated that cells within the central region of the micro-contact printed aggregates were undergoing apoptosis (Figure 4.1c); live/dead staining verified that the cell death occurred initially in the center of the aggregates similar to the current *in vitro* system (see Supplemental Data, Figure 3). 200 μ m diameter micro-contact printed aggregates on 38.2 kPa PA gels formed calcifications within 4 days, with apoptotic activity present at 24 hours. Calcification, as measured by positive staining of Alizarin Red S, was replicated with high fidelity in this model (Figure 2a). Average number of aggregates calcified at one week was 67.8 ± 0.5 (mean \pm SEM) as determined by five consecutive trial runs of one-week duration. To determine if cell death was mediated by the apoptotic pathway, a subset of aggregates were cultured with Z-VAD-FMK. Cells were treated with Z-VAD-FMK for three days prior to being transferred to the micro-contact patterned PA gels. Z-VAD-FMK reduced the number of calcifications by about 75% compared to untreated controls (Figure 4.1c). Combined these findings suggest that dystrophic calcification is present in micro-contact printed aggregates and apoptosis is the mechanism of cell death.

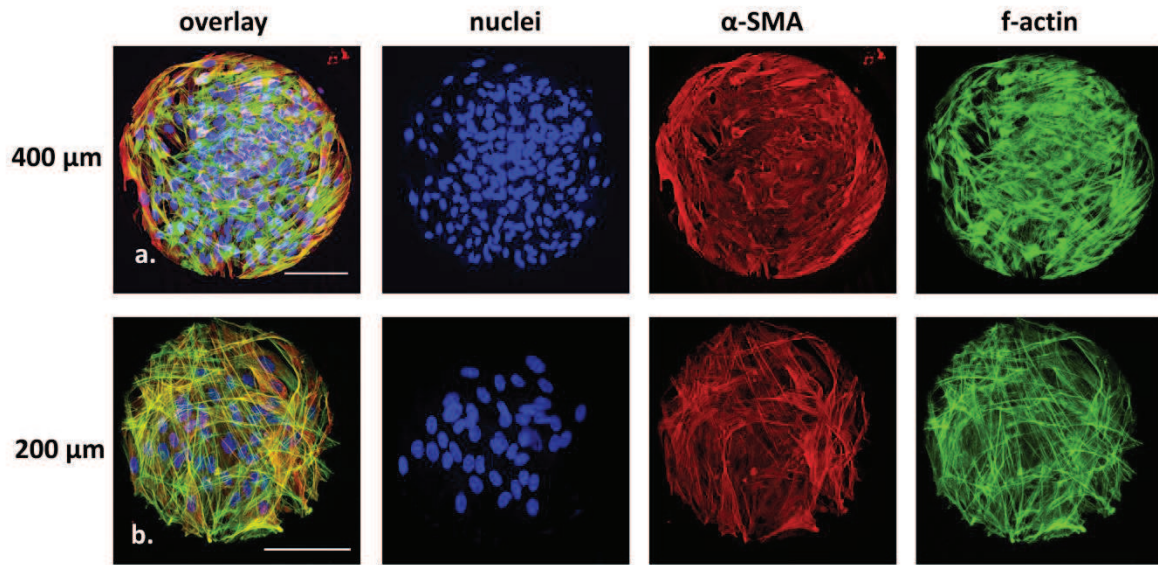


Figure 4.2 Myofibroblastic phenotype, as indicated by α -SMA incorporation into stress fibers is present in micro-contact printed valvular interstitial cell aggregates. a) Representative staining in a 400 μm diameter aggregate cultured on 38 kPa gel. Overlay and separate channels showing high α -SMA incorporation along aggregate periphery. *scale bar = 100 μm* . b) 200 μm diameter aggregate cultured on 38 kPa gel. Overlay and separate channels showing high α -SMA incorporation along aggregate periphery. *scale bar = 100 μm* .

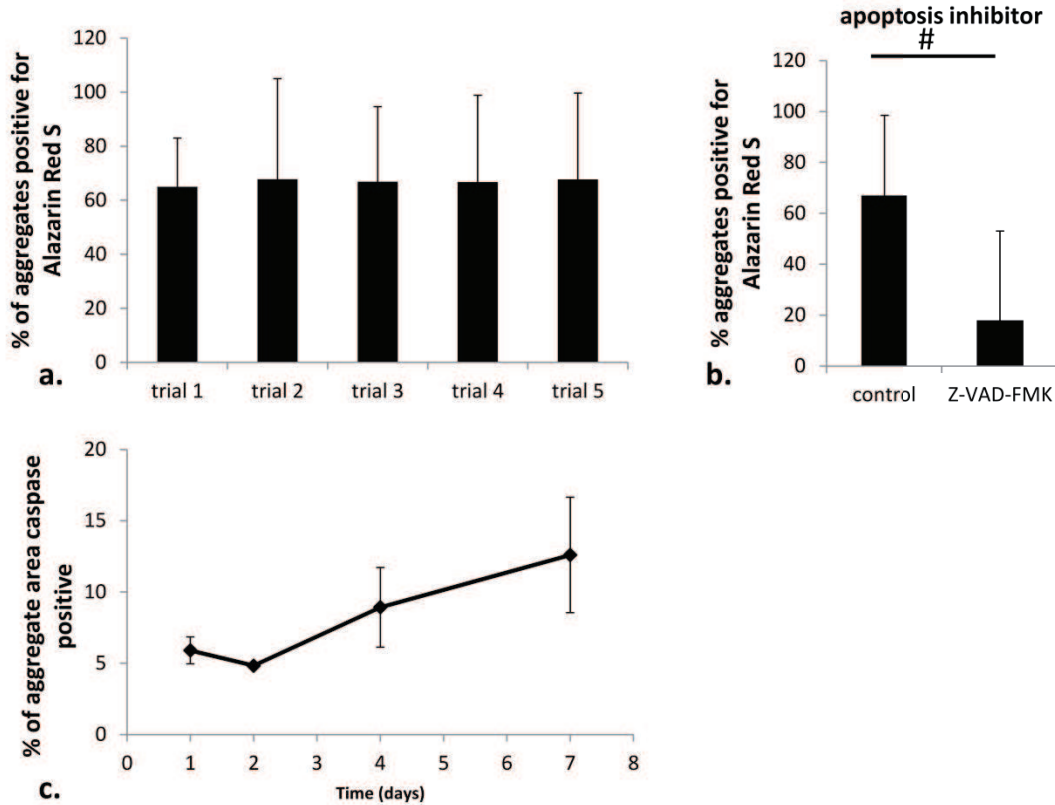


Figure 4.3: Micro-contact printing method for *in vitro* model of calcific aortic valvular disease results in calcification with high fidelity. a) Aggregates that stain positive for Alazarin Red S, an indicator of calcification, were replicated with high fidelity during different trials of our experiments. On average, 67% aggregates of 200 μ m diameter aggregates on 38.2 kPa PA gel stained positive for calcification at one week. This was repeated in five separate one week time course experiments. b) Calcification may be mediated by apoptosis as decreasing caspase activity with Z-VAD-FMK, a pan caspase inhibitor, resulted in \sim 65% less calcifications, statistically significant by student t-test $p < 0.05$. Although calcification did not decrease to zero with Z-VAD-FMK, the reduced amount of calcification is consistent with reduction seen by other groups using this inhibitor [16]. c) Repeatability of time-course of apoptosis within valvular interstitial cell aggregates as measured by % of aggregate positive for caspase activity. $n = 100$ aggregates per time-point, repeated three times. Data presented mean \pm SEM.

4.3.2 Scanning Electron Microscopy and X-ray Microanalysis

X-ray micro-analysis was used as a second measure of calcification. Micro-analysis revealed that calcification is present in several forms within the aggregate, and may indicate multiple mechanisms of calcification. False colorization density maps were created by overlaying the electron image and backscatter image. Inspection of areas of high density as determined by backscatter image showed high mineral content with calcium present. Mineralized nanoparticles, which appear to be

exocytosing from the cell as extracellular vesicles were observed with trace amounts of calcium (0.03%). Particles of size range 100-450 nm were observed “clustering” on the apical aggregate surface in the central region of the aggregate (Figure 4.6c). These nano-particle clusters were seen on several aggregates that were examined. Rounded cells were observed in the center of several aggregates examined. These cells had approximately three-fold higher calcium density than the aforementioned nanoparticles. Calcium likely took the form of calcium oxide within these cells (Figure 4.4, Figure 4.5) Rounded cells with large numbers of mineralized, calcium positive nanoparticles within the cells were also found in several aggregates that were examined (Figure 4.4 and Figure 4.5). Dense mineralized particles have been previously reported to have been found in diseased aortic valves (Figure 4.6c). It remains an open research question if mineral content of nanoparticles is similar between *in vivo* calcium nanoparticles, and those that are seen in our *in vitro* model. To our knowledge, this is the first report of mineralized nanoparticles within aggregates *in vitro*, although whole nodules have been examined via X-ray microanalysis methods [95].

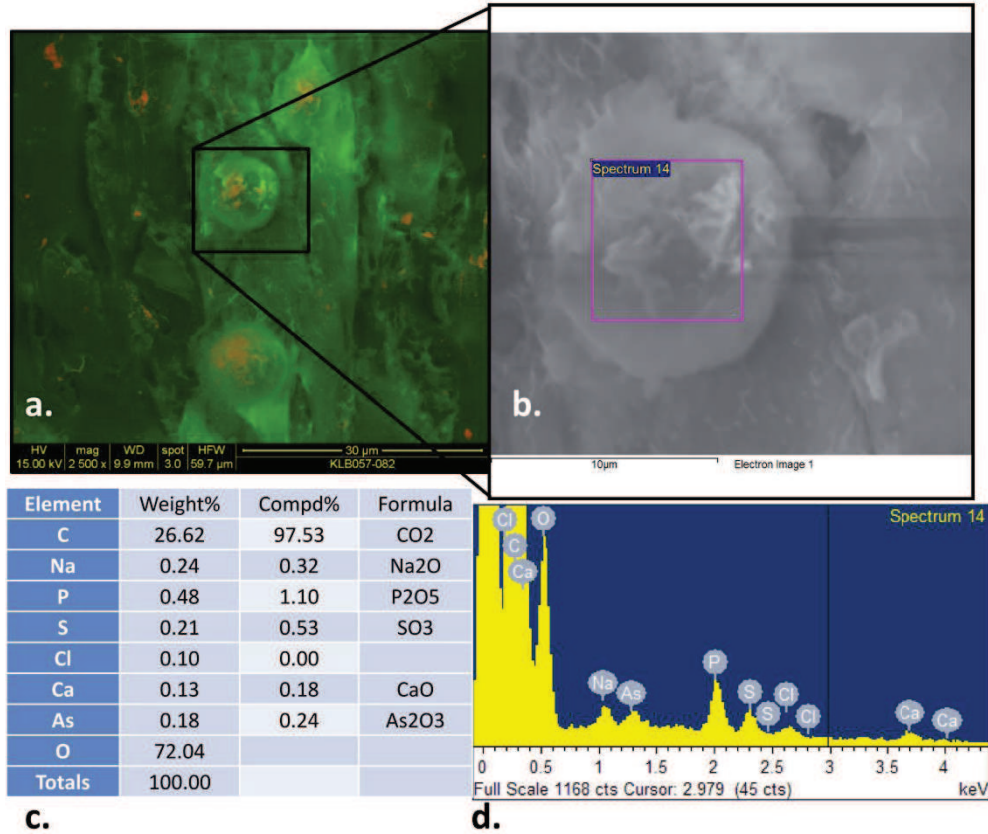


Figure 4.4: Rounded cells in center of aggregate contain mineralization with calcium. a) Density dependent scanning electron image created from overlaying the electron image with the backscatter image. Regions that are more dense, and more likely to contain mineralization show in red. b) Electron image imported for X-ray microanalysis. Region of interest selected with magenta box. c) Elemental composition of selected region. Weight % is indicative of how much ROI chemical makeup is the selected element, formula gives most likely formulation for each element found. d) Elemental spectrum from ROI used to calculate weight percent of the elements.

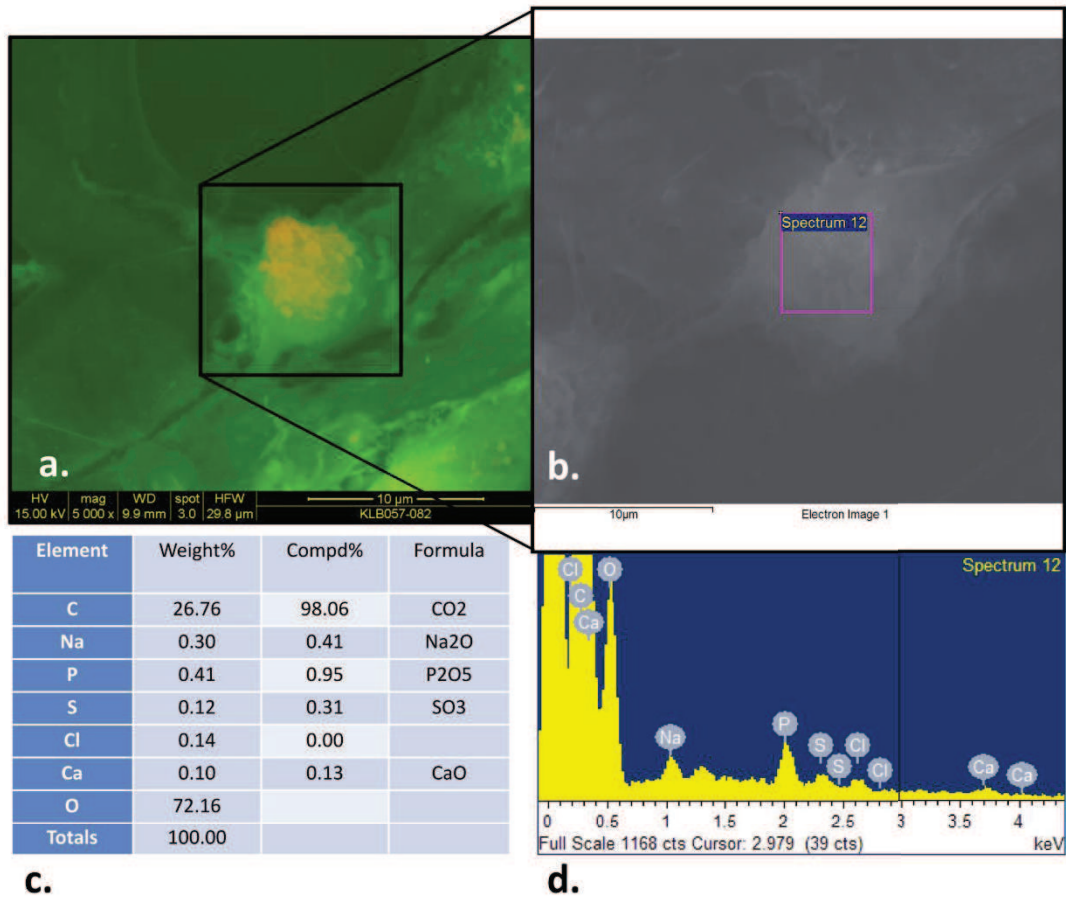


Figure 4.5: Rounded cell with internal accumulation of mineralized nanoparticles. a) Density dependent scanning electron image created from overlaying the electron image with the backscatter image. Regions that are more dense, and more likely to contain mineralization show in red. b) Electron image imported for X-ray microanalysis. Region of interest selected with magenta box c) Elemental composition of selected region. Weight % is indicative of how much ROI chemical makeup is the selected element, formula gives most likely formulation for each element found. d) Elemental spectrum from ROI used to calculate weight percent of the elements.

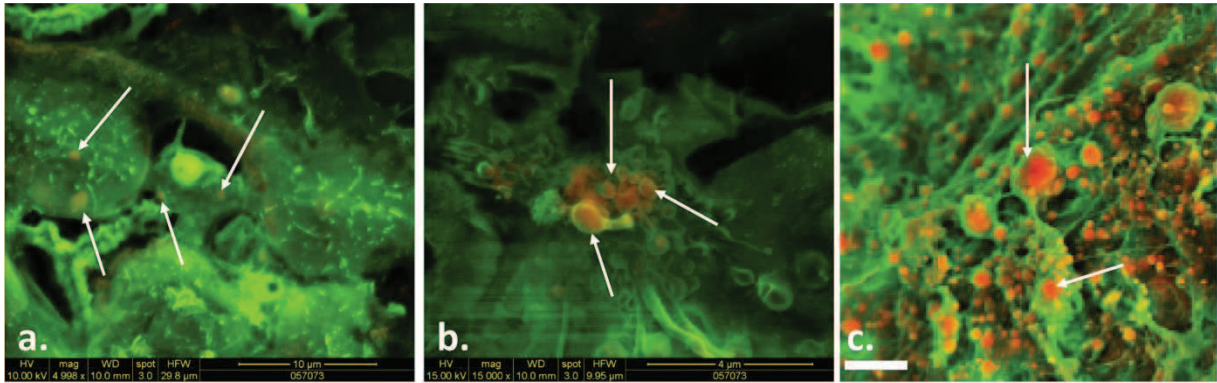


Figure 4.6: Cell originating mineralized nanoparticles may be involved in CAVD *in vivo*. a) SEM density images, red indicates material of higher density, green is background organic material. Dense nanoparticles apparent in cell body of cells within a micro-contact printed aggregate as indicated by white arrows b) Accumulation of mineralized nano-particles on top of micro-contact printed aggregate as indicate by white arrows. Particles may be serving as nucleation sites for additional calcium deposition. c) Dense particles may be involved in earliest stages of CAVD *in vivo*. Mineralized particles are found in valves which do not yet exhibit disease at macroscopic level. Scale bar 3 μ m. Image obtained from [55], reproduced with permission.

4.3.3 Apoptosis and Calcification Occurs in Aggregates of All Sizes

A range of aggregate size has been reported in the literature for studies utilizing the *in vitro* model (Table 1); however, no study to date has investigated the effect that aggregate size may have on cell apoptosis and dystrophic calcification. In addition, it is not known if there is a minimum aggregate size required for pathological calcification. Aggregate size was varied by using 50 μ m, 200 μ m, 300 μ m, and 400 μ m diameter circles. Both the 50 μ m and 200 μ m exhibited caspase within 24 hours. 300 μ m and 400 μ m aggregates exhibited little apoptosis 24 hours after seeding.

Presence of calcium was confirmed in all aggregate sizes at both 1 week and 2 week time-points (Figure 4.7). Calcium staining appeared more intense at two weeks compared to the one week time-point for all aggregate sizes, indicating ongoing mineralization (Figure 4.7, b-i). The number of aggregates that stained positive for calcium increased with time, as did the size of calcifications within the aggregates. Percent of aggregate area encompassed by calcium mineralization varied with aggregate size. For smaller aggregates (<200 μ m diameter), calcium staining encompassed the

whole aggregate while the majority of larger aggregates (>200 μm diameter) had positive staining of calcifications localized within the central region. Presence of calcium corresponded with regions of caspase 3/7 activity (Figure 4.11a, caspase heat maps).

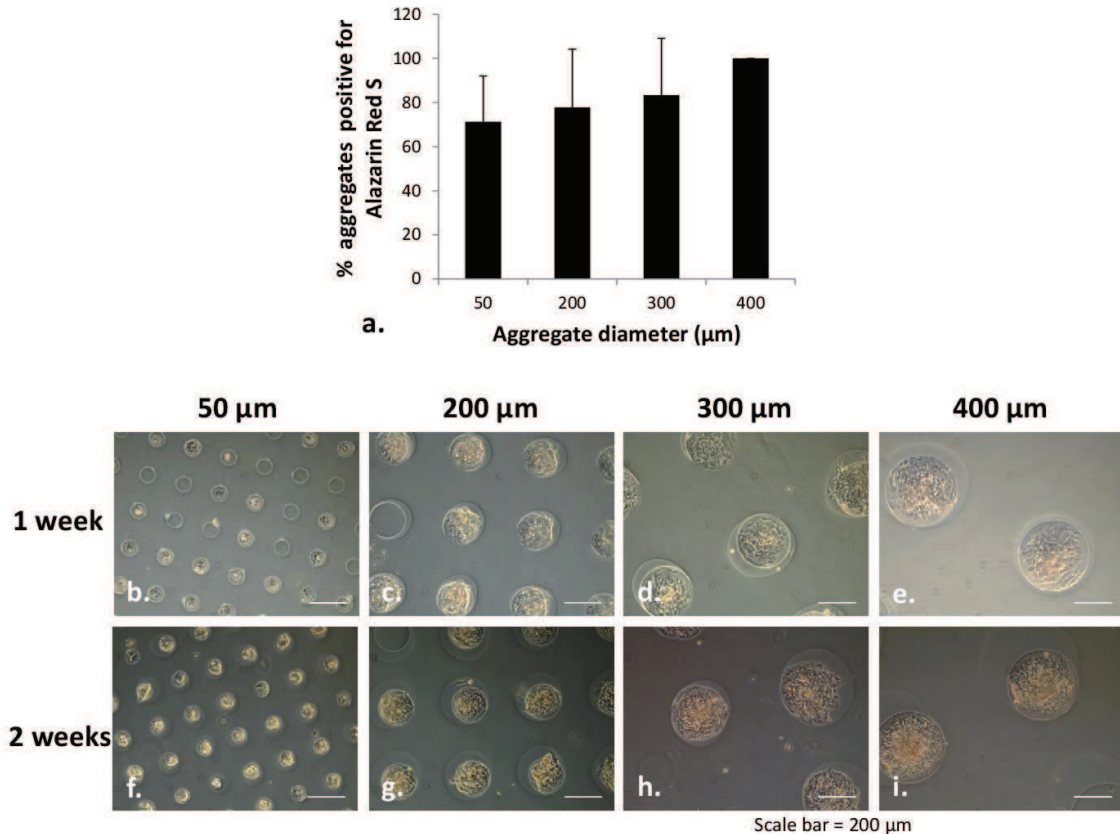


Figure 4.7: Calcification occurs in all aggregates, regardless of size. a) Micro-contact printed aggregates of all sizes were calcified at two weeks. (b-e) Alazarin Red S, a stain for calcium, in 50 μm , 200 μm , 300 μm , and 400 μm micro-contact printed aggregates at one week time-point. (f-i) Alazarin Red S staining became more intense with time in culture, indicating continuing mineralization. Scale bar = 200 μm

Number of cells within the aggregates increased with aggregate size. Cell area, measured by taking total aggregate area and dividing by the number of cells, was unchanged between aggregates of

different diameters. However, VICs within micro-contact printed aggregates had much smaller cell area than VICs within a monolayer formation (supplemental data).

4.3.4 Aggregate Traction Forces Scale with Size and Substrate Modulus

To determine if differently sized aggregates have different mechanical environments that may contribute to pathology, traction force was measured. Total overall traction force of aggregates increases with aggregate size and substrate stiffness. Stress maps of tractions revealed that the highest measured substrate stress transfer was at the aggregate periphery (indicated by red colorization of stress maps). Interestingly, aggregates on the same substrate stiffness but varying diameters had approximately the same average stress (Figure 4.8). Maximum substrate stress was positively correlated with aggregate diameter.

Traction force was then investigated for aggregates cultured on varying moduli of polyacrylamide gels. Aggregates generated increasing amounts of traction force with increasing substrate stiffness. Average substrate stress and maximum substrate stress was positively correlated with substrate moduli. Despite varying moduli of polyacrylamide gels, distribution of tension appeared similar with highest measured substrate tractions around the periphery of the aggregate. The greatest increase in measured average stress and substrate stress was on the 76.4 kPa gel (Figure 8). Interestingly, calcification was not correlated with overall traction force, average substrate stress, or maximum substrate stress (Figure 4.9) suggesting that distribution of tension may be more critical to pathology initiation than actual measured mechanical environment. However, more research is needed to confirm this hypothesis.

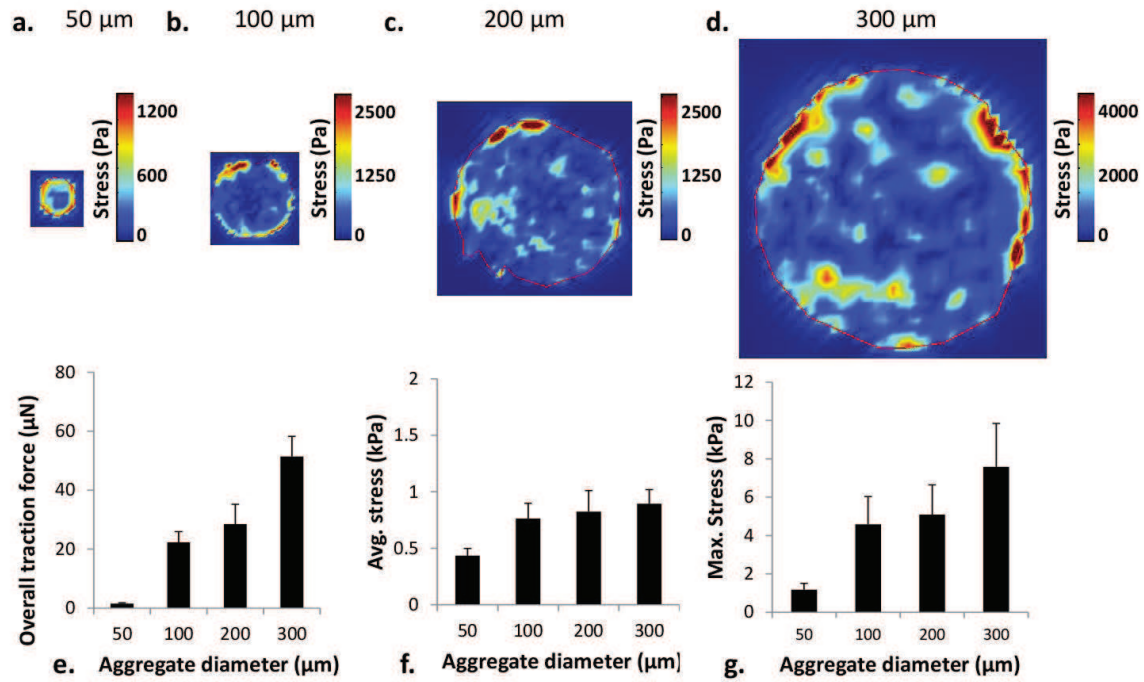


Figure 4.8: Aggregate overall traction force increases with aggregate size. (a-d) substrate stress maps for VIC aggregates cultured on 38.2 kPa PA gel. Areas of highest substrate stress were localized to the periphery of the aggregate. (e) Overall traction force increased linearly with aggregate diameter. (f) Interestingly, average stress within the aggregates was approximately equal between aggregates of all sizes (g) Maximum substrate stress was positively correlated with aggregate size.

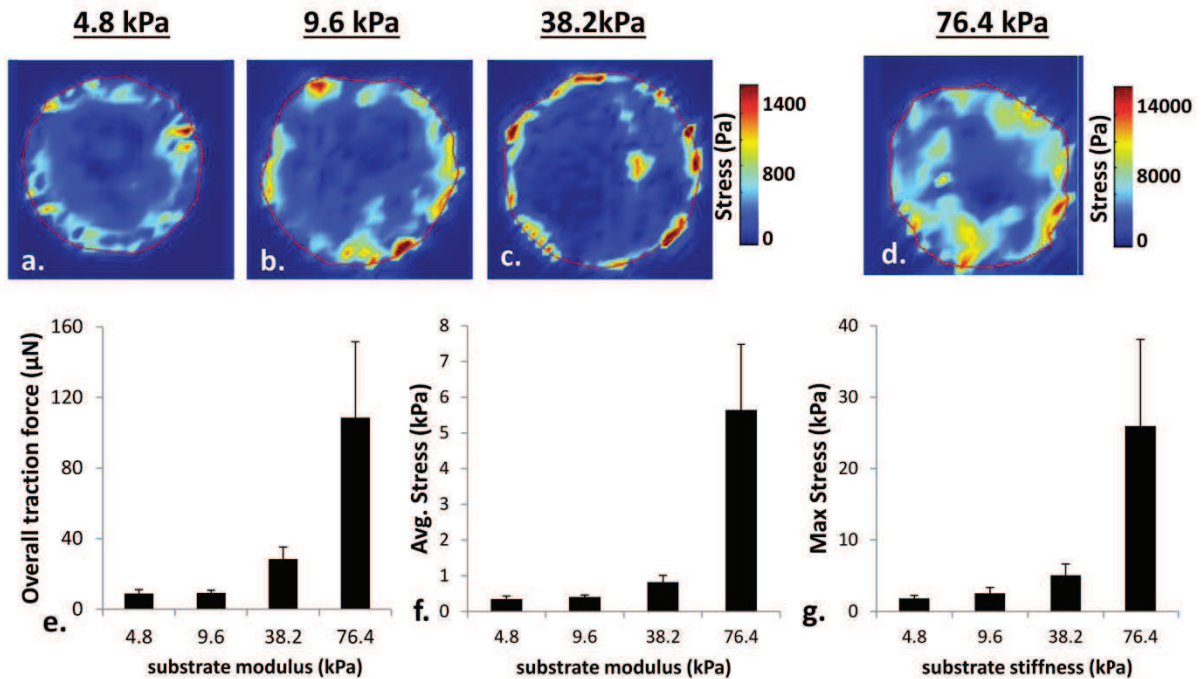


Figure 4.9: Aggregate overall traction force increases with substrate stiffness. (a-d) stress maps of traction of aggregates on increasing stiffness of polyacrylamide gel. Highest traction forces were primarily localized to the periphery of the aggregate, potentially indicating different mechanical environments between center and edge cells. e) Overall traction force increased with substrate stiffness, as did the magnitude of average stress (f), and magnitude of maximum stress (g).

4.3.5 Substrate Modulus Threshold for Calcification

As VICs are mechanosensitive cells and have increased myofibroblastic activity on stiffer substrates [80, 81, 84], micro-contact printed circles were created on varying moduli of polyacrylamide gels to determine if stiffer substrates induce greater calcification as myofibroblastic activity is higher.

Additionally, substrate modulus has been proposed to dictate mechanism of calcification with softer substrates favoring osteogenic calcification (calcium nodules with an absence of cell death) [16, 95].

Caspase 3/7 activity was observed on all substrate moduli tested, indicating apoptotic activity (and dystrophic calcification) is present. Micro-contact printed aggregates on all substrate moduli tested stained positive for calcium as determined by Alizarin Red S (Figure 4.10). Substrate modulus

appeared to create a threshold for calcification, above 9.6 kPa, no increase in aggregates staining positive for calcification was observed. This could also indicate the myofibroblastic phenotype reaches maximum activity above 10 kPa which corresponds to transitional stiffness for VICs in the literature [80].

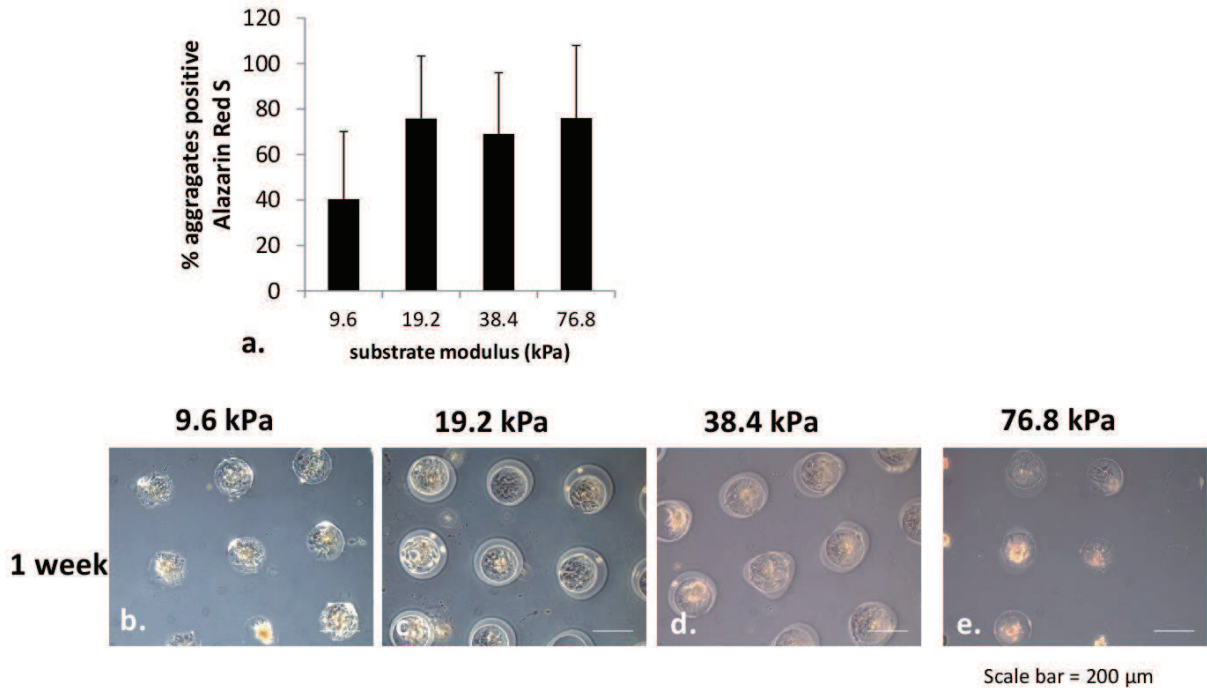


Figure 4.10: Calcification occurs in 200 μ m diameter aggregates on all moduli of PA gels tested. a) Threshold effect of substrate stiffness appear to occur on polyacrylamide gels of moduli stiffer than 10 kPa. This threshold level agrees in literature with reported values of the transitional stiffness for VIC myofibroblastic differentiation. (b-e) 10x phase images of aggregates positive for Alizarin Red S staining on all moduli tested.

4.3.6 TGF- β 1 is Not Required for Apoptosis or Calcification

Many groups using the current *in vitro* model supplement cultures with TGF- β 1 to increase aggregation and calcification response. As micro-contact printing circumvents the need for the cells to aggregate, treatment of micro-contact printed VICs with TGF- β 1 would identify this cytokine's effects on apoptosis and calcification post aggregation. Cells were pre-treated with TGF- β 1 for five days, and then were continued to be cultured in the presence of TGF- β 1 for one week. TGF- β 1 treated aggregates had slightly less caspase activity (as measured by % of aggregate positive for calcium). Heat maps of caspase activity showed highest activity in central regions of aggregates. These heat maps averaged multiple aggregate caspase data together by taking the mean pixel intensity at each location. Number of aggregates averaged to generate each image is given below

each respective heat map. TGF- β 1 heat maps appeared to have more punctate caspase activity, while control aggregates had large clusters of caspase activity, potentially indicating multiple cells undergoing apoptosis simultaneously (Figure 4.11). TGF- β 1 treated aggregates appeared to have slightly increased mineralization as Alazarin Red S staining was more intense than respective controls at one week. Number of aggregates positive for Alazarin Red S was slightly higher in those that had been treated with TGF- β 1 (Figure 4.11), though this was not significant, indicating that TGF- β 1 is not required for calcification.

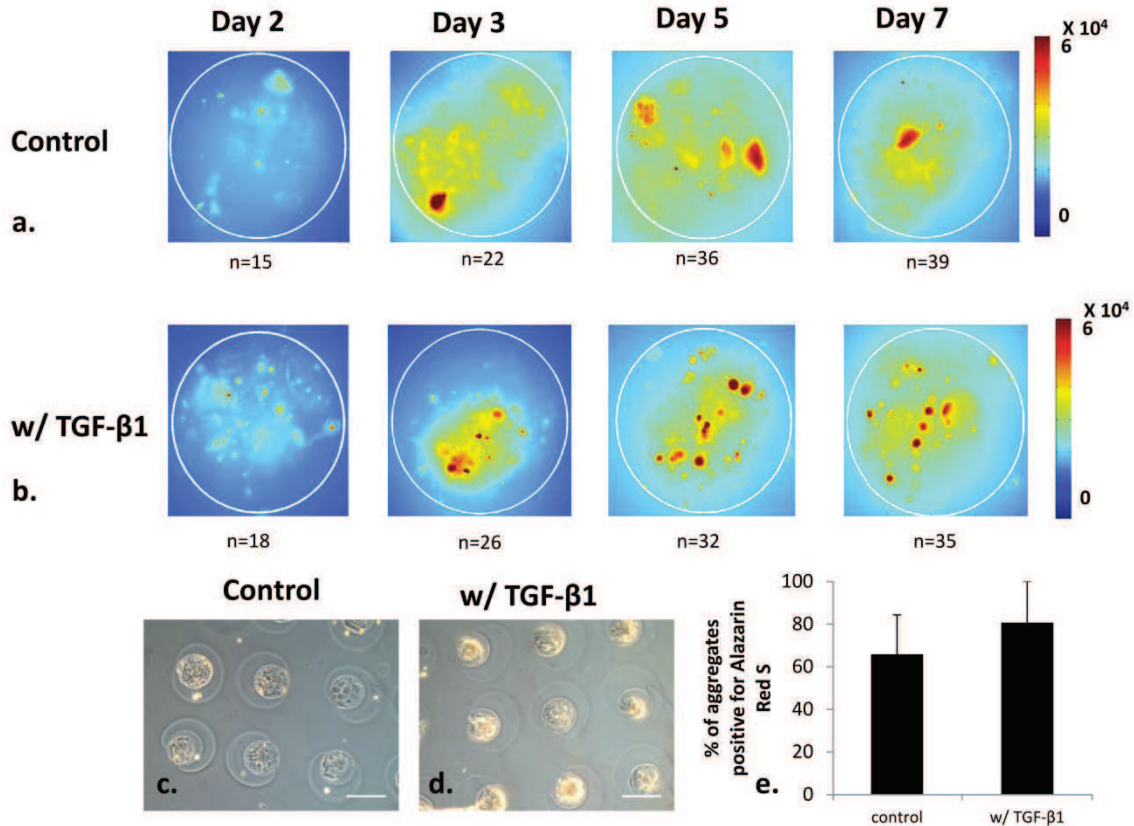


Figure 4.11: TGF- β 1 increased mineralization activity, but did not increase caspase 3/7 activity. a) Time course of caspase 3/7 activity in 200 μ m diameter aggregates on 38.2 kPa polyacrylamide gel. b) Time course of caspase 3/7 activity in 200 μ m diameter aggregates on 38.2 kPa polyacrylamide gel treated with TGF- β 1. Images of aggregates were acquired at 40x, centered using a custom MATLAB script, and “stacked.” Average pixel intensity at each location was taken to create heat map. Red indicates most prominent caspase 3/7 activity. c) Alazarin Red S staining in 200 μ m diameter aggregates on 38.2 kPa polyacrylamide gel and d) 200 μ m diameter aggregates on 38.2 kPa polyacrylamide gel treated with TGF- β 1. e) Samples treated with TGF- β 1 had a slight increase in number of aggregates staining positive for calcium.

4.3.7 Pravastatin Did not Decrease Calcification

As a proof-of-concept for utilizing this system as a high-content *in vitro* screen for drug analysis, pravastatin was used to pre-treat a subset of VICs which were then seeded into micro-contact printed protein circles forming aggregates. Statins have been used in several clinical trials in hopes in reversing calcific aortic valve disease, but without success. In our model, pravastatin failed to

decrease apoptotic activity or calcification within micro-contact printed aggregates indicating that pravastatin is not a valid treatment therapy once aggregates have already formed (Figure 4.12).

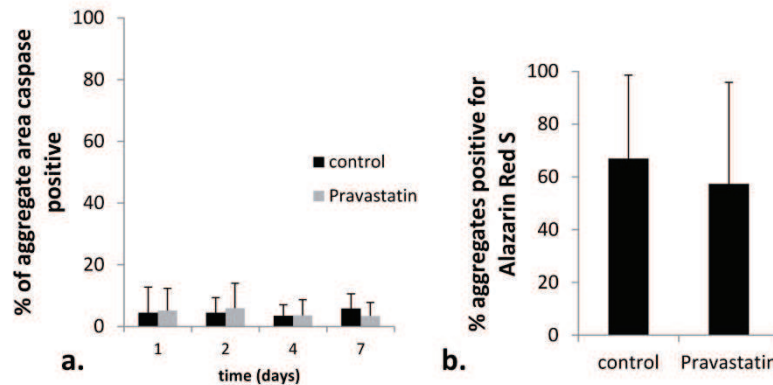


Figure 4.12: Pravastatin did not reduce apoptotic activity or % of aggregates which stained positive for calcification. a) Time-course of apoptotic activity between control aggregates and aggregates that had been treated with pravastatin were almost identical, suggesting that pravastatin does not reduce apoptotic activity within micro-contact printed *in vitro* model. b) Pravastatin did not reduce number of calcifications as determined by orange staining with Alizarin Red S within micro-contact printed samples.

4.4 Discussion

In this work, we have shown that aggregate calcification initiates rapidly following aggregation as controlled by culture on collagen micro-contact printed circles. Controlling aggregates within micro-contact printing allows for *in vitro* calcifications to form in a highly repeatable and reproducible manner. Using micro-contact patterning to control aggregate size, we have shown that calcification occurs within all aggregate sizes within one week. As the time in culture increases, so too does the intensity of Alizarin Red S staining, suggesting on-going mineralization processes. As an additional measure of calcification, we used SEM combined with X-ray microanalysis to analyze elemental composition within various regions of the aggregates and have discovered calcifications in several

forms including nanoparticles of calcium oxide and mineralization within rounded cells located in the center of the aggregate. It remains to be determined if the mineralized nanoparticles within cells and clustering of mineralized nanoparticles on the apical surface of the aggregates are two independent mechanisms of calcification or if these two types of calcification are different facets of the same mechanism. In addition, we have observed caspase 3/7 activity within our micro-contact printed aggregates in as early as 24 hours, in a highly repeatable and reproducible manner. By micro-contact printing on different stiffness polyacrylamide gels we have shown that this dystrophic calcification occurs regardless of aggregate size or substrate stiffness. TGF- β 1 is not required in order to get dystrophic calcific nodules on polyacrylamide gels; although TGF- β 1 does not increase caspase activity, it does appear to increase mineralization as evidenced by the darker Alizarin Red S staining. Mechanism of cell death appears to be apoptosis dependent as blocking with Z-VAD -FMK, a pan caspase inhibitor, decreased both apoptotic activity and the calcium staining within the micro-contact printed aggregates. As this model can initiate apoptosis and calcification rapidly, and size of aggregates is highly controlled, we hope that this can be used in the future as a high-throughput platform for screening promising pharmaceuticals candidates for CAVD as well as elucidating the mechanisms behind apoptosis within the central region. As a proof-of-concept method for testing potential pharmaceuticals, Pravastatin was used as a pre-treatment for a subset of samples though no reduction in calcification was observed. This result is in agreement with clinical trials data, where patients did not experience any reversal of calcification with a Pravastatin regimen.

4.4.1 Rapid Calcification Formation *In Vitro*

Our unique approach to create aggregates utilizing micro-contact printing on polyacrylamide gels initiates apoptosis within 24 hours in smaller aggregate sizes (200 μ m diameter and 50 μ m diameter). This is much faster than the earliest reported nodule formation currently in the literature, which is 48 hours by Merryman and colleagues. Merryman and colleagues report

dystrophic calcification which initiated only when VICs had been pre-treated with TGF- β 1 for 24 hours prior to application of cyclic stretch [17]. No calcific nodules were observed in control groups that been either treated with 5 ng/ml TGF- β 1 or cells that had been cultured at confluence and underwent cyclic strain for 48 hours. This led the authors to hypothesize that it was the combination of TGF- β 1 and cyclic strain which disrupted the monolayer culture leading to aggregate formation. Few apoptotic VICs are present within monolayers, indicating there are differences in mechanical and biochemical cues between monolayers and aggregates which initiate apoptosis.

Our analysis of cell spread area within monolayers indicates that cells within micro-contact printed circles have smaller spread area than those which occur in monolayers. The exact reason for the area differences between monolayer and aggregate cells are not yet determined, but may be due to several factors. First, it is possible that that a high number of cells initially bind to the protein island following cell seeding. However, the cells in the center are unable to spread as large as the cells on the periphery and the physical effect of spread area restriction may initiate the apoptosis within the central region. Secondly, cells along the periphery could be proliferating and this creates a center of the aggregate that is of higher cell density. This increase in cell density cues VICs within the central region to undergo apoptosis. Restriction of geometry has been shown in single cells to induce apoptosis as cells on smaller protein islands underwent higher rates of apoptosis than cells on larger protein islands [103, 170]. Future work should focus on the mechanical environment which may initiate apoptosis within the central region of the aggregate.

4.4.2 Calcifying Apoptotic Cells and Mineralized Particles

Calcified nanoparticles were observed within cells, as determined by X-ray microanalysis. Additionally, what appeared to be accumulated calcified nanoparticles were found on the apical surface of several aggregates examined. Cells release micro-vesicles through exocytosis and these

vesicles are believed to be essential for many cell processes such as intercellular signaling. It remains to be determined if the mineralized particles found within the micro-contact printed aggregates are characterized as extracellular vesicles and if these particles contain enzymes or miRNA, as has been reported vesicles from other cell types. Release of spherical microparticles has been reported previously for VICs in response to strain [90], but to our knowledge, this is the first documentation of calcium nanoparticles within valvular interstitial cell aggregates.

Excitingly, dense mineralized nanoparticles have been reported in diseased valve tissue [55]. These nanoparticles are approximately the same sizes as the ones we observed in the SEM images of our micro-contact printed aggregates. These calcified nanoparticles were present even in apparently “healthy” valves prior to appearance of visible nodules and sclerosis. Stevens and colleagues suggest that these calcified nanoparticles are involved in disease onset and initiation. There is ongoing debate if these vesicles are of cellular origin. Osteoblasts and chondrocytes have been shown to release extracellular vesicles (termed matrix vesicles) from sites on the plasma membrane [171], and it is becoming increasingly recognized the role of matrix vesicles in bone formation [172]. The role of cellular derived vesicles in cardiovascular calcification remains contentious. Aikawa and colleagues report existence of an exosomal pathway in valvular interstitial cells and smooth muscle cells where extracellular vesicles are released and contributed to pathological calcification. Dr. Aikawa posits that extracellular vesicles may be involved in VIC cell signaling and differentiation to osteoblastic phenotypes as miRNAs 30, 125-b, 143, 145 and 155 all influence the expression of a specific set of osteogenic markers such as Smad1, RUNX-2, and alkaline phosphatase and have been found within the extracellular vesicles.

4.4.3 Geometric Control of Cell Behavior

To our knowledge, this is the first use of micro-contact printing to replicate a disease model.

However, geometric control over multicellular behavior has been reported in the literature for some time. Differences in proliferation behavior have been observed between cells along the periphery and centrally located cells on protein islands, indicating different mechanical environments [123].

Piccolo and colleagues examined YAP nuclear localization with multicellular aggregates and found that areas of high stress, such as along the micro-pattern perimeter, promoted YAP translocation to the nucleus [124]. Vunjak-Novakovic and colleagues examined mesenchymal stem cell

differentiation on large (1000 μm) protein rings (200 μm inner diameter) and found osteoblastic lineage commitment varied with location within the ring. This differentiation was primarily localized to regions where cell area was small yet cells still remained elongated (such as the inner edge of a ring and the regions next to the short edges of rectangles) [125]. The differentiation and

proliferation activity observed was abolished with use of cytoskeletal inhibitors, such as Blebbistatin and Y-27632, a Rho pathway inhibitor. Recently, studies investigating cellular alignment within annuli of increasing inner diameter and discs showed higher cellular alignment in areas of highest predicted mechanical stress [173]. Combined these studies show the power of mechanical stresses in regulating multi-cellular behavior, and that cellular behavior within aggregates can vary due to the differences in mechanical stresses through-out the geometry.

4.4.4 Substrate Modulus and Calcification

VICs have been known for many years to be sensitive to substrate modulus. Quinlan et al. showed increased cell spread area and increased α -SMA incorporation into stress fiber with increasing substrate modulus [81]. Benton *et al.* identified a “transitional stiffness” where VIC phenotype switched from fibroblastic to myofibroblastic to be at ~ 7 kPa [80]. Activation to the myofibroblast phenotype appeared not only to depend on substrate stiffness, but also biochemical properties,

such as adhesive peptide sequences incorporated into the thiol-Ene hydrogel [174]. The myofibroblastic phenotype is reversible with a decrease in substrate modulus [84].

To our knowledge, this is the first study to use polyacrylamide gels to study dystrophic calcification. It was presumed that type of calcification was dictated by substrate stiffness as osteogenic calcification was reported by Yip *et. al* on soft collagen gels while dystrophic calcification was found on collagen coated tissue culture polystyrene. Merryman and colleagues use 22 kPa fibronectin coated polyacrylamide hydrogels for creating osteogenic nodule controls and has determined there to be no dystrophic activity as nodules do not uptake propidium iodine, a marker of cell death [95].

4.4.5 Mechanical Characterization of VIC Aggregates

To our knowledge, this is the first study to employ traction force microscopy to measure the traction force and average stress of valvular interstitial cell aggregates. Merryman and colleagues have mechanically characterized valvular interstitial cell aggregates using atomic force microscopy to elucidate differences in osteoblastic and dystrophic nodules once the aggregates had already formed calcifications [95]. Results showed that calcified dystrophic nodules have heterogeneous modulus and topography after calcifications have formed. Additionally, dystrophic nodules had a higher modulus than osteogenic nodules. One of the challenges of biophysical characterization of VIC nodules is that their formation is random, making mechanical measurements on aggregates difficult. In addition, for traction force microscopy, a clear region around the aggregate is needed so calculations are not influenced by nearby cells. In literature, images of calcific nodules usually appear near the edge of a monolayer, preventing traction force calculations. Micro-contact printing enables traction force microscopy of aggregates as the circular patterns direct cell attachment and cells cannot bind to the hydrogel without the protein. This allows for a clear boundary to be created around the aggregate, facilitating accurate traction force measurements.

4.4.6 TGF- β 1 and the *In Vitro* Model of CAVD

TGF- β 1 has been frequently used with the *in vitro* model of CAVD to rapidly initiate the calcification response. The number of calcified nodules greatly increases in the presence of TGF- β 1 [19]. It has been shown that TGF- β 1 mediates the activation of VICs to highly contractile myofibroblasts [12] and these activated cells aggregate followed by the formation of calcifications. Our micro-contact printing method allows the aggregation step to be separated from the subsequent calcification. This is beneficial for studying the pathology initiation downstream of aggregation. It is especially useful for elucidating the role of TGF- β 1, and if the cytokine is required only for aggregation initiation, but also for disease progression through the calcification. As we did not see any significant differences between TGF- β 1 and control groups with respect to caspase activity and calcium staining, our results suggest that TGF- β 1 primarily affects the ability of VICs to aggregate, but once VICs have formed aggregates (as simulated with geometric restriction on micro-contact printed protein surfaces), the disease progressed through a largely TGF- β 1 independent mechanism.

TGF- β 1 is involved with myofibroblast differentiation, and increasing cytoskeletal tension within individual cells. It has been proposed that high cytoskeletal tension is needed for aggregation to occur. Culture in the presence of TGF- β 1 was not sufficient to induce aggregation and calcification within 48 hours on fibronectin flexcell plates [17], although other groups report aggregates under these conditions at one-week [9, 12]. It was only when TGF- β 1 was combined with cyclic stretch that aggregates developed indicating that aggregate formation requires extraordinarily high intracellular tension which is found in the myofibroblastic phenotype. When cellular tension was decreased either by decreasing expression of α -SMA actin [19] or with inhibiting Rho-pathway activity [18], nodule development was reduced or eliminated entirely.

Ex vivo, TGF- β 1 has been implicated in CAVD as study of explanted valves reveals significantly more TGF- β 1 localized within the extracellular matrix of diseased valve cusps when compared to healthy control valve leaflets. TGF- β 1 positive areas are in close proximity to calcified nodules suggesting association between the cytokine and calcification [11].

4.4.7 Statins for preventing CAVD

Statins have been suggested as a potential pharmacological treatment which has shown great promise with inhibiting atherosclerotic calcification in the vascular system. However, the results from clinical trials investigating applications for CAVD have been mixed [8]. *In vitro* statins have been investigated by several research groups with respect to inhibiting or reversing VIC calcification. Benton et. al showed that although pravastatin is useful for decreasing nodules in culture; statins were unable to reverse the progression once nodules had already formed [19], and suggested that statins may be useful, but in a preventative role. We found that statins failed to decrease calcifications in this *in vitro* model system, likely as the geometric restriction simulated correctly nodule formation, adding additional support that our model is accurate at reproducing the pathological environment which occurs in the *in vitro* model for dystrophic calcification. Our pre-treatment of VICs with pravastatin failed to inhibit calcifications, suggesting that either the five day pre-treatment was not long enough to prevent the disease phenotype from occurring, or that the geometric restriction and constraint itself is enough to initiate disease progression regardless of pharmacological pre-treatment. Additional research groups' results with statins suggest potentially limited clinical use. Monzack and colleagues showed that success of statins with preventing calcification appeared to be substrate dependent [175] while work by Wu et al. showed that success of statins was dependent upon the specific VIC subtypes within cell population [176]. Statins may be useful for patients with a specific aortic valve protein composition or cell population, but in clinical practice it may be impossible to identify these individuals.

4.5 Conclusions

In this work, we have shown that the *in vitro* model for calcific aortic valve disease is able to be replicated with micro-contact printing on polyacrylamide hydrogels. The utility of this method allows for tight control over aggregate shape, enabling investigation of aggregate size on time-course of pathological calcification. It was shown that apoptosis and dystrophic calcification is present in aggregates of all sizes. Mechanical characterization via traction force microscopy showed different mechanical environments between aggregates of different sizes, total traction force increased with size of aggregate. Further work is needed to elucidate the role of mechanical environment on apoptosis initiation within central regions of the aggregate. As polyacrylamide gels have easily tunable mechanical properties, investigation of the effect of substrate modulus on calcification was enabled. Dystrophic calcification was replicated on all moduli tested. Presence of TGF- β 1 was not required to initiate apoptosis and calcification, although it slightly increased mineralization as determined by Alizarin Red intensity. Pravastatin did not reduce number of calcifications, indicating pravastatin may not be a suitable pharmacologic treatment for reversal of calcification once aggregation has occurred.

4.6 Acknowledgements

We would like to thank Dr. Dirk Albrecht (WPI, BME) for assistance in wafer design; Laura Aurillo and Ross Lagoy of Albrecht for wafer manufacturing and stamp casting, and Vicki Huntress for microscopy assistance. Special thanks to University of Massachusetts Medical School Electron Microscopy Core and Dr. Gregory Hendricks for assistance with SEM imaging and x-ray microanalysis.

Chapter 5: The Distribution of Tension within Valvular Interstitial Cell Aggregates and Its Role in Disease Initiation

Heather A. Cirka¹, Vivian Liang¹, and Kristen L. Billiar¹

1. Department of Biomedical Engineering, Worcester Polytechnic Institute, Worcester, MA, 01609

5.0 Abstract

Calcific aortic valvular disease (CAVD) is the most prevalent valvular disorder in the developed world. Despite the high incidence, much is still unknown about mechanisms initiating the disease. An *in vitro* model has been developed which replicates the calcification seen *in vivo*. In the model, Valvular interstitial cells (VICs) first aggregate, then cells within the center undergo apoptosis and calcification ensues. Tension has been implicated in initiating the aggregation process; however, the distribution of tension has never been examined within the valvular interstitial cell aggregates. In this study, the different mechanical environments that exist within the center and periphery of the VIC aggregates and the role they may be playing in disease initiation are examined. Specifically, low tension environments have been known to initiate apoptosis in myofibroblasts. The hypothesis that a differing mechanical environment within the central portion of the aggregate may induce low cell tension and apoptosis is investigated. Several immunohistochemistry markers were used to qualitatively examine tension differences between the center and peripheral cells, and a finite element model of contraction was used to predict mechanical state. Modulation of the aggregate geometry shows that caspase 3/7 activity continues to occur within regions of low tension. Increasing aggregate tension with mechanical stimulation reduced caspase 3/7 activity. Combined, these results suggest that mechanical tension may be a key factor in VIC fate determination and could potentially be exploited for therapeutic purposes.

5.1 Introduction

Calcific aortic valvular disease (CAVD) is the most prevalent valvular disorder in the developed world. In the United States, it is believed that 81 million Americans are affected [2] with the prevalence expected to increase as the population ages. Calcifications, which form on the valve leaflets by currently unknown mechanisms, inhibit valve function and cause stenosis and

regurgitation. To date, there are no pharmaceuticals or alternative therapies to slow, halt, or reverse disease progression; the sole means of treatment is a complete valve replacement.

Approximately 95,000 aortic valve replacement surgeries were performed in the United States in 2010, the majority of which were necessitated by CAVD. Development of additional treatments for CAVD has been hindered as currently there are no adequate animal models which can accurately recreate the calcification seen on explanted disease valves in humans [10]. Additionally, *Ex vivo* examination of disease valves only reveals the end-state of disease, giving no indication of pathology initiation or progression (Dr. Frederick Schoen, personal communication).

An *in vitro* model has been developed which replicates the calcification seen *in vivo*. This model involves seeding valvular interstitial cells (VICs) at high density, often in the presence of TGF- β 1, into tissue culture polystyrene dishes. After the VICs aggregate, cells within the center of the aggregate undergo apoptosis and calcifications develop within one to three weeks. Although simplistic, this model has revealed several factors which increase the frequency of aggregation and subsequent calcification. Notably, factors that increase intracellular tension and differentiation to myofibroblastic phenotype also increase aggregation. These include culture in the presence of TGF- β 1 [12], culture on stiff surfaces [16], and culture on fibrin coated surfaces [9], as well as culture in conditions that combine TGF- β 1 and cyclic mechanical stretch [17]. Although there has been a great deal of work done to understand the factors increasing aggregation, there remain few hypotheses as to why the cells at the center of the aggregate undergo apoptosis. To date, the current knowledge is that aggregation is required for the calcification, but the mechanisms initiating the apoptosis and calcification in the center of the aggregate remain elusive.

Merryman and colleagues have proposed the hypothesis that aggregation occurs when VICs, which usually reside within a healthy monolayer in culture, become activated to the highly contractile

myofibroblastic phenotype. The monolayer essentially “rips apart” due to extraordinarily high tension. This tearing creates the cell death and initiates aggregate formation. Although an intriguing hypothesis, if the monolayer were to tear apart and create aggregates, the cell death would occur on the periphery of the aggregate, while experimentally, the cell death and calcification are found within the aggregate center.

We hypothesize that cells at the center of the aggregate undergo apoptosis as a result of the low tension environment. Induction of apoptosis has been shown to occur in a variety of low tension mechanical environments. Physical cues that induce apoptosis include the following: release of contractile cell-populated collagen gels from rigid anchors [99], inhibiting adhesion to extracellular matrix proteins [100], low substrate modulus [33, 91, 101] and restricting cell spread area [103, 104]. Although cell tension is not usually measured in tandem in these studies, separate studies demonstrate that cells free-floating in gels generate minimal tension [105], blocking integrin-extracellular matrix binding leads to a decrease in traction force [106], and cells within a smaller spread area generate weaker traction forces [82, 107-109].

Non-uniform cell-generated tension within cell aggregates has been shown to regulate other aspects of cell behavior. Chen and colleagues used micro-contact printing to control cell growth. They observed higher proliferation around the periphery than in the center of the protein islands. The proliferation rates of these cells agreed well with thermo-cooling computational models that predict areas of highest stress along aggregate periphery [123]. Additionally, yes associated protein-1 (YAP-1) undergoes differential nuclear localization depending upon center versus edge location of cells. In single cells, studies have shown that YAP-1 only translocate to the nucleus for cells under high tension [177]. YAP-1 was shown localize to the nucleus for cells along the periphery of protein islands, but not in the center [124]. Finally, stem cells whose differentiation has been shown to be

dependent upon cytoskeletal tension [32, 122] have been shown to differentiate to different lineages depending upon the location within micro-contact printed rings[125]. Collectively, these studies indicate that culture within micro-contact printed protein islands induces varying mechanical environments depending upon location within the aggregate.

Although micro-contact printing has been used extensively to study geometric control of single cells and groups of cells, to date, has ever been employed as a disease model. The micro-contact printing method on polyacrylamide gels was introduced in Chapter 4 will be used to study mechanical tension differences between the center and the edge cells. Factors that have been shown to indicate cytoskeletal tension differences, including α -SMA intensity and incorporation into stress fibers, stress fiber alignment, and nuclear YAP localization will be examined. These results strongly indicate that the cells in the center are experiencing less tension than those along the periphery. Finally, the tension will be modulated by changing the aggregate geometry and applying external loads to alter the apoptotic time-course and calcification.

5.2 Methods

5.2.1 Microcontact printing stamp design for control of aggregate geometry

The design of the polydimethylsiloxane stamps for micro-contact printing is described in Chapter 4. Because changes in geometry alter the distribution of tension, ovals were used in addition to circular shapes.

5.2.2 Tunable substrate preparation

Polyacrylamide gels of 38 kPa were created as described in Chapter 4.

5.2.3 Microcontact printing

The micro-contact printing process was replicated as described in Chapter 4.

5.2.4 Finite Element Modeling

Abaqus CAE was used to create a computational model of VIC aggregates. The VIC aggregate thickness was determined from confocal z-stacks of the aggregates (representative z-stack shown in supplemental data). The cell layer is assumed to behave as an elastic isotropic material with a Young's modulus of 500 Pa, Poisson ratio of 0.49, and 10 μm thickness. A two-step computational model was used to simulate a contracting cell layer. In order to introduce contractility to the system computationally, two different modeling steps were performed. In the first step, a pre-strain of 10% is created with the aggregate. The circular cell layer was stretched in the radial direction to create a residual stress in the system. This pre-strain magnitude has been used for similar modeling work previously reported [178] as well as having been found experimentally by studying pre-strain of cell stress fibers [179]. In the second step, the outer edge of the sample is fixed and the sample is released. This simulation results in a stress distribution in the cell layer. All simulations were three-dimensional, with finite-element mesh density corresponding to a spacing of 5 μm per node. Stress and strain tensors were calculated throughout the structure and the maximum principal stress at the bottom of the cell layer reported. We would like to thank Sina Askarinejad of Rahbar Lab at Worcester Polytechnic Institute for assistance in creating the model and the analysis.

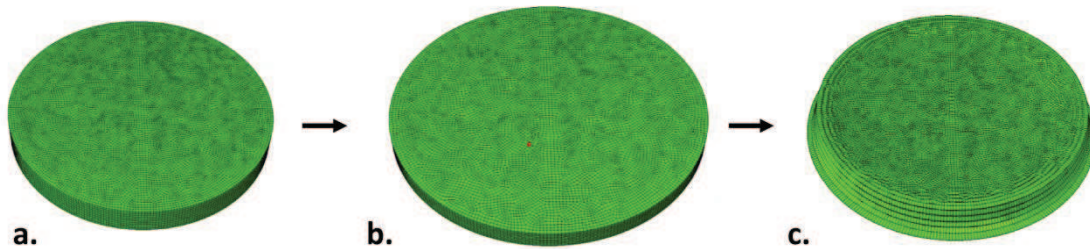


Figure 5.1: Schematic of magnetic finite element model. a) the initial model defined as a linear elastic, isotropic material with a Young's modulus of 500 Pa, Poisson ratio of 0.49, and cell aggregate height of 20 μm . b) Model was stretched 10% to induce a pre-strain in the system c) outer edge of the aggregate was fixed, and the material released.

5.2.5 Cell culture

Valvular interstitial cells (VICs) were isolated from porcine heart valve leaflets obtained from a local abattoir (Blood Farm, Groton, MA) within three hours of tissue harvest per published protocols [168]. Cells from passages 3-7 were used for all experiments. Cells were seeded at densities consistent with literature to encourage monolayer formation and complete cell coverage of the micro contact printed area (100,000 cells/cm²). Media was changed every 4 days.

Transfected VICs which constitutively express nuclear YAP were generously donated by Dr. Dan McCollum of University of Massachusetts Medical School.

5.2.6 Ligand coating magnetic beads

Ferric oxide microbeads (Sigma-Aldrich) were obtained with an average of 5 micron diameter. A collagen solution was prepared by adding 1 mg/mL collagen solution (Advanced Biomatrix) with 10% 0.1 M NaOH to bring the pH up to 7.4. The microbeads were mixed vigorously into the solution and sonicated for ten minutes to reduce clumping. The magnetic beads were allowed to incubate in the

collagen solution for one hour at room temperature. Beads were then rinsed by centrifugation, aspiration of waste solution, and resuspension of the beads in DPBS without calcium and magnesium (Cellgro). The microbeads were sonicated for an additional ten minutes to prevent clumping and then used immediately.

5.2.7 Applying ligand coated magnetic beads to aggregates

VICs were allowed to culture overnight on top of the polyacrylamide gels prior to application of ligand coated microbeads. The media was then changed and 10 μ L of microbead mixture was added to the sample for each milliliter of media. The petri dishes were then gently shaken to disperse the microbeads evenly over the sample. Microbeads were allowed to incubate with the sample for 40 minutes inside the incubator, with occasional shaking to minimize microbead clumping. After incubation, the sample was rinsed vigorously with DPBS (-) until excess beads were removed. Fresh media was then added to the cells. Microbeads preferentially located to the center of the aggregates, despite having been randomly applied to the sample, perhaps suggesting different integrin expression between center/edge cells.

5.2.8 Magnetic pull

Ceramic magnets of varying magnetic fields were purchased from Duramagnetics. Magnets were placed on top of samples prepared with magnetic microbeads. The magnetic field produced by the magnet then pulled on the microbeads, exerting an upward force on the cellular aggregates (see diagram in Figure 1). Control cells without magnetic microbeads were also cultured within the magnetic field, an additional control of samples cultured solely with magnetic microbeads not under a magnetic field were used. Samples were allowed to incubate underneath a magnet for one week. An overview of the methods of 5.2.6-5.2.8 is shown in Figure 5.2.

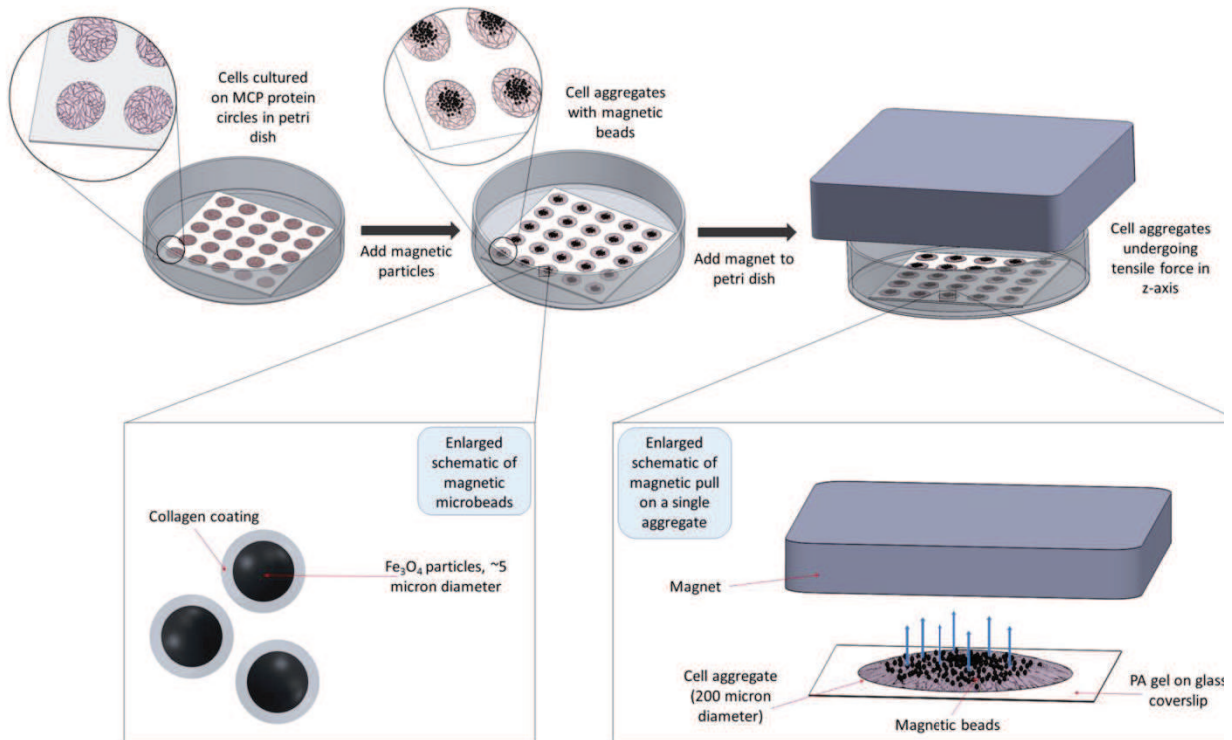


Figure 5.2: Schematic of magnetic bead experiment. (left) VIC aggregates were formed using micro-contact printing method as described in chapter 4. (middle) Collagen coated magnetic beads were placed into the dish so they attached to the aggregates. Method of application resulted in aggregates having magnetic beads primarily within central region. (inset 1) Enlarged schematic showing collagen coated ferromagnetic beads. (right). A magnet is placed on top of petri dishes created an upward tensile force in the z-direction. (inset 2) Enlarged schematic of a single aggregate with ferromagnetic microparticles and upward force.

5.2.9 Caspase Activity

Caspase 3/7 activity was used as a measure of apoptosis detection. CellEvent® Caspase 3/7 Green ReadyProbes® Reagent (Thomas-Scientific) was used according to the manufacturer's guidelines. As a positive control, cells were treated with 1 μM staurosporine (Apex Bio), a broad spectrum protein kinase inhibitor, for 48 hours. Caspase 3/7 activity was quantified manually by visually thresholding the amount of caspase-positive region within an aggregate using ImageJ.

5.2.10 Immunohistochemistry

Cells were fixed with 4% Paraformaldehyde (USB Products) for fifteen minutes and permeabilized with 0.25% Triton-X (Calbiochem). Cells were blocked with 1.5% goat serum (Invitrogen) and stained for alpha smooth muscle actin (Sigma). Cells were counter-stained with Alexa-fluor 488 phalloidin (Thermo-Scientific) and Hoechst (Thermo-Scientific). Antibodies used: anti- α SMA (Sigma, A2547).

To allow for imaging, coverslips were affixed to glass slides using SHUR/Mount™ Toluene-Based Liquid Mounting Medium (Ted Pella, Redding, CA). Prolong-gold (Life Technologies, Grand Island, NY) was then added to the polyacrylamide gel. Images for time-course imaging of caspase activity were acquired using a using a Zeiss inverted microscope and CCD camera. Z-stacks of micro-contact printed aggregates were also acquired at 63x magnification with a confocal microscope (Leica Microsystems).

5.2.11 Regional cell spread area analysis

To determine if cell spread area decreased within the central region of the aggregate, cell spread area was estimated. ImageJ was used to calculate total area of the aggregate. The aggregate center was manually identified from visual inspection of the actin staining and a circle was superimposed on the image whose diameter was equal to the radius of the aggregate. Nuclei within the superimposed circle were labeled “central cells”, while those outside the superimposed circle were labeled “edge cells”. Cell area was estimated by dividing the areas of each region by the number of nuclei found within each area. A schematic of analysis is shown in Figure 5.4.

5.2.12 Stress fiber analysis

Custom MATLAB code was created to analyze regions of aggregate images for stress fiber alignment. Two dimensional fast Fourier transforms (FFTs) were used to assess stress fiber periodicity (indicating stress fiber alignment). One phalloidin image from a non-micro-contact-printed

aggregate and one phalloidin from a micro-contact-printed aggregate were used to compare stress fiber-alignment differences potentially created by restricting cells to protein islands.

Further, sub-image FFT analysis was done to measure stress fiber alignment in the micro-contact printed aggregates. The f-actin image (1024 x 1024 pixels) was first converted to a 16 bit grayscale image. It was then broken up into (32 x 32 pixel) sub-images. The mean pixel value was subtracted from each subimage to remove the 0 Hz component of the FFT. The 2-D FFT was then computed. Using the matlab code `fftshift()`, the FFT was centered at the origin. The sub-image FFT was then binarized and fit to an ellipse. The threshold used to convert to a binary image was consistent across all sub-images with and image. The ellipse major and minor axis were calculated and the ratio was subtracted from 1. For a circular shaped 2D-FFT, created by a random array of stress fibers, the alignment index was 0. A highly aligned section of stress fibers will have an alignment index close to 1. Heat maps were created to graphically show the regions of high and low alignment.

5.3 Results

VICs are a mechanosensitive cell type and alter their α -SMA actin expression and incorporation into stress fibers as a function of substrate stiffness [81]. Biophysical analysis of individual VICs on substrates of varying stiffness shows their ability to alter tension as measured by traction force microscopy (Figure 2a), a form analysis conducted on similar cell types[78]. Atomic force microscopy of VICs cultured on substrates of varying stiffness revealed that cytoskeletal tension is positively correlated with cell stiffness. These findings show that cell stiffness could potentially be used as a surrogate measurement for analysis of tension distribution within multi-cellular aggregates. Initially, we examined the mechanical environments of aggregates that were formed without micro-contact printing. We found that cell stiffness was significantly lower ($p < 0.05$) within the center of the aggregates, indicating a lower tension state. Cells within the center of the aggregate have a reduced

ability to spread due to proximity to neighboring cells. To confirm that cells with spread area restriction have a reduced ability to generate tension, micro-contact printing was used. 40 μm diameter circles were used to restrict cell spread area, and a low seeding density (2,000 cells per cm^2) was used to ensure that only one cell attached to each circle. Cells that had grown within the protein circle generated $\sim 80\%$ lower traction force than unconstrained cells (Figure 3c). These results indicate that the tension state between cells within the center of the aggregate and those along the periphery are likely different.

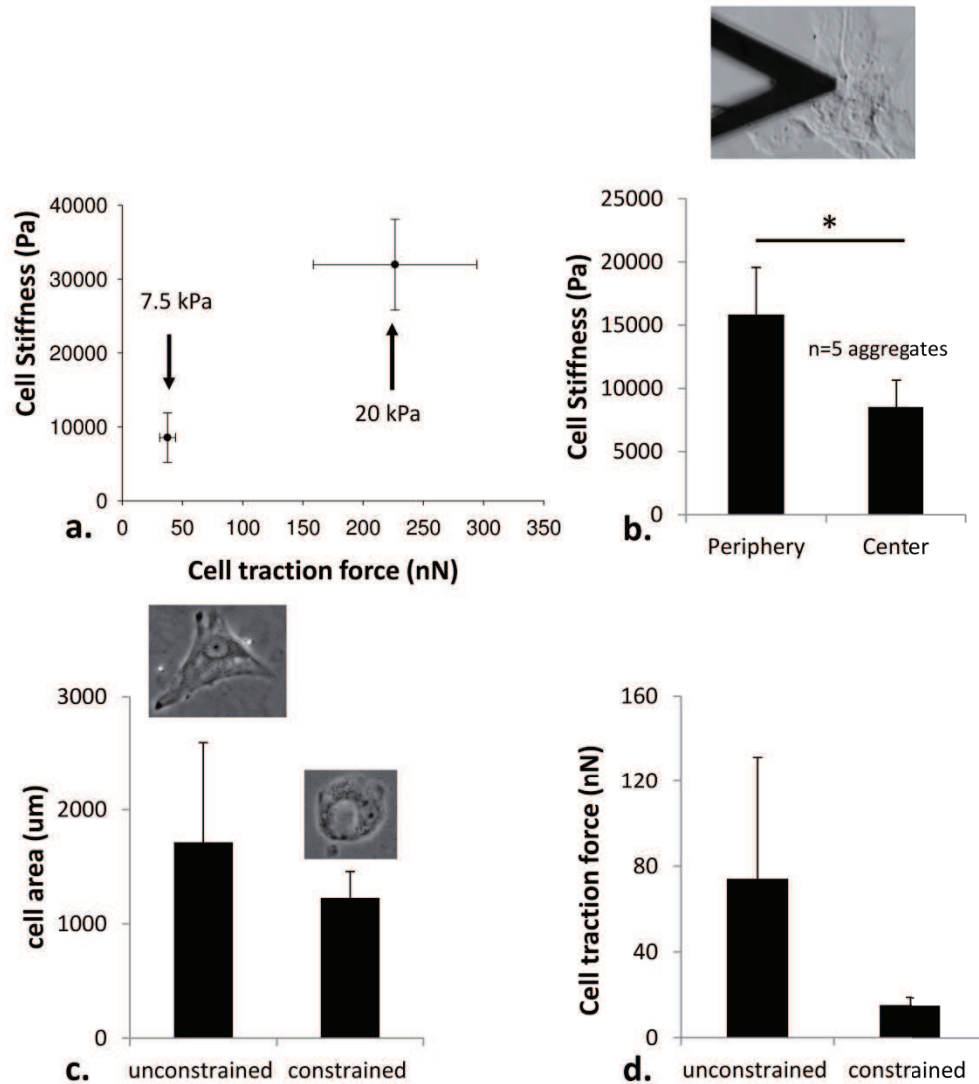


Figure 5.3 Preliminary support for hypothesis a) Biophysical analysis of VICs cultured on 7.5 kPa and 20 kPa polyacrylamide gels shows that VICs have positive correlation of traction force and cell stiffness as measured by AFM indentation, similar to relationship between cell pre-stress and stiffness as reported by Stamenovic and colleagues. This relationship shows that stiffness can be used as a surrogate measurement for cell tension when cell traction force measurements are not an option. Values reported are mean \pm standard deviation. b) Cell stiffness varies with location in the aggregate. Inset showing triangular cantilever over a cellular aggregate in culture for five days. Values reported are the average stiffness of five $20\ \mu\text{m} \times 20\ \mu\text{m}$ force maps using a $0.06\ \text{N/m}$ cantilever with a $5\ \mu\text{m}$ diameter bead tip. c) Constraining individual VICs reduced ability to spread as evidenced by a decrease in area. Insets show representative unconstrained cell (left) and constrained cell (right). d) This spread area restriction, simulating center of aggregate, results in a marked decrease ($\sim 80\%$) in ability to generate tension, as measured by cell traction force.

5.3.1 Regional cell area analysis

Cells have been shown to have an increased ability to generate cell with increasing cell spread area [82]. As an indirect measure of tension, cell area was evaluated in both the central aggregate region, defined as the circle encompassed by $\frac{1}{2}$ the radial length, and edge region of the aggregate. Aggregates of 50 μm , 200 μm , 300 μm , and 400 μm were examined. Cell area was relatively consistent between regions of aggregates of different diameter (Figure 5.4). On average, central cells had a cell spread area of 250 μm^2 , while those on the edge had a spread area of 500 μm^2 . The reduce spread area within the central regions of the aggregate was statistically significant for aggregates of every diameter (two-way ANOVA, $p < 0.05$).

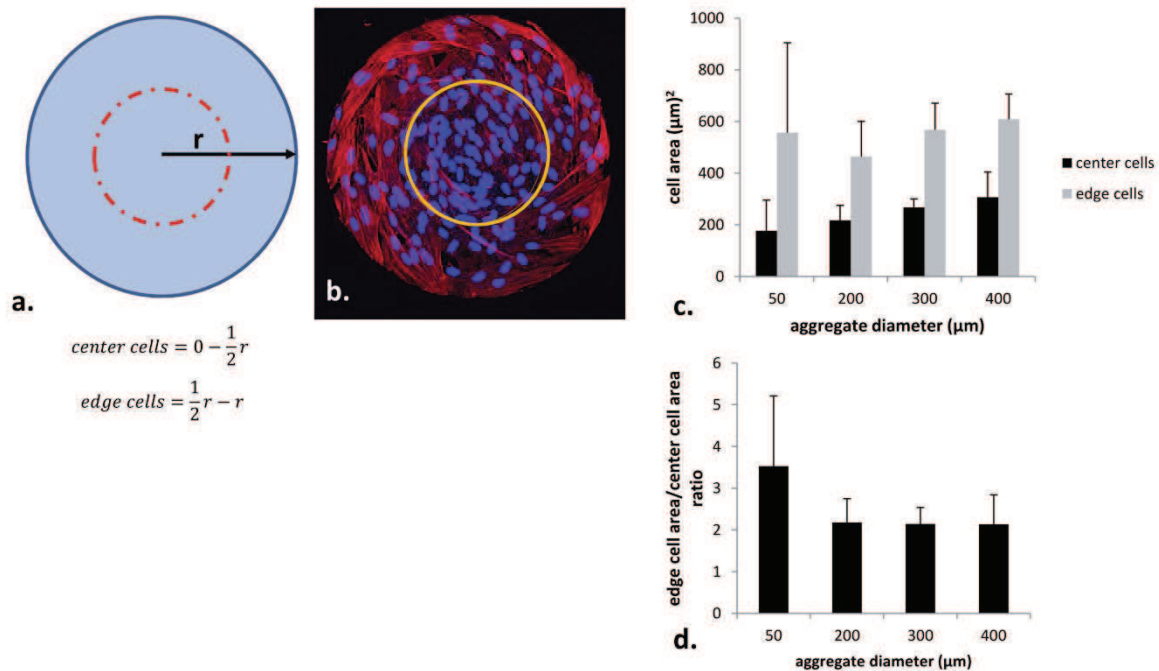


Figure 5.4 Cells within central region of the aggregate have smaller area than those along the aggregate periphery. a) schematic of cell area analysis for center versus edge cells. Center was defined as a circle that was $\frac{1}{2}$ the length of the radius b) representative image analysis. A circle was drawn on the aggregate using imageJ. The number of cell nuclei within the region of interest were counted. As the area of the circle is known, cell area was determined as an average of circular area divided by the number of nuclei. c) the cell area in aggregates of increasing diameter. Cell area was

fairly constant, regardless of aggregate size. d) ratio of edge cell area/center cell area.

5.3.2 Stress fiber analysis as indication of tension environment

As an estimate of differences in tension between the center and the edge of aggregates, stress fibers alignment was analyzed using two-dimensional FFTs on select regions of the aggregate. A two dimensional FFT (2D-FFT) analyzes the periodicity of an image. If the stress fibers are strongly aligned in one direction, there will be a repeating pattern that can be quantified with a 2D-FFT. If there are no repeating patterns (no stress fiber alignment), this will essentially be a random image. As stress fibers carry tension along their length, an estimation of tension state can be gleaned from alignment. Upon analyzing three regions per aggregate (as shown below in Figure 5.3), it was found that the center of the aggregates, for both non-micro-contact printed and micro-contact printed aggregates was highly random, and there was no preferred directionality for stress fiber alignment. In contrast, both aggregates saw more fiber alignment along the periphery. However, the micro-contact printed aggregate did have more alignment, potentially contributing to the circumferential transfer of tension, as evidenced by the 2D-FFTs (Figure 5.5d,f and 5.5a,c, respectively). This alignment is similar conceptually to the “purse-string” hypothesis in wound healing, whereby the redirection of tensional forces contributes to a mechanical signal inducing apoptosis in the center of a closing wound. The high fidelity calcification of the micro-contact printed *in vitro* model, as highlighted in chapter 4, may be due to its ability to align stress fibers.

To further evaluate the alignment within micro-contact printed aggregates, sub-image FFT analysis was done over the entire image. Each 1024 x 1024 pixel image was broken up into 32 x 32 pixel sub-images, creating 1024 different analysis areas over the image (subimage size was approximately 8 μm x 8 μm). Fitting the 2D-FFT to an ellipse gave an indication of alignment degree, as a very elongated ellipse would have a high degree of alignment and when the minor/major axis ratio was

subtracted from 1, would be close to one. On the contrary, poorly aligned stress fibers would have a circular 2D-FFT which when fit to an ellipse, the ratio of minor/major axis would be close to 1, and when that value was subtracted from 1, the alignment index value would be close to zero. Sub-image FFT analysis of aggregates of increasing diameter showed that regardless of aggregate size, alignment of the stress fibers was highest along aggregate periphery (as shown by heat map columns in Figure 5.6).

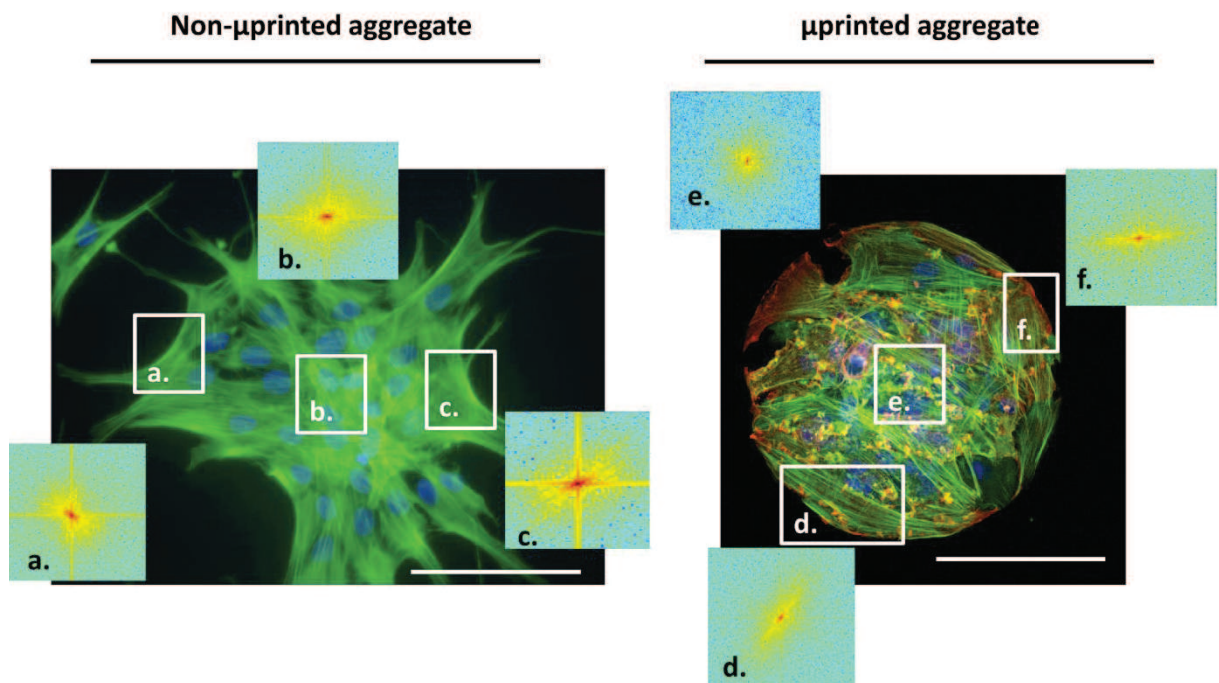


Figure 5.5: Stress fiber analysis indicates stronger directional tension transfer on edge of aggregate as compared to center in both non μ printed and μ print aggregates. Left) Non-micro-contact printed aggregate. Three regions were analyzed using two dimensional FFTs to show fiber alignment. Notice strongest fiber alignment was seen in the peripheral regions of the aggregate (a,c) while no alignment was observed in the center of the aggregate. Right) Micro-contact-printed aggregate. (d,f) Peripheral alignment of stress fibers was observed, indicating tension transfer along fiber length. Like the non-micro-contact-printed aggregate, there was no fiber alignment in the center. Scale bar = 100 μ m.

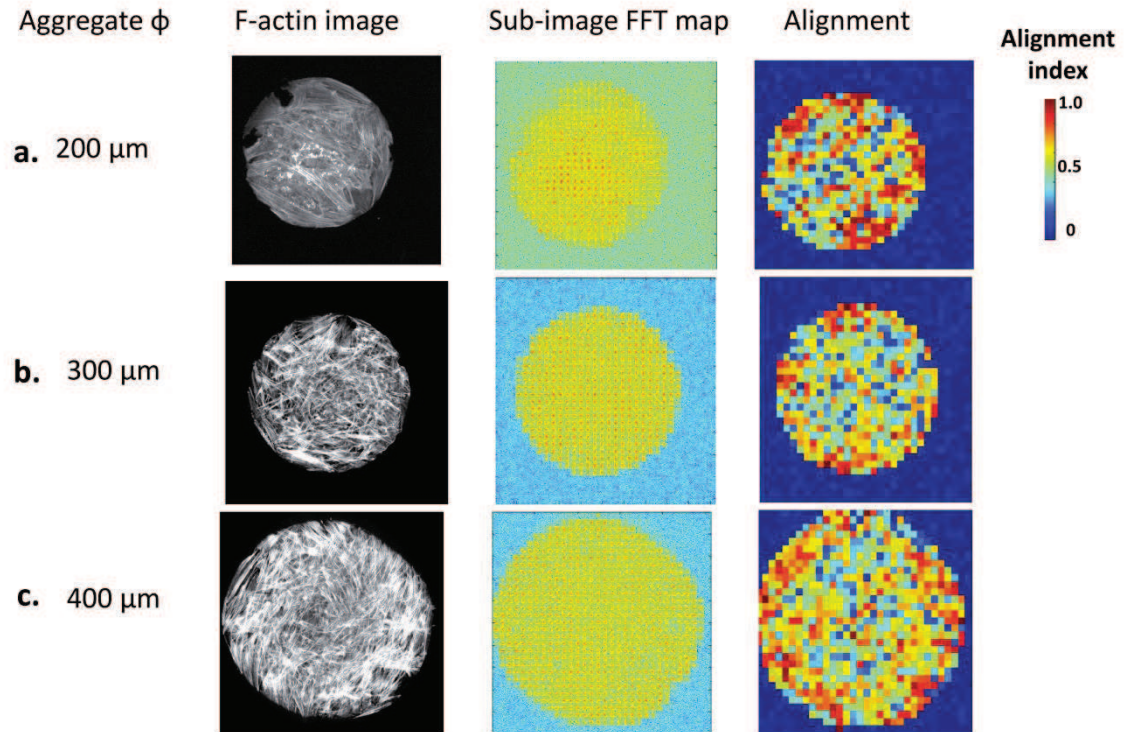


Figure 5.6: Stress fiber sub-image analysis indicates stronger directional tension transfer on edge of aggregate regardless of aggregate size. a) 200 μm diameter aggregate f-actin image, sub-image 2D-FFT plot, and alignment index. b) 300 μm diameter aggregate f-actin image, sub-image 2D-FFT plot, and alignment index c) 400 μm diameter aggregate f-actin image, sub-image 2D-FFT plot, and alignment index. Regardless of aggregate size, alignment (as indicated by red in alignment heat map) was greatest at periphery of aggregate.

5.3.3 YAP localization suggests different mechanical environment between center and edge of aggregate.

Piccolo and colleagues have shown that YAP is a mechanosensitive pathway, and YAP localization gives indication of the mechanical environment of the cells as cells of soft substrates or cultured in high density with restricted spread area did not have nuclear YAP localization, while cells in sparse culture or on stiff substrates had YAP translocate to the nucleus. As a qualitative measure of tension distribution within the micro-contact printed aggregates, location of YAP was assessed. As shown in Figure 5.7, the majority of peripheral cells had YAP localized to the nucleus, suggesting a higher

tension state, while cells within the center of the aggregate had cytosolic YAP, consistent with cells in a lower tension environment.

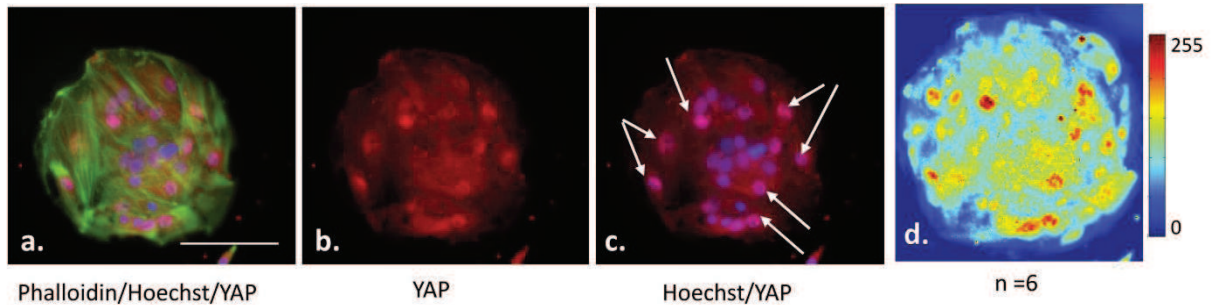


Figure 5.7: YAP undergoes nuclear translocation for cells on the aggregate periphery. a) 200 μm diameter aggregate on 38. kPa PA gel stained with phalloidin (green) showing f-actin stress fibers, Hoechst (blue) nuclear stain, and antibodies for YAP (red). scale bar = 100 μm b) Red channel showing YAP nuclear localization in peripheral cells c) overlay of red and blue channels to show YAP nuclear localization in peripheral cells. Nucleus appears purple where red and blue overlay, indicating YAP nuclear activity (white arrows). d) YAP heat map compiled from six different aggregates to show intensity distribution of YAP within the aggregates. Notice areas of highest intensity are along the periphery of the 200 μm diameter aggregate.

5.3.4 Constitutive YAP expression

To determine if YAP nuclear localization is sufficient to prevent apoptosis, cells were transfected to have continual YAP nuclear localization. Constitutive YAP expression appeared to affect VIC mechanosensing, as cells did not increase in area and had a more rounded morphology (Figure 5.8a and Figure 5.8b) on all substrates as evidenced by the high form factor, a measure of the number of cellular extensions (defined in Ch. 3). Although, YAP nuclear localization has been suggested in other types of fibroblasts to drive myofibroblastic differentiation, cells that had constitutive YAP expression had smaller spread area compared to control cells (myofibroblasts are known for being large spread cells, with large focal adhesions and α -SMA incorporation into stress fibers). YAP constitutively active cells had similar proliferation rates to control cells in sparse culture, but when plated in micro-contact printed aggregates, cells appeared to lack contact inhibition and continued proliferating (Figure 5.9). At 7 days, few aggregates remained in the printed pattern and instead

appeared as rounded cell clumps. Interestingly, although these cells were rounded, detached and appeared unhealthy, many still had plasma membrane integrity as shown by intracellular esterase activity (green). Few cells stained with ethidium homodimer-1 (red) (Figure 5.8). Additionally, no visible calcifications were detected.

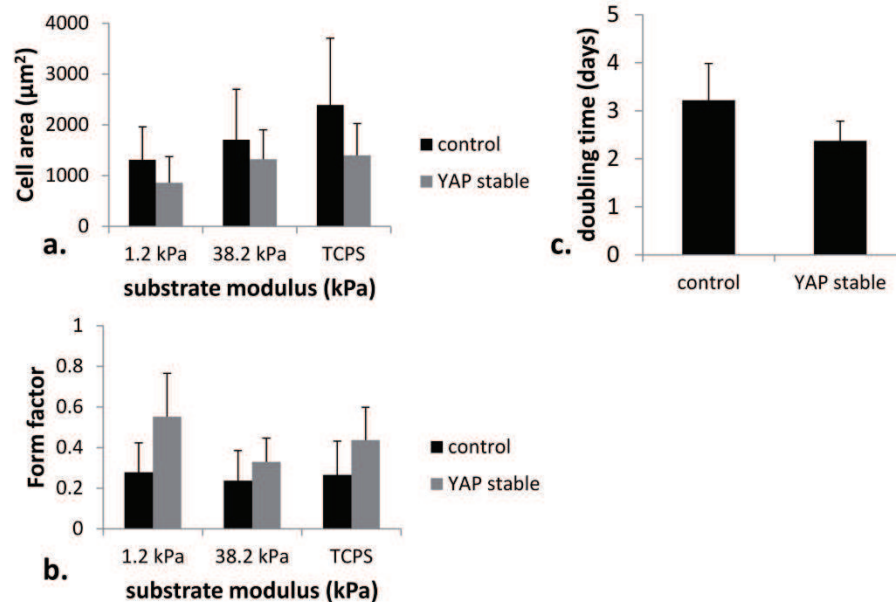


Figure 5.8: Constitutively active YAP interferes with mechanosensing. a) Control cells and VICs expressing constitutively active nuclear YAP were grown on PA gels of two moduli as well as TCPS. Control VICs increased spread area with increased substrate modulus; however, YAP constitutively active cells appeared unable to sense substrate compliance as area did not increase with substrate stiffness. b) Form factor, a measure of the number of cellular extensions, was larger for YAP stable cells, indicating a more rounded morphology. The smaller the form factor, the greater the number of cellular extensions. c) Although nuclear YAP allows for cellular proliferation, control cells and constitutively active YAP cells had similar rates of proliferation.

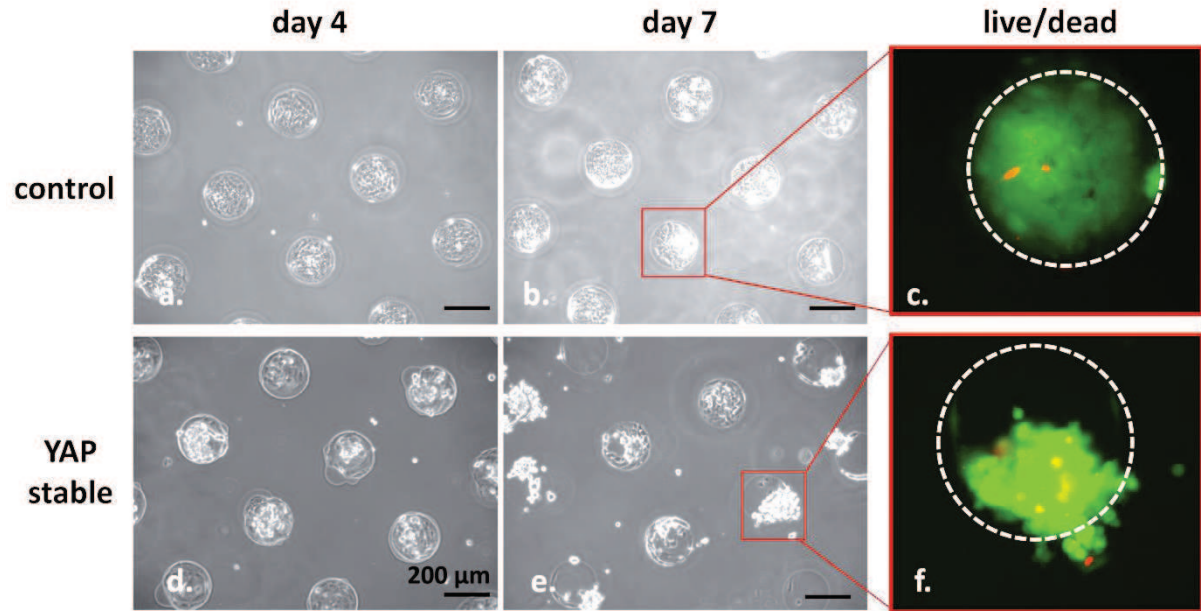


Figure 5.9: Constitutively active results in over-proliferation in micro-contact printed patterns. a) and b) Phase images for control cells at day 4 and day 7. c) Live (green)/dead (red) showing cell death primarily localized to central region of aggregate. White outline indicates edge of aggregate. d) and e) Phase images for YAP constitutively active cells days 4 and 7 in culture. f) Live/dead image of constitutively active YAP cells. Notice that even though cells are rounded, and many are apparently no longer bound to the surface, there is surprisingly little ethidium homodimer-1 staining, indicating that these cells still have an intact plasma membrane. No calcifications were observed in cultures with constitutively active YAP expression.

5.3.5 α -SMA actin intensity correlates with high stress, as predicted by FEA model

As a second qualitative measure of tension, α -SMA actin intensity distribution was assessed in aggregates of increasing diameters. Images of several aggregates (indicated in Figure 5.10) were “stacked” and the mean pixel intensity at each location was used to create the final α -SMA actin intensity heat map. In aggregates of all sizes, α -SMA was most strongly expressed in peripheral cells. The distribution of α -SMA intensity was then compared to predicted stress distributions by finite element model of contraction. As shown in Figure 5.10, α -SMA actin intensity correlated well with areas of high stress predicted by the models.

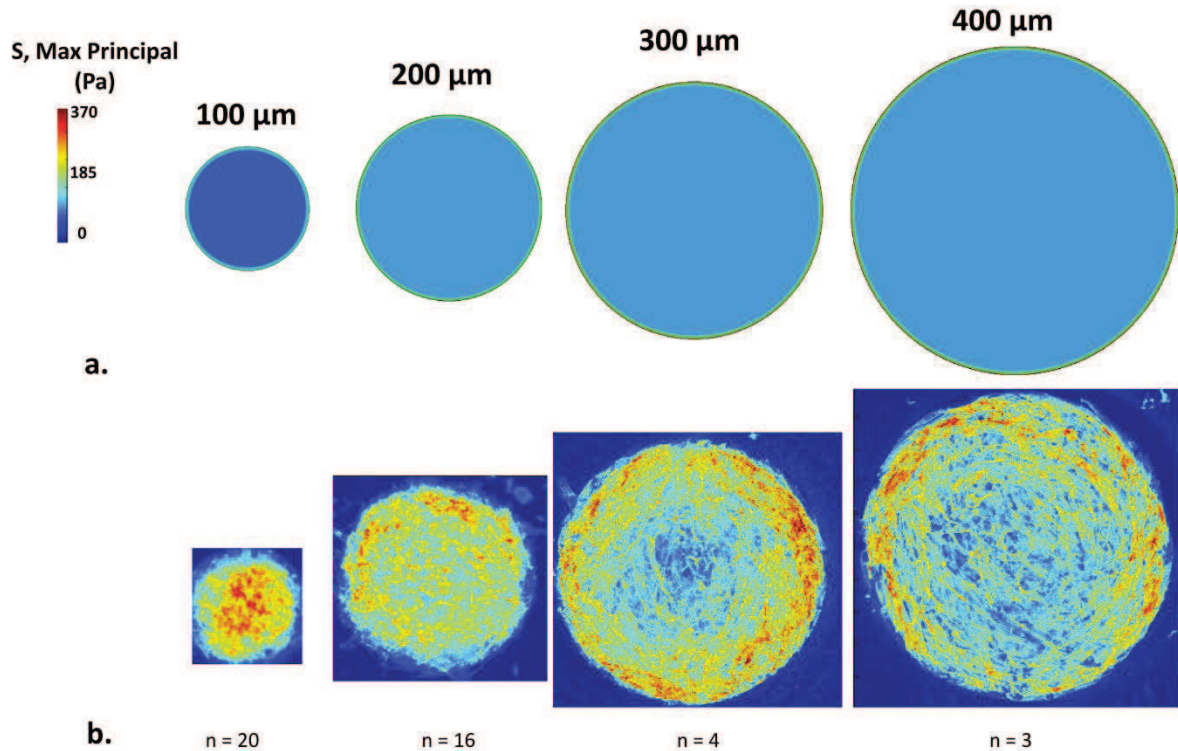


Figure 5.10: α -SMA intensity correlates well with Max Principal Stress predicted by pre-strain model. a) Von Mises stress on substrate for thermal cooling model of contractility predicted for aggregates of increasing diameter. Modeling courtesy of Sina Askarinejad, Rahbar Lab, Worcester Polytechnic Institute. b) Heat maps of α -SMA intensity within aggregates of increasing diameter. Mean intensity value for each pixel location displayed in heat map. N indicates the number of aggregates which were analyzed to create heat map shown. Notice that intensity correlates reasonably well with Von Mises stress, suggesting that although simplistic, the thermal cooling model is adequate at predicting mechanical environment within the aggregate.

5.3.6 Finite element model predicts distribution of tension varies with geometry

Next, after becoming fairly confident in the tension distribution of circular aggregates, we sought to modulate the distribution of tension, to determine if caspase and calcium staining correlated with areas of low tension. In Figure 5.11, the finite element predictions of maximum principal stress are shown. The tension distribution changes with geometry, although the areas of low tension remain in the center of the shape.

5.3.7 Caspase activity occurs in areas of low tension

Caspase and calcification activity in aggregates whose shapes had been modulated to control the tension distribution was assessed. We predicted that areas of low tension would have higher caspase activity and is where calcification would occur. Aggregate area was held constant, but ellipses of increasing elongation were created. Using a caspase 3/7 detection reagent, apoptotic activity was monitored with time. Figure 5.11 shows representative phase/caspase overlay images from aggregates of each geometry. As seen in the figure, caspase activity occurs within the center of the shape. This activity also correlates nicely with areas of lowest tension within the geometry as predicted by finite element model of contraction.

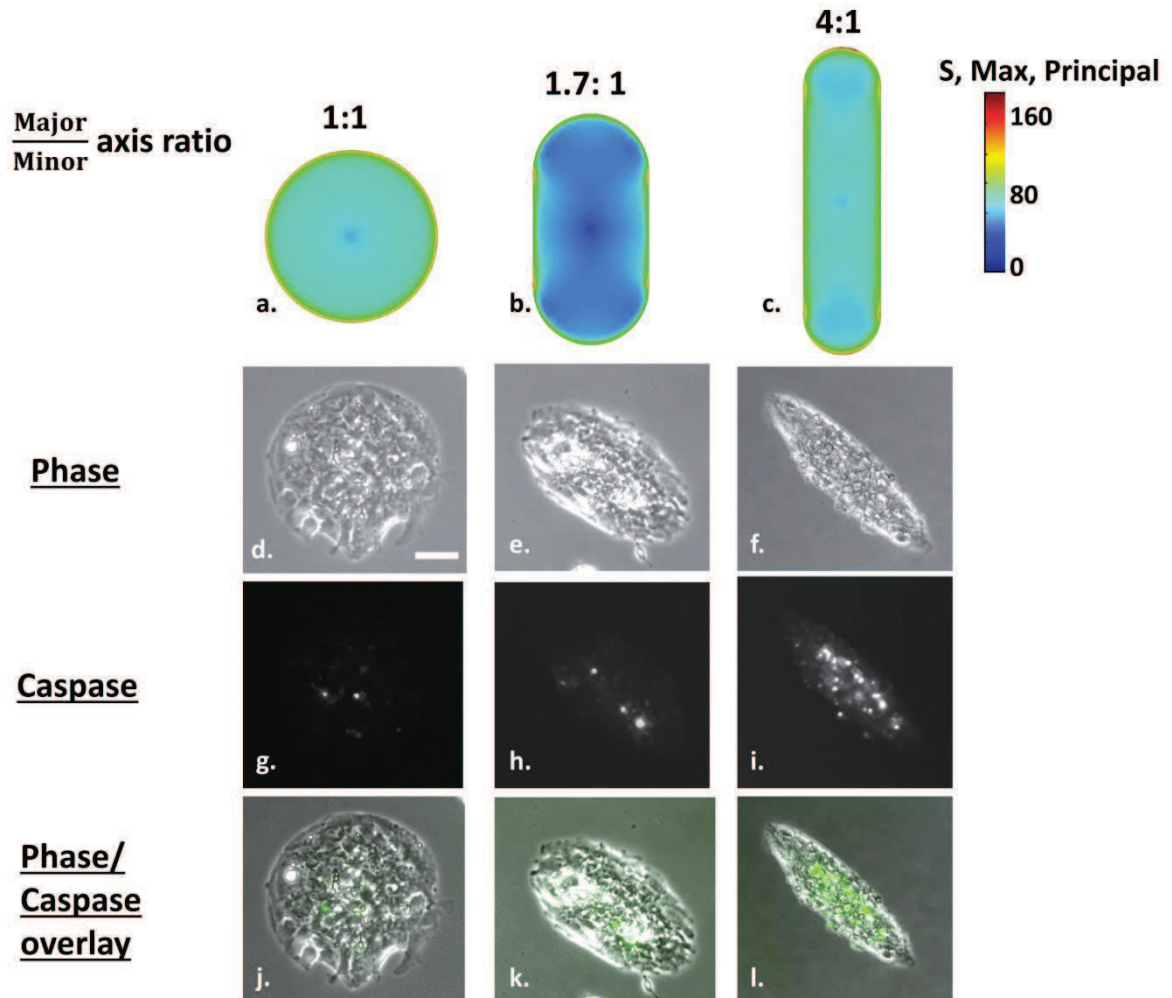


Figure 5.11: Caspase activity occurs most frequently in areas of low tension, as predicted by finite element model of contraction, regardless of shape. (a-c) FE model of contraction for different geometries. Low area of tension within the VIC aggregate appears in the center. (d-f) Phase images of aggregates created in different geometries on 40 kPa PA gel. (a) represents control 200 μm diameter circular aggregates used in other experimental studies in chapter 4. (g-i) Caspase activity in aggregates of increasing elongation. (j-l) Green pseudo-color shows areas of apoptotic activity in phase/caspase overlay in. Caspase activity occurs most prominently in areas of low tension in the center of the shape as predicted by the FE model. Scale bar = 50 μm .

5.3.8 Application of mechanical force reduced apoptosis and incorporation of α -SMA into stress fibers

Lastly, the tension in the center of the aggregate was increased via application of force to determine if the mechanical stimulation was sufficient for a reduction in apoptosis. Collagen coated magnetic microbeads were placed on the center of the aggregates and a magnetic field was applied, creating an upward force (Figure 1) on the beads. Control aggregates were cultured in the presence of a magnetic field without microbeads. In addition, a separate sample of aggregates was cultured with microbeads, but not within the field to determine the effect of microbeads alone.

Culture in the presence of microbeads was enough to reduce the apoptotic activity (Figure 5.13); however, the strongest effect of apoptotic reduction was seen when the aggregates were cultured within a magnetic field and the ligand coated beads were applying an upward force. The combination of microbeads and magnet had a profound effect on α -SMA expression within the aggregates. The contractile protein α -SMA gives a strong indication of phenotypic state in fibroblastic cells. When α -SMA is incorporated into stress fibers, as seen by the orange color in control aggregates (Figure 5.12), cells are considered myofibroblastic. However, the combination of microbeads and magnet resulted in mainly cystolic α -SMA expression in aggregates where force was applied. The effect of microbeads alone on α -SMA was not as apparent with some aggregates maintaining filamentous actin, while others had mainly cystolic α -SMA actin. Interestingly, although the microbeads were placed mainly in the center of the aggregates, the cystolic α -SMA was found throughout the aggregates cultured with microbeads in the presence a magnet field. As both groups of aggregates cultured with microbeads saw a reduction in caspase activity, this would suggest that in addition to mechanical forces which may be influence apoptotic signals, ligand signaling may also play a role.

Finally, we sought to compare number of cells within each aggregate, to ensure that microbeads were not influencing attachment rates or proliferation. As shown in Figure 5.13b, number of cells attached within the three groups was not statistically different. Although, there was less apoptotic activity in groups with microbeads and microbeads and magnet, there appears to have not been an increase in proliferation.

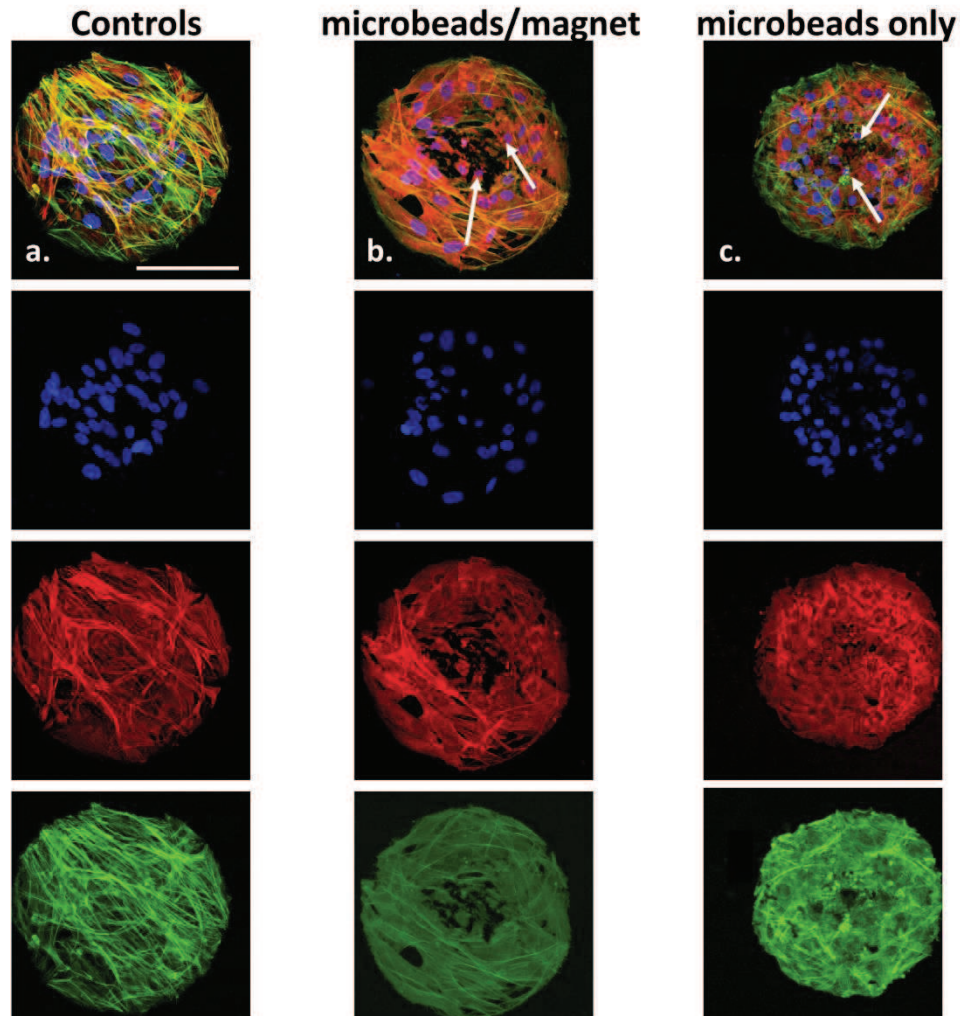


Figure 5.12: Presence of magnetic microbeads affects α -SMA incorporation into stress fibers. α -SMA (red), f-actin (green), nuclei (blue) *scale bar = 100 μ m* (a) Representative images of 200 μ m aggregates on 38.2 kPa PA gel without microbeads, cultured in the presence of a magnetic field for seven days. Notice orange hue where the α -SMA is incorporated into stress fibers. (b) Collagen-coated magnetic microbeads (white arrows) on aggregates cultured in the presence of a magnetic field for seven days. α -SMA is entirely cytosolic throughout the aggregate, indicating reversal of the myfibroblastic phenotype. (c) Aggregates cultured with magnetic microbeads, but without magnet. Effect of microbeads alone was not as strong as within presence of magnet with respect to cytosolic α -SMA. Some aggregates still did have α -SMA in stress fibers. Insets of each channel shown below main figure. *Scale bar = 100 μ m*

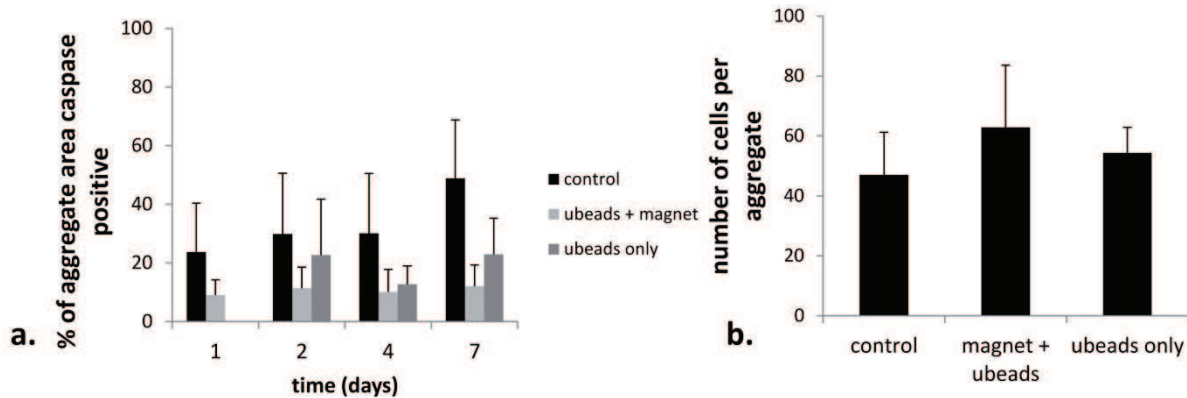


Figure 5.13: Presence of magnetic microbeads reduces caspase activity. a) Caspase 3/7 activity was reduced in the presence of μ beads as measured by % of aggregate area positive for caspase. Reduction was most prominent when magnetic force was applied. Control aggregates increased in apoptotic activity with time in culture while magnetic data presented as mean \pm sd. b) Cell number was not significantly between groups, suggesting that although magnetic force decreased apoptosis, it did not increase proliferation. Credit: Vivian Liang

5.4 Discussion

In this work, we proposed that differing mechanical environments between center and peripheral cells in VIC aggregates may be involved in disease initiation. For central cells, the decreased ability to maintain homeostatic tension would result in a mechanical cue to initiate programmed cell death (apoptosis). Preliminary biophysical analysis of VIC aggregates that had not been micro-contact printed suggested that VICs in the center cells are under lower tension than cells on the edge. This was further examined with the micro-contact printed aggregate model. Cell spread area was estimated for the two regions of the aggregate (center and edge) by measuring the aggregate area, superimposing a circle in ImageJ on the image that whose diameter was equal to the radius of the aggregate and counting cell nuclei within each respective region. Cell spread area was over two times greater in the edge cells than in the center cells. Although this is an indirect measure of tension, cells of increasing spread area are able to generate large amounts of cytoskeletal tension, as measured by traction force microscopy [82]. YAP nuclear localization, an indication of a high

tension environment, was not found within the central region of the aggregate and only underwent nuclear localization in peripheral cells. This was further confirmed with heat maps of α -SMA intensity staining. The contractile protein α -SMA was most strongly expressed in peripheral cells than central cells for all aggregates, regardless of size. The α -SMA intensity heat maps correlated well with a finite element model of contraction, suggesting that, although this model makes a number of assumptions, it does predict the mechanical environment within the aggregate. This model was then used to predict stress distributions of aggregates of varying polarization, yet controlled area. By altering the aggregate geometry, the stress distribution has been changed, although areas of lowest stress were still in the center of the shape. Next, we examined if location of apoptosis and calcification would follow the areas of low stress, as predicted by the model. Caspase activity was highest in the areas of low stress in agreement with the hypothesis. Lastly, tension distribution was modulated by applying magnetic microbeads to the aggregates and placing them within a magnetic field. The ligand-coated microbeads decreased apoptotic activity and this effect was most prominent within a magnetic field, although the beads themselves were moderately effective.

5.4.1 Distribution of tension

Tension has been shown to play a role in the aggregation process [16], as conditions of high tension, such as culture on stiff substrates, in the presence of TGF- β 1 [12], and increased Rho-pathway signaling [18] all increase aggregation. However, how the distribution of tension affects cellular behavior within VIC aggregates is not currently known. To date, no studies have examined the tension state within VIC aggregates themselves, nor attempted to quantify the different mechanical environments that may be created within the VIC aggregates. To be complete, atomic force microscopy measurements have been done on calcified nodules [95], as well as on individual VICs

and nuclei [76], but the hypothesis that there may be a distribution of tension which initiates disease onset is a novel concept.

The distribution of tension has been recognized for a decade as potentially instrumental in regulating cell behaviors in the developing embryo. Human beings and all organisms in the kingdom Animalia evolve from a single fertilized egg, called a zygote. The single-cell zygote then divides until it becomes approximately 32 cells large; this is termed the blastocyst. At the blastocyst stage, the tri-layer structure of the organism evolves (ie the endoderm, the mesoderm, and the ectoderm) with formation of the blastocyst cavity. Although embryology and organ development is still a very active area of research, it is believed that the endoderm becomes the endothelial lining of the digestive tract and associated glands, respiratory system, and bladder and urinary system while the mesoderm evolves into tissues which form the mesenchyme, mesothelium, and non-epithelial blood cells. It has become increasingly accepted that cells with widely different behaviors and lineage commitments must be controlled not only by cytokines but from the mechanical environment, as cytokines would not have the precision necessary to discern cells just microns apart [180].

Drosophila Melanogaster (common fruit fly) wing development is one of the more frequently used models for the study of morphogenesis, and many findings about the importance of mechanical state to organogenesis and development have been uncovered with this model. Using the principals of photoelasticity, Nienhaus et. al determined that there was different mechanical stress in various regions of the developing wing discs by measuring stress birefringence [181]. The differing mechanical environments have been shown to be essential for activating tissue patterning genes in *Drosophila Melanogaster* larva.

Distribution of tension has shown to affect a range of cellular behaviors in multicellular aggregates in two-dimension culture. Areas of high tension were shown to increase proliferation [123] and YAP

localization [124, 177]. Position within a multicellular aggregate has also been shown to affect stem cell lineage commitment. Vunjak-Novakovic and colleagues examined MSC differentiation on large (1000 μm) rings (200 μm inner diameter) and found that osteoblastic lineage commitment varied with location within the ring. This differentiation was primarily localized to regions where cell area was small yet cells still remained elongated (such as the inner edge of a ring and the regions next to the short edges of rectangles) [125]. The differentiation and proliferation activity observed was abolished with the use of cytoskeletal inhibitors, such as Blebbistatin and Y-27632. Together, these studies show the power of mechanical stresses in regulating multi-cellular behavior, and that cellular behavior within aggregates can vary due to the differences in mechanical stresses throughout the geometry.

Although this work focused on low-tension environments and induction of apoptosis, cell tension and apoptosis regulation, or dysregulation, can be seen in virtually all other disease states. For example, cancer is caused by the absence of cell death and Alzheimer's disease is the result of increased cell death. Although this statement is a great simplification, a recent study in Italy did show that these were somewhat related. In the elderly population, Alzheimer's patients had a much lower incidence of certain types of cancer, while cancer patients had a lower incidence of dementia [182]. The broad reaching goal of this work is to provide support for the concept that diseases should not be considered as simply a dysregulation of apoptosis, but that cell death or absence of it, is the result of something which happens earlier, and that is the result altered cell tension. We propose that development of future pharmaceuticals, be they small molecules, anti-bodies, etc., should focus on the modulation of cell tension in the appropriate "direction".

In addition to CAVD, altered cell tension state has been implicated in the progression of cancer. Atomic force microscopy has also shown cancer cells with decreased stiffness (decreased cell

tension) to have increased metastatic potential [183, 184]. In addition, decreasing the cell tension with myosin-II inhibitor resulted in an increase in invasion capabilities [183]. Cancer cells appear unable to sense substrate rigidity as they do not alter cell area like healthy cells [33]. 3-D growth of cancer cells in tumor spheroids within collagen gels shows high compressive stress experienced within the center of the spheroid inducing apoptosis and necrosis [185]. This growth is similar to what we observed in this 2-D micro-contact printed model, although our data should not be directly compared to 3-D data due to increased complexity of such data. Finally, compressive stress is interpreted differently between center and peripheral cells of the tumor spheroid suggesting that mechanical stress may effect signal transduction within multicellular systems.

Measurement of the tension states within multicellular systems is challenging. The most common forms of measuring cell tension, traction force microscopy, are unusable in these systems as it is impossible to assign bead/post displacement from which force values are calculated to a specific cell within the multicellular system. However, new computational methods, such as monolayer stress microscopy (MSM) have been used to study epithelial cell migration [186, 187]. Prior to MSM, cell stiffness measurements were used as cytoskeletal tension has been shown to be linearly correlated with cell traction force [78]. Additional surrogate measures by immunohistochemistry have also been used in the literature, such as YAP nuclear localization [124] and vinculin size [128]. In this chapter, we qualitatively examined differences in tension between the center and the peripheral cells by evaluating f-actin alignment, YAP localization, and α -SMA intensity. All immunohistochemistry analysis strongly indicates a lower tension environment within the center of the aggregate than is experienced by the cells along the periphery.

In this chapter, “tension” was used to mean the amount a cell is able to contract against the substrate. We postulated that cells in the center of the aggregate are not able to contract as much

as the cells on the periphery. All experimental evidence agrees with this hypothesis, but there are other aspects of the mechanical environment that may be causing the apoptosis in the center of the cell. These include loss of cell polarity (elongation) and exposure to an isotropic mechanical state. Cells in the center of the aggregate are denser than the cells on the periphery, resulting in both smaller spread area, and less elongated, cuboidal shaped cells. Cell polarity has been shown to be necessary for f-actin polymerization and stress fiber formation [188]. In 2D culture, VICs are highly polarized and elongated cells. As elongation correlates with increased traction force [107, 136], reducing polarity also decreases tension. Few studies have examined the role of anisotropic cell morphology and directionality of mechanical forces on apoptosis, future experiments could be designed to tease apart the overlap between cell tension and the lack of anisotropic cell morphology in central aggregate cells. Secondly, as shown with the Von Mises stress plots in Figures 5.7 and 5.8, cells within the center of the aggregate experience an isotropic stress state, while cells along the periphery of the aggregate have anisotropic stress states due to differences in radial and circumferential stress.

Myofibroblasts, identified by α -SMA positive stress fibers, are implicated in many pathologies affecting mankind such as asthma [189], idiopathic pulmonary fibrosis, hepatic cirrhosis, myelofibrosis, systemic sclerosis, Dupuytren's contracture, hypertrophic scars, aortic valve sclerosis and keloids [190]. It is important to understand that myofibroblasts are essential for many bodily functions required for organism survival such as proper wound closure, tissue maintenance and repair. Persistence of the myofibroblast phenotype is believed to be a critical for the onset and propagation of these fibroproliferative disorders; therefore, understanding factors which encourage fibroblast de-differentiation may prove beneficial to the aforementioned disease states. This mechanosensitive cell type has shown to revert to the fibroblast phenotype when substrate stiffness

was reduced [84], though reducing tension state, such as boundary release of a collagen gel have been shown to initiate apoptosis [99].

5.4.2 YAP in myofibroblastic differentiation

YAP is the downstream target of the Hippo pathway and is considered to be a mechanosensitive pathway. YAP localization has been shown to be indicative of tension state for cells on different substrates and in different density cultures [124]. YAP has been implicated in several cell types to drive myofibroblast activation [128, 191, 192]. Additionally, when YAP was excluded from the nucleus, cells had decreased tension levels [128], consistent with a fibroblast phenotype. We used recombinant cells which had YAP constitutively expressed to test the hypothesis that nuclear YAP would prevent apoptosis and calcification within the center of our micro-contact printed aggregates. Surprisingly, VICs that had constitutively active YAP were smaller than control cells. VICs in the myofibroblastic state have large spread areas (Chapter 3). Constitutively active YAP appeared to make the cells lack contact-inhibition. The micro-patterns “over-proliferated” and the cell clumps detached. Constitutively active YAP expression has been shown in mammary epithelial cells to confer tumorigenic phenotypes and partial resistance to the chemotherapy drug Paclitaxel [193]. Nuclear YAP is involved with MSC differentiation. Piccolo and colleagues were able to rescue MSC differentiation from adipogenic lineages (which predominates on soft substrates) to osteogenic lineage (which occur on stiff substrates) [194]. YAP localization was sufficient to “trick” cells in thinking they were on a mechanically stiff substrate. However, our constitutively active cell line appeared to be insensitive to substrate stiffness, and only slightly increased area when cultured on stiff substrates and did not have any changes in form factor as has been previously reported for control VICs [28].

5.4.3 Altering myofibroblast behavior with mechanical force

Collagen type I coated magnetic beads when placed near the center of the aggregates decreased apoptosis. This effect was significant when aggregates were in the presence of a magnetic field and beads provided an upward force, presumably increasing the tension on the central cells. The way in which a vertical (z-direction) force translates to a measurable increase in cell generated tension (in the x-y plane) can be visualized by considering a simple truss system. In a simple truss, if there is a load placed upon the structure, in the vertical direction, this will translate into an x and y component in reaction forces (depending upon the configuration of pins/rollers when considering statically determinant trusses). As a cell has a fibrous network (which can be analogous to truss members) and is connected to the substrate at discrete locations (analogous to pins), it is logical that a z-direction force, would cause in-plane reaction forces. Future work with this system could experimentally measure this increase in cell generated tension.

This technique was developed by McCulloch and colleagues and has been used to study α -SMA regulation in cardiac fibroblasts [195]. They found that static force application through collagen receptors reduces constitutive α -SMA mRNA and protein that is mediated by p38 [195]. Our findings of diffuse, cytoplasmic α -SMA when aggregates were cultured with microbeads under a magnetic field is in agreement with these results. Another very similar study using identical methods saw increased α -SMA expression in neo-natal cardiac fibroblasts that had been cultured on TCPS < 24 hours with applied load, but for cells that had been cultured for three days α -SMA was decreased by 32% [88]. This apparently paradoxical effect was dependent upon baseline α -SMA expression (fibroblasts take ~72 hours to incorporate α -SMA into their stress fibers) and appears to be mediated by the MAPK pathways. These findings suggest integrin signaling may play a role in disease progression and appears to be a promising avenue for future discovery. It also raises the possibility of a prospective treatment option for early stages of CAVD as micro-particles are in the

development stage for treatment of numerous diseases [196-198]. Future experiments to isolate the contributions of ligands to the prominent effect seen in α -SMA could involve using Concanavalin A (conA) which instead of binding to a ligand receptor, would bind to the glycosugars located on the cell membrane. This would separate the effect of the ligand from the local stiffness created by the 5 μm diameter microsphere. An additional interesting experiment would be if coating the beads with n-cadherin elicited the same effect. Research has shown that cells are capable of generating measurable forces, comparable to integrins, through n-cadherins [199]. Coating non-ferromagnetic microparticles, such as glass microbeads, would ensure that the α -SMA response is not material specific. Finally, evaluation of α -SMA when using anti-n-cadherin molecules in combination with integrin coated microbeads would determine the contribution of n-cadherin molecules to the cytosolic protein response.

5.4.4 Comparison of computational model and experimental data

The computational finite element model of a VIC aggregate is based on a number of assumptions, including that the cells behave as isotropic, linear elastic, homogenous material with consistent modulus throughout. We know that this is a great simplification as magnetic bead twisting rheometry measurements have shown viscoelastic behavior of the cytoskeleton [79]; the cytoskeleton is not a homogenous material but a filamentous network. Additionally, atomic force microscopy force mapping measurements of cells in culture have shown a wide variety of different moduli in sub-regions of the cell depending upon if the atomic force microscopy probe was indenting over a stress fiber, the cell nucleus, or other organelles [200]. Our computational model predicted that for a circular aggregate, the central region would have a very low stress level of 0-40 Pa, the middle region would have upwards of 80 Pa, and the very edge of the aggregate would see the highest stress level of 160 Pa. Substrate stress beneath aggregates was measured in chapter 4. For aggregates cultured on the 40 kPa PA gel and of 200 μm diameter, the minimum stress values in

the center were comparable to what was predicted by the model of 0-40 kPa. However, higher stress regions along the aggregate periphery were one fold higher than what was predicted by the computational model, suggesting that VICs are capable of contracting (and therefore having a greater pre-strain value), then the stress fibers measured experimentally [179]. Myofibroblastic VICs have been shown to have minimal increase in contraction when potassium chloride was added to the media, suggesting these cells are generating maximum force [201]. Future iterations of the model could increase the pre-strain value computationally to get closer to the measured substrate stresses. However, the purpose of including the model in this work was not to measure VIC aggregate contraction but to simulate the distribution of tension within the aggregate. To determine the tension distribution, the exact magnitude of the parameters does not matter. As can be seen from our results, the model predicts increased tension (shown by an increase in maximum substrate stress in the bottom of the cell layer) which is in agreement of our experimental findings of high stress fiber alignment, incorporation of α -SMA into stress fibers along the aggregate periphery, and YAP localization to the nucleus in peripheral cells.

5.5 Conclusion

Differences in mechanical environments have been shown to affect proliferation and mesenchymal fate in micro-patterned systems. In this chapter, I provide evidence that there is a difference in the mechanical environment between the center of and edge of valvular interstitial cell aggregates.

Atomic force microscopy measurements of cell stiffness shows that low tension exists in the center of non-micro-contact printed aggregates. Spread area restriction, which is present in aggregate center, reduces the ability for VICs to generate tension. Examination of stress fiber alignment using 2-D FFTs shows that there is little to no alignment in center of the aggregates, for both non-micro-contact printed and micro-contact printed aggregates. Immunohistochemistry analysis of nuclear

YAP, an indication of high tension state shows the greatest localization in the aggregate periphery. α -SMA, which incorporates into stress fibers in high tension state, had highest expression along aggregate periphery. α -SMA expression correlated with areas of highest maximum principal stress as predicted by a finite element model. The finite element model was then used to examine stress distributions in aggregates of constant area, but changing geometry. Micro-contact printing of aggregates with constant area and increased elongation showed that apoptosis occurred most frequently in the areas of low tension, regardless of geometry. Finally, collagen coated magnetic microbeads were added to the aggregates to apply upward force when aggregates were placed in a magnetic field. This resulted in a visible reduction in α -SMA expression in stress fibers.

5.6 Acknowledgements

I would like to thank Dr. Nima Rahbar and Sina Askarinejad for assistance with the finite element modeling.

Chapter 6: Discussion, Limitations, and Future Work

The work presented herein examines two different aspects of mechanical regulation of valvular interstitial biology. The first aim focused on single valvular interstitial cell traction force response to cyclic stretch, and the second validated a novel *in vitro* disease model for calcific aortic valvular disease and the effects of the distribution of tension within the aggregate on disease initiation and progression. Both aspects of VIC biology, how single cells regulate their tension and phenotype in dynamic environments and the different mechanical environments within cell aggregates and respective VIC behavior provide valued information which is useful to understanding calcific aortic valvular disease initiation and progression.

6.1.1 Study objectives Aim 1

Aim 1 consisted of validating a method for long-term stretch of VICs on hydrogels of tunable modulus and evaluating the traction force response to stretch as it varied with cell pre-stress.

Prior to this work, valvular interstitial cell traction force response to cyclic stretch was only inferred from measurement of cell area [28]. A number of technical challenges made completion of these experiments difficult. The first is that polyacrylamide does not bind well to silicone materials. The protocol that was developed by Quinlan et al. is enormously finicky and is extraordinarily challenging for attaching soft polyacrylamide gel formulations. The second was that Flexcell™ plates, the commercially available system for stretching cells, were completely unsuitable for traction force measurements. Lubrication applied to bottom of Flexcell™ plates to allow for the membrane to slide easily across the vacuum posts (necessary for stretching the membrane) is not easily removed, making obtaining clear images necessary for traction force microscopy impossible. In addition, the Flexcell™ plate membrane is quite thick; for inverted scopes, such as the Zeiss, the working distance of objectives represents a limitation to data acquisition. To circumvent these challenges, a custom

cell culture well (with <150 μm thick bottom membrane), custom cell stretch device, and graphical user interface were created. The strain field of the well was validated to ensure homogenous strain in the area where traction force images would be taken (center of the well). The creation of these custom wells also was unique and innovative as the bottom membrane is cast at the same time as the rest of the well, ensuring the bottom membrane is perfectly taunt, enabling correct strain transfer as well as clear imaging.

VICs have been shown to be sensitive to substrate stiffness, altering their shape, area, and α -SMA incorporation into stress fibers depending on the substrate modulus [28, 80, 81, 84]. I have shown that VIC response to stretch is dependent upon initial prestress condition. Under conditions of high prestress, VICs decrease their cell area, traction force, contractile moment and maximum substrate stress in response to long-term cyclic stretch. Increasing cell tension with differentiation to the myofibroblast phenotype by culture in the presence of TGF- β 1 did not prevent this response. Although it did increase cell traction force for statically cultured cells compared to static VICs untreated with TGF- β 1, the same decrease in traction force, cell area, contractile moment and maximum substrate stress was observed. This has strong implications for regulation of the myofibroblast phenotype. VICs readily activate in culture from quiescent fibroblast-like cells to the highly contractile, synthetic myofibroblast phenotype. This phenotype is advantageous for remodeling during injury, but too high a population of valve myofibroblasts have been implicated in calcific aortic valvular disease; in addition, presence of too high a population of myofibroblasts has hampered the creation of successful tissue engineered heart valves (TEHV) as high residual stress in novo tissues causes retraction during implantation and renders the valve unsuitable due to the backflow of blood from the aorta to the left ventricle. Reversal of the myofibroblast phenotype with stretch has been reported for lung myofibroblasts [26]. Although α -SMA incorporation into stress fibers has been correlated with increased traction force [66], we did not directly evaluate α -SMA

expression in these experiments. Our results from traction force data indicate that myofibroblast phenotype in VICs may be reversible if cultured in the presence of dynamic stretch, but further experimentation needs to be conducted to confirm this finding.

The second major finding from our first aim is that cells with low cell prestress increase their traction force in response to mechanical stretch. A low prestress state was accomplished to ways, via chemically inhibiting myosin-II motors as well as mechanically by culturing on a low-modulus substrate. Myosin motor inhibition has been shown to decrease traction force in stem cells [127], as well as rapidly decrease VIC traction force within 20 minutes (data not published). Blebbistatin treated cells trended to increase cell traction force, contractile moment, and cell area with stretch, although this was not significant. VICs cultured on soft (0.6 kPa) gels had a rounded morphology, in agreement with earlier studies [28], but when stretched, elongated, increased in cell spread area, traction force, maximum substrate stress, and contractile moment. Although the traction force for cells cyclically stretched on soft substrates was three-fold lower than the traction force for stiff controls, these cells were still able to reorient.

In addition to looking at overall cell traction force, we also calculated traction moment as defined in [202], which is the combination of traction forces weighted by their corresponding x and y coordinates. As defined, a cell contractile moment will be negative if the cell is contracting inward (pulling towards itself) and positive if the cell is pushing outward (away from the cell body). Cell traction moment, unlike cell traction force, is not an absolute value magnitude. This is advantageous because the signage provides valuable information about the cell contraction state that is lost with only a cell traction force calculation. Although most studies to date report inward pulling forces as well as negative contractile moment, Sheetz and colleagues reported negative forces on micro-posts (micro-posts that are being pushed away from the cell) for cells that were stretched on very soft

substrates [29] possibly indicating growth of the cell outward as increased cell area has been observed for cells on very soft substrates [28, 29]. Interestingly, we observed positive contractile moments for half of the control cells that had been treated with Blebbistatin, all of the stretched cells that had been treated with Blebbistatin and stretched cells on soft, indicating outward displacements of the cell. To our knowledge, this is the first time cell traction force has been measured for cells treated with Blebbistatin and that a positive contractile moment and outward displacements have been observed. A possible explanation for the outward displacement with Blebbistatin treatment is that the myosin II motors become inhibited with Blebbistatin and cannot contract against the actin filaments which continue to polymerize outward.

As the reorientation response observed on very low modulus materials conflicts with current findings of reorientation on soft collagen gels with short-term stretch [30], the experiment was repeated with an additional cell type, U2OS, a human osteosarcoma cell line. At 12 hours, osteosarcoma cells were reoriented in the direction perpendicular to stretch, consistent with our findings in VICs. Combined, our studies of soft and stiff substrates support the theory of “homostatic tension set-point” for cells and that this tension set-point varies with the mechanical environment. To date, there are no models which can accurately predict all of the observed cellular behaviors from our experiments and we hope our data can aide in the creation of more complete mathematical and phenomenological models of cell tension with dynamic stimulation as well as cell reorientation.

6.1.2 Study objectives Aim 2

Study objectives of this aim were two-fold: first, we validated a reliable and repeatable method for creating high-content *in vitro* assay for the study of dystrophic mechanisms in calcific aortic valve disease, and the second, to use this model to test the hypothesis that low tension within the

aggregate center initiates apoptosis. Dystrophic calcification is characterized by presence of the myofibroblastic phenotype, cell death, and calcification. α -SMA positive stress fibers were used to determine presence of the myofibroblastic phenotype. α -SMA, when incorporated into stress fibers, is indicative of a highly contractile, high tension cell-type.

To ensure that cell death was present, we stained aggregates with ethidium homodimer-1 to evaluate plasma membrane integrity. Cells that are considered “dead” uptake the dye and appear red under a fluorescent microscope. To evaluate type of cell death, we added caspase3/7 live detection reagent. This reagent was advantageous because it was relatively non-toxic to cells and allowed evaluation of caspase signal over multiple time-points and also allowed us to record location within the aggregate that positive staining occurred. In addition, to confirm the mechanism of cell death was indeed apoptosis, we cultured a subset of samples with Z-VAD-FMK. This reagent is a pan-caspase inhibitor and would interfere with caspase 3/7 effector signaling and prevent apoptosis. Culture with Z-VAD-FMK resulted in a profound decrease in calcification, suggesting the mechanism of cell death was indeed apoptosis.

Finally, to confirm that the micro-contact printing model was indeed an accurate representation of dystrophic calcification, mineralization was evaluated. Micro-contact printed aggregates were seen several times to have apparent calcifications within two days of culture, but as Alizarin Red S is a terminal stain, it was assessed at day seven for all model validation trials. At one week, aggregates were assessed for calcification via positive red staining due to Alazarin Red S binding to free calcium ions. The micro-contact printing model worked with high fidelity, on average 67% of aggregates stained positive for Alizarin Red at one week. To further investigate the type of calcification seen in the aggregates, SEM and X-ray microanalysis was used. Calcium was found in the center of

aggregates, mainly in the form of calcium oxide. The calcium was found in two forms: within mineralized nanoparticles and what appears to be apoptosing cells, as discussed in 6.2.4.

After validation of the model, we were able to form the aggregates with high fidelity to allow for analysis of stress distribution within cell aggregates and the role low tension environments play on apoptosis. We hypothesized that VICs were undergoing apoptosis within the center of the aggregate as the central region of the aggregate is a low tension environment and cells are no longer able to maintain homeostatic tension. VICs are considered a fibroblastic-like cell, and are capable of differentiating into myofibroblasts in conditions of high tension. The first work to show that mechanical environments are capable of affecting myofibroblastic fate was done in 3D collagen gels by Grinnell and colleagues [99]. The release of boundaries around the 3D collagen gel model triggered apoptosis in these cells. Chen and colleagues have shown that when cells are not able to maintain tension via spread area restriction, incidence of apoptosis increases [136]. We first confirmed that tension distribution may vary within valvular interstitial aggregates that were not micro-contact printed. This was done first by biophysical analysis of VICs. VICs on cultured on stiff substrates (a higher tension environment) had increasing stiffness and increasing traction force. The relationship between traction force and stiffness appeared to be linearly dependent. The same relationship between stiffness and cell traction force was found by Stamenovic and colleagues between tension, termed cell prestress in the study, and stiffness as measured by magnetic bead twisting rheometry [78]. These findings suggest that cell stiffness is a reasonable estimation of the tension state of the cell. AFM analysis on five aggregates revealed there is a distribution of tension within the aggregates; the center of the aggregate was less stiff than the peripheral cells, implying a state of lower tension. To confirm cells that were restricted from spreading, such as those within the center of the aggregate, micro-contact printing was used to restrict spread area to a $40\phi\ \mu\text{m}$ collagen

island and traction force was measured. Spread area restriction greatly decreased the ability of cells to generate tension.

As currently quantitative measures of tension within cell aggregates are challenging and rely on a number of assumptions, we sought to qualitatively evaluate the differing mechanical environments using immunohistochemistry. Three parameters were considered: Stress fiber alignment, YAP nuclear localization and α -SMA intensity. As an estimate of differences in tension between the center and the edge of aggregates, stress fibers alignment was analyzed using two-dimensional fast-fourier transform on select regions of the aggregate. It was found that the center of the aggregates, for both non- μ contact printed and μ contact printed aggregates was highly random, and there was no preferred directionality for stress fiber alignment. In contrast, both aggregates saw more fiber alignment along the periphery. As stress fibers carry tension along their length, an estimation of tension state can be gleaned from alignment. YAP nuclear localization was found to occur when cells were under high tension environments, such as in sparse culture and on stiff hydrogels while cytosolic YAP was found in low tension environments, such as on soft substrates or in dense monolayers [124]. In our aggregates, YAP nuclear localization was mainly confined to cells along the aggregate periphery, indicating a higher tension environment between the center and the edge. We further probed this finding with the average α -SMA intensity for aggregates of increasing size and compared these heat maps with maximum principal stresses predicted by the finite element model of contraction. The average α -SMA intensity was greatest along the periphery of the aggregate. This distinction in α -SMA intensities was more noticeable as the average size of the aggregate increased. The correlation between α -SMA intensity and maximum principal stress suggested that although a number of assumptions had been made, such as assuming the cells behave as a linear, elastic, isotropic material, the finite element model of contraction did adequately predict the stress state within the aggregates.

The finite element model was then used to predict maximum principal stresses for aggregates of increasingly elongated geometries but constant area. The model predicted that areas of low tension would remain in the center of the shape, but that the distribution of tension changes with the geometry. Micro-contact printed stamps were then designed to allow for aggregates to be created with constant area, but with ellipses of increasing linearity to determine if caspase and calcification activity would follow areas of low tension within the aggregate. Caspase activity was found to occur with highest frequency in areas of low tension (visual observation), supporting our hypothesis that the pathology initiates as cells undergo apoptosis as they are no longer able to hold their homeostatic tension.

As a final method for testing our hypothesis, we mechanically modulated the tension distribution by applying ligand-coated ferromagnetic beads to the center of the aggregates and applying an upward force by placing the aggregates within the magnetic field. The application of magnetic beads markedly reduced caspase activity, suggesting that apoptosis was prevented with this mechanical stimulation. Not only did this upward force reduce caspase activity; there was a profound effect on α -SMA expression. α -SMA became noticeably cystolic with the combination of microbeads and the magnetic field. Microbeads alone were able to decrease the caspase activity as well; however, the effect was not as noticeable. Although apoptosis was reduced, proliferation was not increased as the number of cells counted within aggregates of each category was not noticeably different.

Although not a main focus of aim two, VICs were genetically engineered to constitutively express nuclear YAP to determine if nuclear YAP was sufficient to prevent apoptosis. Culture of these constitutively active YAP cells on differing substrates of polyacrylamide gels, showed little area change, suggesting that constitutively active YAP in VICs interferes with mechanosensing, as spread area remained unchanged. Proliferation rates were not affected between constitutively active YAP

and controls. However, nuclear YAP did not reduce apoptosis in our *in vitro* model. Cells instead appeared to lack contact inhibition, creating over populated “cell clumps” which had poor adhesion to the substrate.

In summary, the objectives of aim two were met by 1) validating a reproducible, high-fidelity model for dystrophic calcification and 2) using this model to provide evidence in support of the hypothesis that a low tension environment induces apoptosis within the VIC aggregates.

6.2.1 Study limitations and future work: Aim 1

The major limitation of aim 1 was that individual cells were not tracked over time with stretch and the reported values are of a population average and not of a single cell before/after stretch. To my knowledge this has not been done and the work of aim 1 is the first study to date to have measured traction force after long-term cyclic stretch. However, as individual cells were not tracked, conclusions cannot be made about changes the pre- and post- stretch traction levels, magnitudes of maximum substrate stress, and cell area, etc. The way the stretch system was designed currently makes it impossible to track an individual cell over time and future work should focus on redesigning the system to allow for stretch about a central point which can remain in view of a microscope for the duration of the stretch cycle. The device as is, has four motors which stretch the custom well from one fixed corner either uniaxially or biaxially, the cells within the field of view of the microscope when the well is in the relaxed state, slide out of view when the well is stretched. This makes tracking the same few cells overtime with stretch extremely difficult.

For designing future experiments, smaller time increments would yield a great deal of information about how cells undergo reorientation, especially on soft substrates where the cells must first elongate from a rounded morphology and to undergo reorientation. It seems logical that a cell that is rounded an unable to generate enough cytoskeletal tension to spread would first elongate in the

direction of stretch as it is capable of generating tension against the stretch, as was found by Kaunas and colleagues [30]. However, if these cells are capable of orientation, and do reorient towards the angle of zero strain as others have reported [156], how is it possible that these cells on soft substrates are able to maintain their cell spread area, and elongation if the membrane is essentially static in this direction? This remains an open research question and whose answer will provide a unique view of cell mechanosensing.

To further understand the regulation of the VIC myofibroblast phenotype future experiments should assess α -SMA incorporation into the f-actin stress fibers and extracellular matrix protein synthesis in conjunction with traction force activity of the cells. As mentioned previously, stretch has shown to reverse the myofibroblast phenotype for lung myofibroblastic cells [26]. However, how stretch impacts the VIC myofibroblast phenotype is still not well understood. Several studies have suggested that mechanical stimulation with stretch induce a disease phenotype in this cell type. Merryman and colleagues use stretch, in conjunction with TGF- β 1, to induce aggregation for studying dystrophic calcification. Others have reported increased collagen production, an indication of the myofibroblastic phenotype, that is dependent on strain and production of calcium micro-particles with stretch. However, as VICs are naturally in a highly dynamic environment in the heart valve, it seems somewhat skeptical that stretch of just a few hours can cause disease and is an adequate representation of a physiologically relevant phenotype.

Finally, this study was done on a two dimensional surface while the cells in the native heart valve are in a three-dimensional environment. Cells behave much differently in three dimensions than in two dimensions. For example, cell spreading in three dimensions is not merely the result of substrate stiffness, but density of extracellular matrix. In poly(ethylene glycol) (PEG), hyaluronic acid, and methacrylated gelatin hydrogels, cell spreading and α SMA staining are more intense in the most

compliant gels which have the lowest monomer concentration [203, 204]. In addition to space availability in the ECM, increasing integrin binding sites by adding exogenous RGD peptides increases VICs ability to spread and form stress fibers [205]. However, traction force microscopy in three-dimensional matrices is more complex. Mainly, the protein gels frequently used in three-dimensional culture such as fibrin and collagen, unlike polyacrylamide gels, are non-linear and allow for force-transmission at much greater distances [206]. In addition, solving finite element equations with nonlinear materials is much more complex as the material modulus (hence the calculated traction force values) varies with the loading conditions. Despite these challenges, understanding how valvular interstitial cells regulate tension in three-dimensional protein gels is the most clinically relevant and would have valuable applications for creating *de novo* tissue engineered heart valves.

6.2.2 Study limitations and future work: Aim 2

6.2.2.1 Cell type

Porcine aortic VICs were used instead of human VICs. Healthy human valves are extraordinarily difficult to obtain, and the only tissue samples that are available are valves that had been removed because of pathology. Often studies that utilize human VICs do so from healthy portions of a diseased valve. Due to the difficulties in obtaining human tissues, and the likely variability of using diseased cells from different patients, we sought to identify a cell type from a comparable species which would give us similar yet consistent results. Porcine cells have been used in a multitude of studies with the *in vitro* CAVD model [12, 17, 18, 97, 175]. In contrast to the difficulties in obtaining human tissue, porcine hearts are readily available from control animals for other experiments or can be obtained through a slaughterhouse. The similarities of pig and human hearts have been explored with respect to pigs becoming transgenic donors to humans [207, 208]. However, there are

important differences between the species with respect to how the heart sits in the body cavity. Pigs have a classical valentine heart shape while the human heart has a trapezoidal frontal projection. Humans are bipedal while pigs are quadrupedal; with gravity playing an important role in the evolution of each species cardiovascular system.

Both human and porcine aortic valves have a trilaminar structure, consisting of the ventricularis, spongiosa, and fibrosa. However there are small differences between aortic valve anatomy of humans and pigs. The length of the free edge of the aortic valve leaflets are shorter in pigs than in humans [209]. The percent of circumference contribution by each leaflet is also different between species. For humans, it is the non-coronary cusp which contributes the most to valvular circumference, while for pigs it is the right coronary cusp [209]. Finally, humans have less myocardial support of the aortic valve. For humans 43% of the valve has muscle attachment while in pigs it is larger at 56% [209]. The differences in geometry, as well as differences in the overall heart orientation within the body cavity, and the differences in human and pig stance, means that the blood flow through the aorta's of the different species' hearts is not identical and the mechanical environment that each valvular interstitial cell population experiences will likely be different. Certainly, prior to proceeding with using this model as an *in vitro* drug screen for development of targeted therapies to treat CAVD, experiments with human valves to ensure they have the same calcification response on micro-contact printed geometries is absolutely warranted. Porcine VICs do; however, have a number of similarities with human VICs which makes them a suitable experimental cell type. The blood pressures of pigs is similar to humans, but slightly higher (145/105 systolic/diastolic and 120/80 respectively). They have a similar heart rate (100 bpm, average healthy human has 60 bpm) and a comparable cardiac output to humans.

6.2.2.2 Measurement of protein transfer

Integrin density has been shown to affect VIC aggregation potential on rigid materials [9], as well as cell spreading response on compliant hydrogels [210]. However, in these studies we did not measure the protein density which adhered to the hydrogel and assumed 100% transfer from the stamp to the polyacrylamide. As protein has been shown to adhere differently to polyacrylamide gels depending upon composition (and therefore stiffness) [210], it's possible that different stiffness gels tested in these experiments had different amounts of protein coatings and ligand density. The effect of ligand density might be more crucial to determine in non-microcontact printed cells aggregation will occur rather than if apoptosis and calcification will occur once the cells have aggregated. In contrast to the current model of just seeding cells on TCPS, in our system aggregation has already occurred and is simulated by the restriction of cells on micro-contact printed protein islands. Apoptosis and calcification were observed on all stiffness tested; although, the rate of calcification was slightly less on 9.6 kPa gels. This difference could potentially be from different attachment propensities on softer materials or perhaps a different ligand density.

6.2.2.3 Role of integrin signaling

VIC aggregation response as well as response to statins has been shown to be dependent upon protein coatings in experiment on TCPS, highlighting the importance of integrin signaling in disease initiation [9, 175, 211]. Collagen and fibronectin coated polystyrene were shown to be preventative against aggregation while fibrin appears to enhance the aggregation process [9]. In these studies, I only used collagen type I for both aim one and two to coat the polyacrylamide gel in addition to micro-contact printing purposes. Collagen type I is found in the native valve [212, 213], and as such was a logical choice for these experiments. Integrins $\alpha 1\beta 1$ and $\alpha 2\beta 1$ bind to monomeric collagen. It remains an open research question if fibrin or another protein could create a faster and more robust calcification response.

An additional finding of note was that collagen type I coated magnetic beads when placed near the center of the aggregates actually decreased apoptosis. This effect was significant when aggregates were in the presence of a magnetic field and beads provided an upward force, presumably increasing the tension on the central cells. This technique was developed by McCulloch and colleagues and has been used to study α -SMA regulation in cardiac fibroblasts [195]. They found that static force application through collagen receptors reduces constitutive α -SMA mRNA and protein that is mediated by p38 [195]. Our findings of diffuse, cytoplasmic α -SMA when aggregates were cultured with microbeads under a magnetic field is in agreement with these results. Another very similar study using identical methods saw increased α -SMA expression in neo-natal cardiac fibroblasts that had been cultured on TCPS < 24 hours with applied load, but for cells that had been cultured for three days α -SMA was decreased by 32% [88]. This apparently paradoxical effect was dependent upon baseline α -SMA expression (fibroblasts take ~72 hours to incorporate α -SMA into their stress fibers) and appears to be mediated by the MAPK pathways. These findings suggest integrin signaling may play a role in disease progression and appears to be a promising avenue for future discovery. It also raises the possibility of a prospective treatment option for early stages of CAVD as micro-particles are in the development stage for treatment of numerous diseases [196-198].

6.2.2.4 Protein coating

As mentioned above, the protein coating is critical to VIC aggregation and calcification response with culture on TCPS [9]. Additionally, efficacy of statins in preventing aggregation and calcification was dependent upon the type of coating [20]. Combined, these results suggest the importance of the extracellular matrix and integrin signaling in the disease pathology. In this study, we used collagen type I for all of the micro-contact printing as it is one of the major component proteins of the native heart valve. Although collagen was reported in earlier literature to be “protective” against

calcification [9], VIC aggregates that formed on our micro-patterned geometries exhibited apoptotic activity and calcification. This suggests that protein coating may be more important to cue the “aggregation” step, but once the cells have aggregated, apoptosis and calcification proceed regardless of integrin signaling. To test the hypothesis that apoptosis and calcification will occur regardless of type of ligand signalling, future work should involve micro-contact printing of other protein types, including fibronectin and fibrin.

6.2.2.5 Importance of cell-cell contacts

Cadherins are a type of cell-to-cell contact. Cadherin expression is cell type specific, and it is possible that cadherin profiles are different between fibroblasts and myofibroblasts [63]. Cadherin-11 has been shown to be necessary for aggregation to occur and has been observed in diseased valves [97]. Within groups of cells, there appears to be an inter-play between cadherin and integrin expression. Cells within the center of the aggregate of cells have increased cell-cell force transfer compared to cell-integrin force transfer [214]. The blocking of cadherins “encourages” cells to bind to the substrate via integrins [214]. In our hypothesis, we postulate that the decrease in integrin binding within the central cells decreases cell tension, inducing apoptosis. Cells undergo apoptosis and the lipid membrane serves as a nucleation site for intracellular calcium. As these cells are bound to their neighbors via cadherins, they do not float away or are able to be cleared by the immune system and instead serve as nucleation sites for calcium.

6.2.2.6 Mechanisms initiating apoptosis: Role of YAP/TAZ

Increasingly, the physical and mechanical properties of the cellular microenvironment are being recognized as potent modulators of cell phenotype and fate. However, how these mechanical signals are sensed and converted into changes in gene expression has remained elusive and is the one of the “holy grails” of the field of mechanotransduction [177]. A potentially promising nuclear

transcription factor which cytoskeletal tension appears to control is YAP/TAZ. These nuclear transcription factors are the downstream effectors of the Hippo pathway, and have received much attention in the field on embryology as they are involved in organ development. YAP/TAZ nuclear localization results in different outcomes depending on cell type, and has been shown to be involved with proliferation and osteogenesis. Excitingly, it appears that cytoskeletal tension via actomyosin contractility can control YAP/TAZ localization, independent of the Hippo pathway [194]. Cytoskeletal regulation of YAP/TAZ appears independent of integrin signaling, the logical upstream molecule of a mechanically activated pathway. When spreading was artificially induced using poly-Lys-coated substrates (non-integrin binding), nuclear YAP/TAZ localization occurred [215] suggesting that the cytoskeletal tension itself is capable of YAP/TAZ regulation. In addition, cell spreading on micro-pillars supported YAP/TAZ nuclear localization, even though the ECM ligand contact area was reduced by about 90% [194]. Furthermore, it has been shown in mesenchymal stem cells that cytoskeletal to nuclear strain regulates YAP/TAZ translocation to the nucleus [127] and that a physical nuclear connection to the cytoskeleton via linker of nucleus and cytoskeleton (LINC) complexes, such as Nesprin-1, is required for YAP/TAZ translocation to occur [127]. Finally, TGF- β 1 has been shown to activate YAP which promotes nuclear localization and activity of Smad1 and Smad3 [216, 217]. In the nucleus YAP associates with transcription expression of genes such as connective tissue growth factor and the β 2 integrin [218].

The role of YAP/TAZ in our model is an interesting area for further research. Like others, we found that the central cells of the micro-contact printed aggregates exclude YAP from the nucleus [194], indicating that they are under lower tension. However, whether YAP exclusion itself is necessary and sufficient to induce apoptosis is not currently known, but would provide a mechanistic answer to how the apoptosis within the central cells initiates. To determine if YAP nuclear localization was sufficient to prevent apoptosis a cell line was created that had constitutively active YAP nuclear

expression. While these cells did not have proliferation rates significantly faster than the controls, these cells apparently lacked contact inhibition and continued to proliferate when constrained to protein circles. Cells appeared to float away, presumably undergoing apoptosis; however, these cells did not stain positive for makers of cell death. Piccolo and colleagues were able to rescue MSC differentiation from adipogenic lineages (which predominates on soft substrates) to osteogenic lineage (which occur on stiff substrates) [194]. YAP localization was sufficient to “trick” cells in thinking they were on a mechanically stiff substrate. However, our constitutively active cell line appeared to be insensitive to substrate stiffness, and only slightly increased area when cultured on stiff substrates and did not have any changes in form factor as has been previously reported for control VICs [28]. As VICs are mechano-sensitive cells, YAP may be involved in regulation of the myofibroblast phenotype, as discussed in section 6.2.3.

6.2.3 Regulation of the myofibroblastic phenotype

Several environmental factors inducing activation and differentiation into the myofibroblast phenotype have been identified [9, 12, 81, 211] including substrate stiffness and TGF- β 1, but the exact molecular pathways which initiate this differentiation remain unknown. One potential nuclear transcription factor of interest is YAP/TAZ. As mentioned above, YAP/TAZ has been shown to cross-talk with TGF- β 1 signaling [216, 217]. Additionally, one of the genes YAP/TAZ has been shown to regulate is the β 2 integrin [218], enabling increased contractile activity. Large spread area has been shown to be necessary for nuclear localization of YAP [124, 177]. In parallel, force has been shown to be necessary for myofibroblast differentiation due to α -SMA incorporation into stress fibers [88, 157], and larger cells are able to generate more contractile force [82]. YAP has also been shown to drive myofibroblast differentiation in lung fibroblasts [128] as well as skin fibroblasts [191]. Regulation of YAP to control myofibroblast differentiation of VICs could be a potential target of pharmaceuticals and is an interesting area for future research.

Although there is no treatment currently for fibro-calcific diseases, a conceptual idea, “mechanomedicines” [8], has been proposed to regulate the tension of myofibroblasts in hopes of reversing disease progression. For CAVD, potential pharmaceuticals that have been tried in several recent clinical trials are statins [4]. Statins did not improve outcomes for patients with CAVD [219-221]. *In vitro*, statins have been shown to reduce presence of myofibroblasts by reducing α -SMA expression [19]. However, statins were not effective in treating calcific nodules once they had formed, suggesting a time-dependence of drug administration [19]. Pravastatin was used in chapter 4 with the micro-contact printing model as an example to show utility as a potential drug assay for promising pharmaceutical candidates. We, like Benton, found that Pravastatin was incapable of reversing mineralization activity once the aggregates had formed (aggregates form immediately with the micro-contact printed model). This supports the hypothesis by Benton et. al that Pravastatin may be useful for treatment before disease onset to discourage progression, but it is incapable of reversing calcification once it has occurred.

6.2.4 Similarities to CAVD

Future work should be done to show the similarity of this micro-contact printed model to calcification observed in native disease valves. Several studies have examined explanted disease valves [7, 11, 41, 55]. Our micro-contact printed model replicates some of the hallmarks of CAVD reported, including presence of the myofibroblast phenotype [7, 41] and apoptosis [11]. Scanning electron microscopy of the *in vitro* model on tissue culture polystyrene has shown that dicalcium phosphate dihydrate (DCPD) is the predominate form of calcium in calcium positive aggregates. Approximately ~60% of aggregates that stain positive for calcium have DCPD compared to a much lower percentage (~10%) that has hydroxyapatite [9]. Other forms of calcification observed in the *in vitro* model include octacalcium phosphate (~20%) and tricalcium phosphate (~15%)[9].

Hydroxyapatite is one of the main components in bone, and it is contentious whether bone forming mechanisms are involved in the formation of the calcified nodules (“osteogenic calcification”). Mohler observed what appeared to be bone marrow in the center of calcified regions of diseased valves in a small subset of the pathological specimens examined [7]. Stevens and colleagues examined VIC nodules and compared them calcium nodules formed by bone cells via Raman spectroscopy; these calcium nodules formed by each cell type had distinctly different peak shifts, suggesting different calcium deposition and mineralization [164]. Notably, VIC nodules *in vitro* lacked the 960 cm^{-1} apatite peak which has been reported in disease explanted valves [164, 222]. However, the representative phase images shown in the manuscript appear to be more of a monolayer of VICs rather than an aggregate; the poor reliability of the model may have resulted in analysis of not “true aggregates”, and potentially incorrectly analyzing highly confluent monolayers instead.

Nano-analytical methods of calcified valves have revealed that mineralized calcium nanoparticles appear prior to disease calcification, and even in apparently “healthy -to-the-eye” tissue these nanoparticles can be found [55]. Elena Aikawa (Harvard University and Brigham and Women’s Hospital) has also shown micro-particle mineralization in excised valves (NAVBO presentation). Stevens and colleagues have shown that these nano-particles are present in atherosclerotic lesions in other areas of the cardiovascular system. Currently, it is not known if the mineralized particles initiate the disease phenotype, or if it is a by-product of the disease. Selected area electron diffraction analysis of disease valves has revealed that the calcium present in explanted valves is highly crystalline, even more so than the hydroxyapatite found in bone [55]. Excitingly, SEM and X-Ray microanalysis studies of our micro-contact printed model appeared to reveal two mechanisms of calcification. The first is that mineralized nanoparticles which apparently release from cells as they have been found below the plasma membrane in SEM images become trapped in the

extracellular matrix fibers of the aggregate. These particles were approximately the same size as those reported in disease valve tissue. These particles can aggregate together, forming large clusters. The second form of calcification appears to occur within rounded cells located in the center of the aggregate. Several aggregates that were examined contained these rounded cells with mineralized nanoparticles in locations where we have observed apoptosis. If these mechanisms (mineralizing rounded central cells and mineralized nanoparticles found on the surface of the aggregate) are inter-related remains an open research question.

Although the micro-contact printed model improves upon the current *in vitro* model for CAVD becoming vastly more reproducible and efficient, it is still a two dimensional, static model which is greatly simplified from the complex, dynamic, three-dimensional environment of the native heart valve. In moving towards a more realistic representation of the heart valve, there are several next steps one could take with the model. The first is using this model in a dynamic environment. Chapter 3 of this dissertation measured traction force with stretch and found that traction forces change with dynamic culture, decreasing tension. It would be interesting to see, if the tension distribution within the aggregate changes with stretch. Inflation of micro-contact printed protein islands of cells was shown to induce YAP nuclear localization in central cells, an indication of increasing tension [124]. Perhaps this mechanical means of increasing tension is sufficient to reduce apoptosis in the central region of the aggregate.

In addition to dynamic stimulation, creating a three dimensional model would also be more realistic than a flat, planar environment. I envision two ways of transitioning to a three-dimensional model of CAVD. The first, is growing valvular interstitial cells within PDMS wells and allowing them to self-aggregate, forming three dimensional spheres, similar to tumor spheroids. This method has been used previously to create and mechanically test tumor spheroids [223]. However, one issue

complicating potentially going forward in this manner is that apoptosis could be cued from limited diffusion of nutrients and oxygen while in two-dimensions, diffusion is not a problem. It would be difficult to separate the effects of mechanical environment from diffusion related cell death. A second method for creating a three-dimensional environment reminiscent of the valve structure is to embed the valvular interstitial cells within a hydrogel. Anseth and colleagues developed a matrix metalloproteinase (MMP) degradable poly(ethylene glycol) (PEG) hydrogel system as a tool for characterizing VIC function in 3D. The system showed that VICs were responsive to TGF β -1 in three dimensions by incorporation of α -SMA and production of collagen I indicating a transition to the myofibroblastic phenotype, but VICs did not form aggregates within the system. Aikawa and colleagues recently cultured VICs in a three-dimensional hydrogel of hyaluronic acid and gelatin crosslinked with methacrylic anhydride. Osteogenic calcification was induced by culturing in osteogenic media [40]. Control VICs that were not cultured osteogenic media did not form calcifications. Combined these results suggest that VICs behave differently in three dimensions than in two dimensions, and studying dystrophic calcification in three dimensions still remains challenging.

6.2.5 Fibro-calcific diseases: impact of the model

We do not believe the results to be VIC specific, and do believe that this model can be used with other types of fibroblasts. There are many different types of fibro-calcific diseases including, Dupuytren disease and calcinosis cutis (Cushing's disease), as well as genetic conditions such as Pseudoxanthoma elasticum (PXE); although, calcific aortic valve disease is potential the most well-known as it has large prevalence and a considerable effect on mortality. The mechanism behind fibro-calcific diseases may be similar (with apoptosis playing an initial role prior to the onset of calcification). Specifically with our model, human dermal fibroblasts (courtesy of the Pins lab at WPI) were seeded onto a \sim 10 kPa PA gel. These fibroblasts had been pre-treated with 5 ng/mL TGF- β 1

for five days prior to seeding to trigger differentiation to the myofibroblast phenotype. Caspase 3/7 activity was evaluated using the live cell event marker for apoptosis. Apoptotic activity was apparent in the dermal fibroblast aggregates by day 4, see Figure 6.1. The ability to use the model with numerous fibroblast types provides an avenue for finding potential medicinal treatments that are applicable to multiple disease states.

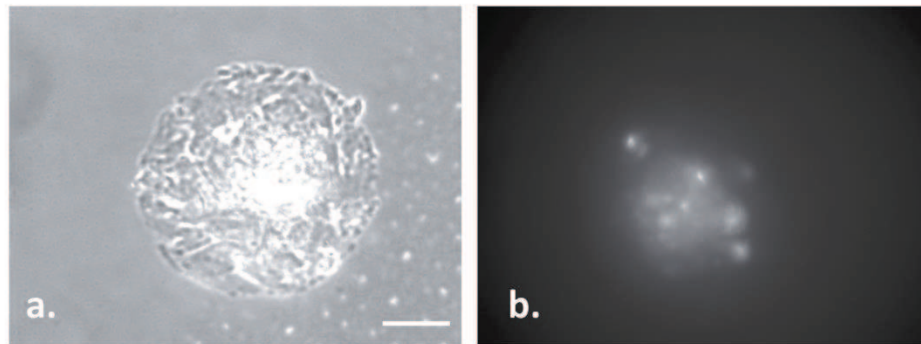


Figure 6.1. Human dermal fibroblasts also exhibited apoptotic activity when cultured in micro-patterned substrates on polyacrylamide. a) phase image of 200 μm aggregate on ~ 10 kPa PA gel. b) caspase 3/7 activity within aggregate indicating apoptosing cells in central regions of the aggregate.

An additional interesting avenue for future research would be to use this system to create and study atherosclerotic lesions. Smooth muscle cells might have similar behavior when cultured in this system. Micro-contact printed geometries could be created on a compliant surface, such as silicone sheeting, and then “rolled” to create a tube, mimicking an artery. This adaptation to the model may be useful for studying the effect of cytokines and pharmacologics which increase collagen deposition to stabilize the calcification, making it less likely to rupture and cause secondary incidents of stroke, heart attack or pulmonary embolism [8].

6.2.6 Cell movement and proliferation in aggregates

The hypothesis that cells within the center undergo apoptosis due to low cell tension is somewhat simplistic as center and edge cells do not stay in one constant location over time. Cells are capable

of migration, even in dense monolayers where there is “no apparent room” to navigate around other cells. This raises the question, if cells can migrate between the center and edge regions, and experience different mechanical environments, at what point does the apoptosis occur? Could the central cells navigate to the edge region and “save” themselves from entering apoptosis? Once a cell dies, does it restrict the movement of other cells and limit how many cells can be in the central region, or can other cells push the dead cell “out of the way”? Furthermore, the cells also are capable of proliferation within these dense aggregates as well. Confluence, we have learned, is a somewhat relative term, and just because the protein patterned area is covered with cells does not mean that proliferation will not occur. Shown in figure 6.2 are two aggregates of different sizes that were tracked with Hoechst over one day. The 200 μm aggregate showed no change in cells over the 24 hour period, while the 400 μm aggregate saw an increase in cells from 97 to 107. Future work should focus on tracking aggregates over time to understand the impact of migration and proliferation on apoptotic activity.

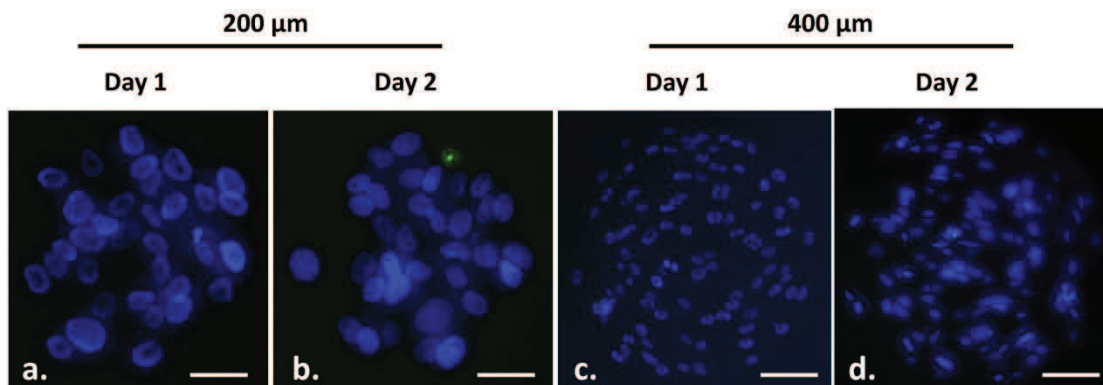


Figure 6.2. 24 time course shows migration and proliferation within aggregates. a) day 1 200 μm diameter aggregate on 40 kPa PA gel. scale bar = 50 μm b) 24 hours later, same 200 μm aggregate. Cell number did not change between time points. scale bar = 50 μm c) 400 μm diameter aggregate on 40 kPa PA gel on day 1 and d) day 2. Cell number within aggregate increased from 97 to 107. scale bar = 100 μm

6.2.7 Caspase and cell death, the importance of aggregate tracking

The apoptosis analysis done in the dissertation was based on a population of aggregates. Caspase analysis presented was not the result of tracking individual aggregates over time. Future work should develop methods of accurate time-lapse microscopy in order to evaluate how long the caspase signal stays active in valvular interstitial cell aggregates. In addition to tracking caspase activity with time, ethidium homodimer-1 uptake (a marker for cell death which localizes to the nucleus) could be measured over-time to evaluate how aggregate cell death changes over time.

6.3 Clinical Significance

The clinical impact of the presented model is two-fold. The first is it allows clinical researchers to have a more reliable, repeatable model system for generating valvular interstitial cell aggregates to better understand the mechanisms behind the apoptosis and calcification which appear to initiate the pathology. The second is that the micro-contact printing system is translatable to an *in vitro* platform to test potential pharmaceutical candidates. This product could help pharmaceutical companies identify molecular targets of calcification, as well as test antibodies, small molecules, and pharmacologic agents that could slow, halt or reverse the calcification process. These biomimetic aggregates created with micro-contact printing have the advantage over the current system in that they are highly controllable, resulting in consistent, repeatable time-course of apoptotic and calcification activity.

Studying CAVD *in vivo* remains challenging as currently there are no widely accepted animal models for this disease. The valve response which initiates calcification does not naturally occur in rodent models (the most “low-cost” animal model). Calcification can be induced in small animals by feeding a high fat diet; however, the relevance of this model to humans is debatable as valve calcification

has not been correlated with high lipid levels in the blood stream. Additionally, examination of explanted disease valves reveals only one time-point of the pathology, often at late-stages where little mechanistic insight into disease initiation can be gleaned.

We hope that wide acceptance and usage of this model system will enable studies into the apoptotic signaling cascades, allowing for the identification of promising molecular targets, as well as providing further understanding of the mechanisms of calcification. Further, we believe this technology is translatable in two forms. The first would be a license agreement (as this *in vitro* system for generating valvular interstitial cell aggregates is patented), where companies could adapt this technology for use “in-house”, the second would be a small “start-up”/contract research organization to evaluate and report on the effectiveness of the medicinal agents at the request of the company.

Chapter 7: Thesis Conclusions

Aim 1:

A novel stretch device, custom well, and software program was created and validated to allow for uniaxial and biaxial cyclic stretch to be applied to custom cultured cells. As the custom wells are made out of polydimethylsiloxane, polyacrylamide gels were able to be covalently attached using a method developed previously in our lab, enabling traction force measurements. Using a spacer, the bottom of the well was cast at the same time as the sides, allowing for the bottom membrane to be perfectly taut which facilitated clear imaging. In addition, the well mold was designed so that the bottom membrane was sufficiently thin (~150 μm) so even with attachment of 70 μm thick hydrogel, clear images could be obtained for traction force analysis. VICs were cyclically stretched for 24 hours after being allowed to attach to the polyacrylamide gel overnight. It was found for conditions of high cell tension, “high prestress”, cells decreased spread area, traction force, and maximum substrate stress with stretch. These results were repeated and confirmed with U2OS as an additional cell type. Prestress was decreased in a subset of experiments by using both chemical (Blebbistatin) and mechanical (low substrate modulus) means. For cells under low prestress, spread area, traction force, and maximum substrate stress increased with 24 hours cyclic stretch.

Contractile moment, the combination of traction forces weighted by their corresponding x and y coordinates, was also computed. As defined, a cell contractile moment will be negative if the cell is contracting inward (pulling towards itself) and positive if the cell is pushing outward (away from the cell body). For VICs that had an intact cytoskeleton (not inhibited with Blebbistatin), contractile moment was negative, in agreement with most of the reported literature values. However, for

Blebbistatin treated VICs, contractile moment was positive for half of the control VICs and all of the stretched VICs, a unique and novel finding.

Finally, reorientation response was examined for VICs under both high and low prestress conditions. VICs reoriented perpendicular to stretch in all experimental conditions, the exception being the subset that had been treated with Blebbistatin, which oriented parallel to stretch. As VICs reorientation perpendicular to stretch on low modulus gels conflicted results found in literature, the experiment was repeated with U2OS cells on a low modulus substrate with identical findings.

Aim 2:

In aim two, a novel method for creation of aggregates for the study of dystrophic calcification *in vitro* is developed and validated. The *in vitro* model for calcific aortic valve disease is able to be replicated with micro-contact printing on polyacrylamide hydrogels. Aggregates formed calcifications in a highly repeatable manner, as determined by Alazarin Red S staining. Scanning electron microscopy and X-ray micro-analysis revealed that calcium predominates in the form of calcium oxide within the aggregates. Calcification was found both in mineralized nanoparticles both as well as in what appears to be apoptosing cells. Whether these mechanisms of mineralization are distinct or inter-related remains an open research question

The utility of micro-contact printing allows for tight control over aggregate shape, enabling investigation of aggregate size on time-course of pathological calcification. Alazarin Red S was used to confirm calcification in our control aggregates, which we defined as 200 μm diameter on 38 kPa PA gel. SEM and X-ray micro-analysis was used as a second measure of calcification and identify the chemical form of calcium within the aggregates. Interestingly, two types of mineralization was found within the aggregates: mineralized spheroid micro-particles which accumulated on the aggregate surface as well as mineralization within what appeared to be apoptosing cells due to their rounded

morphology. It was shown that apoptosis and dystrophic calcification is present in aggregates of all sizes. Micro-contact printing also enables aggregate formation on all stiffness of polyacrylamide; dystrophic calcification was found to occur regardless of substrate stiffness. Traction force of the aggregates showed that overall traction force increases both with aggregate size and substrate stiffness. Additionally, the center of the aggregates had low substrate stress in all conditions. TGF- β 1, although frequently used in literature to increase aggregation in the *in vitro* model, did not increase apoptotic activity, but did slightly affect mineralization as Alazarin Red S staining was more intense. Pravastatin, a potential pharmaceutical for treatment of CAVD had no effect on mineralization within aggregates or caspase activity. This suggests that pravastatin is not suitable for disease prevention or reversal once the CAVD has progressed to the point where cell aggregates are present.

The model was then used to answer the hypothesis: do cells undergo apoptosis within the center of the aggregate because they are experiencing a low tension environment. Atomic force microscopy measurements of cell stiffness show that low cell stiffness, an indication of cell tension, exists in the center of non-micro-contact printed aggregates. Spread area restriction, which is present in aggregate center, reduces the ability for VICs to generate tension. Examination of stress fiber alignment using 2-D FFTs shows that there is little to no f-actin alignment in center of the aggregates, for both non-micro-contact printed and micro-contact printed aggregates.

Immunohistochemistry analysis of nuclear YAP, an indication of high tension state shows the greatest localization in the aggregate periphery. α -SMA, which incorporates into stress fibers in high tension state, had highest expression along aggregate periphery. α -SMA expression correlated with areas of maximum principal stress as predicted by a finite element model of contraction. The finite element model was then used to examine stress distributions in aggregates of constant area, but changing geometry. Micro-contact printing of aggregates with constant area and increased

elongation showed that apoptosis occurred most frequently in the areas of low tension, regardless of geometry. Finally, collagen coated magnetic microbeads were added to the aggregates to apply upward force when aggregates were placed in a magnetic field. This resulted in a visible reduction in α -SMA expression in stress fibers.

References

1. Go, A.S., D. Mozaffarian, V.L. Roger, E.J. Benjamin, J.D. Berry, M.J. Blaha, S. Dai, E.S. Ford, C.S. Fox, and S. Franco, Heart disease and stroke statistics--2014 update: A report from the American Heart Association. *Circulation*, 2014. **129**(3): p. e28.
2. Lindroos, M., M. Kupari, J. Heikkilä, and R. Tilvis, Prevalence of aortic valve abnormalities in the elderly: An echocardiographic study of a random population sample. *Journal of the American College of Cardiology*, 1993. **21**(5): p. 1220-1225.
3. Otto, C.M. and B. Prendergast, Aortic-valve stenosis—from patients at risk to severe valve obstruction. *New England Journal of Medicine*, 2014. **371**(8): p. 744-756.
4. Hermans, H., P. Herijgers, P. Holvoet, E. Verbeken, B. Meuris, W. Flameng, and M.-C. Herregods, Statins for calcific aortic valve stenosis: Into oblivion after saltire and seas? An extensive review from bench to bedside. *Current Problems in Cardiology*, 2010. **35**(6): p. 284-306.
5. Vesely, I., Heart valve tissue engineering. *Circulation Research*, 2005. **97**(8): p. 743-755.
6. Merryman, W.D. and F.J. Schoen, Mechanisms of calcification in aortic valve disease: Role of mechanokinetics and mechanodynamics. *Current Cardiology Reports*, 2013. **15**(5): p. 1-7.
7. Mohler, E.R., F. Gannon, C. Reynolds, R. Zimmerman, M.G. Keane, and F.S. Kaplan, Bone formation and inflammation in cardiac valves. *Circulation*, 2001. **103**(11): p. 1522-1528.
8. Hutcheson, J.D., E. Aikawa, and W.D. Merryman, Potential drug targets for calcific aortic valve disease. *Nature Reviews Cardiology*, 2014. **11**(4): p. 218-231.
9. Rodriguez, K.J. and K.S. Masters, Regulation of valvular interstitial cell calcification by components of the extracellular matrix. *Journal of Biomedical Materials Research Part A*, 2009. **90**(4): p. 1043-1053.
10. Bowler, M.A. and W.D. Merryman, *In vitro* models of aortic valve calcification: Solidifying a system. *Cardiovascular Pathology*, 2015. **24**(1): p. 1-10.
11. Jian, B., N. Narula, Q.-y. Li, E.R. Mohler, and R.J. Levy, Progression of aortic valve stenosis: Tgf- β 1 is present in calcified aortic valve cusps and promotes aortic valve interstitial cell calcification via apoptosis. *The Annals of Thoracic Surgery*, 2003. **75**(2): p. 457-465.
12. Walker, G.A., K.S. Masters, D.N. Shah, K.S. Anseth, and L.A. Leinwand, Valvular myofibroblast activation by transforming growth factor- β implications for pathological extracellular matrix remodeling in heart valve disease. *Circulation Research*, 2004. **95**(3): p. 253-260.
13. Taylor, P.M., P. Batten, N.J. Brand, P.S. Thomas, and M.H. Yacoub, The cardiac valve interstitial cell. *The international Journal of Biochemistry & Cell Biology*, 2003. **35**(2): p. 113-118.
14. Cushing, M.C., J.-T. Liao, and K.S. Anseth, Activation of valvular interstitial cells is mediated by transforming growth factor- β 1 interactions with matrix molecules. *Matrix Biology*, 2005. **24**(6): p. 428-437.
15. Hinz, B., The myofibroblast: Paradigm for a mechanically active cell. *Journal of Biomechanics*, 2010. **43**(1): p. 146-155.
16. Yip, C.Y.Y., J.-H. Chen, R. Zhao, and C.A. Simmons, Calcification by valve interstitial cells is regulated by the stiffness of the extracellular matrix. *Arteriosclerosis, Thrombosis, and Vascular Biology*, 2009. **29**(6): p. 936-942.
17. Fisher, C.I., J. Chen, and W.D. Merryman, Calcific nodule morphogenesis by heart valve interstitial cells is strain dependent. *Biomechanics and Modeling in Mechanobiology*, 2013. **12**(1): p. 5-17.

18. Gu, X. and K.S. Masters, Role of the rho pathway in regulating valvular interstitial cell phenotype and nodule formation. *American Journal of Physiology-Heart and Circulatory Physiology*, 2011. **300**(2): p. H448-H458.
19. Benton, J.A., H.B. Kern, L.A. Leinwand, P.D. Mariner, and K.S. Anseth, Statins block calcific nodule formation of valvular interstitial cells by inhibiting α -smooth muscle actin expression. *Arteriosclerosis, Thrombosis, and Vascular Biology*, 2009. **29**(11): p. 1950-1957.
20. Monzack, E.L. and K.S. Masters, A time course investigation of the statin paradox among valvular interstitial cell phenotypes. *American Journal of Physiology-Heart and Circulatory Physiology*, 2012. **303**(7): p. H903-H909.
21. Zhao, R., K.L. Sider, and C.A. Simmons, Measurement of layer-specific mechanical properties in multilayered biomaterials by micropipette aspiration. *Acta Biomaterialia*, 2011. **7**(3): p. 1220-1227.
22. Vesely, I. and R. Noseworthy, Micromechanics of the fibrosa and the ventricularis in aortic valve leaflets. *Journal of Biomechanics*, 1992. **25**(1): p. 101-113.
23. Merryman, W.D., H.D. Lukoff, R.A. Long, G.C. Engelmayr, R.A. Hopkins, and M.S. Sacks, Synergistic effects of cyclic tension and transforming growth factor- β 1 on the aortic valve myofibroblast. *Cardiovascular Pathology*, 2007. **16**(5): p. 268-276.
24. Ku, C.-H., P.H. Johnson, P. Batten, P. Sarathchandra, R.C. Chambers, P.M. Taylor, M.H. Yacoub, and A.H. Chester, Collagen synthesis by mesenchymal stem cells and aortic valve interstitial cells in response to mechanical stretch. *Cardiovascular Research*, 2006. **71**(3): p. 548-556.
25. Xu, S., A.C. Liu, H. Kim, and A.I. Gotlieb, Cell density regulates *in vitro* activation of heart valve interstitial cells. *Cardiovascular Pathology*, 2012. **21**(2): p. 65-73.
26. Blaauboer, M.E., T.H. Smit, R. Hanemaaijer, R. Stoop, and V. Everts, Cyclic mechanical stretch reduces myofibroblast differentiation of primary lung fibroblasts. *Biochemical and Biophysical Research Communications*, 2011. **404**(1): p. 23-27.
27. Lo, C.-M., H.-B. Wang, M. Dembo, and Y.-I. Wang, Cell movement is guided by the rigidity of the substrate. *Biophysical Journal*, 2000. **79**(1): p. 144-152.
28. Quinlan, A.M.T., L.N. Sierad, A.K. Capulli, L.E. Firstenberg, and K.L. Billiar, Combining dynamic stretch and tunable stiffness to probe cell mechanobiology *in vitro*. 2011.
29. Cui, Y., F.M. Hameed, B. Yang, K. Lee, C.Q. Pan, S. Park, and M. Sheetz, Cyclic stretching of soft substrates induces spreading and growth. *Nature Communications*, 2015. **6**.
30. Tondon, A. and R. Kaunas, The direction of stretch-induced cell and stress fiber orientation depends on collagen matrix stress. *PloS One*, 2014. **9**(2): p. e89592.
31. Birukov, K.G., V.P. Shirinsky, O.V. Stepanova, V.A. Tkachuk, A.W. Hahn, T.J. Resink, and V.N. Smirnov, Stretch affects phenotype and proliferation of vascular smooth muscle cells. *Molecular and Cellular Biochemistry*, 1995. **144**(2): p. 131-139.
32. Engler, A.J., S. Sen, H.L. Sweeney, and D.E. Discher, Matrix elasticity directs stem cell lineage specification. *Cell*, 2006. **126**(4): p. 677-689.
33. Wang, H.-B., M. Dembo, and Y.-L. Wang, Substrate flexibility regulates growth and apoptosis of normal but not transformed cells. *American Journal of Physiology-Cell Physiology*, 2000. **279**(5): p. C1345-C1350.
34. Weyts, F., B. Bosmans, R. Niesing, J. Leeuwen, and H. Weinans, Mechanical control of human osteoblast apoptosis and proliferation in relation to differentiation. *Calcified Tissue International*, 2003. **72**(4): p. 505-512.
35. Garg, V., A.N. Muth, J.F. Ransom, M.K. Schluterman, R. Barnes, I.N. King, P.D. Grossfeld, and D. Srivastava, Mutations in notch1 cause aortic valve disease. *Nature*, 2005. **437**(7056): p. 270-274.

36. Thanassoulis, G., C.Y. Campbell, D.S. Owens, J.G. Smith, A.V. Smith, G.M. Peloso, K.F. Kerr, S. Pechlivanis, M.J. Budoff, and T.B. Harris, Genetic associations with valvular calcification and aortic stenosis. *New England Journal of Medicine*, 2013. **368**(6): p. 503-512.
37. Katz, R., N.D. Wong, R. Kronmal, J. Takasu, D.M. Shavelle, J.L. Probstfield, A.G. Bertoni, M.J. Budoff, and K.D. O'Brien, Features of the metabolic syndrome and diabetes mellitus as predictors of aortic valve calcification in the multi-ethnic study of atherosclerosis. *Circulation*, 2006. **113**(17): p. 2113-2119.
38. Owens, D.S., R. Katz, J. Takasu, R. Kronmal, M.J. Budoff, and K.D. O'Brien, Incidence and progression of aortic valve calcium in the multi-ethnic study of atherosclerosis (mesa). *The American Journal of Cardiology*, 2010. **105**(5): p. 701-708.
39. Otto, C.M., I.G. Burwash, M.E. Legget, B.I. Munt, M. Fujioka, N.L. Healy, C.D. Kraft, C.Y. Miyake-Hull, and R.G. Schwaegler, Prospective study of asymptomatic valvular aortic stenosis clinical, echocardiographic, and exercise predictors of outcome. *Circulation*, 1997. **95**(9): p. 2262-2270.
40. Hjortnaes, J., C. Goettsch, J.D. Hutcheson, G. Camci-Unal, L. Lax, K. Scherer, S. Body, F.J. Schoen, J. Kluin, and A. Khademhosseini, Simulation of early calcific aortic valve disease in a 3d platform: A role for myofibroblast differentiation. *Journal of Molecular and Cellular Cardiology*, 2016. **94**: p. 13-20.
41. Otto, C.M., J. Kuusisto, D.D. Reichenbach, A.M. Gown, and K.D. O'Brien, Characterization of the early lesion of 'degenerative' valvular aortic stenosis. Histological and immunohistochemical studies. *Circulation*, 1994. **90**(2): p. 844-853.
42. Thubrikar, M.J., S.P. Nolan, J. Aouad, and J.D. Deck, Stress sharing between the sinus and leaflets of canine aortic valve. *The Annals of Thoracic Surgery*, 1986. **42**(4): p. 434-440.
43. Thubrikar, M.J., J. Aouad, and S.P. Nolan, Patterns of calcific deposits in operatively excised stenotic or purely regurgitant aortic valves and their relation to mechanical stress. *The American Journal of Cardiology*, 1986. **58**(3): p. 304-308.
44. Caira, F.C., S.R. Stock, T.G. Gleason, E.C. McGee, J. Huang, R.O. Bonow, T.C. Spelsberg, P.M. McCarthy, S.H. Rahimtoola, and N.M. Rajamannan, Human degenerative valve disease is associated with up-regulation of low-density lipoprotein receptor-related protein 5 receptor-mediated bone formation. *Journal of the American College of Cardiology*, 2006. **47**(8): p. 1707-1712.
45. Schoen, F.J., R.J. Levy, and H.R. Piehler, Pathological considerations in replacement cardiac valves. *Cardiovascular Pathology*, 1992. **1**(1): p. 29-52.
46. Golomb, G., F.J. Schoen, M. Smith, J. Linden, M. Dixon, and R. Levy, The role of glutaraldehyde-induced cross-links in calcification of bovine pericardium used in cardiac valve bioprostheses. *The American Journal of Pathology*, 1987. **127**(1): p. 122.
47. Bloomfield, P., Choice of heart valve prosthesis. *Heart*, 2002. **87**(6): p. 583-589.
48. Chan, W.S., S. Anand, and J.S. Ginsberg, Anticoagulation of pregnant women with mechanical heart valves: A systematic review of the literature. *Archives of Internal Medicine*, 2000. **160**(2): p. 191-196.
49. Vitale, N., M. De Feo, L.S. De Santo, A. Pollice, N. Tedesco, and M. Cotrufo, Dose-dependent fetal complications of warfarin in pregnant women with mechanical heart valves. *Journal of the American College of Cardiology*, 1999. **33**(6): p. 1637-1641.
50. Bloomfield, P., D.J. Wheatley, R.J. Prescott, and H.C. Miller, Twelve-year comparison of a bjork–shiley mechanical heart valve with porcine bioprostheses. *New England Journal of Medicine*, 1991. **324**(9): p. 573-579.

51. Edmunds Jr, L.H., R.E. Clark, L.H. Cohn, G.L. Grunkemeier, D.C. Miller, and R.D. Weisel, Guidelines for reporting morbidity and mortality after cardiac valvular operations. *The Journal of Thoracic and Cardiovascular Surgery*, 1996. **112**(3): p. 708-711.
52. Vesely, I., The evolution of bioprosthetic heart valve design and its impact on durability. *Cardiovascular Pathology*, 2003. **12**(5): p. 277-286.
53. Weska, R.F., C.G. Aimoli, G.M. Nogueira, A.A. Leirner, M.J. Maizato, O.Z. Higa, B. Polakiewicz, R.N. Pitombo, and M.M. Beppu, Natural and prosthetic heart valve calcification: Morphology and chemical composition characterization. *Artificial Organs*, 2010. **34**(4): p. 311-318.
54. Farzaneh-Far, A., D. Proudfoot, C. Shanahan, and P. Weissberg, Vascular and valvar calcification: Recent advances. *Heart*, 2001. **85**(1): p. 13-17.
55. Bertazzo, S., E. Gentleman, K.L. Cloyd, A.H. Chester, M.H. Yacoub, and M.M. Stevens, Nano-analytical electron microscopy reveals fundamental insights into human cardiovascular tissue calcification. *Nature Materials*, 2013. **12**(6): p. 576-583.
56. Weinberg, E.J., P.J. Mack, F.J. Schoen, G. García-Cardeña, and M.R.K. Mofrad, Hemodynamic environments from opposing sides of human aortic valve leaflets evoke distinct endothelial phenotypes in vitro. *Cardiovascular Engineering*, 2010. **10**(1): p. 5-11.
57. Gould, S.T., E.E. Matherly, J.N. Smith, D.D. Heistad, and K.S. Anseth, The role of valvular endothelial cell paracrine signaling and matrix elasticity on valvular interstitial cell activation. *Biomaterials*, 2014. **35**(11): p. 3596-3606.
58. Aikawa, E., P. Whittaker, M. Farber, K. Mendelson, R.F. Padera, M. Aikawa, and F.J. Schoen, Human semilunar cardiac valve remodeling by activated cells from fetus to adult implications for postnatal adaptation, pathology, and tissue engineering. *Circulation*, 2006. **113**(10): p. 1344-1352.
59. Balachandran, K., P. Sucusky, and A.P. Yoganathan, Hemodynamics and mechanobiology of aortic valve inflammation and calcification. *International Journal of Inflammation*, 2011. **2011**.
60. Choquet, D., D.P. Felsenfeld, and M.P. Sheetz, Extracellular matrix rigidity causes strengthening of integrin–cytoskeleton linkages. *Cell*, 1997. **88**(1): p. 39-48.
61. Suter, D.M., L.D. Errante, V. Belotserkovsky, and P. Forscher, The ig superfamily cell adhesion molecule, apcam, mediates growth cone steering by substrate–cytoskeletal coupling. *The Journal of Cell Biology*, 1998. **141**(1): p. 227-240.
62. Sawada, Y. and M.P. Sheetz, Force transduction by triton cytoskeletons. *The Journal of Cell Biology*, 2002. **156**(4): p. 609-615.
63. Hinz, B. and G. Gabbiani, Cell-matrix and cell-cell contacts of myofibroblasts: Role in connective tissue remodeling. *Thrombosis and Haemostasis-Stuttgart*, 2003. **90**(6): p. 993-1002.
64. Hinz, B., G. Celetta, J.J. Tomasek, G. Gabbiani, and C. Chaponnier, Alpha-smooth muscle actin expression upregulates fibroblast contractile activity. *Molecular Biology of the Cell*, 2001. **12**(9): p. 2730-2741.
65. Hinz, B., D. Mastrangelo, C.E. Iselin, C. Chaponnier, and G. Gabbiani, Mechanical tension controls granulation tissue contractile activity and myofibroblast differentiation. *The American Journal of Pathology*, 2001. **159**(3): p. 1009-1020.
66. Chen, J., H. Li, N. SundarRaj, and J.H.C. Wang, Alpha-smooth muscle actin expression enhances cell traction force. *Cell Motility and the Cytoskeleton*, 2007. **64**(4): p. 248-257.
67. Igotz, R.A. and J. Massagué, Cell adhesion protein receptors as targets for transforming growth factor- β action. *Cell*, 1987. **51**(2): p. 189-197.

68. Geiger, B., T. Volberg, D. Ginsberg, S. Bitzur, I. Sabanay, and R.O. Hynes, Broad spectrum pan-cadherin antibodies, reactive with the c-terminal 24 amino acid residues of n-cadherin. *Journal of Cell Science*, 1990. **97**(4): p. 607-614.
69. Hatta, K. and M. Takeichi, Expression of n-cadherin adhesion molecules associated with early morphogenetic events in chick development. *Nature*, 1986.
70. Ko, K., P. Arora, W. Lee, and C. McCulloch, Biochemical and functional characterization of intercellular adhesion and gap junctions in fibroblasts. *American Journal of Physiology-Cell Physiology*, 2000. **279**(1): p. C147-C157.
71. Hoorde, L.v., K. Braet, and M. Mareel, The n-cadherin/catenin complex in colon fibroblasts and myofibroblasts. *Cell Communication & Adhesion*, 1999. **7**(2): p. 139-150.
72. Shin, C.S., F. Lecanda, S. Sheikh, L. Weitzmann, S.L. Cheng, and R. Civitelli, Relative abundance of different cadherins defines differentiation of mesenchymal precursors into osteogenic, myogenic, or adipogenic pathways. *Journal of Cellular Biochemistry*, 2000. **78**(4): p. 566-577.
73. Yonemura, S., M. Itoh, A. Nagafuchi, and S. Tsukita, Cell-to-cell adherens junction formation and actin filament organization: Similarities and differences between non-polarized fibroblasts and polarized epithelial cells. *Journal of Cell Science*, 1995. **108**(1): p. 127-142.
74. Hoffmann, I. and R. Balling, Cloning and expression analysis of a novel mesodermally expressed cadherin. *Developmental Biology*, 1995. **169**(1): p. 337-346.
75. Liu, H., Y. Sun, and C.A. Simmons, Determination of local and global elastic moduli of valve interstitial cells cultured on soft substrates. *Journal of Biomechanics*, 2013. **46**(11): p. 1967-1971.
76. Wyss, K., C.Y. Yip, Z. Mirzaei, X. Jin, J.-H. Chen, and C.A. Simmons, The elastic properties of valve interstitial cells undergoing pathological differentiation. *Journal of Biomechanics*, 2012. **45**(5): p. 882-887.
77. Merryman, W.D., P.D. Bieniek, F. Guilak, and M.S. Sacks, Viscoelastic properties of the aortic valve interstitial cell. *Journal of Biomechanical Engineering*, 2009. **131**(4): p. 041005.
78. Wang, N., I.M. Tolić-Nørrelykke, J. Chen, S.M. Mijailovich, J.P. Butler, J.J. Fredberg, and D. Stamenović, Cell prestress. I. Stiffness and prestress are closely associated in adherent contractile cells. *American Journal of Physiology-Cell Physiology*, 2002. **282**(3): p. C606-C616.
79. Stamenović, D., Effects of cytoskeletal prestress on cell rheological behavior. *Acta Biomaterialia*, 2005. **1**(3): p. 255-262.
80. Kloxin, A.M., J.A. Benton, and K.S. Anseth, In situ elasticity modulation with dynamic substrates to direct cell phenotype. *Biomaterials*, 2010. **31**(1): p. 1-8.
81. Quinlan, A.M. and K.L. Billiar, Investigating the role of substrate stiffness in the persistence of valvular interstitial cell activation. *Journal of Biomedical Materials Research Part A*, 2012. **100**(9): p. 2474-2482.
82. Califano, J.P. and C.A. Reinhart-King, Substrate stiffness and cell area predict cellular traction stresses in single cells and cells in contact. *Cellular and molecular bioengineering*, 2010. **3**(1): p. 68-75.
83. Kloxin, A.M., J.A. Benton, and K.S. Anseth, *in situ* elasticity modulation with dynamic substrates to direct cell phenotype. *Biomaterials*, 2010. **31**(1): p. 1-8.
84. Wang, H., S.M. Haeger, A.M. Kloxin, L.A. Leinwand, and K.S. Anseth, Redirecting valvular myofibroblasts into dormant fibroblasts through light-mediated reduction in substrate modulus. *PLoS One*, 2012. **7**(7): p. e39969.
85. Balachandran, K., S. Konduri, P. Sucusky, H. Jo, and A.P. Yoganathan, An ex vivo study of the biological properties of porcine aortic valves in response to circumferential cyclic stretch. *Annals of Biomedical Engineering*, 2006. **34**(11): p. 1655-1665.

86. Balachandran, K., P. Sucusky, H. Jo, and A.P. Yoganathan, Elevated cyclic stretch alters matrix remodeling in aortic valve cusps: Implications for degenerative aortic valve disease. *American Journal of Physiology-Heart and Circulatory Physiology*, 2009. **296**(3): p. H756-H764.
87. Gould, R.A., K. Chin, T.P. Santisakultarm, A. Dropkin, J.M. Richards, C.B. Schaffer, and J.T. Butcher, Cyclic strain anisotropy regulates valvular interstitial cell phenotype and tissue remodeling in three-dimensional culture. *Acta Biomaterialia*, 2012. **8**(5): p. 1710-1719.
88. Wang, J., H. Chen, A. Seth, and C.A. McCulloch, Mechanical force regulation of myofibroblast differentiation in cardiac fibroblasts. *American Journal of Physiology-Heart and Circulatory Physiology*, 2003. **285**(5): p. H1871-H1881.
89. Smith, K.E., S.A. Metzler, and J.N. Warnock, Cyclic strain inhibits acute pro-inflammatory gene expression in aortic valve interstitial cells. *Biomechanics and Modeling in Mechanobiology*, 2010. **9**(1): p. 117-125.
90. Bouchareb, R., M.-C. Boulanger, D. Fournier, P. Pibarot, Y. Messaddeq, and P. Mathieu, Mechanical strain induces the production of spheroid mineralized microparticles in the aortic valve through a rhoa/rock-dependent mechanism. *Journal of Molecular and Cellular Cardiology*, 2014. **67**: p. 49-59.
91. Marinković, A., J.D. Mih, J.-A. Park, F. Liu, and D.J. Tschumperlin, Improved throughput traction microscopy reveals pivotal role for matrix stiffness in fibroblast contractility and tgf- β responsiveness. *American Journal of Physiology-Lung Cellular and Molecular Physiology*, 2012. **303**(3): p. L169-L180.
92. Kural, M.H. and K.L. Billiar, Regulating tension in three-dimensional culture environments. *Experimental Cell Research*, 2013. **319**(16): p. 2447-2459.
93. Worthington, J.J., J.E. Klementowicz, and M.A. Travis, Tgf β : A sleeping giant awoken by integrins. *Trends in Biochemical Sciences*, 2011. **36**(1): p. 47-54.
94. Wipff, P.-J., D.B. Rifkin, J.-J. Meister, and B. Hinz, Myofibroblast contraction activates latent tgf- β 1 from the extracellular matrix. *The Journal of Cell Biology*, 2007. **179**(6): p. 1311-1323.
95. Chen, J., J.R. Peacock, J. Branch, and W.D. Merryman, Biophysical analysis of dystrophic and osteogenic models of valvular calcification. *Journal of Biomechanical Engineering*, 2015. **137**(2): p. 020903.
96. Chrzanowska-Wodnicka, M. and K. Burridge, Rho-stimulated contractility drives the formation of stress fibers and focal adhesions. *The Journal of Cell Biology*, 1996. **133**(6): p. 1403-1415.
97. Hutcheson, J.D., J. Chen, M. Sewell-Loftin, L.M. Ryzhova, C.I. Fisher, Y.R. Su, and W.D. Merryman, Cadherin-11 regulates cell–cell tension necessary for calcific nodule formation by valvular myofibroblasts. *Arteriosclerosis, Thrombosis, and Vascular Biology*, 2013. **33**(1): p. 114-120.
98. Hsieh, M.H. and H.T. Nguyen, Molecular mechanism of apoptosis induced by mechanical forces. *International Review of Cytology*, 2005. **245**: p. 45-90.
99. Grinnell, F., M. Zhu, M.A. Carlson, and J.M. Abrams, Release of mechanical tension triggers apoptosis of human fibroblasts in a model of regressing granulation tissue. *Experimental Cell Research*, 1999. **248**(2): p. 608-619.
100. Boudreau, N., C.J. Sympton, Z. Werb, and M.J. Bissell, Suppression of ice and apoptosis in mammary epithelial cells by extracellular matrix. *Science*, 1995. **267**(5199): p. 891.
101. Zhang, Y.-H., C.-Q. Zhao, L.-S. Jiang, and L.-Y. Dai, Substrate stiffness regulates apoptosis and the mrna expression of extracellular matrix regulatory genes in the rat annular cells. *Matrix Biology*, 2011. **30**(2): p. 135-144.

102. Mih, J., F. Liu, D. Tschumperlin, and A. Marinković, Transitions in matrix stiffness uncouple lung fibroblast proliferative and morphological responses from cytoskeletal tension. *Am Journal of Respiratory Critical Care Medicine*, 2011. **183**: p. A3562.
103. Chen, C.S., M. Mrksich, S. Huang, G.M. Whitesides, and D.E. Ingber, Geometric control of cell life and death. *Science*, 1997. **276**(5317): p. 1425-1428.
104. Kim, H., A. Sengupta, M. Glogauer, and C.A. McCulloch, Filamin a regulates cell spreading and survival via β 1 integrins. *Experimental Cell Research*, 2008. **314**(4): p. 834-846.
105. John, J., A.T. Quinlan, C. Silvestri, and K. Billiar, Boundary stiffness regulates fibroblast behavior in collagen gels. *Annals of Biomedical Engineering*, 2010. **38**(3): p. 658-673.
106. Pinto, V.I., V.W. Senini, Y. Wang, M.P. Kazembe, and C.A. McCulloch, Filamin a protects cells against force-induced apoptosis by stabilizing talin-and vinculin-containing cell adhesions. *The FASEB Journal*, 2014. **28**(1): p. 453-463.
107. Rape, A.D., W.-h. Guo, and Y.-l. Wang, The regulation of traction force in relation to cell shape and focal adhesions. *Biomaterials*, 2011. **32**(8): p. 2043-2051.
108. Jain, N., K.V. Iyer, A. Kumar, and G. Shivashankar, Cell geometric constraints induce modular gene-expression patterns via redistribution of hdac3 regulated by actomyosin contractility. *Proceedings of the National Academy of Sciences*, 2013. **110**(28): p. 11349-11354.
109. Solon, J., I. Levental, K. Sengupta, P.C. Georges, and P.A. Janmey, Fibroblast adaptation and stiffness matching to soft elastic substrates. *Biophysical Journal*, 2007. **93**(12): p. 4453-4461.
110. Mih, J.D., A. Marinkovic, F. Liu, A.S. Sharif, and D.J. Tschumperlin, Matrix stiffness reverses the effect of actomyosin tension on cell proliferation. *Journal of Cell Science*, 2012. **125**(24): p. 5974-5983.
111. Favaloro, B., N. Allocati, V. Graziano, C. Di Ilio, and V. De Laurenzi, Role of apoptosis in disease. *Aging*, 2012. **4**(5): p. 330.
112. Ananthakrishnan, R. and A. Ehrlicher, The forces behind cell movement. *International Journal of Biological Sciences*, 2007. **3**(5): p. 303.
113. Lemmon, C.A., C.S. Chen, and L.H. Romer, Cell traction forces direct fibronectin matrix assembly. *Biophysical Journal*, 2009. **96**(2): p. 729-738.
114. Harris, A.K., D. Stopak, and P. Wild, Fibroblast traction as a mechanism for collagen morphogenesis. 1981.
115. Beningo, K.A. and Y.-L. Wang, Flexible substrata for the detection of cellular traction forces. *Trends in Cell Biology*, 2002. **12**(2): p. 79-84.
116. Ladoux, B. and A. Nicolas, Physically based principles of cell adhesion mechanosensitivity in tissues. *Reports on Progress in Physics*, 2012. **75**(11): p. 116601.
117. Han, S.J., K.S. Bielawski, L.H. Ting, M.L. Rodriguez, and N.J. Sniadecki, Decoupling substrate stiffness, spread area, and micropost density: A close spatial relationship between traction forces and focal adhesions. *Biophysical Journal*, 2012. **103**(4): p. 640-648.
118. Chen, C., R. Krishnan, E. Zhou, A. Ramachandran, D. Tambe, K. Rajendran, R.M. Adam, L. Deng, and J.J. Fredberg, Fluidization and resolidification of the human bladder smooth muscle cell in response to transient stretch. *PLoS One*, 2010. **5**(8): p. e12035.
119. Mann, J.M., R.H. Lam, S. Weng, Y. Sun, and J. Fu, A silicone-based stretchable micropost array membrane for monitoring live-cell subcellular cytoskeletal response. *Lab on a Chip*, 2012. **12**(4): p. 731-740.
120. Shao, Y., J.M. Mann, W. Chen, and J. Fu, Global architecture of the f-actin cytoskeleton regulates cell shape-dependent endothelial mechanotransduction. *Integrative Biology*, 2014. **6**(3): p. 300-311.

121. Hubmayr, R.D., S.A. Shore, J.J. Fredberg, E. Planus, R. Panettieri, W. Moller, J. Heyder, and N. Wang, Pharmacological activation changes stiffness of cultured human airway smooth muscle cells. *American Journal of Physiology-Cell Physiology*, 1996. **271**(5): p. C1660-C1668.
122. Kilian, K.A., B. Bugarija, B.T. Lahn, and M. Mrksich, Geometric cues for directing the differentiation of mesenchymal stem cells. *Proceedings of the National Academy of Sciences*, 2010. **107**(11): p. 4872-4877.
123. Nelson, C.M., R.P. Jean, J.L. Tan, W.F. Liu, N.J. Sniadecki, A.A. Spector, and C.S. Chen, Emergent patterns of growth controlled by multicellular form and mechanics. *Proceedings of the National Academy of Sciences of the United States of America*, 2005. **102**(33): p. 11594-11599.
124. Aragona, M., T. Panciera, A. Manfrin, S. Giullitti, F. Michielin, N. Elvassore, S. Dupont, and S. Piccolo, A mechanical checkpoint controls multicellular growth through yap/taz regulation by actin-processing factors. *Cell*, 2013. **154**(5): p. 1047-1059.
125. Wan, L.Q., S.M. Kang, G. Eng, W.L. Grayson, X.L. Lu, B. Huo, J. Gimble, X.E. Guo, V.C. Mow, and G. Vunjak-Novakovic, Geometric control of human stem cell morphology and differentiation. *Integrative Biology*, 2010. **2**(7-8): p. 346-353.
126. Jungbauer, S., H. Gao, J.P. Spatz, and R. Kemkemer, Two characteristic regimes in frequency-dependent dynamic reorientation of fibroblasts on cyclically stretched substrates. *Biophysical Journal*, 2008. **95**(7): p. 3470-3478.
127. Driscoll, T.P., B.D. Cosgrove, S.-J. Heo, Z.E. Shurden, and R.L. Mauck, Cytoskeletal to nuclear strain transfer regulates yap signaling in mesenchymal stem cells. *Biophysical Journal*, 2015. **108**(12): p. 2783-2793.
128. Liu, F., D. Lagares, K.M. Choi, L. Stopfer, A. Marinković, V. Vrbanac, C.K. Probst, S.E. Hiemer, T.H. Sisson, and J.C. Horowitz, Mechanosignaling through yap and taz drives fibroblast activation and fibrosis. *American Journal of Physiology-Lung Cellular and Molecular Physiology*, 2015. **308**(4): p. L344-L357.
129. Lauffenburger, D.A. and A.F. Horwitz, Cell migration: A physically integrated molecular process. *Cell*, 1996. **84**(3): p. 359-369.
130. Tranquillo, R.T., M.A. Durrani, and A.G. Moon, Tissue engineering science: Consequences of cell traction force. *Cytotechnology*, 1992. **10**(3): p. 225-250.
131. Kapanci, Y., S. Burgan, G. Pietra, B. Conne, and G. Gabbiani, Modulation of actin isoform expression in alveolar myofibroblasts (contractile interstitial cells) during pulmonary hypertension. *The American Journal of Pathology*, 1990. **136**(4): p. 881.
132. Hinz, B., Tissue stiffness, latent tgf- β 1 activation, and mechanical signal transduction: Implications for the pathogenesis and treatment of fibrosis. *Current Rheumatology Reports*, 2009. **11**(2): p. 120-126.
133. Wang, J.H. and J.-S. Lin, Cell traction force and measurement methods. *Biomechanics and Modeling in Mechanobiology*, 2007. **6**(6): p. 361-371.
134. Wang, J.H. and B. Li, The principles and biological applications of cell traction force microscopy." 2010.
135. Yeung, T., P.C. Georges, L.A. Flanagan, B. Marg, M. Ortiz, M. Funaki, N. Zahir, W. Ming, V. Weaver, and P.A. Janmey, Effects of substrate stiffness on cell morphology, cytoskeletal structure, and adhesion. *Cell Motility and the Cytoskeleton*, 2005. **60**(1): p. 24-34.
136. Oakes, P.W., S. Banerjee, M.C. Marchetti, and M.L. Gardel, Geometry regulates traction stresses in adherent cells. *Biophysical Journal*, 2014. **107**(4): p. 825-833.
137. Quinlan, A.M.T., L.N. Sierad, A.K. Capulli, L.E. Firstenberg, and K.L. Billiar, Combining dynamic stretch and tunable stiffness to probe cell mechanobiology in vitro. *PloS One*, 2011. **6**(8): p. e23272.

138. Krishnan, R., C.Y. Park, Y.-C. Lin, J. Mead, R.T. Jaspers, X. Trepata, G. Lenormand, D. Tambe, A.V. Smolensky, and A.H. Knoll, Reinforcement versus fluidization in cytoskeletal mechanoresponsiveness. *PLoS One*, 2009. **4**(5): p. e5486.
139. Nagayama, K., A. Adachi, and T. Matsumoto, Heterogeneous response of traction force at focal adhesions of vascular smooth muscle cells subjected to macroscopic stretch on a micropillar substrate. *Journal of Biomechanics*, 2011. **44**(15): p. 2699-2705.
140. Wang, N., I.M. Tolić-Nørrelykke, J. Chen, S.M. Mijailovich, J.P. Butler, J.J. Fredberg, and D. Stamenović, Cell prestress. I. Stiffness and prestress are closely associated in adherent contractile cells. *American Journal of Physiology- Cell physiology*, 2002. **282**(3): p. C606-616.
141. Krishnan, R., E.P. Canović, A.L. Iordan, K. Rajendran, G. Manomohan, A.P. Pirentis, M.L. Smith, J.P. Butler, J.J. Fredberg, and D. Stamenović, Fluidization, resolidification, and reorientation of the endothelial cell in response to slow tidal stretches. *American Journal of Physiology-Cell Physiology*, 2012. **303**(4): p. C368-C375.
142. Schneider, C.A., W.S. Rasband, and K.W. Eliceiri, NIH image to imageJ: 25 years of image analysis. *Nature Methods*, 2012. **9**(7): p. 671-675.
143. Frey, M.T., I.Y. Tsai, T.P. Russell, S.K. Hanks, and Y.-I. Wang, Cellular responses to substrate topography: Role of myosin II and focal adhesion kinase. *Biophysical Journal*, 2006. **90**(10): p. 3774-3782.
144. Goldwyn, A.M., P. Kaiser, J.P. Spatz, C. Ballestrem, and R. Kemkemer, The kinetics of force-induced cell reorganization depend on microtubules and actin. *Cytoskeleton*, 2010. **67**(4): p. 241-250.
145. Pender, N. and C. McCulloch, Quantitation of actin polymerization in two human fibroblast sub-types responding to mechanical stretching. *Journal of Cell Science*, 1991. **100**(1): p. 187-193.
146. Costa, K.D., W.J. Hucker, and F.C. Yin, Buckling of actin stress fibers: A new wrinkle in the cytoskeletal tapestry. *Cell Motility and the Cytoskeleton*, 2002. **52**(4): p. 266-274.
147. Trepata, X., L. Deng, S.S. An, D. Navajas, D.J. Tschumperlin, W.T. Gerthoffer, J.P. Butler, and J.J. Fredberg, Universal physical responses to stretch in the living cell. *Nature*, 2007. **447**(7144): p. 592-595.
148. Gavara, N., P. Roca-Cusachs, R. Sunyer, R. Farré, and D. Navajas, Mapping cell-matrix stresses during stretch reveals inelastic reorganization of the cytoskeleton. *Biophysical Journal*, 2008. **95**(1): p. 464-471.
149. Pirentis, A.P., E. Peruski, A.L. Iordan, and D. Stamenović, A model for stress fiber realignment caused by cytoskeletal fluidization during cyclic stretching. *Cellular and Molecular Bioengineering*, 2011. **4**(1): p. 67-80.
150. Hayakawa, K., N. Sato, and T. Obinata, Dynamic reorientation of cultured cells and stress fibers under mechanical stress from periodic stretching. *Experimental Cell Research*, 2001. **268**(1): p. 104-114.
151. Kaunas, R., P. Nguyen, S. Usami, and S. Chien, Cooperative effects of rho and mechanical stretch on stress fiber organization. *Proceedings of the National Academy of Sciences of the United States of America*, 2005. **102**(44): p. 15895-15900.
152. Wang, J.H.-C., P. Goldschmidt-Clermont, J. Wille, and F.C.-P. Yin, Specificity of endothelial cell reorientation in response to cyclic mechanical stretching. *Journal of Biomechanics*, 2001. **34**(12): p. 1563-1572.
153. Iba, T. and B.E. Sumpio, Morphological response of human endothelial cells subjected to cyclic strain *in vitro*. *Microvascular Research*, 1991. **42**(3): p. 245-254.

154. Yoshigi, M., E.B. Clark, and H.J. Yost, Quantification of stretch-induced cytoskeletal remodeling in vascular endothelial cells by image processing. *Cytometry Part A*, 2003. **55**(2): p. 109-118.
155. Dartsch, P., H. Hämmerle, and E. Betz, Orientation of cultured arterial smooth muscle cells growing on cyclically stretched substrates. *Cells Tissues Organs*, 1986. **125**(2): p. 108-113.
156. Faust, U., N. Hampe, W. Rubner, N. Kirchgessner, S. Safran, B. Hoffmann, and R. Merkel, Cyclic stress at mhz frequencies aligns fibroblasts in direction of zero strain. *PLoS One*, 2011. **6**(12): p. e28963.
157. Goffin, J.M., P. Pittet, G. Csucs, J.W. Lussi, J.-J. Meister, and B. Hinz, Focal adhesion size controls tension-dependent recruitment of α -smooth muscle actin to stress fibers. *The Journal of Cell Biology*, 2006. **172**(2): p. 259-268.
158. Kaunas, R. and S. Deguchi, Multiple roles for myosin ii in tensional homeostasis under mechanical loading. *Cellular and Molecular Bioengineering*, 2011. **4**(2): p. 182-191.
159. Shu, S., X. Liu, and E.D. Korn, Blebbistatin and blebbistatin-inactivated myosin ii inhibit myosin ii-independent processes in dictyostelium. *Proceedings of the National Academy of Sciences of the United States of America*, 2005. **102**(5): p. 1472-1477.
160. Hsu, H.-J., C.-F. Lee, and R. Kaunas, A dynamic stochastic model of frequency-dependent stress fiber alignment induced by cyclic stretch. *PLoS One*, 2009. **4**(3): p. e4853.
161. De, R., A. Zemel, and S.A. Safran, Dynamics of cell orientation. *Nature Physics*, 2007. **3**(9): p. 655-659.
162. Wei, Z., V.S. Deshpande, R.M. McMeeking, and A.G. Evans, Analysis and interpretation of stress fiber organization in cells subject to cyclic stretch. *Journal of Biomechanical engineering*, 2008. **130**(3): p. 031009.
163. Northrup, W.F., K.A. DuBois, V.R. Kshetry, J. Teskey, and D. Nicoloff, Trends in aortic valve surgery in a large multi-surgeon, multi-hospital practice, 1979-1999. *Journal of Heart Valve Disease*, 2002. **11**(6): p. 768-779.
164. Cloyd, K.L., I. El-Hamamsy, S. Boonrungsiman, M.A. Hedegaard, E. Gentleman, P. Sarathchandra, F. Colazzo, M.M. Gentleman, M.H. Yacoub, and A.H. Chester, Characterization of porcine aortic valvular interstitial cell 'calcified' nodules. *PLoS One*, 2012. **7**(10).
165. Krishnan, R., D.D. Klumpers, C.Y. Park, K. Rajendran, X. Trepate, J. Van Bezu, V.W. Van Hinsbergh, C.V. Carman, J.D. Brain, and J.J. Fredberg, Substrate stiffening promotes endothelial monolayer disruption through enhanced physical forces. *American Journal of Physiology-Cell Physiology*, 2011. **300**(1): p. C146-C154.
166. Moussus, M., C. der Loughian, D. Fuard, M. Courçon, D. Gulino-Debrac, H. Delanoë-Ayari, and A. Nicolas, Intracellular stresses in patterned cell assemblies. *Soft matter*, 2014. **10**(14): p. 2414-2423.
167. Clement, A.L., T.J. Moutinho, and G.D. Pins, Micropatterned dermal–epidermal regeneration matrices create functional niches that enhance epidermal morphogenesis. *Acta Biomaterialia*, 2013. **9**(12): p. 9474-9484.
168. Gould, R.A. and J.T. Butcher, Isolation of valvular endothelial cells. *Journal of Visualized Experiments: JoVE*, 2010(46).
169. Gregory, C.A., W.G. Gunn, A. Peister, and D.J. Prockop, An alizarin red-based assay of mineralization by adherent cells in culture: Comparison with cetylpyridinium chloride extraction. *Analytical Biochemistry*, 2004. **329**(1): p. 77-84.
170. Dike, L.E., C.S. Chen, M. Mrksich, J. Tien, G.M. Whitesides, and D.E. Ingber, Geometric control of switching between growth, apoptosis, and differentiation during angiogenesis

- using micropatterned substrates. *In Vitro Cellular & Developmental Biology-Animal*, 1999. **35**(8): p. 441-448.
171. Leach, R., Z. Schwartz, T. Johnson-Pais, D. Dean, M. Luna, and B. Boyan, Osteosarcoma hybrids can preferentially target alkaline phosphatase activity to matrix vesicles: Evidence for independent membrane biogenesis. *Journal of Bone and Mineral Research*, 1995. **10**(11): p. 1614-1624.
 172. Golub, E.E., Role of matrix vesicles in biomineralization. *Biochimica et Biophysica Acta - General Subjects*, 2009. **1790**(12): p. 1592-1598.
 173. He, S., C. Liu, X. Li, S. Ma, B. Huo, and B. Ji, Dissecting collective cell behavior in polarization and alignment on micropatterned substrates. *Biophysical Journal*, 2015. **109**(3): p. 489-500.
 174. Gould, S.T., N.J. Darling, and K.S. Anseth, Small peptide functionalized thiol-ene hydrogels as culture substrates for understanding valvular interstitial cell activation and de novo tissue deposition. *Acta Biomaterialia*, 2012. **8**(9): p. 3201-3209.
 175. Monzack, E.L., X. Gu, and K.S. Masters, Efficacy of simvastatin treatment of valvular interstitial cells varies with the extracellular environment. *Arteriosclerosis, Thrombosis, and Vascular Biology*, 2009. **29**(2): p. 246-253.
 176. Wu, B., S. Elmariah, F.S. Kaplan, G. Cheng, and E.R. Mohler, Paradoxical effects of statins on aortic valve myofibroblasts and osteoblasts implications for end-stage valvular heart disease. *Arteriosclerosis, Thrombosis, and Vascular Biology*, 2005. **25**(3): p. 592-597.
 177. Halder, G., S. Dupont, and S. Piccolo, Transduction of mechanical and cytoskeletal cues by yap and taz. *Nature reviews Molecular Cell Biology*, 2012. **13**(9): p. 591-600.
 178. Liu, C., S. He, X. Li, B. Huo, and B. Ji, Mechanics of cell mechanosensing on patterned substrate. *Journal of Applied Mechanics*, 2016. **83**(5): p. 051014.
 179. Deguchi, S., T. Ohashi, and M. Sato, Tensile properties of single stress fibers isolated from cultured vascular smooth muscle cells. *Journal of Biomechanics*, 2006. **39**(14): p. 2603-2610.
 180. Mammoto, T. and D.E. Ingber, Mechanical control of tissue and organ development. *Development*, 2010. **137**(9): p. 1407-1420.
 181. Nienhaus, U., T. Aegerter-Wilmsen, and C.M. Aegerter, Determination of mechanical stress distribution in drosophila wing discs using photoelasticity. *Mechanisms of Development*, 2009. **126**(11): p. 942-949.
 182. Musicco, M., F. Adorni, S. Di Santo, F. Prinelli, C. Pettenati, C. Caltagirone, K. Palmer, and A. Russo, Inverse occurrence of cancer and alzheimer disease a population-based incidence study. *Neurology*, 2013. **81**(4): p. 322-328.
 183. Xu, W., R. Mezencev, B. Kim, L. Wang, J. McDonald, and T. Sulchek, Cell stiffness is a biomarker of the metastatic potential of ovarian cancer cells. *PLoS one*, 2012. **7**(10): p. e46609.
 184. Swaminathan, V., K. Mythreye, E.T. O'Brien, A. Berchuck, G.C. Blobe, and R. Superfine, Mechanical stiffness grades metastatic potential in patient tumor cells and in cancer cell lines. *Cancer Research*, 2011. **71**(15): p. 5075-5080.
 185. Cheng, G., J. Tse, R.K. Jain, and L.L. Munn, Micro-environmental mechanical stress controls tumor spheroid size and morphology by suppressing proliferation and inducing apoptosis in cancer cells. *PLoS one*, 2009. **4**(2): p. e4632.
 186. Serra-Picamal, X., V. Conte, R. Vincent, E. Anon, D.T. Tambe, E. Bazellieres, J.P. Butler, J.J. Fredberg, and X. Trepat, Mechanical waves during tissue expansion. *Nature Physics*, 2012. **8**(8): p. 628-634.
 187. Trepat, X., M.R. Wasserman, T.E. Angelini, E. Millet, D.A. Weitz, J.P. Butler, and J.J. Fredberg, Physical forces during collective cell migration. *Nature Physics*, 2009. **5**(6): p. 426-430.

188. Zemel, A., F. Rehfeldt, A. Brown, D. Discher, and S. Safran, Optimal matrix rigidity for stress-fibre polarization in stem cells. *Nature Physics*, 2010. **6**(6): p. 468-473.
189. Brewster, C.E., P.H. Howarth, R. Djukanovic, J. Wilson, S.T. Holgate, and W.R. Roche, Myofibroblasts and subepithelial fibrosis in bronchial asthma. *American Journal of Respiratory Cell and Molecular Biology*, 1990. **3**(5): p. 507-511.
190. Huang, C. and R. Ogawa, Fibroproliferative disorders and their mechanobiology. *Connective tissue research*, 2012. **53**(3): p. 187-196.
191. Piersma, B., S. de Rond, P.M. Werker, S. Boo, B. Hinz, M.M. van Beuge, and R.A. Bank, Yap1 is a driver of myofibroblast differentiation in normal and diseased fibroblasts. *The American journal of pathology*, 2015. **185**(12): p. 3326-3337.
192. Lee, M.-J., M.R. Byun, M. Furutani-Seiki, J.-H. Hong, and H.-S. Jung, Yap and taz regulate skin wound healing. *Journal of Investigative Dermatology*, 2014. **134**(2): p. 518-525.
193. Cordenonsi, M., F. Zanconato, L. Azzolin, M. Forcato, A. Rosato, C. Frasson, M. Inui, M. Montagner, A.R. Parenti, and A. Poletti, The hippo transducer taz confers cancer stem cell-related traits on breast cancer cells. *Cell*, 2011. **147**(4): p. 759-772.
194. Dupont, S., L. Morsut, M. Aragona, E. Enzo, S. Giulitti, M. Cordenonsi, F. Zanconato, J. Le Digabel, M. Forcato, and S. Bicciato, Role of yap/taz in mechanotransduction. *Nature*, 2011. **474**(7350): p. 179-183.
195. Wang, J., A. Seth, and C. McCulloch, Force regulates smooth muscle actin in cardiac fibroblasts. *American Journal of Physiology-Heart and Circulatory Physiology*, 2000. **279**(6): p. H2776-H2785.
196. Goldenheim, P., D. Donigi-Gale, R. Sackler, P. Lacouture, and M. Chasin, *Administration of microparticles in a form suitable for injection and containing active agents suitable for treating or diagnosing a disease or painful condition in joints in a patient in need, safe and effective procedure; sustained*, 2003, Google Patents.
197. Lamprecht, A., H.R. Torres, U. Schäfer, and C.-M. Lehr, Biodegradable microparticles as a two-drug controlled release formulation: A potential treatment of inflammatory bowel disease. *Journal of Controlled Release*, 2000. **69**(3): p. 445-454.
198. Martinez, M.C., S. Tual-Chalot, D. Leonetti, and R. Andriantsitohaina, Microparticles: Targets and tools in cardiovascular disease. *Trends in pharmacological sciences*, 2011. **32**(11): p. 659-665.
199. Ganz, A., M. Lambert, A. Saez, P. Silberzan, A. Buguin, R.M. Mège, and B. Ladoux, Traction forces exerted through n-cadherin contacts. *Biology of the Cell*, 2006. **98**(12): p. 721-730.
200. Emad, A., W.F. Heinz, M.D. Antonik, N.P. D'Costa, S. Nageswaran, C.-A. Schoenenberger, and J.H. Hoh, Relative microelastic mapping of living cells by atomic force microscopy. *Biophysical Journal*, 1998. **74**(3): p. 1564-1578.
201. Kural, M.H. and K.L. Billiar, Mechanoregulation of valvular interstitial cell phenotype in the third dimension. *Biomaterials*, 2014. **35**(4): p. 1128-1137.
202. Butler, J.P., I.M. Tolić-Nørrelykke, B. Fabry, and J.J. Fredberg, Traction fields, moments, and strain energy that cells exert on their surroundings. *American Journal of Physiology-Cell Physiology*, 2002. **282**(3): p. C595-C605.
203. Benton, J.A., B.D. Fairbanks, and K.S. Anseth, Characterization of valvular interstitial cell function in three dimensional matrix metalloproteinase degradable peg hydrogels. *Biomaterials*, 2009. **30**(34): p. 6593-6603.
204. Duan, B., L.A. Hockaday, E. Kapetanovic, K.H. Kang, and J.T. Butcher, Stiffness and adhesivity control aortic valve interstitial cell behavior within hyaluronic acid based hydrogels. *Acta biomaterialia*, 2013. **9**(8): p. 7640-7650.

205. Benton, J.A., C.A. DeForest, V. Vivekanandan, and K.S. Anseth, Photocrosslinking of gelatin macromers to synthesize porous hydrogels that promote valvular interstitial cell function. *Tissue Engineering Part A*, 2009. **15**(11): p. 3221-3230.
206. Buxboim, A., K. Rajagopal, B. Andre'EX, and D.E. Discher, How deeply cells feel: Methods for thin gels. *Journal of Physics: Condensed Matter*, 2010. **22**(19): p. 194116.
207. Cooper, D., Y. Ye, L. Rolf Jr, and N. Zuhdi, The pig as potential organ donor for man in *Xenotransplantation*. 1991, *Springer*. p. 481-500.
208. Crick, S.J., M.N. Sheppard, S.Y. HO, L. Gebstein, and R.H. Anderson, Anatomy of the pig heart: Comparisons with normal human cardiac structure. *Journal of Anatomy*, 1998. **193**(01): p. 105-119.
209. Sands, M.P., E.A. Rittenhouse, H. Mohri, and K.A. Merendino, An anatomical comparison of human, pig, calf, and sheep aortic valves. *The Annals of Thoracic surgery*, 1969. **8**(5): p. 407-414.
210. Engler, A., L. Bacakova, C. Newman, A. Hategan, M. Griffin, and D. Discher, Substrate compliance versus ligand density in cell on gel responses. *Biophysical Journal*, 2004. **86**(1): p. 617-628.
211. Gu, X. and K.S. Masters, Regulation of valvular interstitial cell calcification by adhesive peptide sequences. *Journal of Biomedical Materials Research Part A*, 2010. **93**(4): p. 1620-1630.
212. Schoen, F., Aortic valve structure-function correlations: Role of elastic fibers no longer a stretch of the imagination. *The Journal of Heart Valve Disease*, 1997. **6**(1): p. 1-6.
213. Schenke-Layland, K., I. Riemann, F. Opitz, K. König, K. Halbhuber, and U. Stock, Comparative study of cellular and extracellular matrix composition of native and tissue engineered heart valves. *Matrix Biology*, 2004. **23**(2): p. 113-125.
214. Maruthamuthu, V., B. Sabass, U.S. Schwarz, and M.L. Gardel, Cell-ecm traction force modulates endogenous tension at cell-cell contacts. *Proceedings of the National Academy of Sciences*, 2011. **108**(12): p. 4708-4713.
215. Zhao, B., L. Li, L. Wang, C.-Y. Wang, J. Yu, and K.-L. Guan, Cell detachment activates the hippo pathway via cytoskeleton reorganization to induce anoikis. *Genes & Development*, 2012. **26**(1): p. 54-68.
216. Alarcón, C., A.-I. Zaromytidou, Q. Xi, S. Gao, J. Yu, S. Fujisawa, A. Barlas, A.N. Miller, K. Manova-Todorova, and M.J. Macias, Nuclear cdks drive smad transcriptional activation and turnover in BMP and TGF- β pathways. *Cell*, 2009. **139**(4): p. 757-769.
217. Varelas, X., P. Samavarchi-Tehrani, M. Narimatsu, A. Weiss, K. Cockburn, B.G. Larsen, J. Rossant, and J.L. Wrana, The crumbs complex couples cell density sensing to hippo-dependent control of the TGF- β -smad pathway. *Developmental cell*, 2010. **19**(6): p. 831-844.
218. Zhao, B., X. Ye, J. Yu, L. Li, W. Li, S. Li, J. Yu, J.D. Lin, C.-Y. Wang, and A.M. Chinnaiyan, Tead mediates yap-dependent gene induction and growth control. *Genes & Development*, 2008. **22**(14): p. 1962-1971.
219. Rossebø, A.B., T.R. Pedersen, K. Boman, P. Brudi, J.B. Chambers, K. Egstrup, E. Gerds, C. Gohlke-Bärwolf, I. Holme, and Y.A. Kesäniemi, Intensive lipid lowering with simvastatin and ezetimibe in aortic stenosis. *New England Journal of Medicine*, 2008. **359**(13): p. 1343-1356.
220. Gerds, E., A.B. Rossebø, T.R. Pedersen, K. Boman, P. Brudi, J.B. Chambers, K. Egstrup, C. Gohlke-Bärwolf, I. Holme, and Y.A. Kesäniemi, Impact of baseline severity of aortic valve stenosis on effect of intensive lipid lowering therapy (from the seas study). *The American Journal of Cardiology*, 2010. **106**(11): p. 1634-1639.

221. Chan, K.L., K. Teo, J.G. Dumesnil, A. Ni, and J. Tam, Effect of lipid lowering with rosuvastatin on progression of aortic stenosis results of the aortic stenosis progression observation: Measuring effects of rosuvastatin (astronomer) trial. *Circulation*, 2010. **121**(2): p. 306-314.
222. Otero, E.U., S. Sathaiyah, L. Silveira, P.M.A. Pomerantzeff, and C.A.G. Pasqualucci, Raman spectroscopy for diagnosis of calcification in human heart valves. *Journal of Spectroscopy*, 2004. **18**(1): p. 75-84.
223. Aoun, L., P. Weiss, A. Laborde, B. Ducommun, V. Lobjois, and C. Vieu, Microdevice arrays of high aspect ratio poly (dimethylsiloxane) pillars for the investigation of multicellular tumour spheroid mechanical properties. *Lab on a Chip*, 2014. **14**(13): p. 2344-2353.

Appendix A

A.1 Valvular Interstitial Cell Isolation Protocol

Protocol modified from:

Gould R.A., Butcher J.T. (2010). Isolation of Valvular Endothelial Cells. JoVE. 46.
<http://www.jove.com/details.php?id=2158>, doi: 10.3791/2158

Preparation (do day before tissue harvest)

1. Autoclave:
 - a. Serrated tissue forceps
 - b. Tissue scissors
 - c. Cotton swaps
2. Make Sterile Collagenase media
 - a. Use normal media 10% FBS +1% Anti-Anti in DMEM
 - b. Measure 600 U/ml collagenase II
 - c. Add collagenase type II to media
 - d. Filter sterile
 - e. Keep on rocker to ensure homogenized solution

Steps to isolate valve leaflets

1. Excise the aortic root
2. Thoroughly rinse the aortic root with cold sterile, DPBS
3. Isolate valve leaflets (3 per valve) from the root and place directly in sterile 15 ml conical tube filled with 12 mL cold DPBS
4. Shake several times to remove debris
5. Keep on ice
6. Place tissues in sterile hood

Steps to isolate valvular interstitial cells

1. Fill a sterile 15 mL centrifuge tube with 10 mL collagenase solution per valve
2. Immediately place them in the appropriate 15 mL conical tube with collagenase solution
3. Make sure to check the samples after 6 hours. If sufficient digestion has occurred at 6 hours, immediately proceed to step 4.
4. Mix the degraded tissue gently with a stereological pipette until the cell suspension becomes homogenized
5. Centrifuge the digest for 5 min at 1000 rpm and aspirate the supernatant
6. Add 5mL of media to the tube and centrifuge a second time, and aspirate the suspernatent

7. Re-suspend the centrifuged endothelial cells in 5 mL of porcine media and plate in a T-75 flask
8. Let the cells grow 1-2 days before changing the media. Tissue debris is normal.

A.2 PDMS Well Mold Design

The PDMS well mold design was built off of a design made by an MQP team. For details of their design as well as finite element modeling of strain fields with applied stretch please refer to their capstone report available at the WPI library. *Advanced Cell Culture Well for Mechanobiology* by: Jeffery Pruden, Jennifer Mann, Jeffery Kelly, and Daniela Garcia.

A.3 Creation of PDMS wells, releasing wells from mold, and cleaning mold

Protocol developed by Heather Cirka, modified from Jennifer Mann (WPI MQP team 2012)

The purpose of this experiment is to create PDMS wells which can be used with the cell stretch device. PDMS wells are able to be treated so they can attach to polyacrylamide gels (see appendix D) to allow for traction force studies. It has been noted that 1:10 PDMS was too rigid and ripped when stretched 10%, therefore, 1:15 PDMS (crosslinker:base mass ratio) was used for uniaxial experiments and 1:20 PDMS was used for equibiaxial experiments

Materials:

- Well Mold (3 pieces of polycarbonate)
- Metal Spacer
- 5 x ¼ inch No. 8 screws
- 4 x 1 inch No. 6 screws
- Polydimethylsiloxane base and crosslinker –Sylgard 184
- Balance
- Weigh boat
- Transfer pipette
- Vacuum dessicator
- House vacuum
- ½ inch long metal pins

Methods:

Creating PDMS wells

Place weigh boat on balance and tare machine

Measure enough PDMS base to fill the four well mold. (About 60 g) into weigh boat

Add desired amount of cross-liner. For 60g and wells for uniaxial experiments, add 4 g of crosslinker

Mix vigorously and thoroughly with transfer pipette

Place weighboat in dessicator under house vacuum for 1 hour

While under vacuum, prepare the mold:

Ensure that the mold is clean, take care not to scratch the bottom surface of the mold as it will effect stretch of the wells. It is better to use your fingers to rub off PDMS from previous runs than kim wipes or paper towels

Using ¼ inch No. 8 screws, screw together bottom piece, metal spacer and middle piece

When PDMS has been under vacuum for one hour, carefully pour PDMS into mold. *Take care as to not form any bubbles*

If bubbles do form, use N₂ gas air gun or scapel blade to pop them. Additionally, mold can be placed in dessicator (Pins lab) for one hour to remove any bubbles

Carefully top of mold ontop of PDMS, again *take care as to not form any bubbles as bubbles formed with the cover are even more difficult to remove.*

Secure top of mold with 4 x 1 inch No. 6 screws. ***Do not over tighen screws!!*** Over tightening the screws “arcs” the top plate and you well will have an un even thickenss

Place mold onto two test tube holders so that the sides are supported and the mold is level. If the mold is tilted, wells will not be a uniform thickness

Heat oven to 65 degrees. Allow PDMS to polymerize for five hours. ***Best results were found for molds polymerized at 5 hours, do not leave molds overnight.***

Remove from oven and place on bench top to cool to room temperature

Removing polymerized wells from mold

Extreme care must be taken when removing well from the molds as the molds are very delicate and the bottom membrane is easily torn. If difficult is found with removing the wells, the mold can be coated with a silence (details below). One coating of the silane is good for many runs of making molds.

Ensure that the mold has cooled to room temperature. Do not attempt to remove the wells if the mold is warm.

Fill a glass pyrex dish with 70% ethanol and completely submerge the well.

Using pliers remove metal pins, wipe pins with kim wipe to remove ethanol and prevent rusting

Remove screws holding top mold and bottom mold in place

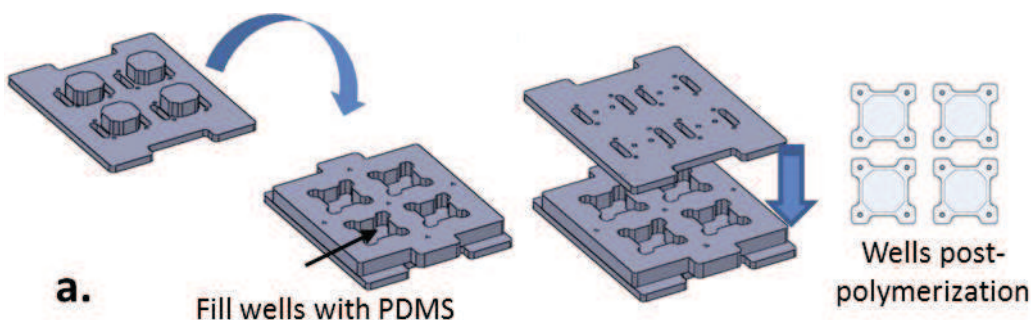
Let mold sit undisturbed in ethanol for 5-15 minutes.

Gently pull up on bottom layer mold, alternate sides to be even, bottom layer of mold should easily release.

Using scalpel blade, liberate the metal spacer carefully from the PDMS. Take care not to tear the membranes.

Push corners of wells through the middle layer of the mold to the top of the mold side. Carefully pull up on mold to pull wells “through” the middle layer and separate the middle layer from the top. Sometimes wells attach to the inserts of the top layer of the mold, but should peel away easily

Schematic of custom PDMS mold creation:



Notes: If wells are difficult to release, mold may be put into -20 for one hour and then brought up to room temperature for one hour prior to removal of wells. Working with the mold when its not at room temperature can lead to breaking of the mold.

Additionally, if mold is still difficult to separate, mold can be silanized with a silane

Very Important! There is an established vacuum dessicator for this! MUST BE DONE IN THE HOOD. Silane is a carcinogen and very dangerous to your lungs.

Cleaning Mold

Care must be taken to clean the mold in between “runs”. If any PDMS is left on the mold, particularly the metal spacer, the wells will have an altered thickness, and potentially un-uniform thickness

It is recommended that you do not use kim wipes, paper towels, or any

A.4 Attachment of polyacrylamide gels onto the PDMS wells

Materials:

- 4 custom PDMS culture wells (see Appendix C for instructions)
- 22mm circular glass coverslips (with evaporated bead solution if doing traction force)
- 30 mm diameter o-rings (diameter dimension not critical)
- Glass syringe with gradations (200ul)
- Glass pipettes with gradations (10ml)
- Pipet-Aid
- Plasma Prep, plasma oxidizer (chem. dept)
- 3-(Trichlorosilyl)propyl methacrylate (TPM, Sigma 64205, store in fridge under desiccator and N₂)

- Heptane
- Carbon tetrachloride
- Hexane
- Vacuum
- Vacuum desiccator
- 40% Acrylamide (Biorad) - refrigerator
- 2% Bis-acrylamide (Biorad) - refrigerator
- 1x PBS
- TEMED (Biorad) – Chemical shelf
- 10% aqueous solution of APS in DI (aliquots store in -20)
- Nitrogen tank
- 50 mM HEPES pH to 8.2
- Molecular Sieves (Fluka 69839)
- 1.7 ml eppendorf tube
- 0.65 eppendorf tube
- Test tube rack
- Glass peri dish
- Timer
- Vortex machine

Chemical Hood Prep:

Place the following items in or near the chemical hood:

- Vacuum dessicator
- Glass pippets
- Glass syringes
- Manual pippettor
- TPM
- Glass syringe
- Carbon Tetrachloride
- Hexane
- Heptane
- Waste container (all chemicals can be combined into a single waste container)

1b. label the glass pippets with tape. 'Hexane', 'Heptane' 'Carbon Tetrachloride' and 'Waste'

2. Mass 1g molecular sieves and place in eppendorf tube.

3. Using the glass pipettes and manual pippettor, measure 16 ml heptane and add 4 ml carbon tetrachloride into 50 ml beaker

4. dump 1g molecular sieves into beaker

5. cover solution with larger beaker, so that it does not evaporate.

Plasma treatment of the flexcell plate is time sensitive, after this operation, everything must be done quickly.

Making Polyacrylamide gel solution

Method was adapted from Wen lab

Materials:

- 40% acrylamide solution
- 2% acrylamide solution
- TEMED
- HEPES pH 8.2
- 10% APS aliquot from freezer and kept on ice
- Vortex machine
- 0.65 mL test tube
- 1.7 mL test tube

Methods:

Make 'stock solution' in 1.7 ml Eppendorf tube

Depending on the stiffness, add correct amount of acrylamide, bis-acrylamide, and HEPES (pH to 8.2) totaling 1 ml of solution 1.7 ml Eppendorf tube

Vortex polyacrylamide stock solution

Add 250 μ L of stock solution to 0.65 mL Eppendorf tube

Add 0.9 μ L of TEMED to 0.65 mL tube

Do not add APS until you are ready to have the gel polymerize

Vortex the 10% APS solution, then add 2.5 μ L of 10% APS to the PA gel solution in the 0.65 mL tube

Solution should polymerize within 7 minutes

Plasma treatment of PDMS wells

Materials:

- Plasma machine (Chemistry department)
- PDMS wells

Directions:

Take note of the plasma prep machine. The vacuum and 'on' switches are down and the 'meter' switch is up. The level knob should be turned completely to the left.

1. Open gas regulator
2. turn on plasma prep machine by pressing large square red button
3. allow the machine to run for three minutes (to warm up). The longer you are able to run it, the better the results may be.
4. carefully remove sample container from device. Place slits facing downward.
5. put uncovered PDMS wells (they should not be in a petri) glass sample container, make sure the sample is level for equal plasma treatment on all surfaces
6. replace sample container *CAREFULLY* as to not damage the glass rod
7. to turn on vacuum pump, flip vacuum switch up
8. Press gently on the sample container to ensure there is a tight seal
9. Close mesh door
10. Wait for the vacuum pressure to stabilize.
11. Flip the on switch up
12. Turn the level knob to 40
13. Adjust the tuning knob until there is a magenta glow around the sample.
14. turn level knob to maximum
15. Adjust with tuning knob until there is no noise and the plasma is bright purple (it will soon switch to bright blue once all the air in the container has been removed)
16. Set timer for 2 minutes, start timer at this point
17. after two minutes has past, turn level knob all the way to the left.
18. Flip 'on' and 'vacuum' switches off in that order
19. turn off vacuum pump
20. wait for the vacuum to release. DO NOT TURN OFF PLASMA PREP UNTIL VACUUM HAS RELEASED. The machine must be on in order for the vacuum to release.
21. when the vacuum is released the sample container will slightly pop out.
22. carefully remove sample container, it might be warm/hot. Do so with caution

23. immediately cover treated PDMS wells. The surface is activated and will react with components in the air.

24. turn off plasma machine

25. close regulator

It is important to work quickly from this point forward. It has been noticed that the process of PA gels attaching to PDMS membranes works better when the building is not humid and not warm. To get desired results you may have to work after-hours when building is colder (in the winter). Difficulty was had attaching PA gels during the month of August 2014 when the weather was especially humid, no problems one month prior.

Chemical activation of custom PDMS wells

1. Using glass syringe (do not open container, puncture septum) remove 20 microliters of TPM.
2. Holding the syringe vertical just of the surface of the heptane/carbon tetrachloride mixture, expel the TPM and watch the drops fall into the beaker to confirm that there was indeed chemical in your syringe
3. Using glass pipette and pippetor mix the solution
4. place solution (use as much as possible without sucking the molecular sieves into your pipet tip) onto flexcell membranes . Solution should be divided evenly between the six wells. Cover the flexcell plate
5. The solution should be kept on the membrane for 5 minutes. While the solution is reacting with the membrane, take this time to clean the glass syringe (details on syringe cleaning at the end of this document)
6. The membranes will distort due to the chemical treatment and a white residue may deposit on the cover due to the reaction taking place.
7. Remove solution from wells via pipet tip and place in waste beaker/container
8. Rinse membrane with hexanes
9. Place the custom PDMS cell culture wells uncovered into the vacuum desiccator. Ensure that the valve is open. **WARNING: custom wells should be placed on an o-ring. Vacuum restores to original shape and they stick to shelf in desiccator as well as petri dishes. From this point forward, keep custom PDMS wells on o-rings for all work.**
10. Turn on vacuum pump

11. Within a few minutes you should not be able to lift the top of the lid of the desiccator due to the vacuum created
 12. Allow vacuum to pull for 5 minutes for flexcell to return to its normal geometry.
 13. During this time, return to the glass coverslips. Coat thoroughly with Rainx and dry with a kim wipe. Handle the coverslips as little as possible with your hands. Lay coverslips on a clean surface, such as a paper towel.
 14. After the 5 minutes, close valve and CAREFULLY remove vacuum hose (care is needed during this processes because the valve could pull out and expose your chamber to the Atmosphere. The vacuum will immediately be filled with air, causing much turbulence in the chamber and possible destroying your sample).
 15. Allow vacuum to run unattached to the chamber for several seconds before switching off
 16. Bring chamber to bench top. Attach to N₂ and let nitrogen flow through the sample
 17. Allow plate to sit under flow for 5 minutes
 18. Prepare your PA gels by adding 100 microliters APS and 1.5 microliters TEMED.
 19. Agitate eppendorf to ensure mixing of components. Do a couple of quick taps on the agitator, so as not over disturb the gel
 20. Place 50 microliters in the center of the well of the custom PDMS wells. (It is best to do all 6 wells at once)
 21. Using curved tweezers, pick up the coverslip. Hold coverslip in front of the flowing nitrogen to “rinse it” Gently lay the coverslip over the gel. Capillary action will wick the gel underneath the coverslip so you will have a circular gel.
 22. Once the coverslip is sitting on the gel, DO NOT MOVE IT to try and center the cell or adjust the gel for any reason
 23. Allow the gels to polymerize under nitrogen flow for 30 minutes. Leave undisturbed
 24. Turn off nitrogen and let gels sit undisturbed for another 15 minutes.
- The appropriate time to remove coverslips is when a ‘ring’ or space has formed underneath the coverslip. This means the gel has fully polymerized.
25. Removing the coverslip from the gel is an extremely delicate process. If the gel has not fully polymerized it will stick to the coverslip as it is removed. Release the gel from the coverslip by pressing GENTLY around the perimeter of the gel. For the custom cell culture wells, I found it easiest to remove the coverslip when the well was placed on the machine. It sometimes is helpful to add PBS

(or HEPES) prior to removing the coverslip). When applying pressure near the gel, you should see it visibly release from the coverslip. To remove the coverslip, push gently into the membrane until a tiny corner of the gel has released and the coverslip is free. Take a second pair of tweezers and grab the coverslip. Lift the coverslip off in one motion. Make sure that your cover slip does not fall onto the gel if you lose hold of it.

Special note: Gel that has not polymerized around the edges will look like a ruffle. This gel can be removed via tweezers.

26. Gels should be submerged in 1x PBS, covered, and stored in the refrigerator.

References:

Quinlan, A. M. T., Sierad, L. N., Capulli, A. K., Firstenberg, L. E., & Billiar, K. L. (2011). Combining dynamic stretch and tunable stiffness to probe cell mechanobiology in vitro. *PLoS one*, 6(8), e23272.

A.5: Activation of coverslips and glass slides of polyacrylamide gel attachment

Protocol from Wen lab

Materials:

- Glass coverslips (square 22mm and square 25mm is what was used most frequently in this dissertation)
- Aminopropyltrimethoxysilane (Sigma, product number)
- diH₂O
- Two 500 ml beakers
- 0.5% glutaraldehyde
- Ceramic coverslip rack
- Tweezers
- Plastic slide containers Tiny stir bar (should be able to spin freely without hitting any coverslips loaded in the ceramic rack)
- Timer
- Stir plate

Methods:

Fill one of the 500 ml beakers with 150 mL of diH₂O

Add 1.5 mL of Aminopropyltrimethoxysilane

Add tiny stir bar

Place beaker on stir plate, set the turn rate to XX rpm

Add coverslips of desired size to ceramic rack. Using tweezers carefully place into 1.5% aminopropyltrimethoxysilane solution for 30 minutes

Fill second beaker with diH₂O

When treatment time has completed, carefully lift up ceramic coverslip rack and dunk it several times into diH₂O. Excessive rinsing will remove the silane treatment; however two little rinsing will cause an undesirable reaction with gluteraldehyde

Transfer the coverslips to 0.5% gluteraldehyde coverslips storage containers. Keep in fridge until ready to use. Treatment is good for several months

Dispose of 1.5% aminopropyltrimethoxysilane solution in appropriate hazardous waste container

A.6: Creating PDMS Stamps

Materials:

- PDMS base and cross-linker
- Wafer of desired pattern
- Petri dish
- Vacuum desiccator
- Weigh boat
- Scapula for mixing
- Oven set to 55°

Methods:

1. Weigh out 10:1 PDMS (base to cross-linker ratio)
2. Mix thoroughly with a spatula
3. Place in vacuum dessicator, pull a vacuum for 15-20 minutes. Release the vacuum several times to remove bubbles
4. Pour over silicone wafer; ensure there are no bubbles. If bubble remain, place back in the vacuum for another 15 minutes releasing vacuum several times
5. Bake at 55 degrees for 3 hours
6. cool overnight prior to removing stamps

A.7: Preparing bead glass

The purpose of this protocol is to evaporate micro-beads onto glass coverslips. The coverslips can then be placed upon un-polymerized polyacrylamide gel droplets so that a uniform layer of beads becomes attached to the gel.

Materials:

- 100% ethanol
- Plasma cleaner (chemistry lab)

- Fluorescent microbeads, size, company product number
- 22 mm square coverslips. Note: 22 mm circular coverslips and 25 mm square coverslips have also been used
- 1.7 mL Eppendorf tube
- Vacuum Oven (Wen lab)
- Ceramic coverslip rack
- Sonicator
- 500 mL beaker
- Coverslip tweezers (electron microscopy science)
- Brass test tube rack, Wen lab (not critical, just to ensure that the coverslips have a level surface to rest on in the oven).

Methods:

Heat Oven to 140C- 150 C. The temperature is critical, too hot and bead solution evaporates causing bead clumping, too colder and beads clump together forming a cobble stone appearance

Create a 0.5% bead solution in an Eppendorf tube with 1 mL of 100% ethanol and 5 uL of bead solution.

Place coverslips in coverslip rack

Add to 500 mL with ethanol.

Place both the beaker with the coverslips and the Eppendorf tube in a sonicator for 5 minutes

After sonication, remove coverslips and place in oven to dry. When dry, using coverslip tweezers remove from the coverslip rack and place in a petri dish to carry to the UV plasma cleaner.

Place coverslips in plasma cleaner (for instructions on using the plasma cleaner see Appendix D)

Clean for 30s- 1 minute at full power. *Note:* use coverslips within 10 minutes after cleaning. Wait until oven is sufficiently hot prior to starting this step

Place 6 coverslips (no more than six at one time, if doing more see note below) on flat surface (brass test-tube rack) that is compatible with high temperature

Add 35 μ L of bead solution to 22 mm coverslip (if using different size coverslips, adjust volume accordingly)

Wait 10 seconds as the ethanol solution spreads out along the coverslip prior to placing in the oven

After placing in the oven, pull a vacuum until the gauge reads -20

Release vacuum, coverslips are ready to use.

Note: If doing more than six coverslips, the brass test tube rack must be cooled prior to re-use. I accomplished this by dumping it in the ice chest.

A.8 Preparing petri dishes for traction force measurement

Materials:

- Tissue culture polystyrene 60mm dishes or six well plate
- Metal Tissue biopsy punch (~20mm in diameter)
- Bunsen Burner (located in Lambert lab in Chemistry department)
- Oven mitt or other protection from the heat
- Lighter
- Razor Blade

Directions:

Take cover off of petri dish/6- well plate and over turn on bench top

Turn on gas and light Bunsen burner

Heat metal tissue biopsy punch (angle the punch so the tip is up, placing it tip down will direct the flame up towards your hand)

After sufficient heating time, approximately 15 seconds for first punch, apply gently pressure, constant pressure to underside of petri dish

The punch should glide through the material

One through, remove the punched material (inside the biopsy) immediately as if the punch is not hot it will be impossible to do so.

“Sand” rough edges around the punch with a razor blade, be careful not to create cracks in the hole as that will cause the dish to leak later on.

A.9 Micro-contact printing protocol

The protocol for microcontact printing has been broken up into two parts a) activation of polyacrylamide gels with hydrazine hydrate and b) micro-contact printing.

Protocol modified from Vesna Damljanovic

Part I: activation of polyacrylamide gels

Materials:

- Hydrazine hydrate (reagent grade, Sigma-Aldrich)
- Glacial acetic acid (Fluka/Sigma-Aldrich)
- Tweezers

- Ceramic rack
- Three 500 mL beakers
- Glassware for hydrazine hydrate
- Note 1: it is best that all glass ware used for activation with hydrazine hydrate be used only for this activation protocol and kept separate from other laboratory equipment. Hydrazine hydrate is extremely carcinogenic and should only be used in a fume hood.
- Note 2: Hydrazine hydrate comes at 78-82% solution. 55% Hydrazine hydrate was used for activation for all gels in this thesis.

Methods:

1. In the hood, place 3 500 mL beakers. Fill one with 55% hydrazine hydrate, one with 0.05 N acetic acid, and one with di H₂O
2. Fill the ceramic rack with coverslips with gels attached
3. Using tweezers, carefully lower ceramic rack into hydrazine hydrate
4. Allow gels to sit in hydrazine hydrate undisturbed for 2-4 hours
5. After incubation in the hydrazine hydrate, move ceramic rack to 0.05 N acetic acid. Carefully dispose of hydrazine hydrate in the appropriate waste container
6. Incubate gels in acetic acid for 1 hour. At the end of incubation time, transfer gels to diH₂O and allow to rinse for one hour.
7. Store gels in PBS wrapped in parafilm until ready for micro-contact printing. Gels will remain activated for several months.

Part 2: Micro-contact printing

Materials

- 0.1 N Glacial acetic acid
 - Type I collagen (bovine, biomatrix)
 - Sodium acetate
 - Sodium n-periodontate
 - Alexa 488 collagen conjugate (if labeling)
 - PDMS stamps for micro-contact printing
 - Compressed Nitrogen with air gun
1. Prepare and filter sodium acetate buffer
 2. Dilute protein stock to 100 µg/ mL
 3. Add 3.0-3.6 mg/ml Sodium n-periodate crystals, swirl the tube a few times gently
 4. Incubate for one hour at room temperature
 5. Place collagen solution on patterned side of PDMS stamps (or place solution in 100 mm petri dish and add PDMS stamps patterned side down)
 6. Incubate stamps in collagen solution for 45 minutes – 1 hour
 7. While stamps are incubating, remove PA gels from PBS storage. Place in a vacuum desiccator and pull a vacuum using a vacuum pump for 2-20 minutes until gel surface appears dry
 8. When stamps have completed incubation, blow off excise protein with a filtered air gun

9. Gently place the stamp onto PA gel. DO NOT touch stamp after it has been placed on the PA gel.
10. Leave stamps on gel undisturbed for 2 minutes. If desired, better protein transfer has been found if the gels are placed in the oven for two minutes.
11. After stamping, allow gels to sit at room temperature for 10 minutes, then store in 35mm petri dish, full submerged in PBS. Treat with antibiotics/antimycotics before seeding cells.

A.10 Gluing coverslips to Petri dishes for TFM

Norland Optical Glue was used to affix coverslips to the bottom of petri dishes for the purpose of traction force experiments. Norland Optical Glue formulation 63 was purchased in a 30 cc hydrolic syringe (not with plunger). A 20 gauge needle was then placed in the glue syringe to allow for tight control of the application of the glue.

Materials:

- Norland Optical Glue
- Coverslip with gel
- Petri dish with hole

Methods:

1. Aspirate the back of the coverslip and dry with kim wipe
2. Place a drop of norland optical glue at each corner of the coverslip and then place into petri dish
3. Irradiate the gel for 1 minute
4. After glue has polymerized, over turn sample
5. Glue around the hole in the petri dish, ensuring a complete seal with the coverslip
6. Irradiate the sample for 7 more minutes
7. Check to ensure good seal by filling the petri dish with PBS.

A.11 Antibiotic solution for gel sterilization

Antibiotic/antimycotic Solution for gel sterilization

The following solution is placed upon polyacrylamide gels both micro-contact printed or collagen coated that are going to be used for culture for multiple days. As the activation of glass coverslips, polyacrylamide gel fabrication, and micro-contact printing all take place outside of the hood, it is impossible to keep sterile.

The antibiotic/antimycotic cocktail containing 100 µg/mL penicillin–streptomycin (MediaTech), 2.5 µg/mL amphotericin B (Corning), 10 µg/mL ciprofloxacin (Alfa Aesar), and 100 µg/mL gentamycin (Alfa Aesar) described by Clement, et al.

Example Calculations:

Desired amount of antibiotic/antimycotic solution: 500 mL

Total need for each ingredient

Penicillin-streptomycin= $500 \text{ ml} * 100 \frac{\mu\text{g}}{\text{ml}} = 50,000 \mu\text{g}$ of Penicillin-streptomycin

amphotericin B= $500 \text{ ml} * 2.5 \frac{\mu\text{g}}{\text{ml}} = 1250 \mu\text{g}$

ciprofloxacin= $500 \text{ ml} * 10 \frac{\mu\text{g}}{\text{ml}} = 5000 \mu\text{g}$

gentamycin= $500 \text{ ml} * 100 \frac{\mu\text{g}}{\text{ml}} = 50,000 \mu\text{g}$

Product concentrations (as determined by reading the bottle)

Paper reference: Clement AL, Moutinho TJ, Pins GD. *Micropatterned dermal-epidermal regeneration matrices create functional niches that enhance epidermal morphogenesis*. Acta Biomaterialia 2013;9:9474–84. doi:10.1016/j.actbio.2013.08.017.

A.12 Image Acquisition for Traction force**Materials**

- Traction force sample
- 0.25% EDTA Trypsin
- Three fine tipped transfer pipettes
- PBS
- Zeiss microscope

Methods:

1. Label fine tipped transfer pipettes “media”, “PBS”, and “trypsin”.
2. Place sample on microscope, and remove lid. It is of critical importance that the petri dish not be bumped or moved once it has been placed on the microscope and cell positions have been acquired.
3. Open up axiovision software
4. Create a folder, and allow for image capture to go directly into that folder
5. Open up mark/find window.
6. Find desired cells and mark positions with software. It is suggested that the number of cells be between 10-15 cells per sample.
7. Acquire a phase and fluorescent image for each cell
8. Carefully, using fine tipped transfer pipette remove media
9. Add PBS to sample, carefully, so as not to bump the dish
10. Remove the PBS slowly with a fine tipped transfer pipette
11. Add trypsin
12. Check to ensure all cells have detached from the substrate before taking final fluorescent image of the beads.

A.13 Collagen attachment to PDMS and polyacrylamide gels

Materials:

- Type I bovine collagen (biomatrix)
- Sulpho-SANPAH
- Test tube
- HEPES
- 0.02 N glacial acetic acid
- UV light

Methods:

1. Thaw sulpho-SANPAH aliquots
2. Add solution to HEPES to ensure concentration of 0.5 mg/mL (each 20 μ L aliquot makes 2 mL of solution)
3. Place 100-200 μ L of solution on to each PA gel
4. Irradiate the gel with UV light for 5 minutes
5. Rinse with HEPES, for best results repeat once more.
6. Add collagen solution to 0.02 N acetic acid to create 200 μ g/mL concentration.
7. Apply collagen to PA gel, ensure the gel is uniformly covered
8. Incubate at room temperature for 2 hours or overnight.

A.14 Cell Culture Media

The following media was used for culture of VICs, U2OS cells, and HDFs during the course of this thesis.

Final concentrations: 10% FBS, 1% antibiotic/antimycotic

Materials:

- 500 mL bottle of 1x DMEM, Gibco product #:
- Fetal Bovine Serum (FBS), aliquoted into 25 mLs stored in -20
- Antibiotic-Antimycotic product # , aliquoted into 5 mL tubes in -20
- Two extra 50 mL conical tubes

Methods:

- 1.) Place FBS and anti-anti aliquots into warm water bath
- 2.) Remove 55 mL of DMEM from 500 mL bottle using stereological pipette and empty into conical tubes. Aspirate into vacuum container
- 3.) Once thawed, add 50 mL FBS and 5 mL of anti-anti to media container
- 4.) Label with initials, and final concentration 10% FBS and 1% anti-anti

Store in 4C refridgerator

A.15 Traction Force Calculation and Codes

%% The first part of the traction force code is the pre-processing step in which the drift is removed and the cell boundaries outlined. File name is Preprocess2.m

```
clear all;
Dishn='dish1'
posn='pos02'
a1=imread([Dishn, '_fluor_', posn, '.tif']);
a2=imread([Dishn, '_tryp_', posn, '.tif']);
a3=imread([Dishn, '_phase_', posn, '.tif']);

cimg(:,:,3)=zeros(size(a2));
cimg(:,:,1)=double(a2)/(max(double(a2(:)))));
cimg(:,:,2)=double(a1)/(max(double(a1(:)))));
imshow(cimg, []);

for i=1:4;
[xd(i) yd(i)]=im_shift(a1,a2);
xd=mean(xd(i));
yd=mean(yd(i));
end

imshow(a3, []);
rg2=round(getrect);
rg2=round((16*rg2)/16);
rg2(3)=[round(rg2(3)/16)]*16;
rg2(4)=[round(rg2(4)/16)]*16;
%change rg2 (3) and rg2(4)
imgf_a1=imcrop(a1,rg2);
imshow(imgf_a1);
filename=[Dishn,posn, '_wMedium.tif'];
imwrite(imgf_a1,filename);

figure(2),imgf_a2=imcrop(a2,[rg2(1)+xd rg2(2)+yd rg2(3) rg2(4)]);
imshow(imgf_a2);
filename=[Dishn,posn, '_wtrypsin.tif'];
imwrite(imgf_a2,filename);

imgf_a3=imcrop(a3,rg2);
imshow(imgf_a3);
filename=[Dishn,posn, '_phase.tif'];
imwrite(imgf_a3,filename);
close all;

cimg2(:,:,3)=zeros(size(imgf_a2));
tempr=double(imgf_a2)/(max(double(imgf_a2(:))))/4-0.4;
tempg=double(imgf_a1)/(max(double(imgf_a1(:))))/4-0.4;
cimg2(:,:,1)=tempr-tempg;
cimg2(:,:,2)=tempg-tempr;
figure,imshow(cimg2, []);

[xi,yi,iu,iv,D]=mpiv(imgf_a2,imgf_a1,32,32,0.5,0.5,25,25,1, 'mqd', 2, 0);
```

```

[iu_f,iv_f,iu_i, iv_i] = mpiv_filter(iu,iv, 2, 2.0, 3, 0);
[iu_s, iv_s] = mpiv_smooth(iu_i, iv_i, 1);
[xm,ym]=meshgrid([min(xi):xi(2)-
xi(1):max(xi)], [min(yi):mean(diff(yi)):max(yi)]);
figure(4),imshow(cimg2, []);
hold on, quiver(xm',ym',iu_s,iv_s, 'b');
figname=[Dishn,posn, '.tif'];
imwrite(cimg2,figname);
scal=1e-6/2;
xs1=xm'*scal;
ys1=ym'*scal;
dx2=iu_s*scal;
dy2=iv_s*scal;

% Draw cell edge

figure(5),imshow(imgf_a3, [])
[bw,xc,yc]=roipoly;
reg=bwlabel(bw);
[s,l]=bwboundaries(bw);
g=regionprops(l, 'PixelList');
hold on,plot(s{1}(:,2),s{1}(:,1), 'b.')
hold off

%imshow(cimg2, []);

figure(6),hold on, quiver(xm',ym',iu_s,iv_s, 'b');
plot(s{1}(:,2),s{1}(:,1), 'b.')
hold off

% Saving files for Ansys

fid=fopen([Dishn,posn, '_cell.txt'], 'w');
fprintf(fid, '%10.4e \t %10.4e\n', [s{1}(:,2)*scal s{1}(:,1)*scal]');
fclose(fid);
save([Dishn,posn, '_disp.mat'], 'xs1', 'ys1', 'dx2', 'dy2', 'rg2');

```

%%The traction force code then requires a combination of matlab/ansys to model the cell applying the displacement field to the substrate. The main function was created to batch process several cells at one time. The main folder runs the files getnlist2.m, getprnsol2.m, and getTFM.m

%%:

%%main2.m

```

Dishn = '40kPa100um'; % Dish number
img_num= [01 02 03 04 05 06 07 08 09 10]; % image numbers
ansyspos= [01 02 03 04 05 06 07 08 09 10];

% %Generate NLIST files
for i = 1:length(img_num)

```

```

        getNLIST2(Dishn, ansyspos(i), img_num(i));
end

pause;

% % Generate PRNSOL files
for i= 1:length(img_num)
    getPRNSOL2(Dishn, ansyspos(i), img_num(i));
end

pause;

%Calculate Traction Force

for f=1:length(img_num)
    getTFM(Dishn, ansyspos(f), img_num(f));
end

```

Reproduced here are the functions:

```

function getNLIST2(Dishn,ansyspos,img_num)

load([Dishn,'pos', num2str(img_num,'%2.2d'), '_disp.mat']);
scal=1e-6/2;length=rg2(:,3)*scal; width=rg2(:,4)*scal;height=600*scal;
meshsize=16*scal;

% Making ansys text file to define the model

filn=[Dishn,'pos', num2str(img_num,'%2.2d'), '.txt'];
fid=fopen(filn,'w')
line1=['/TITLE,newgel\n','/PREP7\n'];
fprintf(fid,line1);
line2=['ET,1,SOLID185\n'];
fprintf(fid,line2);
line3=['KEYOPT,1,2,0\n','KEYOPT,1,3,0\n','KEYOPT,1,6,0\n'];
fprintf(fid,line3);
line4=['MPTEMP,,,,,,,, \n','MPTEMP,1,0
\n','MPDATA,EX,1,,40000\n','MPDATA,PRXY,1,,0.4\n','!* \n'];
fprintf(fid,line4);
line5=['BLC4,0,0,',num2str(length),',',num2str(width),',',num2str(height),
'\n'];
fprintf(fid,line5);
line6=['AESIZE,ALL,',num2str(meshsize),'\n','MSHKEY,0\n','MSHAPE,1,3d
\n','CM,_Y,VOLU \n','VSEL, , ,
\n','CM,_Y1,VOLU\n','CHKMSH,'VOLU'\n','CMSEL,S,_Y\n'];
fprintf(fid,line6);
line7=['MSHAPE,0,3d \n','MSHKEY,1\n','VMESH,_Y1\n','MSHKEY,0\n'];
fprintf(fid,line7);
line8=['nsel, s, loc, z, 0 \n'];
fprintf(fid, line8);
line9=['/OUTPUT, nlist_',Dishn,'pos', num2str(img_num,'%2.2d'), ', txt
\n'];
fprintf(fid,line9);
line10=['nlist \n'];
fprintf(fid, line10);

```

```

linel1=['/OUTPUT \nFINISH \n'];
fprintf(fid,linel1);
fclose(fid);

infile=[Dishn,'pos',num2str(img_num, '%2.2d'), '.txt'];
outfile = ['nlist_', Dishn, 'pos', num2str(img_num, '%2.2d'), '_2.txt'];
system(['"C:\Program Files\ANSYS Inc\v140\ansys\bin\winx64\ANSYS140.exe" -
b -i ' infile ' -o ' outfile]);

function getPRNSOL2(Dishn, ansyspos,img_num)

load([Dishn,'pos', num2str(img_num,'%2.2d'), '_disp.mat']);
scal=1e-6/2;length=rg2(:,3)*scal; width=rg2(:,4)*scal;height=600*scal;
meshsize=16*scal;

m=readnode(['nlist_',Dishn,'pos',num2str(img_num,
'%2.2d'), '.txt'],2,10,50,7);
nlist=m.nodes;
xn=nlist(:,2); yn=nlist(:,3);
dxn=interp2(xsl',ysl',dx2',xn,yn);
dyn=interp2(xsl',ysl',dy2',xn,yn);

celllist=dlmread([Dishn,'pos',num2str(img_num, '%2.2d'),'_cell.txt']);

xcell=celllist(:,1);
ycell=celllist(:,2);
Incell=inpolygon(xn, yn,xcell, ycell);
index_cell=find(Incell==1);
xpos=xn(index_cell); ypos=yn(index_cell);
xdisp=dxn(index_cell);ydisp=dyn(index_cell);

% Making table for ansys
B=[[1:size(index_cell,1)]' (nlist(index_cell,1)) xpos ypos xdisp ydisp];
B(2:size(xpos,1)+1,:)=B(1:size(xpos,1),:);
B(1,:)=[0:5];
format shortG;
dlmwrite([Dishn,'pos',num2str(img_num,
'%2.2d'),'_table_first1.txt'],B,'\t');

index_outcell=find(Incell==0);
xout=xn(index_outcell); yout=yn(index_outcell);
dxout=dxn(index_outcell); dyout=dyn(index_outcell);
C=[(1:size(index_outcell,1))' (nlist(index_outcell,1)) xout yout dxout
dyout];
C(2:size(xout,1)+1,:)=C(1:size(xout,1),:);
C(1,:)=[0:5];
format shortG;
dlmwrite([Dishn,'pos',num2str(img_num,
'%2.2d'),'_nulfnodes_first1.txt'],C,'\t');

% Making ansys input text file for ansy - to apply the load on top
filn=['ansys_',Dishn,'pos',num2str(img_num, '%2.2d'),'On1.txt'];
fid=fopen(filn,'w');
linel=['/TITLE,newgel\n','/PREP7\n'];
fprintf(fid,linel);

```

```

line2=['ET,1,SOLID185\n'];
fprintf(fid,line2);
line3=['KEYOPT,1,2,0\n','KEYOPT,1,3,0\n','KEYOPT,1,6,0\n'];
fprintf(fid,line3);
line4=['MPTEMP,,,,,,,, \n','MPTEMP,1,0
\n','MPDATA,EX,1,,40000\n','MPDATA,PRXY,1,,0.4\n','!* \n'];
fprintf(fid,line4);
line5=['BLC4,0,0,',num2str(length),',',num2str(width),',',num2str(height),
'\n'];
fprintf(fid,line5);
line6=['AESIZE,ALL,',num2str(meshsize),'\n','MSHKEY,0\n','MSHAPE,1,3d
\n','CM,_Y,VOLU \n','VSEL, , ,
\n','CM,_Y1,VOLU\n','CHKMSH','VOLU'\n','CMSEL,S,_Y\n'];
fprintf(fid,line6);
line7=['MSHAPE,0,3d \n','MSHKEY,1\n','VMESH,_Y1\n','MSHKEY,0\n'];
fprintf(fid,line7);
line8=['*dim,Txy,table,',num2str(size(index_cell,1)),',5,1\n'];
fprintf(fid,line8);
line9=['*tread,Txy,','',Dishn,'pos',num2str(img_num,
'%2.2d'),'_table_first1.txt'\n'];
fprintf(fid,line9);
line10=['*do,i,1,',num2str(size(index_cell,1)),',1\n'];
fprintf(fid,line10);
line11=['d,Txy(i,1),ux,Txy(i,4)\n'];
fprintf(fid,line11);
line12=['d,Txy(i,1),uy,Txy(i,5)\n'];
fprintf(fid,line12);
line13=['*enddo\n'];
fprintf(fid,line13);
line14=['*dim,loadf,table,',num2str(size(index_outcell,1)),',5,1\n'];
fprintf(fid,line14);
line15=['*tread,loadf,','',Dishn,'pos',num2str(img_num,
'%2.2d'),'_nulfnodes_first1.txt'\n'];
fprintf(fid,line15);
line16=['*do,j,1,',num2str(size(index_outcell,1)),',1\n'];
fprintf(fid,line16);
line17=['f,loadf(j,1),fx,0\n','f,loadf(j,1),fy,0\n','f,loadf(j,1),fz,0\n',
'*enddo\n','da,2,ux,0\n','da,2,uy,0\n','da,2,uz,0\n'];
fprintf(fid,line17);
line18=['FINISH\n'];
fprintf(fid,line18);
line19=['/SOLU\n'];
fprintf(fid,line19);
line20=['SOLVE\n'];
fprintf(fid,line20);
line21=['FINISH\n'];
fprintf(fid,line21);
line22=['/POST1\n'];
fprintf(fid,line22);
line23=['nset,s,loc,z,0\n'];
fprintf(fid,line23);
line24=['/OUTPUT,PRNSOL_ Dishn,'pos',num2str(img_num,
'%2.2d'),'txt\n'];
fprintf(fid,line24);
line25=['PRNSOL,s,comp\n'];
fprintf(fid,line25);
line26=['/OUTPUT\n'];

```

```

fprintf(fid, line26);
line27=['FINISH\n'];
fprintf(fid, line27);
fclose(fid);

%send files to ansys and get back the PRNsol file
infile=['ansys_',Dishn,'pos',num2str(img_num, '%2.2d'),'On1.txt'];
outfile = ['PRNSOL_' Dishn,'pos',num2str(img_num, '%2.2d'), '_2.txt'];
system(['"C:\Program Files\ANSYS Inc\v140\ansys\bin\winx64\ANSYS140.exe" -
b -i ' infile ' -o ' outfile]);

function getTFM(Dishn, ansyspos, img_num)

m=readnode(['nlist_',Dishn,'pos',num2str(img_num,
'%2.2d'),'.txt'],2,10,50,7);
nlist=m.nodes;
xn=nlist(:,2); yn=nlist(:,3);
% dxn=interp2(xsl',ysl',dx2',xn,yn);
% dyn=interp2(xsl',ysl',dy2',xn,yn);

celllist=dlmread([Dishn,'pos',num2str(img_num, '%2.2d'),'_cell.txt']);

xcell=celllist(:,1);
ycell=celllist(:,2);
Incell=inpolygon(xn, yn,xcell, ycell);
index_cell=find(Incell==1);
xpos=xn(index_cell); ypos=yn(index_cell);
% xdisp=dxn(index_cell);ydisp=dyn(index_cell);

% index_outcell=find(Incell==0);
% xout=xn(index_outcell); yout=yn(index_outcell);
% dxout=dxn(index_outcell); dyout=dyn(index_outcell);
% C=[(1:size(index_outcell,1))' (nlist(index_outcell,1)) xout yout dxout
dyout];
% C(2:size(xout,1)+1,:)=C(1:size(xout,1),:);
% C(1,:)= [0:5];

ress1=readnode(['PRNSOL_',Dishn,'pos',num2str(img_num,
'%2.2d'),'.txt'],2,17,37,7);
list_1=ress1.nodes;syz_1=list_1(:,6);sxz_1=list_1(:,7);
S1=sqrt((syz_1(:)).^2+(sxz_1(:)).^2);
S1_cell=S1(nlist(index_cell,1));

% Force Calculation
scal=1e-6/2;
meshsize=16*scal;
Area=meshsize*meshsize;

% Layer 1
Force=Area*S1; totForce=sum(Force);
Cell_force=Area*(S1_cell); totForce_cell=sum(Cell_force);

```

```

save([Dishn,'pos',num2str(img_num,'%2.2d'),
'_data.mat'],'xn','yn','S1','S1_cell','Force','totForce','Cell_force','tot
Force_cell');

%Contour Plot and stress distribution

m=round(xn/meshsize)+1;
n=round(yn/meshsize)+1;

% for i=1:max(m);
%     for j=1:max(n);
%         Xn(i,j)=xn(j+(i-1)*max(n));
%         Yn(i,j)=yn(j+(i-1)*max(n));
%         Zn(i,j)=S1(j+(i-1)*max(n));
%     end
% end
% figure,contour(Xn,-Yn,Zn)
% colormap(jet); colorbar;
% xlabel('m'); ylabel('m');
% hold on, plot(celllist(:,1),-celllist(:,2),'r.')
% hold off;

mx=max(xn)/scal;
my=max(yn)/scal;
[xssm,yssm]=meshgrid([0:1:mx],[0:1:my]);
zmsh=griddata(xn/scal,yn/scal,S1,xssm,yssm);
figure, imshow(zmsh,[]);colormap(jet);colorbar;
hold on, plot(xcell/scal,ycell/scal,'r','LineWidth',2);
cbar=colorbar;
set(get(cbar,'ylabel'),'String','Stress [Pa]');
caxis([0 2500]);

```

A.16 Caspase live cell detection reagent

This reagent was purchased and used according to the manufacturer's instructions. Please see:

<https://www.thermofisher.com/order/catalog/product/C10423>

for more information about this product. It was used at working concentration of 1 μ M. 1 μ L of reagent was added for every 2 mL of culture media. Reagent was incubated with cells for 1 hour prior to imaging. The cell culture media and live cell detection reagent was replenished every 48 hours for the duration of the experiment.

A.17 Fixing Cells

To be done in the fume hood. Dispose of paraformaldehyde in hazardous waste. Use proper PPE (personal protective equipment) such as gloves and labcoat

Materials:

- 4% Paraformaldehyde
- Hazardous waste container
- 2 Transfer pipets
- 1x PBS
- Timer

Methods:

1. Place haz waste container, transfer pippets and paraformaldehyde
2. Remove cells from incubator.
3. Bring to lab bench
4. Aspirate media and replace with 1x PBS
5. Bring cells and 1x PBS to chemical hood
6. Remove 1x PBS by draining it into haz waste container using the transfer pipette
7. Apply enough 4% paraformaldehyde to coat the surface you are fixing, you do not need that much volume.
8. Allow the paraformaldehyde to stay on sample for 15 minutes
9. Dispose into haz container
10. Rinse 2x with 1x PBS, disposing each time into haz container.
11. Apply PBS to sample to store

A.18 Staining for α -SMA, Phalloidin, and Hoescht with cover slipping details

(TAG 09/24/08, Edited AZR 02/11/15, Edited VL with HC 05/11/15)

Samples: Cultured cells on glass coverslips or polyacrylamide gels

Primary Antibody: Monoclonal anti-actin α SMA produced in mouse [Sigma, cat#A2547]

Secondary Antibody: Goat anti-mouse immunoglobulin (H+L); conjugated to AlexaFluor 546 [Invitrogen, cat#A11003]

Materials:

- Four Eppendorf tubes or 15 mL conical tubes depending on the number of samples
- PBS or DPBS
- Goat Serum
- Alexafluor-488 Phalloidin
- Hoescht

Methods:

- 1) Gently rinse cells twice in PBS.
- 2) Fix cells in 4% paraformaldehyde (4% PFA) and incubate 20 minutes at room temperature (RT).

- 3) Collect 4% PFA into specified waste container.
- 4) Rinse cells twice in PBS for 5 minutes each.*
- 5) Permeabilize the cells with 0.25% Triton-X 100 in dH₂O for 10 minutes at RT.
- 6) Rinse cells twice in PBS for 5 minutes each.
- 7) Block with 1.5% goat serum (GS) in PBS for 30 minutes at RT.
- 8) Add primary antibody diluted in 1.5% GS in PBS (dilution 1:100); incubate for 1 hour at RT.*
- 9) Wash three times in PBS for 5 minutes each.
1. Add secondary antibody diluted in 1.5% GS in PBS (dilution 1:400); incubate for 45 minutes at RT – SAMPLES SHOULD BE PROTECTED FROM LIGHT FROM THIS POINT ON!
Can also be incubated overnight. As it is important to keep the sample hydrated, I place 35 mm petri dishes (with coverslips inside) within a 100 ml petri dish along with a PBS soaked kim wipe)
- 10) Rinse three times with PBS for 5 minutes each.
- 11) Stain with Alexa fluor-488 phalloidin for 40 minutes (dilute stock 1:100 in PBS)
- 12) Counter stain with Hoechst dye (1:6000; 1.67 µg/ml in dH₂O) for 2 minutes.
- 13) Rinse twice with PBS.
- 14) Coverslip using aqueous (non-organic) mounting medium (Prolong Gold), especially on plastic plates and chamber slides. PROTECT FROM LIGHT!

* STOPPING POINTS:

Step 4 – Fixed cells can be stored in PBS at 4°C if they cannot be stained right away

Step 6 – Primary antibody incubation can be carried out overnight at 4°C if plates/wells/slides are humidified (wet paper towels, etc.) to prevent drying. Overnight incubation at 4°C may work BETTER for some primary antibodies

Step 11 – Stained slides can be photographed later, but it's best not to wait too long. SAMPLES MUST BE PROTECTED FROM LIGHT (wrap in aluminum foil) to prevent loss of fluorescent signal.

Cover slipping protocol

Materials:

- Stained sample
- Tweezers
- Prolong Gold, Life Technologies
- Shur-Mount, Tedpella,
- Disposable transfer pipette
- 25 mm glass coverslips (assuming 22 mm square samples)
- Glass slide
- Clear nail polish

Methods:

Label your slides appropriately.

Carefully take coverslip from staining dish. If wet, gently blot the back with a kim wipe to dry.

Using transfer pippet, place a large droplet of shur-mount on to glass slide. Be careful as to not get any bubbles in the shur-mont.

Carefully place the sample (with the surface that is not of interest to you, ie. the side of the samples that do not have any cells on it) onto the droplet of Shur-mount.

Allow to harden for 1-2 minutes before proceeding to the next step.

For a 22 mm coverslip, use 30 μ L of Prolong gold. Gently tilt the slide so the prolong gold droplet goes all over the sample surface. If there are bubbles, carefully pop them using a scalpel. Take care not to hit your sample.

Using a 25mm glass coverslip (so its slightly larger than your sample) and tweezers (or if you are more comfortable without using tweezers), gently place the coverslip on top of the prolong gold droplet. Be very careful to not get bubbles in the prolong gold as this will make your imaging difficult.

Seal the edges of coverslip with clear nail polish

Image within 5 days for best results.

Notes: Toluene mounting media (Shur-mount) will harden when exposed to air. Take care with storage, close the bottle well, so that it does not harden. Prolong gold as well as Shur-mount can be stored at room temperature.

A.19 Staining for α -SMA, Phalloidin, and alkaline phosphatase

Alkaline Phosphatase Staining Protocol_v1

HC with VL 10/14/2015

Samples: Cultured cells on glass coverslips or polyacrylamide gels

Primary Antibody: Monoclonal anti-alkaline phosphatase produced in goat

Secondary Antibody: anti-goat IgG-Alexa 568 produced in donkey; conjugated to AlexaFluor 546 [Invitrogen, cat# A-11057]

Materials:

- Four Eppendorf tubes or 15 mL conical tubes depending on the number of samples
- PBS or DPBS
- Goat Serum
- Alexafluor488 Phalloidin

- Hoescht

For slides- first: Deparaffinize

1. Heat slides to 60C for 10 mins (oven)
2. Xylene 1 for 10 mins
3. Xylene 2 for 10 mins
4. 100% ethanol for 2 mins (dehydration)
5. 95% ethanol for 2 mins (rehydration)
6. 70% ethanol for 2 mins (rehydration)
7. DI water for 5 mins (change DI 5 times; 1x/min)

Methods:

- 15) Gently rinse cells twice in PBS.
- 16) Fix cells in 4% paraformaldehyde (4% PFA) and incubate 20 minutes at room temperature (RT).
- 17) Collect 4% PFA into specified waste container.
- 18) Rinse cells twice in PBS for 5 minutes each.*
- 19) Permeabilize the cells with 0.25% Triton-X 100 in dH₂O for 10 minutes at RT.
- 20) Rinse cells twice in PBS for 5 minutes each.
- 21) Block with 1.5% goat serum (GS) in PBS for 30 minutes at RT.
- 22) Add primary antibody diluted in 1.5% GS in PBS (dilution 1:50); incubate for 1 hour at RT.*
- 23) Wash three times in PBS for 5 minutes each.
2. Add secondary antibody diluted in 1.5% GS in PBS (dilution 1:400); incubate for 45 minutes at RT – SAMPLES SHOULD BE PREOTECTED FROM LIGHT FROM THIS POINT ON!
Can also be incubated overnight. As it is important to keep the sample hydrated, I place 35 mm petri dishes (with coverslips inside) within a 100 ml petri dish along with a PBS soaked kim wipe)
- 24) Rinse three times with PBS for 5 minutes each.
- 25) Stain with Alexa fluor-488 phalloidin for 40 minutes (dilute stock 1:100 in PBS)
- 26) Counter stain with Hoechst dye (1:6000; 1.67 µg/ml in dH₂O) for 2 minutes.
- 27) Rinse twice with PBS.
- 28) Coverslip using aqueous (non-organic) mounting medium (Prolong Gold), especially on plastic plates and chamber slides. PROTECT FROM LIGHT!

A.20 Staining for vinculin, Phalloidin and Hoescht

Adapted from Jain lab

Materials:

- Cytoskeletal buffer solution (see below)
- 4% paraformaldehyde
- Eppendorf tubes
- Goat serum
- Vinculin antibody:
- Alexafluor-488 phalloidin

- Hoescht
- 15 ml conical tube

Cytoskeleton Buffer Preparation (courtesy of Dr. Anita Shukla)

1. To prepare 250 mL of Cytoskeleton Buffer
 - a. Measure 250 mL milliQ H₂O
 - b. Add 1.25 mL of triton X-100
 - c. Add 25.67 grams sucrose
 - d. 730.50 mg sodium chloride
 - e. 598.78 mg HEPES
 - f. 152.48 mg magnesium chloride-hydrate
2. Bring pH of the solution to 6.8 using 0.1 N NaOH

Methods:

3. Remove growth media from cells
4. Rinse cells with cytoskeleton buffer to remove soluble proteins.
5. Rinse with 250 uL PBS 3 times
6. Add 200 uL of 4% paraformaldehyde to cover the cell monolayer
7. Incubate at room temperature for approximately 10-15 minutes to complete fixation.
8. Permeabilize membrane with 0.25% Triton-X-100 for 10 minutes
9. Block with 4% goat serum in PBS for 30 minutes
10. Incubate in primary antibody overnight at 4C (Vinculin: 1:800 in 4% goat serum in PBS). As it is important to keep the sample hydrated, I place 35 mm petri dishes (with coverslips inside) within a 100 ml petri dish along with a PBS soaked kim wipe)
11. Wash 3x in PBS for 5 minutes
12. Incubate in secondary antibody for 2 hours at room temperature (1:220 in 2% goat serum in PBS)
13. Wash 3x in PBS for 5 minutes
14. Rinse three times with PBS for 5 minutes each.
15. Stain with Alexa fluor-488 phalloidin for 40 minutes (dilute stock 1:100 in PBS)
16. Counter stain with Hoechst dye (1:6000; 1.67 µg/ml in dH₂O) for 2 minutes.
17. Rinse twice with PBS.
18. Coverslip using methods detailed in appendix S with Shurmount and Prolong Gold

A.21 Staining for YAP, Phalloidin and Hoescht

Adapted from Jain lab

Materials:

- 4% paraformaldehyde
- Eppendorf tubes
- Goat serum
- YAP antibody:
- Alexafluor-488 phalloidin
- Hoescht
- 15 ml conical tube

Methods:

19. Remove growth media from cells
20. Rinse cells with cytoskeleton buffer to remove soluble proteins.
21. Rinse with 250 μ L PBS 3 times
22. Add 200 μ L of 4% paraformaldehyde to cover the cell monolayer
23. Incubate at room temperature for approximately 10-15 minutes to complete fixation.
24. Permeabilize membrane with 0.25% Triton-X-100 for 10 minutes
25. Block with 4% goat serum in PBS for 30 minutes
26. Incubate in primary antibody overnight at 4C (YAP: 1:800 in 4% goat serum in PBS). As it is important to keep the sample hydrated, I place 35 mm petri dishes (with coverslips inside) within a 100 ml petri dish along with a PBS soaked kim wipe)
27. Wash 3x in PBS for 5 minutes
28. Incubate in secondary antibody for 2 hours at room temperature (1:220 in 2% goat serum in PBS)
29. Wash 3x in PBS for 5 minutes
30. Rinse three times with PBS for 5 minutes each.
31. Stain with Alexa fluor-488 phalloidin for 40 minutes (dilute stock 1:100 in PBS)
32. Counter stain with Hoechst dye (1:6000; 1.67 μ g/ml in dH₂O) for 2 minutes.
33. Rinse twice with PBS.
34. Coverslip using methods detailed in appendix S with Shurmount and Prolong Gold

A.22 Ligand Coating Magnetic BeadsMaterials:

- Fe₃O₄ beads ~5 μ m in diameter [Sigma No. 310069-25G]
- DPBS (-)
- 0.1 M NaOH
- Sonicator
- 3 mg/mL collagen type I
- 1 mL centrifuge tube
- Centrifuge
- Aspirator

Procedure:

1. In centrifuge tube, dilute stock collagen to 1 mg/mL collagen in DPBS by adding 333 μ L of stock collagen to 666 μ L of DPBS (-).
2. Measure 0.4g of Fe₃O₄ beads. Add to collagen solution.
3. Add 100 μ L of 0.1 M NaOH to increase pH to ~7.4
4. Mix solution vigorously and sonicate for 5 minutes.
5. Incubate beads in solution for 1 hour in room temperature, occasionally inverting the tube for better bead dispersion.

6. Rinse beads three times by centrifuging, aspirating solution, and re-suspending in DPBS (-).
7. Sonicate for 5 minutes and place in 4°C fridge or use immediately for best results. Sonicate prior to usage.

A.23 Adding Magnetic Beads to Cell Aggregates

Materials:

- Collagen coated Fe₃O₄ μbeads in DPBS (-)
- DPBS (-)
- Cells growing on PA gel coverslip in 35 mm petri dish
- Culture hood
- DMEM
- Incubator
- Aspirator

Procedure:

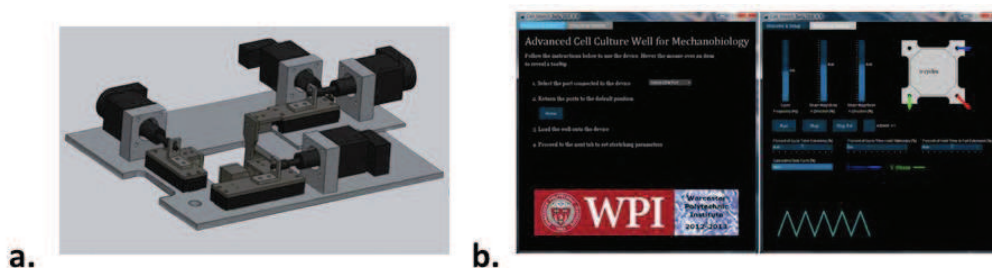
8. In a cell culture hood, remove old media from petri dish with cells and add 2 mL of fresh media.
9. For a high density of μbeads, add 10 μL of Fe₃O₄ μbead solution for each 1 mL media.
10. Gently shake petri dish to disperse μbeads evenly.
11. Place petri dish in 37°C incubator for 40 minutes. Gently shake petri dish every 10 minutes to re-disperse μbeads to minimize clumping.
12. Remove dish from incubator, and aspirate media in hood.
13. Rinse vigorously with DPBS (-) until excess μbeads are removed.
14. Add fresh media to cells and check for μbead attachment under a microscope.
15. Replace petri dish in 37°C incubator.

Appendix B: Supplemental Data

Appendix B.1 Supporting Information for Chapter 3

Design of stretch device

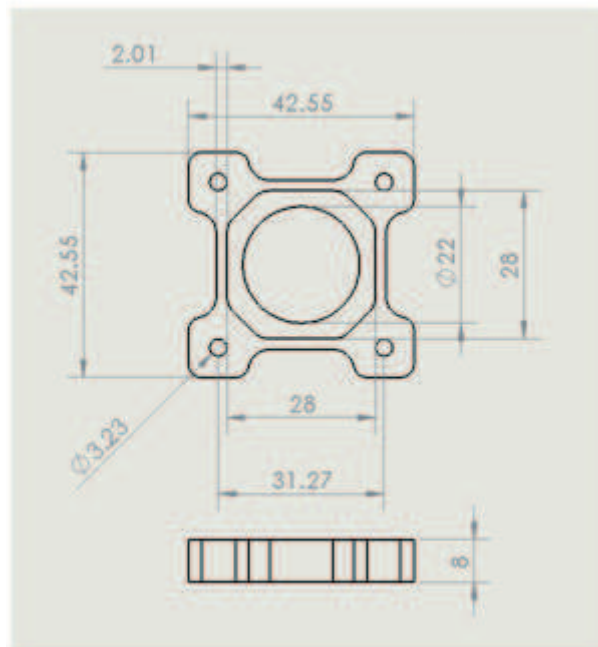
The custom cell stretch device designed for this project contains four stepper motors with encoders, with two in a stacked configuration to apply forces to three of the four corners of the well one corner of the well remains stationary during stretch. Schematic of the device is shown in Supplementary Figure 1a. The motors are attached using motor mounts to an aluminum sub-plate and baseplate which can be placed on-top of a microscope stage for simultaneous stretching and imaging, although the stretching was done in a standard incubator for this study. A microchip controlled by multi-platform integrated development environment (MPIDE) was used to control the motors. Processing® software was used in conjunction with MPIDE to create a graphical user interface which allows the operator to select the waveform, stretch magnitude in both x and y directions, and frequency. A picture of the graphical user interface is shown in Supplementary Figure 1b.



Supplementary Figure S1 (a) Schematic of stretch device showing the four stepper motors with encoders strategically placed atop a baseplate. The motors are secured to the base plate using motor mounts. (b) Graphical user interface for control of the stretch regimen. User can select frequency, magnitude of stretch in the x and y directions, as well as the percent of time in extension, and percent of cycle time held in extension. Representative waveform of stretch regimen changes in real time as user changes the aforementioned settings.

Design of custom well

To perform traction force measurements, a polyacrylamide hydrogel of approximately ~70 μm thick was covalently attached to our custom well using previously established protocol in our lab {Quinlan, 2011 #29}. In order to be able to obtain clear images, the bottom membrane of the culture wells had to be $< 150 \mu\text{m}$ thick. We decided to manufacture the wells out of polydimethylsiloxane (PDMS) as it is relatively inexpensive, optically clear, and non-cytotoxic when fully cured. The molds of the PDMS wells were created out of polycarbonate sheets (TAP plastics, Seattle, Washington). A metal spacer was used to create the thickness of the membrane so that the entire well and well bottom surface could be cast at the same time, ensuring the bottom membrane was perfectly taut allowing better strain transfer. See Supplementary Figure 2 for well dimensions.



Supplementary Figure S2 : Dimensioned drawing created in Solidworks of a polydimethylsiloxane well with attached polyacrylamide gel. The design was optimized to allow for maximal region of homogenous strain in the well's center. Using this design, we are able to get a larger central homogenous region when compared to current commercially available wells. All units are in mm.

Strain field verification- finite element analysis

Finite element models were created of our wells to allow for analysis to determine design parameters which enable a maximally uniform strain field. A model of our custom well was created in Solidworks (Dassault Systems, Waltham, MA). The CAD models were then imported into ANSYS Workbench (ANSYS, Canonsburg, PA). All analyses were conducted in the same manner with identical settings. Meshes were created with 0.00075 m element size, medium relevance center, medium smoothing and medium span angle center, with all other settings set to default. Thermal

strain effects were turned off and large deformations were turned on. The analysis was done with the program-controlled stepping turned off and the number of sub-steps set to 6, allowing for the same time spacing between displacement results for each well. Once the wells were analyzed, ImageJ was used to measure the useable area of the well defined as the central region of uniform strain. When the wall and membrane thickness were optimized, the uniform area measured 70 mm².

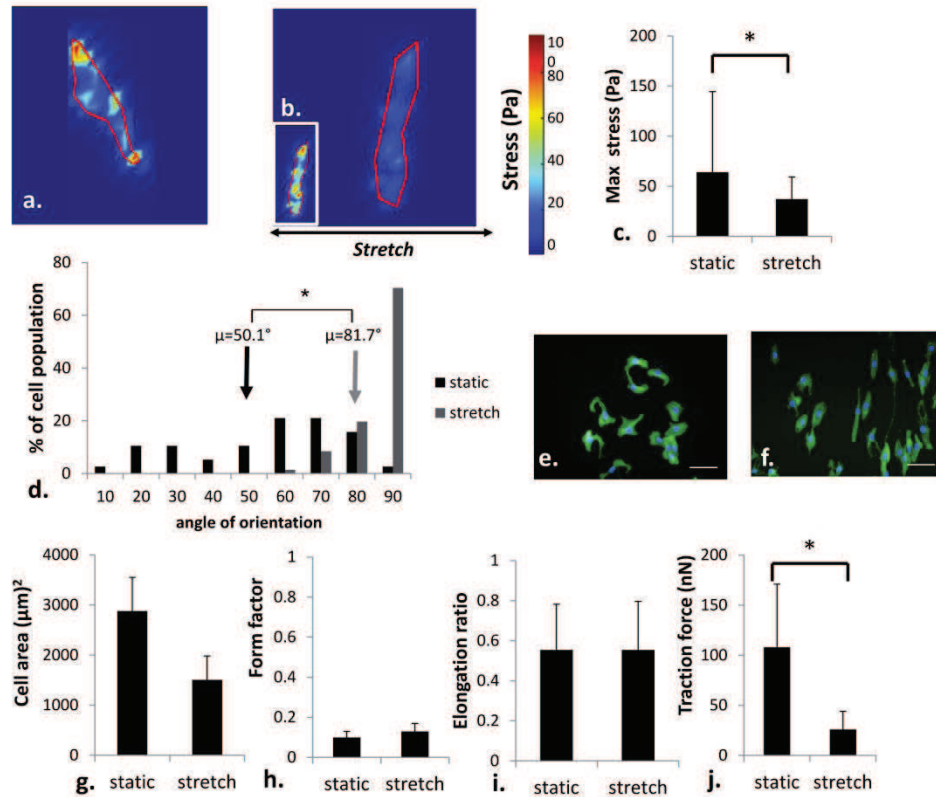
Strain field verification- high density mapping

To measure the strain fields in the wells, a 50:50 mixture of silicon carbide microparticles (Silicon carbide 400 grinding compound, Alfa Aesar, Ward Hill, MA) and reflective paint (Scotchlite Reflective Ink 8017, 3M, St. Paul, MN) was applied to the cell culture surface in three of representative wells to produce a unique light intensity distribution across the well. Videos of the wells were recorded across multiple stretch cycles at 5% and 10% uniaxial nominal strain and 1Hz stretch rate and captured using a Fastec Hispec4 camera at 1696x1730 pixels and 60 frames per second. Videos were collected such that data spanned at least five cycles. Regional displacement fields of the center of the well were computed using our previously published High Density Mapping (HDM) technique{Tao, 2013 #927}. Strain fields were computed from displacement fields by computing local displacement gradients followed by Green's strain in MATLAB. Assuming steady state, strain fields were averaged across several stretch cycles.

Validation experiments with additional cell type

Traction force with long term cyclic stretch

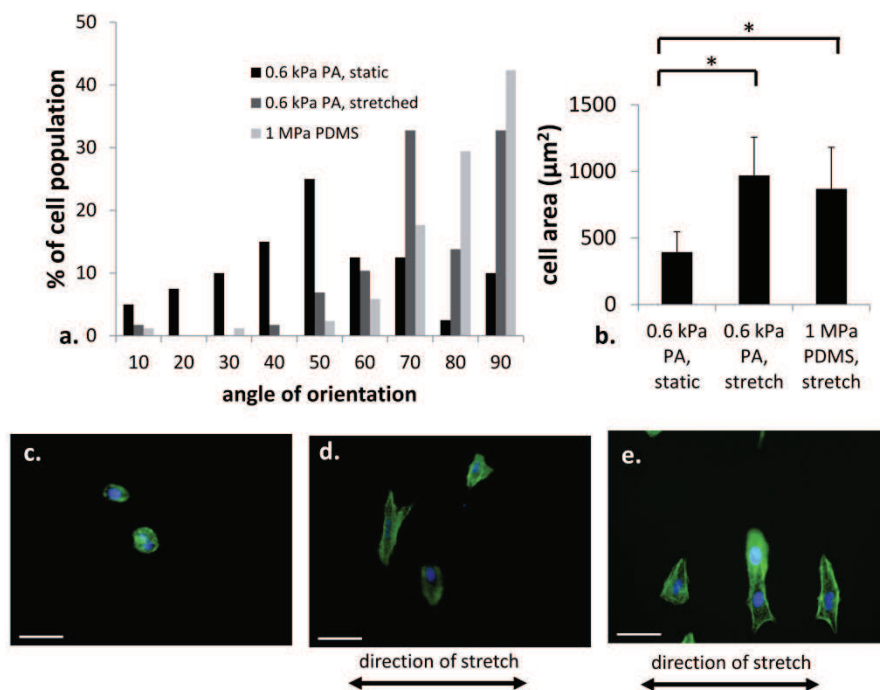
To confirm our results of a decrease in cell traction force with uniaxial stretch, U2OS cells (generously provided by Dr. Roland Kaunas) were cultured and tested under identical conditions. U2OS cells were seeded onto stiff (7.5 kPa) polyacrylamide gel which had been attached to custom PDMS well. Cells were seeded at low density (3,000 cells/cm²) and allowed to attach to gel overnight. Cells were stretched for 24 hours, uniaxially at 1 Hertz in 10% CO₂. Results are shown in Supplemental Figure 3.



Supplemental Figure S3: U2OS traction force and area decrease with uniaxial stretch. Cells were stretched uniaxially at 1 Hz for 24 hours on 7.5 kPa PA gels attached to PDMS substrates. Representative substrate stress plots are shown for (a) static cultured cell and (b) stretched cell. Insert of stretch cell scaled to show maximum and minimum stresses. (c) Maximum substrate stress was greater for static cells than for stretched cells, $p < 0.05$. (d) Static cells had random orientation U2OS that were stretched showed statistically significant alignment perpendicular to stretch, $p < 0.05$. (stretch direction was 0-180). (e) Representative fluorescent images of static U2OS cells and (f) stretch U2OS. Green is actin cytoskeleton and blue is nuclei. (g) Cell area was trended towards being larger for static controls than stretched cells although it was not significant. (h) Shape factor was unaffected by stretch. (i) Elongation was unaffected by stretch (j). Cell traction force was significantly lower in stretched cells verses controls.

Reorientation on soft substrates with uniaxial stretch

To determine if soft substrates alter cell reorientation, GFP labelled U2OS cells cultured on 0.6 kPa substrates were subjected to 10% uniaxial stretch. PDMS substrates without polyacrylamide gels attached were used as the stiff substrate comparison group and cells on 0.6 kPa static gels were used as a control. After 12 hours of stretch, cells were fixed with 4% paraformaldehyde and stained for actin (Alexafluor 488 Phalloidin) and nuclei (Hoescht). ImageJ was used to obtain cell area and orientation measurements. In agreement with our studies on VICs, U2OS reoriented perpendicular to stretch. The average angle of reorientation after stretch was not statically different between stiff and soft stretched substrates ($p < 0.05$). See Supplemental Figure 4.

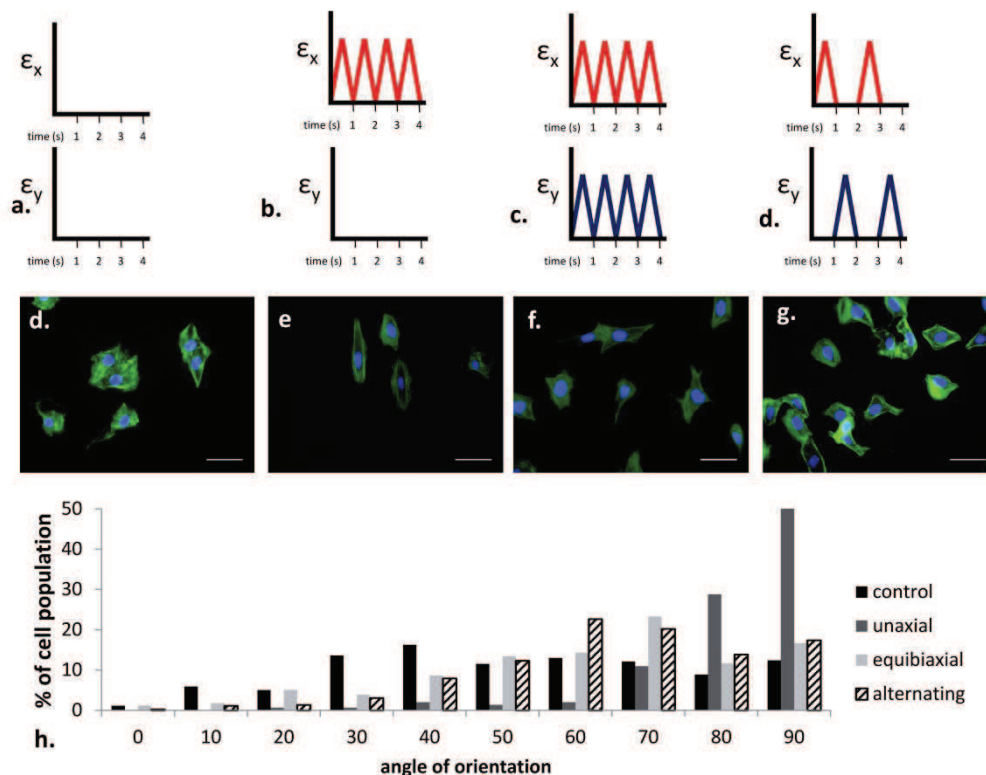


Supplemental Figure S4: U2OS are capable of reorientation on soft substrates with dynamic stretch. (a) % of cell population versus angle of orientation plot for U2OS cells cultured statically on a 0.6 kPa substrate, U2OS cells that had undergone 12 hrs cyclic 10% uniaxial stretch on a 0.6 kPa substrate and U2OS cells that had undergone 12 hrs cyclic 10% uniaxial stretch on a 1 MPa PDMS cell culture well (b) Cell area comparisons between groups. Statistical significance was found in cell area between 0.6 kPa PA gel static culture and 0.6 kPa PA gel culture with stretch, as well as 0.6 kPa PA static culture and 1 MPa PDMS culture with stretch, $p < 0.05$. No statistical difference in cell area was found between 0.6 kPa PA gels culture with stretch and 1 MPa PDMS culture with stretch (ANOVA on ranks). (c) Representative image of U2OS cells on a 0.6 kPa PA, static culture. (d) Representative image of cells on a 0.6 kPa PA, stretch (e) representative image of cells on a 1 MPa PDMS well. Green=actin, blue= nuclei, sb= 50 μm .

Alternating stretch effects reorientation

To ascertain how cells integrate stretch signals over time, GFP labelled U2OS cells were subjected to one of three patterns of stretch: 10% uniaxial stretch, 10% equibiaxial stretch, or alternating uniaxial stretch (10% uniaxial x-direction stretch, followed by 10% uniaxial y-direction of stretch). Statically cultured U2OS cells were used as a control. After 12 hours of stretch, cells were fixed with 4% paraformaldehyde and stained for actin (Alexafluor 488 Phalloidin) and nuclei (Hoescht). ImageJ was used to obtain cell area and orientation measurements. In agreement with our studies of VICs, statically cultured cells had a random orientation. Uniaxially stretched U2OS reoriented perpendicular to stretch, with more than 90% of cells falling within 10 degrees of vertical. No reorientation was observed in cells that were stretched equibiaxially or alternating uniaxially, although distinct morphological differences were observed. The actin cytoskeleton of equibiaxially

stretched groups appeared less robust than other groups, possibly indicating a depolymerization of stress fibers as they were stretched above their maximum tension (see Supplemental Figure 5). The cytoskeleton of alternatingly uniaxial stretched groups appeared diamond in shape with peaks at approximately 45 degrees from the directions of stretch. This finding may indicate that the stress fibers in the direction of either of the stretch directions depolymerized and those at angles of lower stretch were reinforced. To our knowledge this is the first time that the effects of alternating axis stretch have been investigated.

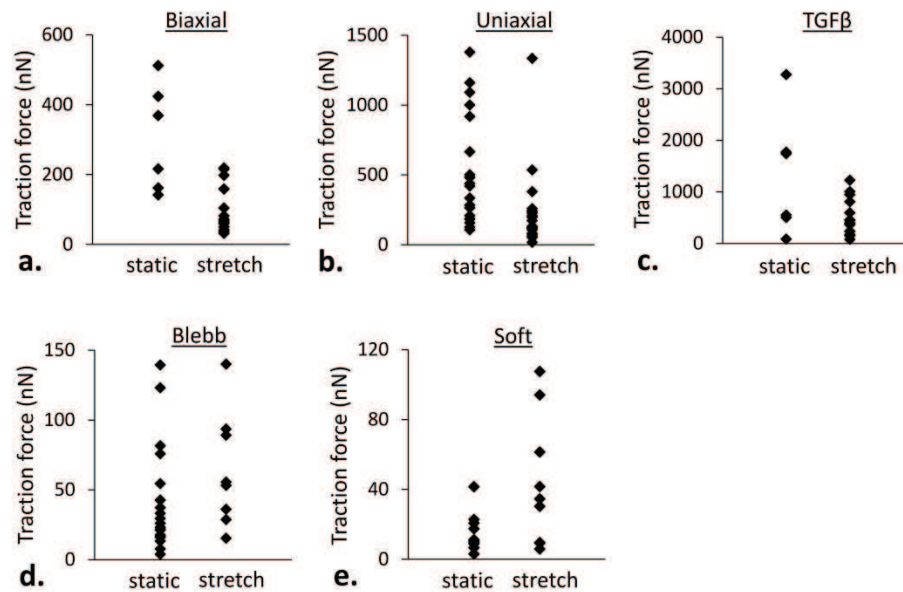


Supplemental Figure S5: Supplemental Figure S5: U2OS cells reorient most strongly in response to uniaxial stretch. U2OS cells were stretched for 12 hours at either 10% 1 Hz uniaxial stretch, 10% equibiaxial stretch, or 10% alternating uniaxial stretch in which the direction of uniaxial stretch was alternated every cycle. Representative strain waveforms for x and y directions of device are illustrated in a) static b) uniaxial c) equibiaxial and d) alternating directions (x then y) of uniaxial stretch. Representative images of each stretch condition are shown for (d) static (e) uniaxially (f) equibiaxial or (g) alternating stretch cells. Green is actin cytoskeleton, blue is nuclei. Scale bar = 50 μm .

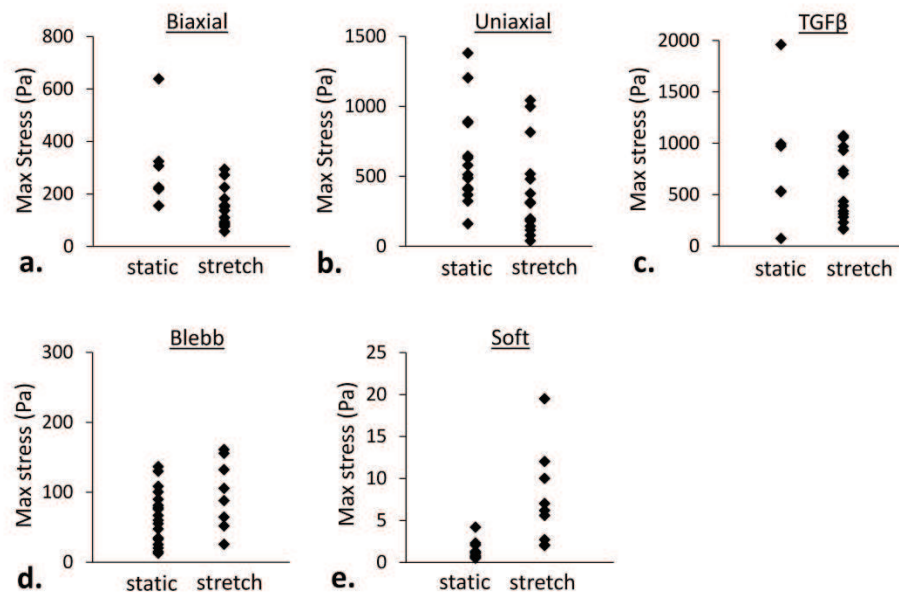
(h) Orientation response of U2OS cells with respect to stretch waveform are represented with a 0-90 histogram. Uniaxial stretch was in the 0-180 direction; Uniaxial stretch most strongly encouraged U2OS cells to reorient.

Raw Data Scatterplots

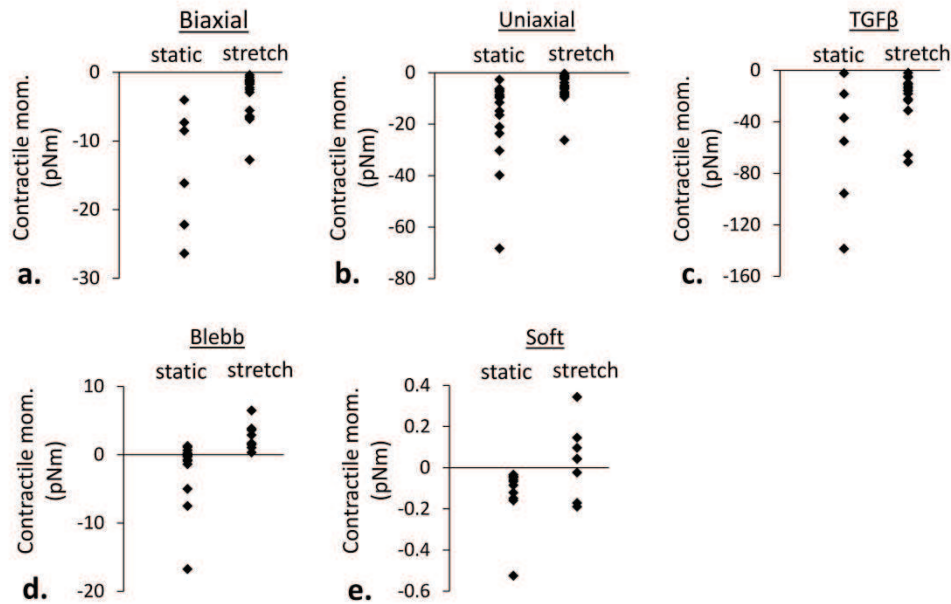
Individual cells were not tracked with stretch over time and numerical values reported in table 1 of the manuscript represent population averages. Actual raw data values from control and stretched cells are shown in scatterplots below.



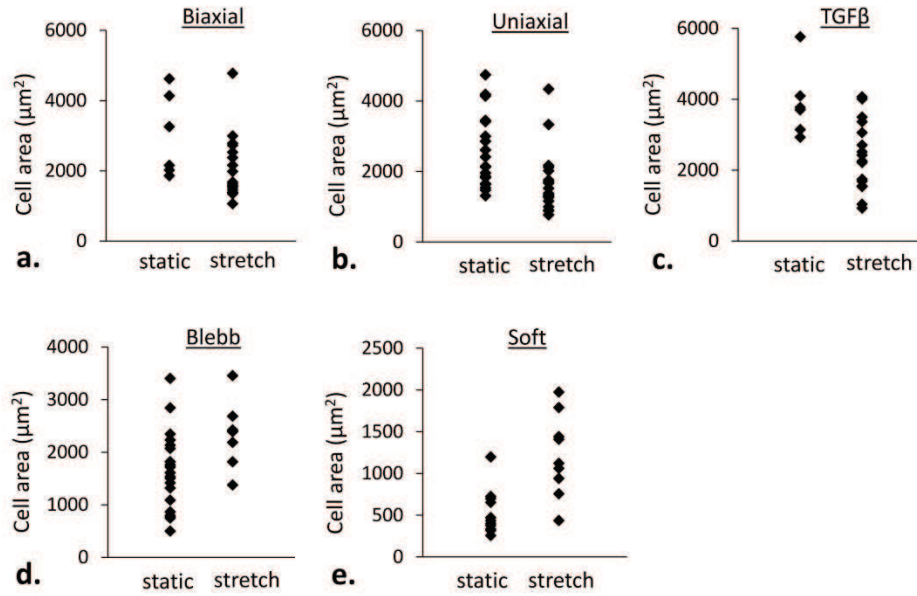
Supplemental Figure S6- scatterplots of traction force values for static control cells and stretched cells showing distributions of raw data. For cells under high pre-stress conditions (cultured on the 7.5 kPa substrate and stretched biaxially, uniaxially, or stretched uniaxially in the presence of TGF- β 1) average traction force decreased with stretch. The opposite was true for cells cultured in low pre-stress conditions. Cells that were treated with Blebbistatin or on the 0.6 kPa substrate increased average traction force with stretch



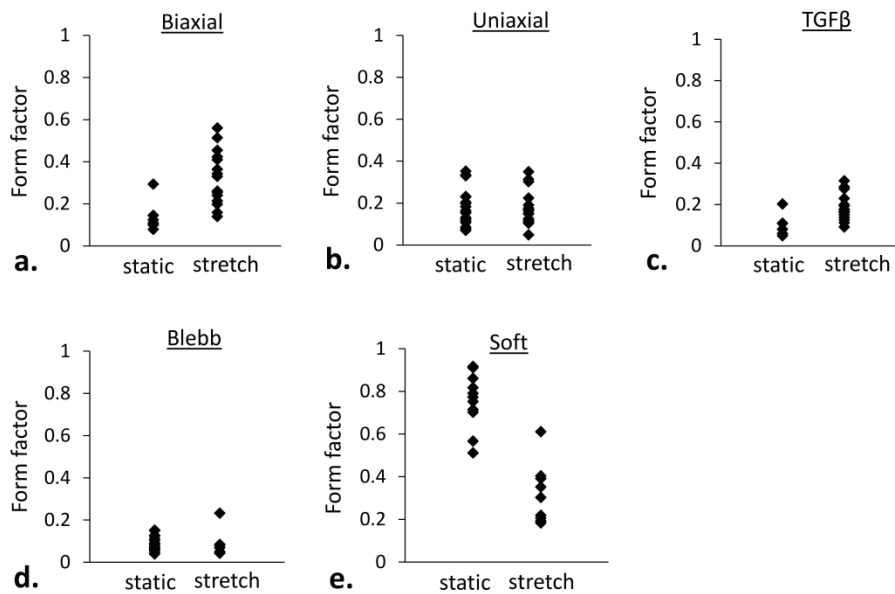
Supplemental Figure S7- scatterplots of maximum substrate stress values for static control cells and stretched cells showing distributions of raw data. For cells under high pre-stress conditions (cultured on the 7.5 kPa substrate and stretched biaxially, uniaxially, or stretched uniaxially in the presence of TGF- β 1) average maximum substrate stress decreased with stretch. The opposite was true for cells cultured in low pre-stress conditions. Cells that were treated with Blebbistatin or on the 0.6 kPa substrate increased average maximum substrate stress with stretch.



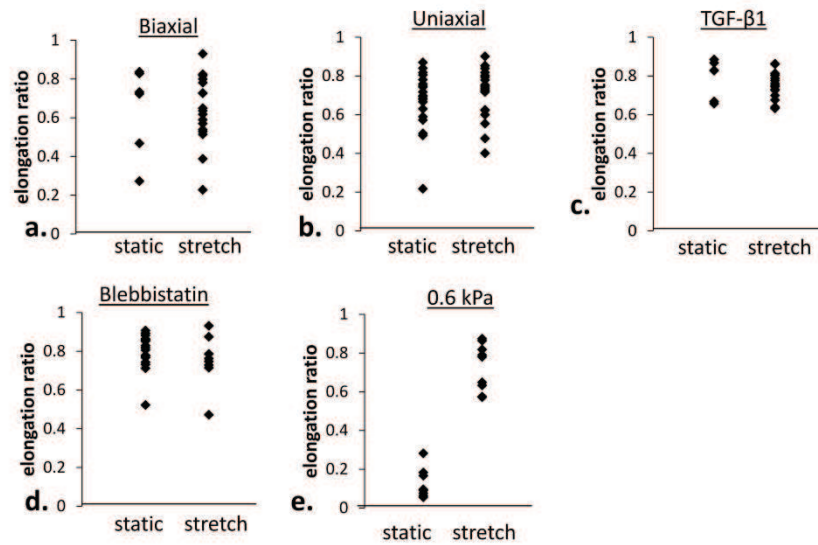
Supplemental Figure S8- scatterplots of contractile moment for static control cells and stretched cells showing distributions of raw data. For cells under high pre-stress conditions (cultured on the 7.5 kPa substrate and stretched biaxially, uniaxially, or stretched uniaxially in the presence of TGF- β 1) contractile moment followed traction force and decreased significantly in all groups. The opposite was true for cells cultured in low pre-stress conditions. Cells that were treated with Blebbistatin or on the 0.6 kPa substrate increased contractile moment with stretch. A negative contractile moment indicates a cell that is pulling inwards, while a positive contractile moment indicates a cell is pushing outward. Blebbistatin caused about half of the control cells and all of the stretched cells to have a positive contractile moment. It is possible with myosin motors inhibited, outward actin polymerization predominates creating the outward pushing motion. Numerical values of mean contractile force and significance are shown in table 1 of the manuscript.



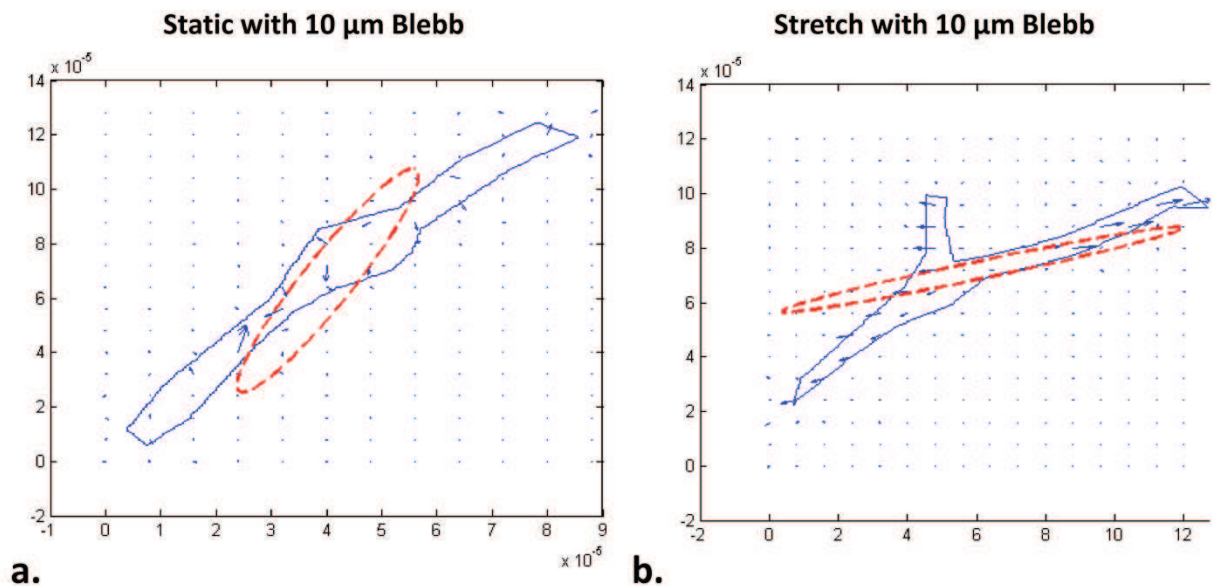
Supplemental Figure 9- scatterplots of cell area values for static control cells and stretched cells showing distributions of raw data. For cells under high pre-stress conditions (cultured on the 7.5 kPa substrate and stretched biaxially, uniaxially, or stretched uniaxially in the presence of TGF- β 1) average cell area with stretch. The opposite was true for cells cultured in low pre-stress conditions. Cells that were treated with Blebbistatin or on the 0.6 kPa substrate increased average cell area with stretch. Numerical values and significance are shown in table 1 of the manuscript.



Supplemental Figure S10- scatterplots of form factor values for static control cells and stretched cells showing distributions of raw data. Numerical values and significance are shown in table 1 of the manuscript.



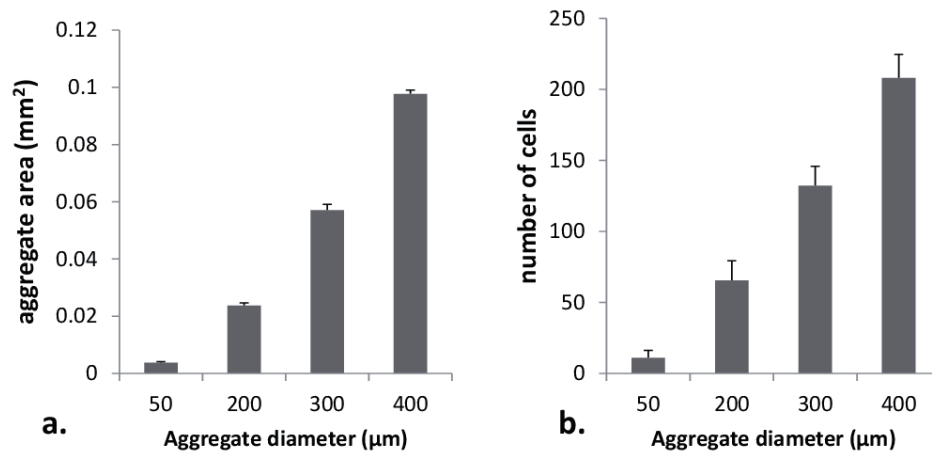
Supplemental Figure 11- scatterplots of extension ratio values for static control cells and stretched cells showing distributions of raw data. No changes in extension were seen with stretch except for the 0.6 kPa group, when increased cellular extension was significant. Numerical values and significance are shown in table 1 of the manuscript.



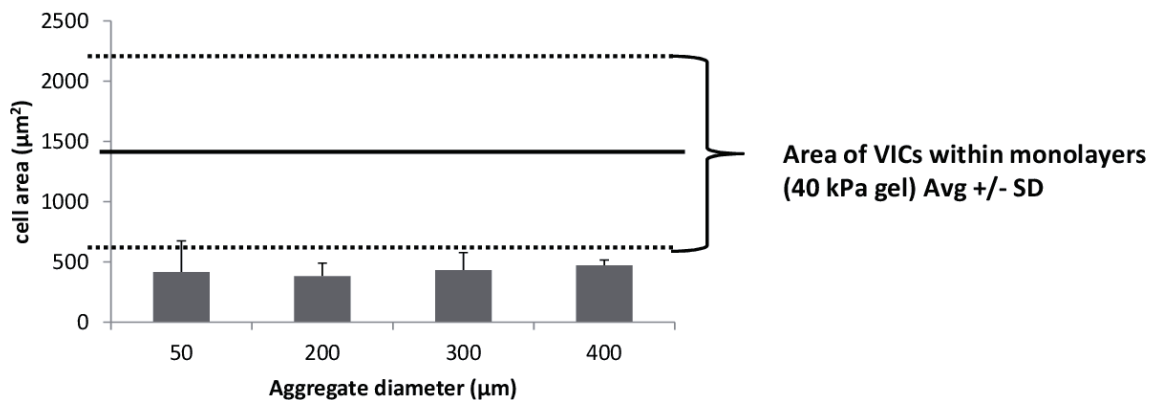
Supplemental Figure 12- Representative images of cell outline (in blue), displacement vectors (blue arrows), and contractile moment (red oval). a) For static cells treated with blebbistatin, half of the

cells had an inward contractile moment, while others had an outward contractile moment. Examination of displacement vectors shows localized regions with outward displacements and inward displacements. Whether the static cells had a positive or negative contractile moment appeared random and did not show a trend with time of data acquisition. b) Stretched cells all had outward pushing displacements and positive contractile moment.

Chapter 4: Supporting Information for a Controlled *In Vitro* Model of Calcific Aortic Valvular Disease



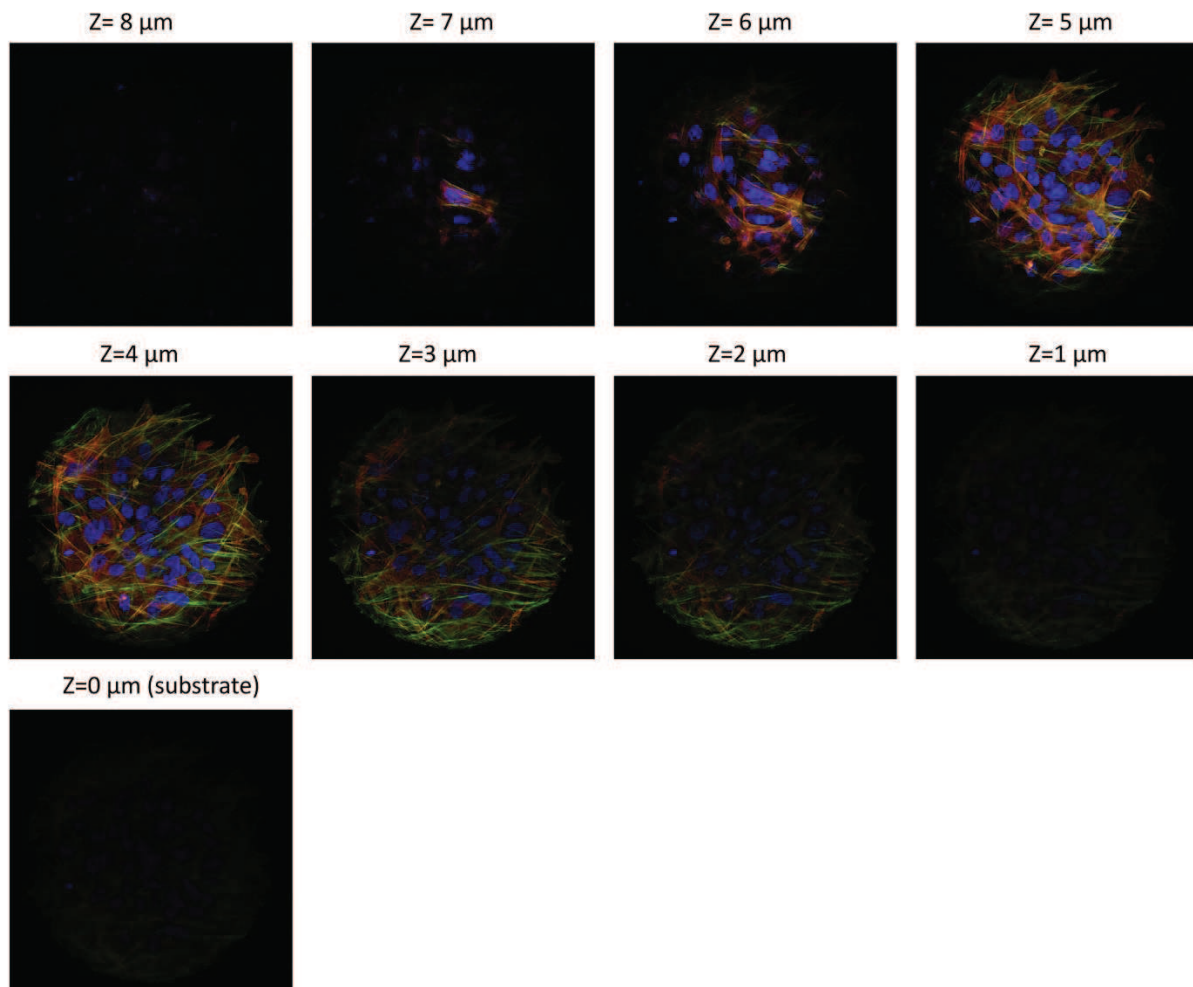
Supplementary Figure 4.1: Micro-contact printing method allows for tight control of aggregate size. a) Aggregates created with micro-contact printing have < 4% variability in size. This control over sizes allows for repeatable calcification time-courses b) Number of cells contained within the aggregate increases with aggregate size.



Supplementary Figure 4.2: Cell area of cells within aggregates does not change with aggregate geometry. Cell area was determined by measuring aggregate area and dividing the area by the number of nuclei within the aggregate.

Chapter 5: Supporting Information for The Distribution of Tension within Valvular Interstitial Cell Aggregates and Its Role in Disease Initiation

Representative confocal z-stack showing aggregates are monolayer.



Supplementary Figure- Z-stack of 200 μm aggregate on 38 kPa PA gel. Aggregates are believed to be monolayers as nuclei do not appear on top of one another. Additionally, aggregates are relatively thick, between 8-16 μm tall on average. Images shown above are 1 μm step size apart; aggregate height in this representative stack is 8 μm.

Appendix C: List of Copy Righted Material and Reprint Permissions

Appendix C.1: Chapter 2 Reprint Permissions

Figure 2.2 was previously published and is approved for noncommercial and educational use provided that the original source and the applicable copyright notice are cited.

Aortic-Valve Stenosis — From Patients at Risk to Severe Valve Obstruction
New England Journal of Medicine

Figure 2.5 was previously published in an open access journal and no permission is required from the authors or the publishers so long as the original authors and source are cited.

Hemodynamics and mechanobiology of aortic valve inflammation and calcification.
International Journal of Inflammation

Figure 2.5 was previously published and copy right permissions were obtained from publisher.

Investigating the role of substrate stiffness in the persistence of valvular interstitial cell activation
Journal of Biomedical Materials Research
License Number: 3776620008441

Figure 2.6- was previously published in an open-access article distributed under the terms of the Creative Commons Attribution License, which permits unrestricted use, distribution, and reproduction in any medium, provided the original author and source are credited.

Combining Dynamic Stretch and Tunable Stiffness to Probe Cell Mechanobiology *In Vitro Cell*

Figure 2.8 was previously published and copyright permissions were obtained from publisher

Figure 2.10 was previously published in an open-access article distributed under the terms of the Creative Commons Attribution License, which permits unrestricted use, distribution, and reproduction in any medium, provided the original author and source are credited.

Role of apoptosis in Disease
Aging

Figure 2.10 was previously published and copyright permissions were obtained from publisher

Figure 2.12 was previously published and copy right permissions were obtained from publisher.

Alpha-smooth muscle actin expression enhances cell traction force
Cytoskeleton
License Number: 3776590570933

Figure 2.13 was previously published and copy right permissions were obtained from publisher.

Decoupling Substrate Stiffness, Spread Area, and Micro-post Density: A Close Spatial Relationship between Traction Forces and Focal Adhesions

Biophysical Journal

License Number: 3776591081907

Figure 2.14 was previously published and permission is not required for reproduction in a thesis/dissertation.

Cell prestress. I. Stiffness and prestress are closely associated in adherent contractile cells

American Journal of Physiology-Cell Physiology

Figure 2.15 was previously published and is approved for noncommercial and educational use provided that the original source and the applicable copyright notice are cited.

Emergent Patterns of Growth Controlled by Multicellular Form and Mechanics.

Proceedings of the National Academy of Sciences of the United States of America

The following subsections originally appeared in *Cirka et al.* “Mechanoregulation of Valvular Interstitial Cell Life and Death” and are reproduced within this document with written permission from Begell Publishing House:

2.3 Valvular Interstitial Cell Mechanobiology

2.3.1 Cell-ECM and cell-cell connections

2.3.2 Mechanical characterization of VIC phenotype

2.3.3 Effect of substrate modulus on VIC phenotype and apoptosis

2.3.4 Cyclic stretch regulation of VIC phenotype and apoptosis

2.3.5 Integration of multiple mechanical signals

2.3.6 Interactions between mechanical and soluble stimuli

2.4 *In Vitro* Models of Calcific Aortic Valve Disease

2.4.1 Mechanoregulation of calcification

2.4.2 Mechanoregulation of apoptosis

